JAEA-Conf 2021-001
INDC(JPN)-207
DOI:10.11484/jaea-conf-2021-001

JAEA-Conf

Proceedings of the 2020 Symposium on Nuclear Data November 26-27, 2020, RIKEN Nishina Center, RIKEN Wako Campus, Wako, Saitama, Japan

(Eds.) Nobuaki IMAI and Hideaki OTSU

Nuclear Science and Engineering Center
Sector of Nuclear Science Research

March 2022

Japan Atomic Energy Agency

日本原子力研究開発機構

国立研究開発法人日本原子力研究開発機構　JAEA イノベーションハブ　研究成果利活用課
〒 319-1195　茨城県那珂郡東海村大字白方 2 番地 4
電話 029-282-6387, Fax 029-282-5920, E-mail:ird-support@jaea.go.jp

JAEA-Conf 2021-001
INDC(JPN)-207

Proceedings of the 2020 Symposium on Nuclear Data
November 26-27, 2020,
RIKEN Nishina Center,
RIKEN Wako Campus, Wako, Saitama, Japan

(Eds.) Nobuaki IMAI*[1] and Hideaki OTSU*[2]

Nuclear Science and Engineering Center, Sector of Nuclear Science Research,
Japan Atomic Energy Agency
Tokai-mura, Naka-gun, Ibaraki-ken

(Received November 17, 2021)

The 2020 Symposium on Nuclear Data was held on-site at RIBF Conference Hall in RIKEN Wako campus on November 26 to 27, 2020, combined with on-line connection conference. The symposium was organized by the Nuclear Data Division of the Atomic Energy Society of Japan (AESJ) in cooperation with Sigma Investigative Advisory Committee of AESJ, Nuclear Science and Engineering Center of Japan Atomic Energy Agency (JAEA), RIKEN Nishina Center, Center for Nuclear Study, The University of Tokyo (CNS), KEK Wako Nuclear Science Center (WNSC), School of Science, The University of Tokyo. In the symposium, six sessions were proposed and held: “Reactor theory and experiments” as a tutorial, “Accelerator Facilities and Nuclear Data’’, “Deep/Machine Learning and Nuclear Physics, Application to Nuclear Data’’, “Nuclear Medicine and Nuclear Pharmacy’’, “Fission, Heavy Ion Nuclear Spectroscopy’’, and “Nuclear Reaction Data’’ as lecture and discussion sessions. In addition, recent research progress on experiments, nuclear theory, evaluation, benchmark and applications were presented in the poster session. The total number of participants was 119, of which 62 were on-site participants. Each oral and poster presentation was followed by an active question and answer session. This report consists of total 40 papers including 15 oral and 25 poster presentations.

Keywords: Nuclear Data Symposium 2020, Experiments, Nuclear Theory, Nuclear Data Evaluation, Benchmark Test, Nuclear Data Applications

---

＊1 Center for Nuclear Study, The University of Tokyo(CNS)
＊2 RIKEN Nishina Center

JAEA-Conf 2021-001
INDC(JPN)-207

2020 年度核データ研究会報告集

2020 年 11 月 26 日～27 日
理化学研究所　和光キャンパス　埼玉県和光市

日本原子力研究開発機構　原子力科学研究部門　原子力基礎工学研究センター

（編）今井　伸明*[1]、大津　秀暁*[2]

（2021 年 11 月 17 日受理）

2020 年度核データ研究会は、2020 年 11 月 26 日～27 日に、埼玉県和光市にある理化学研究所和光キャンパスの RIBF 大会議室にて、オンライン併用の形式で開催された。本研究会は、日本原子力学会核データ部会が主催、日本原子力学会「シグマ」調査専門委員会、日本原子力研究開発機構（原子力機構）原子力基礎工学研究センター、理化学研究所仁科加速器科学研究センター（理研仁科センター）、東京大学原子核科学研究センター（CNS）、高エネルギー加速器研究機構和光原子核科学センター（KEK-WNSC）、東京大学理学部が共催した。今回、チュートリアルとして「原子炉の理論と実験」を、講演・議論のセッションとして、「加速器施設と核データ」、「深層/機械学習と原子核物理、核データへの応用」、「核医学、核薬学」、「核分裂、重イオン核分光」、「原子核反応データ」の 5 セッションを企画し実施した。さらに、ポスターセッションでは、実験、理論、評価、ベンチマーク、応用等、幅広い研究内容について発表が行われた。参加者総数は 119 名でそのうち現地参加は 62 名であった。それぞれの口頭発表及びポスター発表では活発な質疑応答が行われた。本報告集は、本研究会における口頭発表 15 件、ポスター発表 25 件の論文を掲載している。

キーワード：　2020 年度核データ研究会、実験、原子核理論、核データ評価、ベンチマークテスト、核データ応用

原子力科学研究所：〒319-1195　茨城県那珂郡東海村大字白方 2-4
＊1 東京大学原子核科学研究センター
＊2 理化学研究所仁科加速器科学研究センター

Contents

Poster Session

目次

ポスター発表論文

1. 2020 Symposium on Nuclear Data - Programme

Thursday 26 November 2020

Opening/Welcome - RIBF201 (10:30-10:40)
- Presenter: SANAMI Toshiya (KEK)

Facility - RIBF201 (10:40-12:20)
-Conveners: MIYATAKE Hiroari (IPNS, KEK)

Time	Title	Presenter
10:40	仁科センターの核データ活動/ Nuclear Data Activities in Nishina Center	SAKURAI Hiroyoshi (RIKEN Nishina Center for Accelerator-Based Science) IMAI Nobuaki (CNS, Univ. of Tokyo)
11:20	J-PARC における核変換に関連した核データ研究/ Nuclear data study for Accelerator Driven System at J-PARC	MEIGO Shin-ichiro (J-PARC/JAEA)
11:50	大強度重陽子加速器 ImPACT2017 の提案/ Proposal of 1 A class deuteron single cell linac	OKUNO Hiroki (RIKEN Nishina Center for Accelerator-Based Science)

Lunch - RIBF201 (12:20-13:30)

Nuclear Physics1 - RIBF201 (13:30-15:00)

-Conveners: Aritomo, Yoshihiro (Kindai University)

Time	Title	Presenter
13:30	高励起原子核の核分裂確率の統一的な記述/ Unified description of the fission probability for highly excited nuclei	IWAMOTO Hiroki (JAEA) MEIGO Shin-ichiro (J-PARC/JAEA)
14:00	KISS での核分光実験/ Nuclear spectroscopy at KISS	HIRAYAMA Yoshikazu (IPNS, KEK)
14:30	JAEA タンデム加速器でのアインスタイニウムを用いた核分裂実験	HIROSE Kentaro (JAEA)

Coffee - RIBF201 (15:00-15:20)

Conference Photo - RIBF201 (15:00-15:10)

Nuclear Medicine - RIBF201 (15:20-16:50)
-Conveners: MINATO Futoshi (JAEA)

Time	Title	Presenter
15:20	理研 RI ビームファクトリーにおける RI の製造と応用 ～新元素の探索からがんの診断・治療まで～/ Production and Applications of Radioisotopes at RIKEN RI Beam Factory - Search for New Elements through Diagnosis and Therapy of Cancer	HABA Hiromitsu (Nishina Center for Accelerator-Based Science, RIKEN)
15:50	荷電粒子入射反応による医療用 RI 生成断面積測定実験/ Measurements of production cross sections of medical radioisotopes via charged-particle induced reactions	AIKAWA Masayuki (Hokkaido University)
16:20	九州大学における加速器中性子源を用いた RI 製造研究の進捗 2020/ Development of Radioisotopes Production Method by Accelerator-based Neutron: Activity at Kyushu University 2020	KIN Tadahiro (Kyushu University)

Poster - RIBF201 (16:50-20:30)

Title	Presenter
微視的平均場模型を用いた U-236 の核分裂経路の研究/ Study of the fission path energy of U-236 using microscopic mean-field model	FUJIO Kazuki (Tokyo Institute of Technology)
^{258}Md 原子核による核分裂過程の理論解析/ Theoritical analysis of the fission process by ^{258}Md	ISHIZAKI Shoma (Kindai University)
準核分裂における質量と角度の相関の起源/ The origin of correlation between mass and angle in quasi-fission	AMANO Shota (Kindai University)
動力学模型による核分裂過程での中性子放出/ Neutron emission during fission process by dynamical model	YAMASAKI Ryota (Kindai University)
動力学模型による中性子過剰核の核分裂計算：r プロセスシミュレーションに向けて/ The fission fragments of neutron-rich nuclei by the Langevin method toward application to r-process calculations	OKUBAYASHI Mizuki (Kindai University)
二体分解反応における非共鳴バックグラウンドの理論的評価/ Theoretical evaluation of non-resonant background strength in binary breakup reaction	NAKAMOTO Riu (Kansai University)
JENDL-5 のためのコバルト 59 に対する中性子核データの評価/ Evaluation of Neutron Nuclear Data on Cobalt-59 for JENDL-5	IWAMOTO Nobuyuki (JAEA)
JENDL/AD-2017 から作成した SCALE6.2 の ORIGEN ライブラリ/ SCALE6.2 ORIGEN library produced from JENDL/AD-2017	KONNO Chikara (JAEA)

米国フェルミ国立加速器研究所(FNAL) における 120 GeV 陽子を用いた弾き出し損傷断面積の実験計画/ Experimental plan for displacement damage cross sections using 120-GeV protons at FNAL	IWAMOTO Yosuke (JAEA)
異なる崩壊データライブラリを用いた燃料デブリから放出される光子スペクトルの比較/ Comparison of photon spectra emitted from fuel debris using different decay data libraries	MATSUMURA Taichi (JAEA)
FFAG 加速器を用いた加速器駆動核変換システムのための核データ測定: 核破砕中性子測定/ Experimental program of nuclear data for accelerator-driven nuclear transmutation system using FFAG accelerator – First subprogram: spallation neutron measurement	NAKANO Keita (JAEA)
ANNRI での高速中性子断面積測定のための中性子フィルターシステムの開発/ Neutron Filtering System for Fast Neutron Cross-Section Measurement at ANNRI	ROVIRA LEVERONI Gerard (JAEA)
試料回転法を用いた中性子捕獲断面積の高精度化のための新たな手法/ A New Method to Reduce Systematic Uncertainties of Capture Cross Section Measurement Using a Sample Rotation System	KODAMA Yu (Tokyo Institute of Technology)
高強度中性子ビームを用いた核データ測定のための中性子検出器の開発/ Development of a neutron detector for nuclear data measurement using high-intensity neutron beam	NAKANO Hideto (Tokyo Institute of Technology)
BNCT のための絶対熱外・高速中性子束強度測定検出器の開発/ Development of Absolute Epi-thermal and Fast Neutron Flux Intensity Detectors for BNCT	AOKI Kazushi (Osaka Univ.)
14MeV 中性子による大角度弾性散乱反応断面積ベンチマーク実験のための放射化検出器の最適化/ Optimization of Activation Detector for Benchmark Experiment of Large-angle Elastic Scattering Reaction Cross Section by 14MeV Neutrons	TAKEHARA Ryohei (Osaka Univ.)
Am-Be 中性子線源を用いたコンクリートの含水量非破壊測定法の実験的検証/ Nondestructive Determination of Water Content in Concrete Using Am-Be Neutron Source - Experimental Verification -	MIYAJI Yoshihiro (Osaka Univ.)
16.6MeV における中重核の光中性子生成に対する JENDL/PD-2016.1 と実験データの二重微分断面積の比較/ Comparison of double-differential cross sections between JENDL/PD-2016.1 and experimental data for photo-neutron production of medium-heavy nuclei at 16.6 MeV	TRAN Kim Tuyet (SOKENDAI/KEK)
原子炉廃止措置におけるクリアランス検認に必要な放射化放射能量の核データに由来する不確かさ評価手法の開発/ Development of Evaluation Method of Uncertainty of Radioactivity by Propagating Nuclear Data Covariance for Clearance Verification in Decommissioning of Nuclear Power Plants	AMITANI Tatsuki (Tokyo Institute of Technology)

PHITS による p-Li 反応を用いた中性子源 RANS-II の放射線場特性に関する研究/ Study on characteristics of neutron and γ-ray fields at compact neutron source RANS-II facility by simulation by the PHITS code	SUGIHARA Kenta (RIKEN Nishina Center, Kyushu University)
^{nat}Lu 標的に対する 0.4, 1.3, 2.2, 3.0 GeV 陽子入射による核種生成断面積/ Nuclide production cross sections of ^{nat}Lu target irradiated with 0.4-, 1.3-, 2.2-, 3.0-GeV protons	TAKESHITA Hayato (Kyushu University)
COMET Phase-I 実験のための粒子線束と残留放射能の評価/ Estimation of Flux and Residual Radioactivity for the COMET Phase-I Experiment	TOKUNAGA Naoki (Kyushu University)
固体と液体状態での Sn-Pb 合金の全断面積測定/ Measurement of neutron total cross sections of Sn-Pb alloys in solid and liquid states	UEMURA Takuya (Kyoto University)
高放射性核種 ^{90}Sr の陽子及び重陽子誘起反応による核変換に向けた研究/ Research for nuclear transmutation of high-radiotoxic nuclide ^{90}Sr via proton- and deuteron-induced reactions	MATSUMURA Riku (Saitama University)
^{nat}Lu(p,xn)および ^{nat}Lu(d,xn)反応による ^{175}Hf の生成断面積の測定/ Production cross sections of ^{175}Hf in the ^{nat}Lu(p,xn) and ^{nat}Lu(d,xn) reactions	KOMORI Yukiko (RIKEN Nishina Center)
京都大学臨界集合体実験装置と KURNS-LINAC 施設での短寿命 FPγ 線の検出/ Detection of Gamma Ray from Sort-Lived Fission Products at KUCA and KURNS-LINAC	NAUCHI Yasushi (Central Research Institute of Electric Power Industry)

,

Friday 27 November 2020

Nuclear Physics2 - RIBF201 (09:00-10:30)

-Conveners: Terada Kazushi (Kyoto University)

Time	Title	Presenter
09:00	^{93}Zr 及び ^{93}Nb に対する陽子・重陽子入射核破砕反応からの同位体生成/ Isotope production in spallation reaction of ^{93}Zr and ^{93}Nb induced by proton and deuteron	NAKANO Keita (JAEA)
09:30	減速 RI ビームによる原子核物理の展開/ Development of energy-degraded RI beam and expansion of nuclear reaction studies	MICHIMASA Shin'ichiro (CNS, The Univ. of Tokyo)
10:00	重陽子入射反応の理論解析と重陽子核反応データベースの開発/ Theoretical analysis of deuteron-induced reactions and development of deuteron nuclear database	NAKAYAMA Shinsuke (JAEA)

Coffee - RIBF201 (10:30-10:50)

Tutorial - RIBF201 (10:50-12:20)

-Conveners: Chiba Go (Hokkaido University)

Time	Title	Presenter
10:50	原子炉理論の入門/ Introduction to Nuclear Reactor Theory	ENDO Tomohiro (Nagoya University)
11:40	研究炉における炉物理実験の役割と現状について/ Roles and current status of reactor physics experiment in research reactors	PYEON Cheol Ho (Kyoto University)

Lunch - RIBF201 (12:20-13:30)

Deep Learning - RIBF201 (13:30-15:30)

-Conveners: Hiroyuki Koura

Time	Title	Presenter
13:30	深層学習と基礎科学研究への応用について/ Deep Learning for Basic Science	TAKI Masato (Rikkyo University)
14:00	原子核殻模型におけるデータ駆動型アプローチ/ Data-driven approaches for nuclear shell-model calculations	SHIMIZU Noritaka (The University of Tokyo)
14:30	機械学習を用いた核データの生成/ Nuclear data generation using machine learning	IWAMOTO Hiroki (JAEA)

15:00	核データ量産化を目指した RI ビーム実験データ自動較正手法の探求/ Exploration of automated data processing for mass production of nuclear data at RIBF	KAWASE Shoichiro (Kyushu University)

Closing Remarks - RIBF201 (15:30-16:00)

- Presenters: SANAMI Toshiya (KEK); WATANABE Yukinobu (Kyushu University)

FacilityTour - RIBF201 (16:00-17:30)

2. Nuclear Data Activities in Nishina Center

Hiroyoshi SAKURAI †

RIKEN Nishina Center for Accelerator-Based Science
2-1 Hirosawa, Wako, Saitama, 351-0198, Japan
†Email: sakurai@ribf.riken.jp

The nuclear data activities at the heavy-ion accelerator facility "Radioactive Isotope Beam Factory" operated by RIKEN Nishina Center for Accelerator-Based Science are introduced. The activities extending throughout a whole of nuclear chart are categorized into nuclear physics and nuclear engineering. For each of them, present status is reported and special emphasis would be given to recent highlights selected. Future directions of the nuclear data programs are presented.

1 Introduction

In 2006, RIKEN Nishina Center for Accelerator-Based Science (RNC) was established to organize the world-prestigious heavy ion accelerator facility "Radioactive Isotope Beam Factory (RIBF)" [1]. The RIBF facility was constructed as one of the third-generation in-flight facilities to aim at three goals: 1) to discover new quantum phenomena under a large isospin asymmetry through investigating nuclear structure in very neutron-rich nuclei, 2) to elucidate the r-process path in explosive processes of the universe, and 3) to develop new applied sciences based on high energy radioactive isotope (RI) beam. Since the RIBF started operational in 2007, multitudes of data on the nuclear structure and reactions have been produced with RIBF as a nuclear data factory.

The RIBF facility delivers a variety of heavy ion beams of hydrogen to uranium at an energy ranging widely from several MeV/u to 345 MeV/u, and unique experimental devices and spectrometers are equipped [2]. As shown in Fig. 1, beams accelerated at three cyclotrons (AVF, RRC and SRC) and one liniac (SRILAC) serve experimental programs at gas-filled recoil separators (GARIS-II, III), in-gas-cell laser ion source (KISS), and in-flight separators (CRIB, RIPS, BigRIPS). RI beams produced at BigRIPS are delivered to three spectrometers (ZeroDegree, SAMURAI and SHARAQ), and to a storage ring for mass measurement (Rare-RI Ring). The facility has a setup of SCRIT to realize electron-RI scattering, where RIs are produced at an Isotope Separator On-Line (ISOL) based on electron induced-fission.

Nuclear data activities at the RIBF facility have extended throughout a whole of the nuclear chart from a light-mass to a super-heavy region and from stable to proton- and neutron-rich nuclei. The data are in general categorized into reaction data and structure data. The reaction data at RIBF stem from RI productions, secondary reactions with RI beams, and electron-RI scattering. Concerning the structure data, nuclear properties of ground and excited states are obtained at RIBF via spectroscopy of mass, decay, missing-mass, invariant-mass and in-beam gamma. The data produced at the RIBF have been compiled and evaluated by the world nuclear database activities guided by IAEA. JCPRG in Hokkaido University and RNC have established an MoU to cooperate together in nuclear data activities of charged-particle induced reactions.

In this article, the nuclear data activities at RIBF are reviewed. The activities are divided into nuclear physics and nuclear engineering, and for each of them, present status and recent highlights are presented. Future directions of the nuclear data activities at RIBF are discussed.

2 Nuclear Physics

In this section, very recent highlights and activities in nuclear physics with RIBF are demonstrated. First, the activities of superheavy element physics are introduced and second, recent achievements in studying

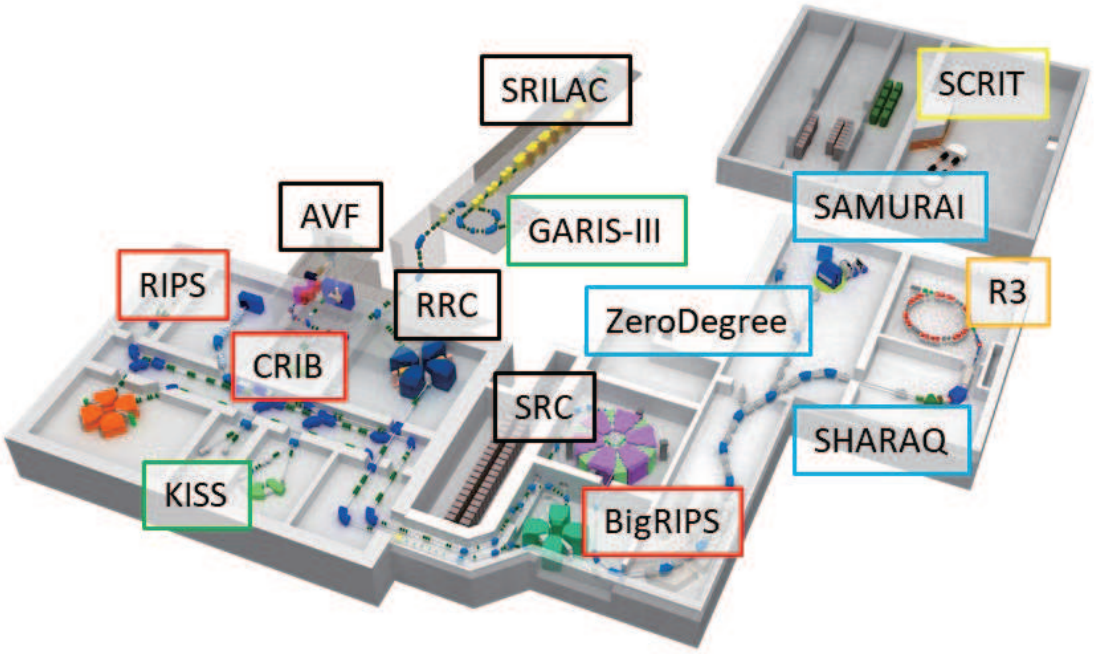

Figure 1: Facility layout of RIBF.

exotic nuclei are shown.

2.1 Superheavy Element

One of the great achievements at RIBF is discovery of Element 113, which was named "Nihonium" by K. Morita and his colleagues in 2016. The superheavy element was produced and identified in three events observed in 2004–2012. The last event in 2012 [3] showed successive alpha-decay down to ^{254}Md, and gave a direct evidence that ^{278}Nh was produced.

The ^{278}Nh isotope was made via the cold fusion reaction with combination of the RILAC linear accelerator and the gas-filled recoil separator GARIS. To conduct further production of superheavy elements, a new separator GARIS-II [4] was designed and constructed to achieve a higher transmission efficiency in the hot fusion reaction, compared with that of GARIS. A KEK-RIKEN collaboration has been formed to measure mass of heavy elements via MR-TOF technique at GARIS-II, and has published results, for example, around Z=100 [5]. The GARIS-II spectrometer was moved to accept heavy-ion beams from RRC in 2017.

A new setup for production of new elements has been established. First, the intensity and energy upgrade of the RILAC was completed in 2020 with 28GHz ECR ion source [6] and super conducting rf-cavities [7], both newly installed. GARIS-III was newly constructed and installed to be coupled with the upgraded RILAC. GARIS-III was designed to have the same performances as of GARIS-II. A new program to search for Element 119 started at the end of 2020.

2.2 Exotic Nuclei

Exotic nuclei with a large isospin-asymmetry have been produced as intense RI beams at RIBF. High energy heavy-ion beams accelerated at SRC are converted to unstable nuclei at production targets via projectile-fragmentation or fission reactions and the nuclei of interest are collected and separated at BigRIPS, then the RI beams are delivered to several experimental devices.

Since 2007, more than 140 new isotopes have been discovered at BigRIPS. One of recent highlights is discovery of the particle stability of ^{60}Ca and other neighboring nuclei [8]. The neutron-drip line for the fluorine and neon isotopes was determined in 2019 [9], and the drip line has been extended for the first time in 20 years.

Shell evolution has been investigated via in-beam gamma spectroscopy, decay-spectroscopy and mass-spectroscopy. Very selected highlights are discovery of new magicity at N=34 in the neutron-rich Ca isotopes [10], double magicity of ^{78}Ni [11], and exotic structure in ^{40}Mg [12]. Shell evolution and shape

deformation was found in ^{75}Cu by employing a new technique of spin-aligned RI beams [13]. Mass spectroscopy of neutron-rich Ca and Ti isotopes confirmed the magicity of N=34 [14], and discovered a deformation region in the neutron-rich Ti isotopes [15]. Neuton-rich nuclei with respect to the double magic nucleus ^{132}Sn have been investigated and all the data obtained so far indicate large shell gaps either at Z=50 or at N=82, and no magicity loss has been found. In 2020, the first high-resolution gamma spectroscopy was carried out with germanium tracking detectors under the HiCARI collaboration.

RIBF has published bunch of half-life data for neutron-rich nuclei [16, 17, 18], which are necessary to understand the r-process nucleosynthesis. The abundance calculation with the new data could reproduce reasonably the r-process abundance pattern, especially for A∼120 region and A∼140-160 region. The third data set [18] has striking and large drops of half-lives at N=97 for Ce, Pr, Nd and Sm and at N=105 for Eu, Gd, Tb and Dy, and has a direct impact in the r-process abundance calculations affecting almost all mass numbers between A=150 and 170.

The new form of nuclei have been found such as two deformed halo-nuclei, ^{31}Ne [19, 20] and ^{37}Mg [21, 22], and two-neutron halo in ^{29}F [23], all of which are located in the deformation region of $9\leq Z\leq 12$ and $20\leq N\leq 28$. Exotic particle-unbound nuclei have been investigated in a light neutron-rich region. Candidate of 'tetra' neutron state was observed with missing mass spectroscopy [24]. This work has made a great trigger to investigate very exotic few-body systems such as ^{7}H. Invariant mass spectroscopy successfully observed the ground state and 2^+ state in ^{26}O [25], and ^{26}O was found to be well-deformed and a barely unbound system beyond the drip line.

Equation-of-State (EOS) in nuclear matter, especially at a high density and high isospin asymmetry, has been highly desired to understand the structure of neutron-stars and to analyze gravitation wave. When the nuclear matter density is increased, many-body forces such as three nucleon force (3NF) become significant in EOS. At RIBF, polarized deuteron + proton elastic scattering has been studied to obtain $T = 1/2$ channel of 3NF [26]. The other works for EOS have been conducted such as a study of Gamow-Teller resonance in ^{132}Sn [27].

3 Nuclear Engineering

The incident of Fukushima Dai-ichi Unit in 2011 has given a trigger to nuclear physicists in Japan to consider possible contributions to nuclear engineering. In 2014, a reaction study with intense ^{137}Cs and ^{90}Sr beams at RIBF was conducted to seek for a transmutation path way to reduce radioactive waste [28, 29]. This experiment initiated a large project, which was awarded ImPACT grant [30] running in fiscal year of 2014-2018. The project focused accelerator-based transmutation for long-lived fission products (LLFPs) in high-level radioactive waste, and conducted research and development for partitioning, reaction data and theory, reaction database, and accelerator system. In the ImPACT project, RIKEN was in charge of studies for nuclear reactions, and also of accelerator developments.

As shown in Fig. 2, based on intense RI beams available at RIBF, a variety of reaction studies were organized with LLFPs such as ^{107}Pd and ^{93}Zr [31, 32, 33, 34, 35]. So called 'inverse kinematics' technique was employed to obtain spallation reaction data. The advantage of the inverse kinematics technique gives clear particle identification for reaction products, and easy control of RI beam energies for study of energy-dependence. In addition, we do not have to prepare RI targets but stable-isotope targets such as protons and deuterons. All these advantages of inverse kinematics lead to nice quality of the data at RIBF.

The reaction study in the ImPACT program was managed under a large domestic collaboration with University of Tokyo, Tokyo Institute of Technology, Kyushu University, Miyazaki University and RIKEN. All the major spectrometers at RIBF, ZeroDegree, SAMURAI and SHARAQ were utilized to identify and analyze reaction products. Zerodegree is suitable for inclusive measurements with relatively heavy fragments. SAMURAI has a wide acceptance in both momentum and scattering angle, hence exclusive measurements were performed to detect reaction products as well as neutrons in projectile frame. At SHARAQ spectrometer, CNS, University of Tokyo and RIKEN worked together to develop an efficient deceleration scheme for RI beams. Study at low energy reactions at ∼20 MeV/u [36, 37], and a new device "OEDO" was installed in the SHARAQ beam line. At the new setup, incomplete fusion reaction data and (d, p) reaction data were obtained with combination of OEDO and SHARAQ, and the data are being prepared for submission.

All these data are very useful to stimulate theoretical works and to improve simulation tools. The reaction data were evaluated by the JAEA nuclear data group and a new data library 'JENDL/ImPACT-

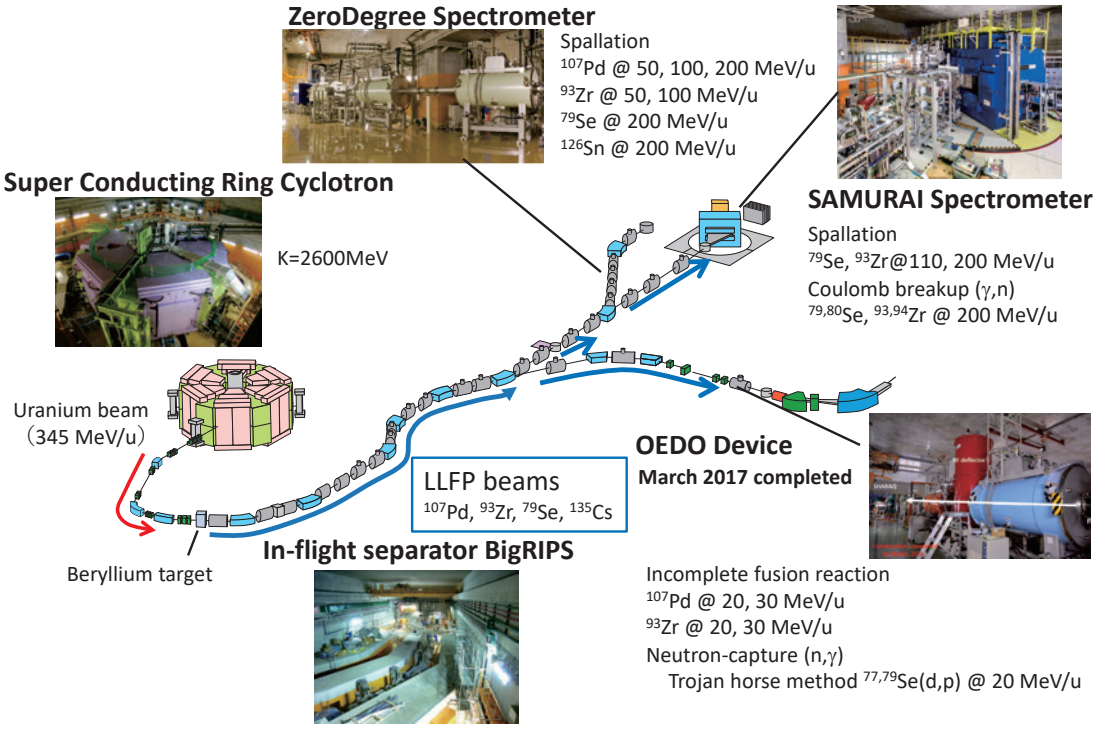

Figure 2: Reaction study for long-lived fission products at RIBF in 2014–2017.

2018' for proton- and neutron-induced reactions up to 200 MeV/u was released [38]. The data library has been a package of the PHITS simulator [39].

The improved simulation tool gave a strategy for LLFP transmutation, and a new transmutation scheme with high-energy neutron produced via deuteron breakup was considered, and a new accelerator scheme delivering 1-ampere deuteron beams has been proposed [40]. In addition, the RIKEN accelerator staff members successfully developed a quarter-wave superconducting RF cavity for efficient acceleration of charged particles [41]. The other transmutation scheme was discussed with 14 MeV neutron produced via muon catalyzed fusion with MERIT [42], that requires negative pion production cross sections with deuteron beams for further designing works.

4 Summary and Outlook

In summary, it would be emphasized that the RIBF facility is the nuclear data factory. Since 2007, RIBF has produced bunch of data of nuclear reaction and structure in both nuclear physics and nuclear engineering, especially for shell evolution, the r-process path, new form of nuclei, EOS and high-level radioactive waste problem.

Unique features of RIBF would be demonstrated to give multitudes of opportunities adapting any demands of nuclear data. RIBF delivers a variety of heavy-ion beams of hydrogen to uranium. Energy of the beams ranges several MeV/u to 345 MeV/u to be employed for any types of reactions. The beams are intense enough to conduct reaction studies and to artificially produce RIs from light and superheavy elements. These powerful beams have been utilized to produce secondary beams of RIs. Several experimental devices serve to separate, identify and analyze reaction products.

In future, the nuclear engineering community would be further encouraged to promote the LLFP reaction data project, and if necessary, to study fission reaction and precise decay measurement for decay heat and neutron-emission probability necessary in designing nuclear reactors, by utilizing RI beams. The RIBF intensity upgrade is planned by installing new charge stripper rings [43]. More intense heavy-ion beams would create more opportunities for reaction study such as (d, p) reaction with low energy RI beams to study neutron-capture reaction, and for reaction study with minor actinides.

References

[1] Yano, Y., The RIKEN RI Beam Factory Project: A status report, *Nucl. Instrum. Methods Phys. Res., Sect. B* 261 (2007) 1009.

[2] Introduction to RI Beam Factory and Users' Information, https://www.nishina.riken.jp/ribf/index.html (accessed:2021-11-17).

[3] Morita, K., Morimoto, K., Kaji, D., *et al.*, New result in the production and decay of an isotope, ^{278}113, of the 113th element, JPSJ 81 (2012) 103201.

[4] Kaji, D., Morimoto, K., Sato, N., *et al.*, Gas-filled recoil ion separator GARIS-II, *Nucl. Instrum. Methods Phys. Res., Sect. B* 317 (2013) 311.

[5] Ito, Y., Schury, P., Wada, M., *et al.*, First Direct Mass Measurements of Nuclides around Z=100 with a Multireflection Time-of-Flight Mass Spectrograph PRL 120 (2018) 152501.

[6] Nagatomo, T., Higurashi, J., Ohnishi, A., *et al.*, NEW 28-GHz SUPERCONDUCTING ELECTRON CYCLOTRON RESONANCE ION SOURCE FOR SYNTHESIZING SUPER-HEAVY ELEMENTS WITH Z >118 Prof. of 23th Int. Workshop on ECR Ion Sources (ECRIS2018), TUA3, 53 (2018).

[7] Yamada, K., Dantsuka, T., Imao, H., *et al.*, Construction of Superconducting Linac Booster for Heavy-Ion Linac at RIKEN Nishina Center, Prof. 19th Int. Conf. on RF Superconductivity (SRF2019), TUP037, 502 (2019).

[8] Tarasov, O.B., Ahn, D.S., Bazin, D., *et al.*, Discovery of ^{60}Ca and Implications For the Stability of ^{70}Ca, *Phys. Rev. Lett.* 121 (2018) 022501.

[9] Ahn, D.S., Fukuda, N., Geissel, H., *et al.*, Location of the Neutron Dripline at Fluorine and Neon, *Phys. Rev. Lett.* 123 (2019) 212501.

[10] Steppenbeck, D., Takeuchi, S., Aoi, N., *et al.*, Evidence for a new nuclear emagic numberf from the level structure of ^{54}Ca *Nature* 502 (2013) 207.

[11] Taniuchi, R., Santamaria, C., Doornenbal, P., *et al.*, ^{78}Ni revealed as a doubly magic stronghold against nuclear deformation *Nature* 569 (2019) 53.

[12] Crawford, H.L., Fallon, P., Macchiavelli, O., *et al.*, First Spectroscopy of the Near Drip-line Nucleus ^{40}Mg, *Phys. Rev. Lett.* 122 (2019) 052501.

[13] Ichikawa Y., Nishibata, H., Tsunoda, Y., *et al.*, Interplay between nuclear shell evolution and shape deformation revealed by the magnetic moment of ^{75}Cu *Nature Physics* 15 (2019) 321.

[14] Michimasa, S., Kobayashi, M., Kiyokawa, Y., *et al.*, Magic Nature of Neutrons in ^{54}Ca: First Mass Measurements of $^{55-57}$Ca, *Phys. Rev. Lett.* 121 (2018) 022506.

[15] Michimasa, S., *et al.*, Mapping of a New Deformation Region around ^{62}Ti, *Phys. Rev. Lett.* 125 (2020) 122501.

[16] Nishimura, S., Li, Z., Watanabe, H., *et al.*, β-Decay Half-Lives of Very Neutron-Rich Kr to Tc Isotopes on the Boundary of the r-Process Path: An Indication of Fast r-Matter Flow, *Phys. Rev. Lett.* 106 (2011) 052502.

[17] Lorusso, G., Nishimura, S., Xu, Z.Y., *et al.*, β-Decay Half-Lives of 110 Neutron-Rich Nuclei across the N=82 Shell Gap: Implications for the Mechanism and Universality of the Astrophysical r Process, *Phys. Rev. Lett.* 114 (2015) 192501.

[18] Wu, J., Nishimura, S., Lorusso, G., *et al.*, 94 β-Decay Half-Lives of Neutron-Rich $_{55}$Cs to $_{67}$Ho: Experimental Feedback and Evaluation of the r-Process Rare-Earth Peak Formation, *Phys. Rev. Lett.* 118 (2017) 072701.

[19] Nakamura, T., Kobayashi, N., Kondo, Y., *et al.*, Halo Structure of the Island of Inversion Nucleus ^{31}Ne, *Phys. Rev. Lett.* 103 (2009) 262501.

[20] Takechi, M., Otsubo, T., Fukuda, M., *et al.*, Interaction cross sections for Ne isotopes towards the island of inversion and halo structures of ^{29}Ne and ^{31}Ne, *Phys. Lett.* B 707 (2012) 357.

[21] Kobayashi, N., Nakamura, T., Kondo, Y., *et al.*, Observation of a p-Wave One-Neutron Halo Configuration in ^{37}Mg, *Phys. Rev. Lett.* 112 (2014) 242501.

[22] Takechi, M., Suzuki, S., Nishimura, D., *et al.*, Evidence of halo structure in ^{37}Mg observed via reaction cross sections and intruder orbitals beyond the island of inversion, *Phys. Rev.* C 90 (2014) 061305(R).

[23] Bagchi,S., Kanungo, R., Tanaka, Y.K., *et al.*, Two-Neutron Halo is Unveiled in ^{29}F, *Phys. Rev. Lett.* 124 (2020) 222504.

[24] Kisamori, K., Shimoura, S., Miya, H., *et al.*, Candidate Resonant Tetraneutron State Populated by the ^{4}He(^{8}He,^{8}Be) Reaction, *Phys. Rev. Lett.* 116 (2016) 052501.

[25] Kondo, Y., Nakamura, T., Tanaka, R., *et al.*, Nucleus ^{26}O: A Barely Unbound System beyond the Drip Line, *Phys. Rev. Lett.* 116 (2016) 102503.

[26] Sekiguchi, K., Witala, H., Akieda, T., *et al.*, Complete set of deuteron analyzing powers from $\vec{d}p$ elastic scattering at 190 MeV/nucleon *Phys. Rev.* C 96 (2017) 064001.

[27] Yasuda, J., Sasano, M., Zegers, R. G. T., *et al.*, Extraction of the Landau-Migdal Parameter from the Gamow-Teller Giant Resonance in ^{132}Sn, *Phys. Rev. Lett.* 121 (2018) 132501.

[28] Wang, H., Otsu, H., Sakurai, H., *et al.*, Spallation reaction study for fission products in nuclear waste: Cross section measurements for ^{137}Cs and ^{90}Sr on proton and deuteron *Phys. Lett.* B 754 (2016) 104.

[29] Sun, X. H., Wang, H., Otsu, H., *et al.*, Spallation and fragmentation cross sections for 168 MeV/nucleon ^{136}Xe ions on proton, deuteron, and carbon targets *Phys. Rev.* C 101 (2020) 064623.

[30] ImPACT: "Reduction and Resource Recycling of High-level Radioactive Waste through Nuclear Transmutation", https://www.jst.go.jp/impact/hp_fjt/en/ (accessed:2021-11-17).

[31] Wang, H., Otsu, H., Sakurai, H., *et al.*, Spallation reaction study for the long-lived fission product ^{107}Pd, *Prog. Theor. Exp. Phys.* 2017 (2017) 021D01.

[32] Kawase, S., Nakano, K., Watanabe, Y., *et al.*, Study of proton- and deuteron-induced spallation reactions on the long-lived fission product ^{93}Zr at 105 MeV/nucleon in inverse kinematics, *Prog. Theor. Exp. Phys.* 2017 (2017) 093D03.

[33] Nakano, K., Watanabe, Y., Kawase, S., *et al.*, Isotope production in proton-, deuteron-, and carbon-induced reactions on ^{93}Nb at 113 MeV/nucleon *Phys. Rev.* C 100 (2019) 044605.

[34] Takeuchi, S., Nakamura T., Shikata, M., *et al.*, Coulomb breakup reactions of ^{93,94}Zr in inverse kinematics *Prog. Theor. Exp. Phys.* 2019 (2019) 013D02.

[35] Wang, H., Otsu, H., Chiga, N., *et al.*, Enhancement of element production by incomplete fusion reaction with weakly bound deuteron *Comm. Phys.* 2 (2019) 78.

[36] Michimasa, S., Imai, N., Dozono, M., *et al.*, New energy-degrading beamline for in-flight RI beams, OEDO, *Nucl. Instrum. Methods Phys. Res., Sect. B* 463 (2020) 143.

[37] Sumikama, T., Ahn, D.S., Fukuda, N., *et al.*, Energy-control and novel particle-identification methods combined with range in a multi-sampling ionization chamber for experiments using slowed-down RI beams *Nucl. Instrum. Methods Phys. Res., Sect. A* 986 (2021) 164687.

[38] Kunieda, S., Furutachi, N., Minato, F., *et al.*, JENDL/ImPACT-2018: a new nuclear data library for innovative studies on transmutation of long-lived fission products, J. of Nucl. Sci. and Tech. 52, 1073 (2019).

[39] Sato, T., Niita, K., Matsuda, N., *et al.*, Particle and Heavy Ion Transport code System, PHITS, version 2.52, J. of Nucl. Sci. Technol. 50, 913 (2013).

[40] Okuno, H., Sakurai, H., Mori, Y., *et al.*, Proposal of a 1-ampere-class deuteron single-cell linac for nuclear transmutation, Proc. Jpn. Acad. Ser. B 95 430-439 (2019).

[41] Yamada, K., Ozeki, K., Kamigaito, O., *et al.*, First vertical test of superconducting QWR prototype at RIKEN, Prof. of LINAC2016, TUPLR061, 598 (2016).

[42] Mori, Y., Taniuchi, A., Kuriyama, Y., *et al.*., Intense Negative Muon Facility with MERIT ring for Nuclear Transmutation, JPS Conf. Proc.21,011063 (2018).

[43] Imao, H., Charge Stripper Ring for RIKEN RI Beam Factory, J. of Instrum. 15, P12036 (2020).

Acknowledgments

I would like to thank the organizers of SND2020 for the safe organization and attractive program. Because of COVID-19 pandemic, they smartly introduced a "hybrid" meeting, where in-person and on-line participations were effectively arranged and managed.

3. Nuclear data study for Accelerator Driven System at J-PARC

Shin-ichiro MEIGO[†1]

[1]J-PARC Center, Japan Atomic Energy Agency, Shirakata 2-4, Tokai, Ibaraki, 319-1195, Japan
[†]Email: meigo.shinichiro@jaea.go.jp

Abstract

To decrease the toxic waste produced at the nuclear reactor, studies of the Accelerator Driven System (ADS) are developing worldwide. Since the neutron production target at ADS is designed to be irradiated by protons in several GeV kinetic energy, a study with the high-energy particles in the kinetic energy region around GeV is essential for the research and development of ADS. However, many accelerator facilities using several GeV-protons built in the 1970s have been shut down due to their lifetime. Eventually, the facilities to be able to use protons with several GeV are scarce in the world. In Japan, J-PARC can only apply for the sake of ADS using the hadron, including proton. Using the 3-GeV proton synchrotron, some studies are going at J-PARC aimed at obtaining the nuclear data of ADS. In this paper, some experiments related to nuclear data for ADS are introduced, such as nuclide production cross section induced by proton and displacement cross section.

1 Introduction

To reduce the hazards associated with the radioactive waste produced in a nuclear reactor, Japan Atomic Energy Agency (JAEA) proposed an accelerator-driven system (ADS) that comprises extremely high-power accelerators (30 MW) with proton kinetic energy of 1.5 GeV [1]. Since the neutron production target at ADS is designed to be irradiated by protons in several GeV kinetic energy, a study with the high-energy particles in the kinetic energy region around GeV is essential for the research and development of ADS. However, many accelerator facilities using several GeV-protons, such as SATURNE at CEA, established for nuclear physics in the 1970s, have been shut down due to their lifetime. Eventually, the facilities to be able to use protons with several GeV, such as AGS at BNL, PS at CERN, and U-10 at ITEP, are scarce in the world. In Japan, J-PARC can only apply for the sake of ADS using the hadron, including proton. Therefore, our group conducted nuclear data studies for ADS at the 3-GeV proton synchrotron (RCS) facility and the beam transport line.

In this paper, some experiments carried out at J-PARC for the nuclear data for ADS using several GeV-protons are introduced, such as nuclide production cross section induced by protons [2, 3] and displacement cross section [4, 5].

2 Displacement cross section

In ADS, Lead–bismuth eutectic (LBE) is used as a target material, and it simultaneously plays the role of a coolant. While designing ADS, damage to the beam-intercepting material is one of

the critical issues. In other high-intensity accelerator facilities, the beam–intercepting material also plays essential roles. To confidently operate a high-power accelerator, damage estimation of the target material is essential. For quantitative specification of the damage to the target material, the displacement per atom (dpa) index is generally employed. A dpa is widely used for the estimation of the damages caused to nuclear reactors and fusion reactors. The dpa is estimated using the particle fluence multiplied with displacement cross section. The cross section is usually obtained using the Norgertt–Robinson–Torrens (NRT) model [6]. In the low-energy region below 20 MeV, the displacement cross section for a proton can be reliably predicted because the Coulomb force mainly causes the displacement. The calculation method for the displacement cross section has been established for the low-energy regions where nuclear reactions produce no particles. However, for the protons in the high-energy region above 20 MeV, the experimental data of the displacement cross section are scarce. Therefore, the displacement cross section has not been adequately studied. Since many reaction channels open (above 20 MeV), calculation codes based on the intra-nuclear cascade model are used to obtain the cross section. Although iron materials play essential roles, such as the beam window for the ADS and target vessels of the spallation neutron source, the experimental data of the displacement cross section have not been observed in the energy region above 20 MeV. For validation and improvement of the dpa evaluation, the experimental data are crucial.

2.1 Experiment of displacement cross section

For the displacement cross-section measurement, we conducted experiments at 3-GeV proton beam transport (3NBT) line at the J-PARC. A vacuum chamber with a cryocooler was installed at the front of the beam dump of the 3-GeV rapid cycling synchrotron (RCS). At the RCS, the kinetic energy of the extracted proton can vary from 0.4 to 3 GeV, altering the timing of the extraction kicker magnet. With the change in the rigidity of the following magnets, the beam was introduced to the sample.

Since there was no space in the beamline introduced to the beam dump, the experimental equipment was installed in the beamline, where the high-intensity proton beam could be delivered to the spallation neutron source in the MLF. Although the low-intensity proton beam was irradiated to sustain the cryogenic temperature of the sample, an additional interlock of the accelerator was required for the experiment owing to safety reasons, which changed the licensing of the RCS described in Japanese law of act concerning prevention from radiation hazards due to radioisotopes.

At the RCS, the kinetic energy of the extracted proton can vary from 0.4 to 3 GeV, altering the timing of the extraction kicker magnet. With the change in the rigidity of the following magnets, the beam was introduced to the sample. For observation of the damage in the sample, the irradiated sample is required to be cooled at a cryogenic temperature (around 10 K), where the recombination of Frenkel pairs is well suppressed owing to thermal motion. With the observation of the resistivity change $\Delta\rho$ due to the irradiation at the cryogenic temperature, the experimental displacement cross section $\sigma_{exp}(E)$, is given by the following,

$$\sigma_{exp}(E) = \Delta\rho/(\overline{\phi(E)}\rho_{FP}), \tag{1}$$

where $\overline{\phi(E)}$ is the average proton fluence at the sample over irradiation time, ρ_{FP} is the resistivity change per Frenkel-pair density for a particular metal, which has an uncertainty of 20%.

A vacuum chamber was installed in front of the 3-GeV beam dump. The chamber that was installed at the beam transport line maintained vacuum pressure less than 10^{-5} Pa using the sputter-ion pumps. The chamber was equipped with a Gifford–McMahon (GM) (Sumitomo Heavy Industries RDK-408D2) cryocooler. The GM cryocooler cooled the sample using an

oxygen-free high-conductivity copper rod and sample holder made of aluminum that was placed at the tip of the copper rod, as shown in **Fig. 1**. The GM cooler comprises two structures: the 1 st and 2 nd stages. At the 1 st and 2 nd stages, the temperatures can reach 40 K and 4 K, respectively. For the measurement of the thermal recovery of the sample, a heater was attached to the copper rod. The assembly of the GM cryocooler and a sample wire was placed on a movable stage to control the irradiation. Since the RCS kicks the beam horizontally for the extraction, the stability of the beam position in the vertical direction is better than in the horizontal.

To obtain the beam window material data used at the ADS, we selected iron as the sample. Before installation, the sample was annealed just less than the melting point to eliminate the defect of the lattice. Each sample was sandwiched between electrical insulation sheets of an aluminum nitride ceramic and held by the holder made of aluminum. To minimize the beam interaction on the holder, we made an aperture with 40-mm diameter for the sample holder. The resistance of the sample was measured using a voltmeter and current source. The sample wire was connected through terminals to both the current source and voltmeter for the compensation of the cable resistance between the sample and instruments. The precision of this resistance measurement was ± 0.01 $\mu\Omega$, corresponding to a resistivity of ± 3 fΩm.

The resistance thermometer on the sample holder was calibrated in the temperature range of 4 –100 K, and a silicon thermometer on the copper column was calibrated between 4 K and the room temperature. The resistance decreased with the temperature. It was observed that the resistance was saturated around the cryogenic temperature ($\sim$4 K).

The electrical resistivity of the sample ρ is expressed as follows: $\rho = RA/L$, where R [Ω] is the measured electrical resistance, A is the area of the sample (4.9×10^{-8} m^2) with a diameter of 250 μm, and L is the length between two potential points (40 mm). To avoid heat introduction to the sample owing to radiation to the sample, the sample was surrounded using double-walled radiation thermal shields made of aluminum. The outer and inner shields with a thickness of 2 and 1 mm, were directly connected to the1 st and 2 nd stage of the GM cooler, respectively. To minimize the scattering of the proton beam on the shields, we placed thin aluminum foils with a thickness of 5 μm and at the beam entrance and exit holes (with a diameter of 40 mm) for both thermal shields. After 6 h of cooling, the temperature of the sample holder was less than 4 K. Note that, in the early period of the experiment, the temperature was not 4 K, but $\sim$20 K. With some trials changing the conditions, the heat was introduced through the measurement cables for the resistance and temperature.

To fit the beam position on the sample precisely, the beam was vertically scanned with the steering magnet placed upstream of the sample along the beam direction. With the observation of the change in resistivity during the scan, the beam position given by the profile monitor was confirmed to be the center of the wire owing to the precious beam control developed at J-PARC [7, 8]. During the beam irradiation, the resistance of the iron sample was observed with the temperature of the sample holder determined using the attached thermometer. Although the sample temperature was not directly observed, it can be expected to be $\sim$4 K. During the irradiation of the sample, the temperature slightly increased. The observed temperature of the holder increased by 0.2 K. After irradiation, the sample resistance was increased by about 0.2 $\mu\Omega$ from the start of the beam irradiation, which was produced due to the displacement.

2.2 Results of displacement cross section

Using Eq(1), the displacement cross sections of iron are obtained. In this work, the resistivity change per Frenkel-pair ρ_{FP} was defined as 2.46×10^{-6} $\pm$ 0.57 Ωm for iron, obtained from another study [9]. It should be mentioned that the error of the present cross-section data was dominated by the one of the resistivity change per Frankel-pair. To obtain high-precision results,

the uncertainties of the resistivity change by Frankel-pair creation need to be improved, which is expected to be achieved using an electron beam.

Figure 2 shows the calculation results using PHITS [10] with intra-nuclear cascade model of INCL-4.6 [11], which are shown as black single-dot and solid red lines. In **Fig. 2**, the evaluated data were given by the Karlsruhe Institute of Technology (KIT) [12] shown as blue dashed and orange two-dotted lines. To PHITS calculation and KIT evaluation, the NRT model, which is widely utilized for evaluation of dpa, and the athermal–recombination–corrected dpa (arc-dpa) model based on molecular dynamics (MD) were applied. The parameters for the arc-dpa given by Nordlund [13] was applied to PHITS. KIT used the binary collisional approximation (arc-dpa-BCA) model for evaluation. The displacement cross section of iron (red solid circles) compared with the previous experimental data by Jung [14] (black solid circles). The current data of iron were found to be lower than the calculation with the NRT model with PHITS and KIT evaluation by about 2 times.

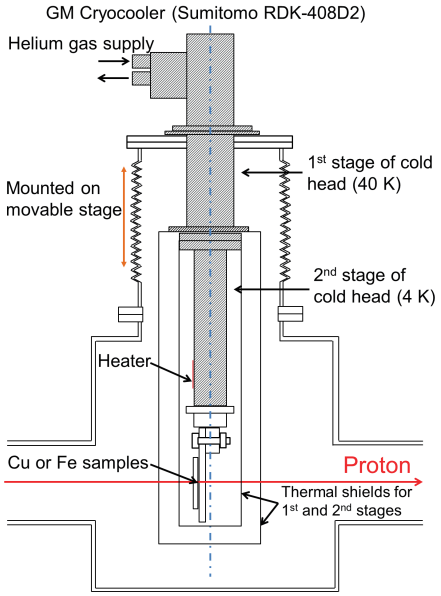

Figure 1: Schematic of the sample, vacuum chamber, and GM cryocooler used for the present experiment.

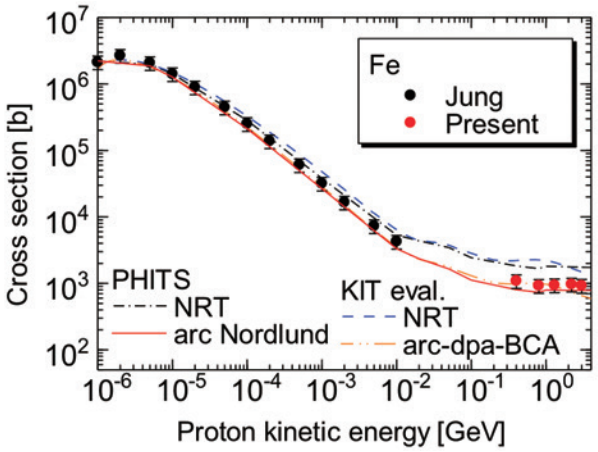

Figure 2: Comparison of the present experimental data for iron with previous experimental data [14], calculation data using PHITS [10] and KIT evaluations [12].

3 Production cross section induced by several GeV-protons

To estimate the residual nuclei in the beam window and the target, the production cross section is required. However, the data are not enough to validate the calculation models. For validation of the calculation model, we have been carried out the production cross section using several GeV-protons. For the experiment, sample changers with sample holders were installed at 3NBT. After irradiation, the sample was observed by the high-pure Germanium detector. With the gamma spectrometry, the production cross section was derived.

As an example, the experimental results of ^{nat}Fe(p,x)^{7}Be is shown in **Fig. 3** compared with the various calculation models and the evaluation data of JENDL/HE-2007. It is shown that INCL++/ABLA07 and INCL/GEM show remarkable underestimation for the kinetic energy range above 1 GeV region. The nuclide of ^{7}Be is mainly produced by the statistical decay

and partially produced by the multifragmentation. On the other hand, the previous calculation model of Bertini/GEM shows good agreement in the energy range above 2 GeV. Although JENDL/HE-2007 shows a good agreement with the experimental results, it shows a slight overestimation for energies above 2 GeV. Using the present experimental results, the evaluation will be improved.

Just the same cross section for ^{56}Fe was measured by the GSI using the inverse-kinematics method, which is also shown in **Fig. 3**. The present data disagree with the data measured at the GSI [15], which is pointed out by the other study [16]. It can be concluded that another study using inverse kinematics has worth to reveal the detailed production process for the improvement of the model.

4 Summary

To evaluate the target materials used in high-intensity proton accelerators, particularly in ADS, experiments for displacement and nuclei production cross-sections measurements were carried out in J-PARC. The displacement cross section of iron irradiated using protons having kinetic energies in the range 0.4 and 3 GeV was successfully obtained. It should be mentioned that the present data for iron is the first experimental data in the projectile energy region above 400 MeV, which is essential for the research and development of ADS. The present experimental data of the displacement cross sections were compared with the calculation using the PHITS and the data evaluated by KIT. The present results showed an overestimation of the cross section using the widely employed NRT model by a factor of 2, this model was preferred for the proton projectile with lower energy than 10 MeV. In contrast, the arc-dpa model shows remarkably good agreement with the present data. For the nuclei production cross section induced by several GeV-protons, further improvements to the model are required to reproduce the cross section. For this sake, we will continue the experiment at J-PARC.

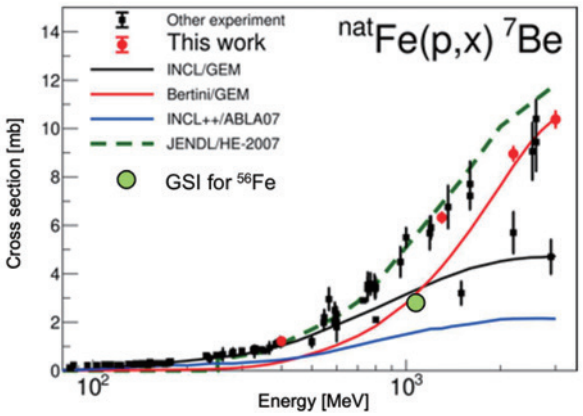

Figure 3: Production cross section of ^{nat}Fe(p,x)^{7}Be as a function of kinetic energy of projectile protons.

Acknowledgment

This paper partially contains the results of “Measurement of displacement cross section at J-PARC for structural material utilized at ADS” entrusted to JAEA by the Ministry of Education, Culture, Sports, Science, and Technology of Japan.

References

[1] Tsujimoto K, Oigawa H, Ouchi N, et al. Research and development program on accelerator driven subcritical system in JAEA, Journal of Nuclear Science and Technology, 2007; 44(3):483–490.

[2] Matsuda H, Meigo S, Iwamoto H, Proton-induced activation cross section measurement for aluminum with proton energy range from 0.4 to 3 GeV at J-PARC, Journal of Nuclear Science and Technology, 2018;55(8):955–961.

[3] Meigo S, Nishikawa M, Iwamoto H, et al., Measurement of aluminum activation cross section and gas production cross section for 0.4 and 3-GeV protons. EPJ Web Conf. 2017;146:11039.

[4] Meigo S, Matsuda H, Iwamoto Y, et al., Measurement of Displacement Cross Section of Structural Materials Utilized in the Proton Accelerator Facilities with the Kinematic Energy above 400 MeV; 2020.

[5] Matsuda H, Meigo S, Iwamoto Y, et al., Measurement of displacement cross-sections of copper and iron for proton with kinetic energies in the range 0.4 – 3 GeV, Journal of Nuclear Science and Technology, 2020;57(10):1141–1151.

[6] Norgett M, Robinson M, Torrens I, A proposed method of calculating displacement dose rates, Nuclear Engineering and Design, 1975;33(1):50 – 54.

[7] Meigo S, Ohi M, Kai T, et al., Beam commissioning for neutron and muon facility at J-PARC, Nuclear Instruments and Methods in Physics Research Section A: Accelerators, Spectrometers, Detectors and Associated Equipment, 2009;600(1):41 – 43.

[8] Meigo S, Ooi M, Fujimori H, Two-parameter model for optimizing target beam distribution with an octupole magnet, Phys Rev Accel Beams, 2020 Jun;23:062802.

[9] Broeders C, Konobeyev A, Defect production efficiency in metals under neutron irradiation, Journal of Nuclear Materials, 2004;328(2):197 – 214.

[10] Iwamoto Y, Niita K, Sawai T, et al., Improvement of radiation damage calculation in PHITS and tests for copper and tungsten irradiated with protons and heavy-ions over a wide energy range, Nuclear Instruments and Methods in Physics Research Section B: Beam Interactions with Materials and Atoms, 2012;274:57 – 64.

[11] Boudard A, Cugnon J, David JC, et al., New potentialities of the liège intranuclear cascade model for reactions induced by nucleons and light charged particles, Phys Rev C, 2013 Jan; 87:014606.

[12] Konobeyev A, Fischer U, Simakov S, Improved atomic displacement cross-sections for proton irradiation of aluminium, iron, copper, and tungsten at energies up to 10 GeV, Nuclear Instruments and Methods in Physics Research Section B: Beam Interactions with Materials and Atoms, 2018;431:55 – 58.

[13] Nordlund K, Zinkle SJ, Sand AE, et al., Improving atomic displacement and replacement calculations with physically realistic damage models, Nature Communications, 2018;9(1):1084.

[14] Jung P, Atomic displacement functions of cubic metals, Journal of Nuclear Materials. 1983; 117:70 – 77.

[15] Napolitani P, Schmidt KH, Botvina AS, et al., High-resolution velocity measurements on fully identified light nuclides produced in ^{56}Fe + and ^{56}Fe+titanium systems, Phys Rev C, 2004 Nov;70:054607.

[16] Titarenko YE, Batyaev VF, Titarenko AY, et al., Cross sections for nuclide production in a ^{56}Fe target irradiated by 300, 500, 750, 1000, 1500, and 2600 MeV protons compared with data on a hydrogen target irradiated by 300, 500, 750, 1000, and 1500 MeV/nucleon ^{56}Fe ions. Phys Rev C. 2008 Sep;78:034615.

4. Proposal of a 1 ampere class deuteron single-cell linac for nuclear transmutation

Hiroki OKUNO[†1], Hiroyoshi SAKURAI [1], and Yoshiharu MORI[2]

[1]Nishina Center for Accelerator-Based Science
[2]Institute for Integrated Radiation and Nuclear Science, Kyoto University
[†]Email: okuno@riken.jp

A 1 ampere class high-intenisty deuteron linac (ImPACT2017 model) is proposed for the mitigation of the long-lived fission products (LLFPs) by nuclear transmutation. This accelerator consists of single-cell rf cavities with magnetic focusing elements to accelerate deuterons beyond 1 A up to 200 MeV/u.

1 Introduction

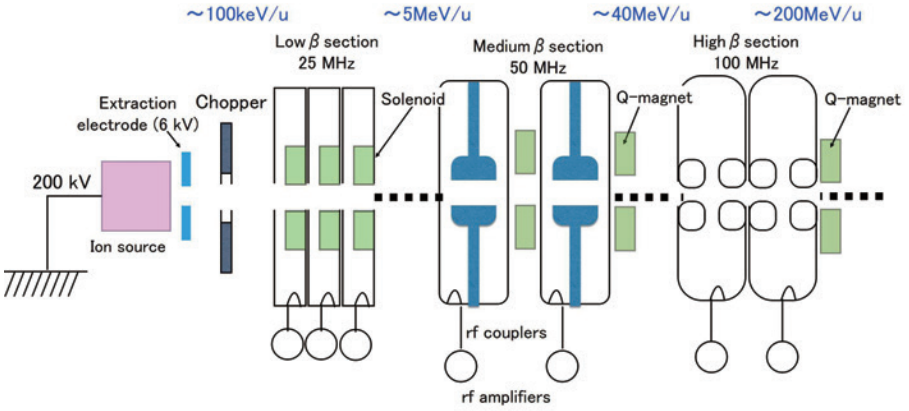

Figure 1: Schematic of a single-cell linac, model ImPACT2017.

High-level radioactive waste from nuclear power plants has been posing a number of inherent problems, including the lack of progress in considering disposal sites [1], possible vulnerabilities in counter-terrorism measures, or so. To address these problems, research and development of partitioning and transmutation technologies are essentially important to determine the most efficient methods for the reduction of radioactivity in waste material [2]. We hereby propose a reasonably feasible transmutation scheme with high-energy neutrons produced by a deuteron beam, where liquid lithium is utilized for the production target [3]. To realize the transmutation scheme, design of a 100-200 MeV/u deuteron accelerator with an intensity of 1 A is highly desired for the transmutation of LLFP nuclides.

We consider a linac that can accelerate deuterons to such a high current. Most modern high-power linacs [3, 4, 5, 6] use a radio frequency quadrupole (RFQ) as a front-end accelerator,

which performs adiabatic rf capture of a direct current (DC) beam from an ion source, transverse focusing, and acceleration. The typical aperture of an RFQ is 1 cm. However, the expected size of the 1-A beam from an ion source amounts up over 10 cm in diameter. It is therefore evident that an RFQ cannot accommodate such large beams with 1 A. In this study, we propose a novel linac that consists of single-cell cavities with magnetic focusing elements to accept a 1-A beam with a large bore. The single-cell linac (SCL) has the following advantages for the acceleration of high-intensity beams:

- Low-frequency rf cavities with a large bore can be used to mitigate strong space charge forces owing to lower beam current density.
- Voltage and phase of each cell can be independently selected to compensate for the space charge effects, and also to implement an efficient bunching function for a DC beam like an RFQ entrance section.

Table 1: Basic parameters of the single-cell linac ImPACT2017. QWR stands for quarter wave resonator.

Ion Source and LEBT	
Energy range (MeV/u)	0.1
Type of IS	Cusp ion source
Particle	deuteron
Beam current (A)	1
Emittance (normalized)	25π mm·mrad
Low-βsection	
Energy range (MeV/u)	0.1-5
Number of cell	90
Cell length (m)	0.25
rf cavity	Normal conducting
	Single gap
Focusing	Solenoid
Medium-β section	
Energy range (MeV/u)	5-40
Number of cell	44
Cell length (m)	1.38
rf cavity	Superconducting
	QWR, Double gaps
Focusing	Quadrupole magnet
High-β section	
Energy range (MeV/u)	40-200
Number of cell	200
Cell length (m)	0.8
rf cavity	Superconducting
	Single gap
Focusing	Quadrupole magnet

2 Scheme

The 1-A deuteron SCL (ImPACT2017 model) consists of four sections: (1) the ion source section, (2) the low-β section, (3) the medium-β section, and (4) the high-β section. Figure 1 shows a schematic layout of this system and the typical parameters of each section are presented in Table 1. In this scheme, a large transverse normalized RMS emittance of 25π mm·mrad is assumed at the injection of the SCL, which is sufficient for relaxing the space charge effect in the beam dynamics. A relatively low rf frequency acceleration system is suitable for a large bore.

In the SCL, the fundamental mode of the longitudinal space charge force could be compensated cell by cell through individual fine rf detuning to beam bunches. The SCL also facilitates individual strong beam focusing against the transverse space charge force with external magnetic focusing elements, such as solenoids and quadrupole magnets.

The ion source produces a current of deuterons, with a magnitude above 1 A. A cusp-field-confinement-type ion source with a large extraction area was chosen because a multi-hole beam extraction system is inevitable for the extraction of such large beam currents. Such ion sources are used for NBI (neutral beam injector) in Tokamak fusion reactors. The structure of the ion source can be seen, for example, in [7]. The Child-Langmuir law estimates that a current of 20 mA/cm^2 can be extracted at maximum through one hole with a diameter of 14 mm when an extraction voltage of 6 kV is applied to the gap of 3 mm. At least 37 holes are required to extract 1 A assuming that the ratio of D^+ to the total current including D_2^+, etc. is 85%. The low-energy beam transport (LEBT) section consists of a series of beam focusing solenoids.

The low-β section is composed of approximately 90 single cells, and each cell includes a single rf cavity with a 25 MHz resonant frequency and a focusing solenoid. The rf cavity has a capacitive plate to maintain the outer diameter under $\sim$2 m and the maximal rf voltage is approximately 300 kV, which is approximately 1.2 K_L, where K_L is discharge limit given as a function of the frequency by Kilpatrick [8]. The transit time factor at 5 MeV/u exceeds 0.95. The rf power except the beam power dissipated by the entire single-cell cavity system is approximately 5 MW.

The rf voltage and phase of every single cavity were appropriately selected to optimize the beam capture and acceleration. The optimization was performed by evaluating the adiabatic parameter, as shown in the following [9] [10] [11]:

$$\Omega_s >> \frac{1}{A}\left|\frac{dA}{dt}\right|, \tag{1}$$

where A is a rf bucket area and Ω_s is the phase (synchrotron) oscillation frequency, and from this criterion, an adiabatic parameter is defined as,

$$n_a = \frac{\Omega_s T_s}{1-[V_i/(V_i+\Delta V)]^{1/2}}. \tag{2}$$

Here, V_i is rf voltage, ΔV increment of rf voltage per cell and T_s transit time per cell.

Good adiabaticity is achieved when the value of the adiabatic parameter n_a exceeds 10 and the DC beam from the ion source can be well-captured by the rf bucket and consequently accelerated. The phase and rf voltage variations should be appropriately optimized to preserve the adiabaticity of the beam capture and acceleration, following the condition shown in eq.(1). The longitudinal beam behavior was simulated for these conditions and the results are plotted in Fig. 2. Evidently, the beam is well captured and is accelerated adiabatically. This rf capture of the DC beam was successfully simulated by a 3D PIC code.

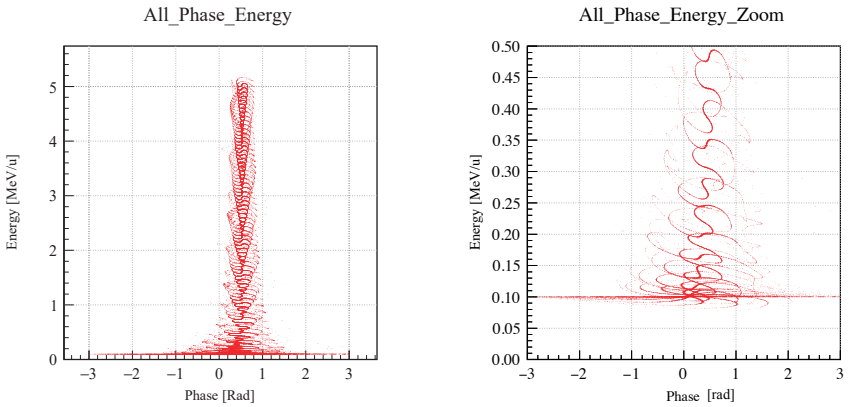

Figure 2: Beam capture and acceleration: left panel shows the entire longitudinal beam motion in the low-β section, while right plot shows the initial phase of the beam capture and acceleration.

The deuteron beam from the low-β section is accelerated up to 40 MeV/u via the medium-β section that consists of 44 superconducting quarter wave resonators (QWRs) at 50 MHz and quadruple magnets between the resonators. The superconducting and/or permanent magnets act as the quadrupole magnet. The schematic layout of the QWR is shown in Fig. 3. The height and diameter of the outer cylinder are 1.62 m and 1.16 m, respectively and the maximal rf voltage is 1.24 MV. The transit time factor is approximately 0.74 at 40 MeV/u and the gap distance is 0.58 m, which corresponds to $\beta\lambda/2$ at 18 MeV/u.

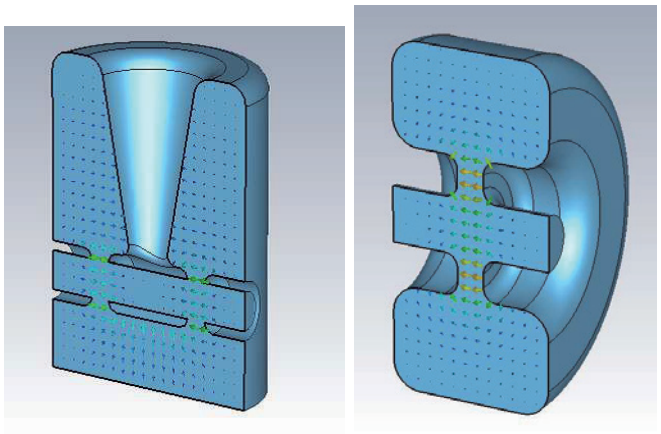

Figure 3: Structure of QWR (left) for the medium β and Reentrant cavity(right) for the high β section. The arrows in the cavities show electric field. Size of the arrow is proportional to strength of the electric field.

The deuteron beam from the medium-β section is accelerated up to 100–200 MeV/u through the high-β section that consisted of 200 superconducting reentrant cavities at 100 MHz and quadruple magnets between the resonators. The superconducting and/or permanent magnets serve as the quadrupole magnet. The schematic layout of the reentrant resonator is shown in Fig. 3. The diameter and the length of the cavity are 1.25 m and 0.6 m, respectively and the maximal rf voltage is 2.3 MV. The transit time factor is approximately 0.96 at 200 MeV/u.

2.1 Summary

A 1 ampere class deuteron linac (ImPACT2017 model) was proposed for the mitigation of the long-lived fission product (LLFP) by nuclear transmutation. This model consists of single-cell rf cavities with magnetic focusing elements to accelerate deuterons beyond 1 A. The beam dynamics and conceptual design for each section were presented and discussed.

References

[1] http://www.scj.go.jp/ja/info/kohyo/pdf/kohyo-22-k159-1.pdf

[2] IAEA Technical Reports Series (2004) No. 435.

[3] Knaster, J., (2017) Overview of the IFMIF/EVEDA project, Nucl. Fusion 57, 102016.

[4] Henderson, S., et al., (2014) The Spallation Neutron Source accelerator system design, Nucl Instrum Meth A, vol. 763, pp. 610-673.

[5] Ed. Peggs, S., (2013) ESS Technical Design Report, ESS-DOC-274.

[6] Pan, W. M., (2012) Chinese ADS Project and Proton accelerator development, Proc. of LINAC2012, TU1A03, Tel-Aviv, Israel.

[7] Kuriyama, M. et al., (1987) The Design, Research and Development of JT-60 Neutral Beam Injector, JAERI-M 87-169 (in Japanese).

[8] Kilpatrick, W. D. (1957) Criterion for Vacuum Sparking Designed to Include Both RF and DC. Rev. Sci. Instr. **28**, 824-826.

[9] Montague, B. W. (1977) Single-particle dynamics - RF Acceleration. Proc. of the first cource of the Int. School of Particle Accelerators. CERN **77-13**, 63-81.

[10] Lilliequis, C. G. and Symon, K. R. (1959) Deviations from adiabatic behavior during capture of particles into an rf bucket. MURA-**491**, 1-9.

[11] Ng, K.Y. (2012) Adiabatic capture and debunching. FNAL Report, FERMILAB-FN-0943-APC, 1-11.

5. Unified description of the fission probability for highly excited nuclei

Hiroki IWAMOTO[†1]

[1]Nuclear Science and Engineering Center, Japan Atomic Energy Agency

[†]Email: iwamoto.hiroki@jaea.go.jp

This paper describes a summary of the spallation reaction and its theoretical model, focusing on the spallation product yields, and then our research work about the improvement of the fission probability model is presented.

1 Introduction

Recently, spallation neutrons produced from the spallation reactions have been utilized for the material and fundamental sciences as well as industrial applications in the spallation neutron source facilities (e.g. MLF at J-PARC [1, 2, 3], ISIS [4], and SNS [5]). In these facilities, Monte Carlo particle transport codes such as PHITS [6], MCNP [7], GEANT4 [8], FLUKA [9] play a significant role in the assessment of radiation dose and inventory of radioactive materials.

In this paper, we briefly describe the spallation reaction and its theoretical spallation model, focusing on spallation product yields; then, our research work on this title is presented.

2 Spallation reaction

2.1 Spallation reaction process

Figure 1 schematizes a process of the spallation reaction. The spallaion reaction starts with a collision between an incident particle and a nucleon which is a constituent of a nucleus. The bombarded nucleon emits solely from the nucleus, hit other nuclons several times, or emits binding to nucleons in the nuclear surface; this process is referred to as the intranuclear cascade process. After this process, the remaining energy is uniformly distributed by repeating soft collisions, which results in a quasi-stable, highly-excited state.

This highly-excited nucleus de-excites by statistically emitting neutrons, charged particles and photons; this process is referred to as the de-excitation process; this process is also known as the evaporation process. For heavy targets such as gold, lead, and uranium, fission occurrs competing with the evaporation.

2.2 Distribution of spallation products and spallation model

Figure 2 compares the mass number distribution of the spallation products produced from the 1-GeV proton-induced ^{208}Pb reaction between the experimental data [10] and calculation results with four major spallation models (i.e. INCL++/ABLA07 [11, 12], INCL++/GEMINI++ [13], INCL4.6/GEM [14], and CEM03.03 [15]). Three humps observed in this figure are referred to as evaporation residues (ER), fission fragments (FF), intermadiate mass fragments (IMF), and light

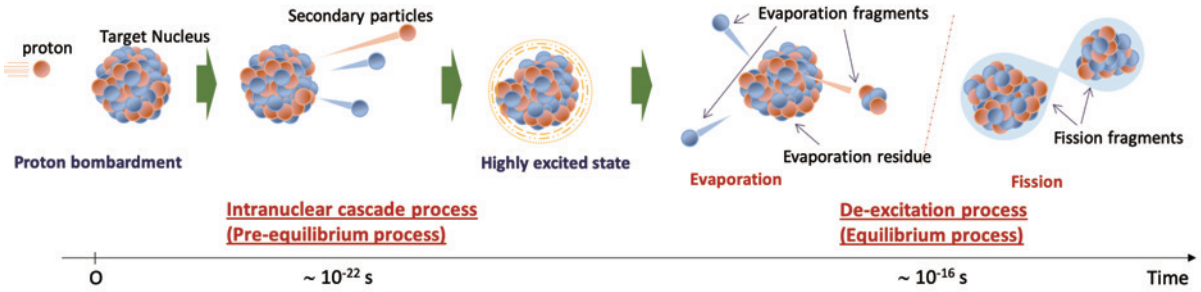

Figure 1: Process of the spallation reaction.

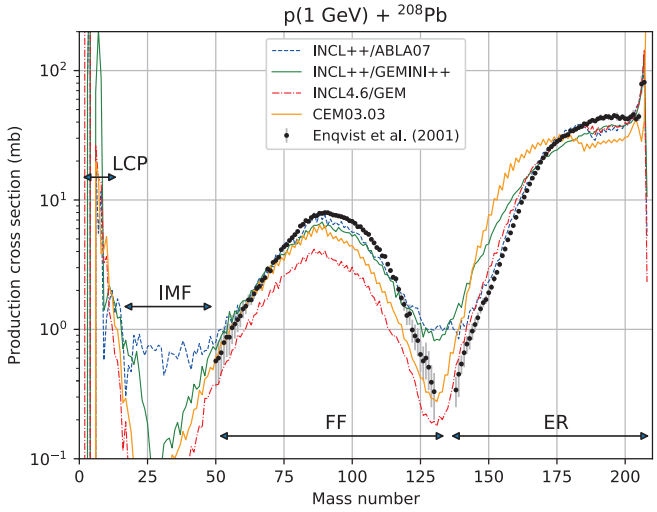

Figure 2: Mass number distribution of the 1-GeV proton-induced ^{208}Pb target reaction.

charged particles (LCP) in order of decreasing mass number. While all models explain the feature of the mass number distribution, they are not very good in terms of the prediction accuracy. For example, INCL4.6/GEM, which is a default spallation model of PHITS, underestimates the fission fragment yields by at most 50%. Because the fission fragments contains volatile radioactive materials such as radioactive kripton, xenon, and iodine, this underestimation may involve a significant problem in terms of the radiation safety of the spallation neutron source facilities. These discrepancies were discussed in detail in our previous work [16].

3 Improvement of fission probability

3.1 Description of fission probability

A recent benchmark analysis of the PHITS code revealed that INCL4.6/GEM implemented in PHITS underestimates the fission fragment yields. This underestimation indicates that the fission probability should be enhanced within the framework of the de-excitation model GEM.

The GEM describes the fission probability as follows.

$$P = \frac{\Gamma_f}{\Gamma_n + \Gamma_f}, \tag{1}$$

where Γ_f and Γ_n represent the decay widths of fission and neutron evaporation, respectively. Although parameters of these decay widths need to be sophisticated as a straightforward method, this approach requires a significant amount of time spent in tuning the model parameters. To avoid this, we modified the fission probability itself instead of the decay widths, which are deduced from a systematics of proton-induced fission cross sections.

The fission cross section $\sigma_{\rm fis}$ and non-elastic cross section $\sigma_{\rm nonel}$ are linked to the following equation:

$$\mathcal{P} = \frac{\sigma_{\rm fis}}{\sigma_{\rm nonel}}, \tag{2}$$

where $\mathcal{P}$ indicates a total fission probability, which can be calculated from the systematics of the proton-induced fission cross sections (Prokofiev systematics [17]) and that of the non-elastic cross sections (Pearlstein–Niita systematics [18]); both are functions of incident proton energy and mass and proton numbers of the target nucleus. However, what we are interested in here is the fission probability which is a function of excitation energy, mass number, and proton number of the highly excited nuleus. To resolve this discrepancy, relationships among information of projectile, target nuclei, and highly-excited nuclei are deduced statistically from the intranuclear cascade model calculation, and the fission probability was determined by multiplying the total fission probability with a function g:

$$P = g \cdot \mathcal{P}(\langle E_p \rangle, \langle Z_t \rangle, \langle A_t \rangle), \tag{3}$$

where $\langle E_p \rangle$, $\langle Z_t \rangle$, and $\langle A_t \rangle$ are the corresponding incident proton energy, proton number, and mass number, respectively. The function g is expressed as

$$g = \max\left(0, \gamma_0 \left(\frac{1}{1+\mathrm{e}^{-\gamma_1(E-\gamma_2)}} - \gamma_3\right)\right), \tag{4}$$

where $\gamma_i\,(i = 0, 1, 2, 3)$ is adjustable parameters to account for the proton-induced fission cross sections, which are expressed as

$$\gamma_0 = 0.46, \quad \gamma_1 = 0.10, \quad \gamma_2 = 57\left(\frac{X_{^{208}\mathrm{Pb}}}{\langle X_t \rangle}\right)^{5.5}, \quad \gamma_3 = \frac{1}{2}\left(\frac{X_{^{208}\mathrm{Pb}}}{\langle X_t \rangle}\right)^{3}, \tag{5}$$

where $X_{^{208}\mathrm{Pb}}$ and $\langle X_t \rangle$ are the fissility parameter for ^{208}Pb and the corresponding fissility parameter for the highly-excited nucleus.

3.2 Results

3.2.1 Fission cross sections

Figure 3 shows examples of the proton-induced and neutron-induced fission cross sections calculated by the proposed model. It is seen that the proposed model reproduces the experimental data fairly well, in contrast to the conventional model. Furthermore, even though this model is constructed by the proton-induced systematics, it is applicable the neutron-induced reactions. It was demonstrated that our model reproduces the experimental fission cross sections over a wide range of subactinide targets for proton-, neutron-, and deuteron-induced reactions. Details can be seen in Iwamoto et al. [19].

3.2.2 Fission fragment production cross sections

Figure 4 presents the proton-induced fission fragment production cross sections for the 1-GeV ^{208}Pb(p, X), 800-MeV ^{197}Au(p, X), and 500-MeV ^{208}Pb(p, X) reactions. Note that both the

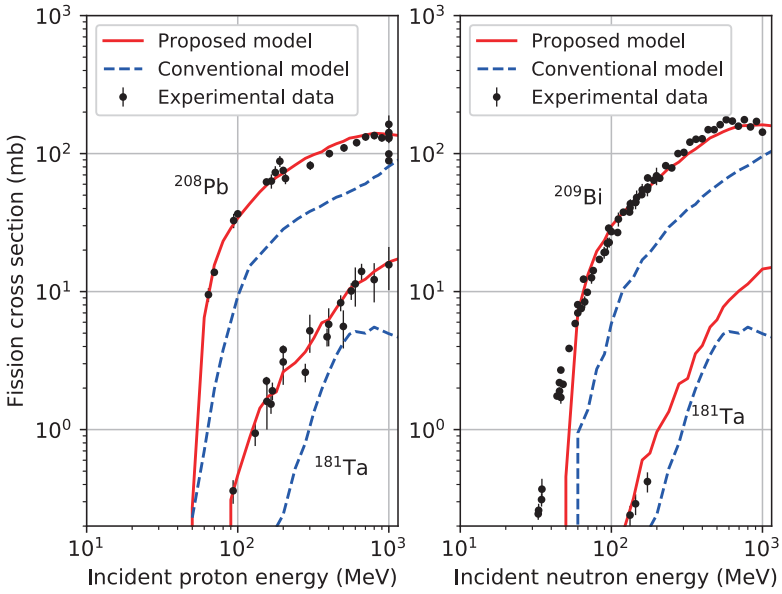

Figure 3: Proton-induced and neutron-induced fission cross sections.

calculated and experimental cross sections indicate independent yields. Although our proposed model can provide the fission cross sections, namely the total fission fragment production cross sections, with markededly improved accuracy, it is observed from this figure that each peak for element uniformly shifts to heavy mass numbers. This means that the fission fragments were computationally produced as uniformly neutron-rich states. The left panels of Figure 5 show $\langle N \rangle / Z$ distributions for the three reactions, comparing between the conventional and proposed models, in which the modified model becomes worse with respect to the $\langle N \rangle / Z$ distributions. As shown in the right panels of Figure 5, we found that this discrepancy is reduced by emitting three neutrons ($\nu = 3$) from the fissioning system. Because the neutron emission is considered to be driven by the excitation energy, we investigated how much excitation energy is required to account for the $\langle N \rangle / Z$ distributions. As a result, it was suggested that excitation energy of about 30–50 MeV is required, which would be consistent with a value deduced from the neutron separation energy; if the separation energy is assumed to be 8 MeV, the minimum energy of the three neutron emission becomes 24 MeV.

4 Conclusions

We have described the spallation reaction and its theoretical spallation model, focusing on spallation product yields, and our research work have been presented. Recently, experimental studies on the spallation reaction have become active in Japan [20, 21, 22]. We hope that the combination of our theretical work and these experiemntal activities will lead to a deeper understanding of the spallation reaction mechanism.

References

[1] Takada, H, et al., Quant. Beam Sci. **1**(2), 2017, pp.8-1–8-26.

[2] Nakajima, K, et al., Quant. Beam Sci. **1**(3), 2017, pp.9-1–10-59.

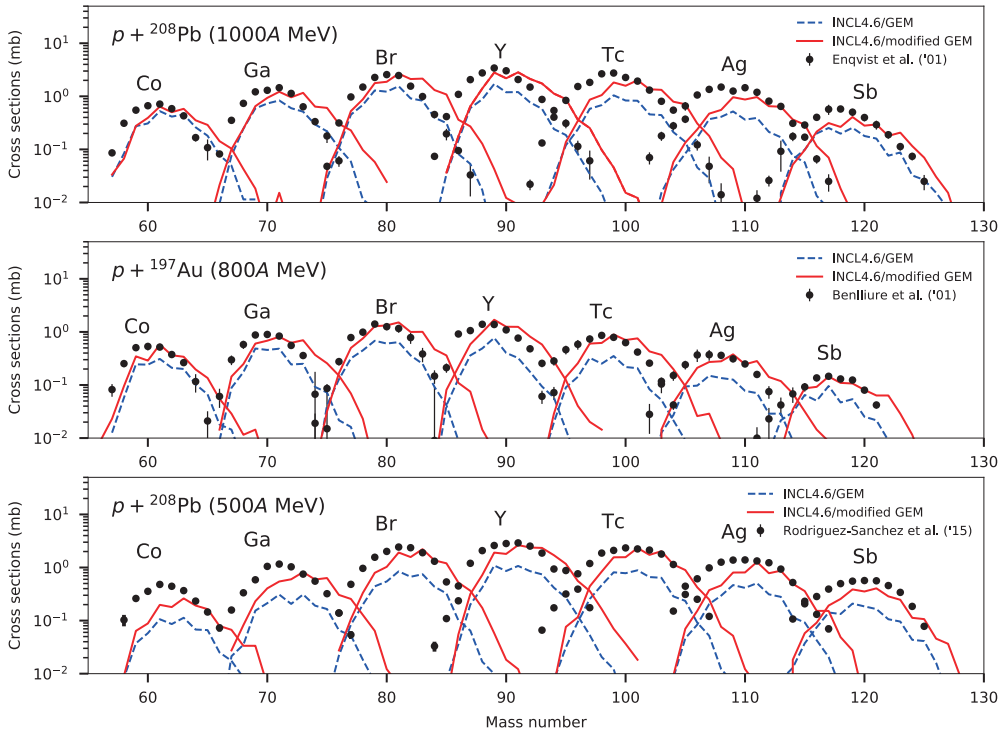

Figure 4: Proton-induced fission fragment production cross sections. Experimental data were taken from Enqvist et al. [10]

[3] Sakasai, K, et al., Quant. Beam Sci. **1**(2), 2017, pp.10-1–10-35.

[4] Thomason, J.W.G., Nucl. Instr. Meth. Phys. Res. A **917**, 2019, pp.61–67.

[5] Mason, T.E., et. al., Phys. B Condens. Matter **385–386**(2), 2006, pp.955–960.

[6] Sato, T., et al., J. Nucl. Sci. Technol. **55**;12, 2018, pp.529–533.

[7] Werner, C.J., et al. Los Alamos National Laboratory report LA-UR-17-29981, 2018.

[8] Allison, J., et al., Nucl. Instr. Meth. Phys. Res. A **835**, 2016, pp.186–225.

[9] Böhlen, T.T., et al., Nucl. Data Sheets **120**, 2014, pp.211–214.

[10] Enqvist, T., et al. Nucl. Phys. A. **686**, 2001, pp.481–524.

[11] Leray, S., et al., J. Phys.: Conf. Series **420**, 2013, 012065.

[12] Kelič, A., et al., INDC(NDS)-0530, IAEA, 2008.

[13] Charity, R.J., Phys. Rev. C **82**, 2010, 014610.

[14] Furihata, S., et al., JAERI-Data/Code 2001-015, 2001.

[15] Mashnik, S.G., Nucl. Phys. A **568**, 1994, pp.703–726.

[16] Iwamoto, H., et al., EPJ Web of Conf. **239**, 2020, pp.06001.

[17] Prokofiev, A.V., Nucl. Instr. Meth. Phys. Res. A **463**, 2001, pp.557–575.

[18] Niita, K., et al., Nucl. Instr. Meth. Phys. Res. B **184**, 2001, pp.406–420.

[19] Iwamoto, H., Meigo, S., J. Nucl. Sci. Technol. **56**;2, 2018, pp.160–171.

[20] Matsuda, H., et al., J. Nucl. Sci. Technol. **55**;8, 2018, pp.955–961.

[21] Matsuda, H., et al., Nucl. Instr. Meth. Phys. Res. A **483**, 2020, pp.33–40.

[22] Wang, H., et al., Phys. Lett. B **754**, 2016, pp.104–108.

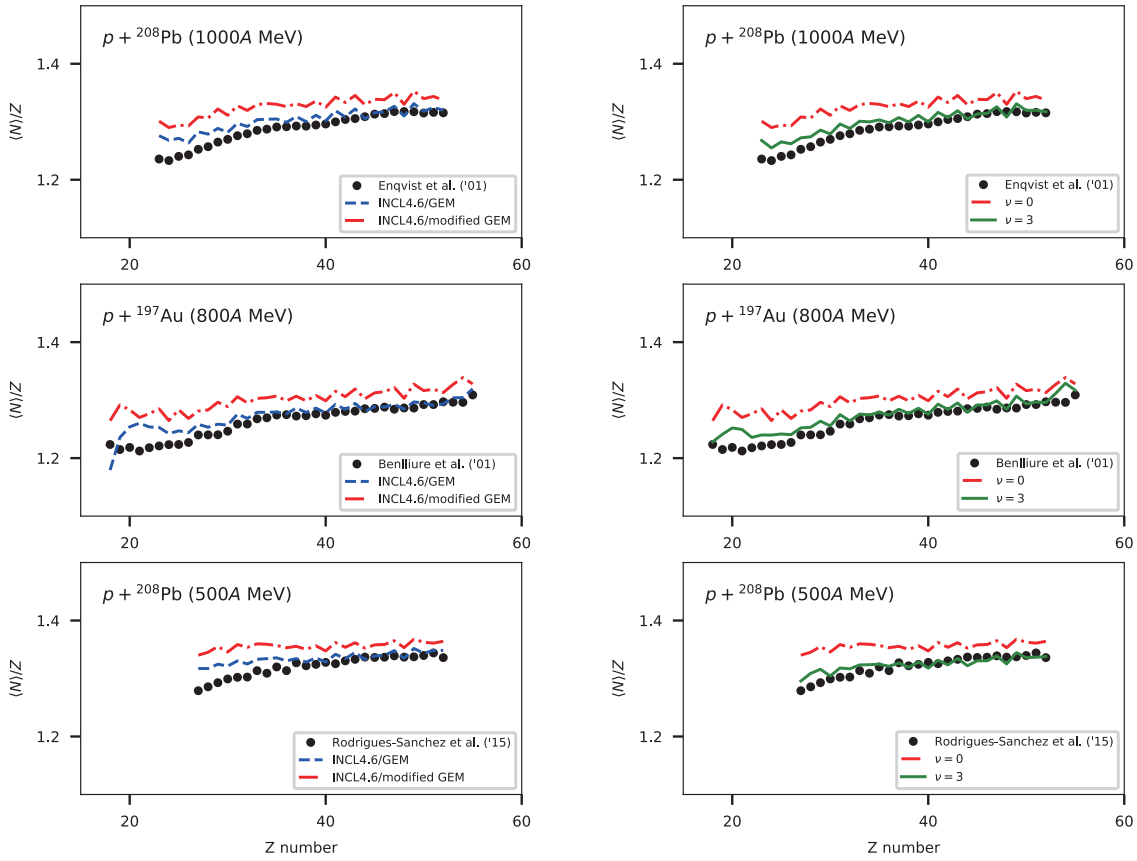

Figure 5: $\langle N \rangle / Z$ distributions as a function of Z number. The left panels show comparison between the conventional and proposed models; the right panels show comparison of the calculation results between $\nu = 0$ and $\nu = 3$, where ν is the number of neutron emission.

Acknowledgements

The author would like to acknowledge many helpful discussions with the co-author of this work [19], Dr. S. Meigo, and Drs. K. Nihsio, T. Sato, T. Ogawa, S. Hashimoto, Y. Iwamoto, T. Fukahori, and T. Kawano. This work was supported by Japan Society fort the Promotion of Science (JSPS) Grants-in-Aid for Young Scientists B [grant number 17K14916].

6. Nuclear spectroscopy at KISS

Yoshikazu HIRAYAMA[†1], Yutaka WATANABE[1], Momo MUKAI[2,1,3], Hyunsuk CHOI[4], Murad AHMED [*2,1], Hironobu ISHIYAMA[1,2], Sunchan JEONG[1,5], Sota KIMURA[2,1,3], Junyoung MOON[5], Michihiro OYAIZU[1], Jinhyung PARK[5], Peter SCHURY[1], Michiharu WADA[1], and Hiroari MIYATAKE[1]

[1]Wako Nuclear Science Center (WNSC), Institute of Particle and Nuclear Studies (IPNS), High Energy Accelerator Research Organization (KEK), Saitama 351-0198, Japan

[2]Graduate School of Pure and Applied Sciences, University of Tsukuba, Ibaraki 305-0006, Japan

[3]Nishina Center for Accelerator-Based Science, RIKEN, Wako, Saitama 351-0198, Japan

[4]Department of Physics and Astronomy, Seoul National University, Seoul 08826, Republic of Korea

[5]Rare Isotope Science Project, Institute for Basic Science (IBS), Daejeon, 305-811, Republic of Korea

[†]Email: yoshikazu.hirayama@kek.jp

Abstract

We developed the KEK Isotope Separation System (KISS) for the nuclear spectroscopy of the nuclei in the vicinity of $N = 126$. The spectroscopy is important not only to study the nuclear structure but also to understand the explosive astrophysical environment for the formation of the third peak in the observed solar r-abundance pattern. We report the experimental results of β-γ spectroscopy and in-gas-cell laser ionization spectroscopy for the nuclei in this heavy region.

1 Introduction

The study of the β-decay half-lives and nuclear masses of waiting-point nuclei with $N = 126$ is crucial to understand the explosive astrophysical environment for the formation of the third peak in the observed solar abundance pattern, which is produced by a rapid neutron capture process (r-process) [1]. For the nuclear spectroscopy in this heavy region, we have developed the KEK Isotope Separation System (KISS) [2, 3]. The KISS is an argon-gas-cell-based laser ion source combined with an on-line isotope separator [4]. The nuclei around $N = 126$ are produced by multi-nucleon transfer reactions (MNT) [5] of ^{136}Xe beam and ^{198}Pt target [6]. For β-γ decay spectroscopy to deduce the half-lives, we developed high-efficiency detector system, which consists of new gas counter (MSPGC) [7, 8] and Super Clover Ge detectors (SCGe). For precise mass measurement, we installed a multi-reflection time-of-flight mass spectrograph (MRTOF-MS) [9]. The KISS facility enabled us to perform in-gas-cell laser ionization spectroscopy from radiation measurements by using the β-γ decay detectors and from ion counting particle-identified by using the MRTOF-MS. Here, we report the present status and experimental results at KISS.

[*]Present address: Department of Physics, Bangladesh University of Textiles, Dhaka 1208, Bangladesh

2 KISS

Figure 1 shows a schematic layout of KISS installed at the RIBF facility in RIKEN. It consists of the gas-cell system shown in the red box in Fig. 1, the laser system, the mass-separator system, the detector station for decay spectroscopy, and the MRTOF-MS for mass measurements.

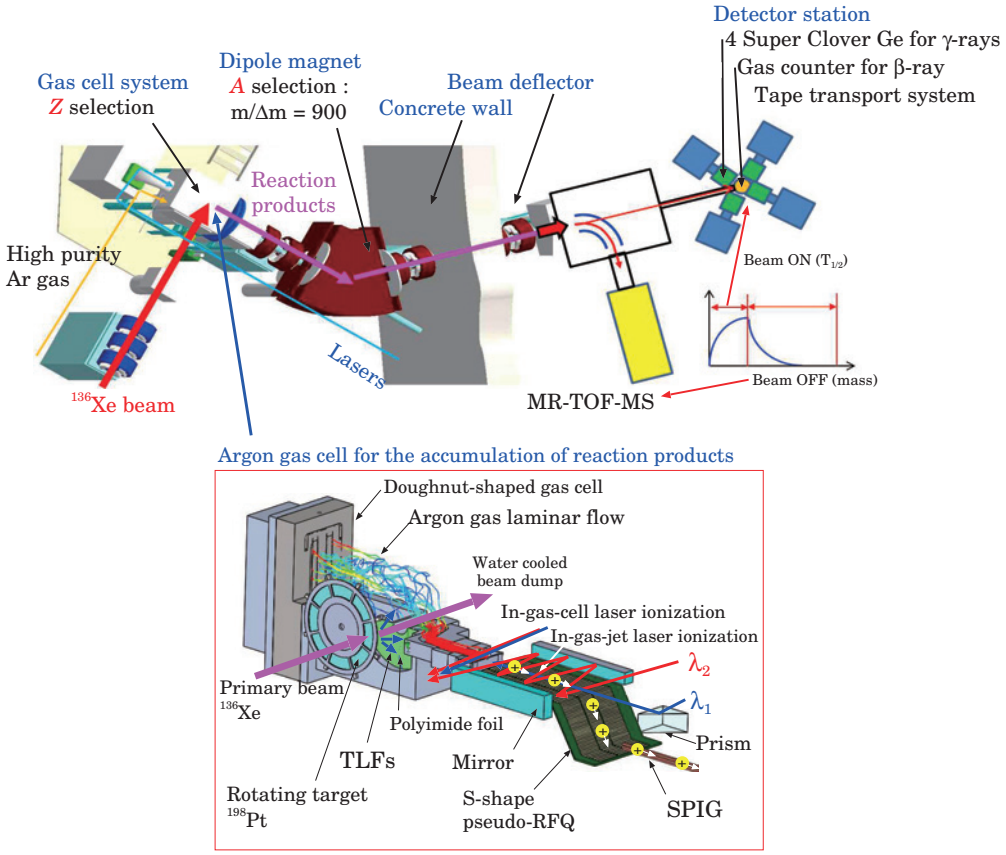

Figure 1: Schematic view of KISS (top), and the KISS gas cell shown in the red box (bottom).

2.1 KISS gas cell system

A primary beam of $^{136}Xe^{20+}$ (∼7 MeV/nucleon, 50 pnA) irradiated production targets such as enriched ^{198}Pt (purity 91.63% and thickness 12.5 mg/cm^2), ^{nat}Pt, and ^{nat}W [6]. Then, the primary beam passed through the beam pipe of the doughnut-shaped gas cell [3] (see Fig. 1) without entering the gas cell, where reaction products of interest are stopped. Finally, the beam was stopped at a water cooled beam dump, which was placed far from the KISS gas cell.

For increasing the production yield, the doughnut-shaped gas cell (see Fig. 1) was developed to avoid the primary beam passing through the gas cell, otherwise plasma effects [18] significantly reduce the efficiency to extract the reaction products from the gas cell. Only the target-like fragments (TLFs) can be implanted into the gas cell with high efficiency, owing to the characteristic large emission angles of TLFs [2]. Then, the TLFs neutralized in the argon gas were transported toward the exit by a optimized argon gas laminar flow [3]. We employed two kinds of two-color two-step laser resonance ionization techniques for selecting the atomic number Z. By applying the in-gas-cell and in-gas-jet laser ionization techniques, we can produce

singly charged ions in this heavy region with Z = 70-78 for β-γ spectroscopy, hyperfine structure (HFS) and mass measurements even though these elements are refractory. The in-gas-cell laser ionization technique is applied for the spectroscopic work which requires higher yields. On the other hand, in-gas-jet laser ionization technique [19], which can selectively ionize ground and isomeric states of the nuclei, is used for much more precise nuclear spectroscopic works.

The laser-produced singly charged ($q = 1$) ions were transported through a S-shaped pseudo-RFQ (S-RFQ) and sextupole ion guide (SPIG), and were accelerated with an energy of 20 kV. Their mass-to-charge ratio (A/q) was selected by a dipole magnet with $A/\Delta A$ = 900. Finally, one kind of isotope was transported to the detector station placed at the neighboring experimental hall for the nuclear spectroscopy.

2.2 Detector station and MRTOF-MS

The detector station has a tape transport device to avoid accumulation of the radioactivity from the daughter nuclei of the separated nuclides under the pulsed beam operation of KISS. An aluminized Mylar tape was moved at the end of each measurement cycle to remove unwanted radioactivity from the detection area. We developed high-efficiency and low-background gas counter, named multi-segmented proportional gas counter (MSPGC) [7, 8], in order to perform β-γ and laser spectroscopic studies by detecting β-particles, X-rays, and internal conversion electrons emitted from rare reaction products. Four Super Clover Ge detectors were installed to detect β-delayed γ-rays and γ-rays of de-excitation transitions from isomeric states. The absolute detection efficiency for γ-rays with an energy of 400 keV and 1000 keV was measured as high as 14% and 10%, respectively, owing to the close setup geometry of approximately 50 mm from the implantation position on the tape.

We can transport KISS beam to the MRTOF-MS by using an electric deflector for producing pulsed beam during the decay curve measurement at the decay station. Half-lives and masses can be simultaneously measured in one experiment as shown in Fig. 1. The measured mass resolving power $R_{\rm m}$ is more than 200,000 which indicates that only 100-ion accumulation is sufficient to determine a nuclear mass with the mass precision $\delta m/m = 10^{-6}$ ($\delta m \approx 100$ keV). The value of $\delta m \approx 100$ keV satisfies with an astrophysical requirement to study the explosive astrophysical environment. The MRTOF-MS has been successfully developed and applied not only to mass measurements [9] but also to the particle identifications for further nuclear spectroscopy such as hyperfine measurements.

3 Experimental results

Due to the difficulties in the production and ion-extraction of the refractory nuclei in this heavy region (Z = 70-78 and $N \leq 126$), spectroscopic study has been scarcely carried out, especially, no laser spectroscopic data for the neutron-rich nuclei (limited to stable nuclei and neutron-deficient nuclei). However, we can access the neutron-rich nuclei of these refractory elements by selecting appropriate production targets at the KISS facility. By using enriched ^{198}Pt, natural platinum and tungsten targets, we extracted 17 neutron-rich nuclei from the KISS gas cell for nuclear spectroscopic works. We have successfully performed decay spectroscopy of ^{195,196,197,198}Os [10, 11, 12], high-K isomer ^{187}Ta [13] and ^{192}Re [14], and also perform in-gas-cell laser ionization spectroscopy of ^{199g,199m}Pt [15], ^{196,197,198}Ir [16], and ^{194,196}Os [17] for determining the magnetic moments and the change of the charge-radii (deformation parameters). We plan to perform the laser spectroscopy for these nuclei as well as the β-γ spectroscopy and mass measurements intensively and systematically.

In the following sections, we introduced experimental results of the laser spectroscopy for

^{196,197,198}Ir [16] and the ^{194,196}Os [17]. In the case of in-gas-cell laser ionization spectroscopy, the measured laser resonance spectrum is generally broadened by a pressure broadening due to the atomic collision with argon atoms in the gas cell (the gas pressure ∼75 kPa). However, we can deduce an isotope shift value from the measured center of gravity frequency of atomic transitions and magnetic dipole moment which governs the resonance width and structure. These physics quantities are very important to discuss the nuclear deformation and structure including a wave-function.

3.1 Laser spectroscopy of ^{196,197,198}Ir isotopes

We successfully performed in-gas-cell laser ionization spectroscopy of ^{196,197,198}Ir [16] for determining the magnetic moments and the change of the charge-radii (deformation parameters). Figure 2 shows the measured HFS spectra by detecting the β-rays emitted from each isotope ($T_{1/2} \sim 10$ min) as a function of laser wavelength.

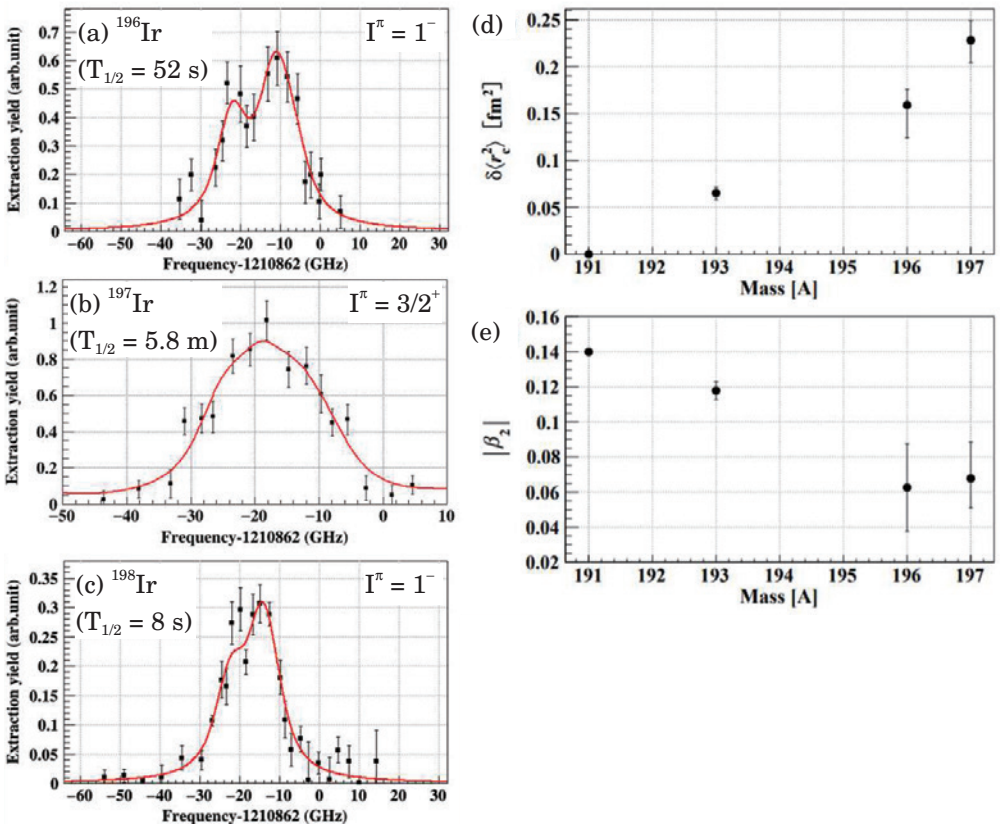

Figure 2: Measured HFS spectra of (a) ^{196}Ir, (b) ^{197}Ir, and (c) ^{198}Ir. The red lines indicate the best fit lines with each spin-parity value. (d) Evaluated change of charge radii, and (e) deduced deformation parameters.

By fitting the measured HFS spectra, we can evaluate the change of charge radii and deformation parameters as shown in Figs. 2-(d) and (e), respectively, from the measured isotope shifts, and discuss the systematic trend [16]. The magnetic moments ($\mu_{\rm exp}$) with spin-parity I^π can be extracted from the measurements as shown in Table 1, and we can suggest the wave-function of each isotope from the theoretical $\mu_{\rm calc}$ calculated by applying strong-coupling model [20]. In order to determine the magnetic moments with spin-parity and wave-functions

more precisely and explicitly, we have been developing an in-gas-jet collinear laser ionization spectroscopy technique [19].

Table 1: Results of the in-gas-cell laser ionization spectroscopy of ^{196,197,198}Ir [16].

Nuclide	I^π	$\mu_{\rm exp}$ ($\mu_{\rm N}$)	$\mu_{\rm calc}$ ($\mu_{\rm N}$)	suggested wave-function
^{196}Ir	1^-	$+0.31^{+0.04}_{-0.20}$	$+0.15^{+0.09}_{-0.03}$	$\pi 3/2^+[402] \otimes \nu 1/2^-[501]$
	2^-	$+0.34^{+0.05}_{-0.14}$	$+0.39^{+0.11}_{-0.04}$	$\pi 3/2^+[402] \otimes \nu 1/2^-[501]$
^{197}Ir	$3/2^+$	$+0.23^{+0.10}_{-0.03}$	$+0.23^{+0.04}_{-0.04}$	$\pi 3/2^+[402]$
^{198}Ir	1^-	$+0.13^{+0.10}_{-0.02}$	$+0.16^{+0.09}_{-0.04}$	$\pi 3/2^+[402] \otimes \nu 1/2^-[510]$

3.2 Laser spectroscopy of ^{194,196}Os isotopes with the assist of MRTOF-MS

Although we have measured the HFS spectra of short-lived ($T_{1/2} \sim 10$ min) isotopes by detecting the β- and γ-rays at the KISS facility successfully, it was difficult to measure the HFS spectra of isotopes with $T_{1/2} > 1$ h by detecting the decay radiations in a limited beam time. However, we can efficiently measure the laser resonance spectra of these isotopes thanks to an ion counting by using the MRTOF-MS without waiting for the radiation decays. The MRTOF-MS can identify clearly the isotopes from the mass-dependent time-of-flight (TOF) spectrum as shown in Fig. 3-(a).

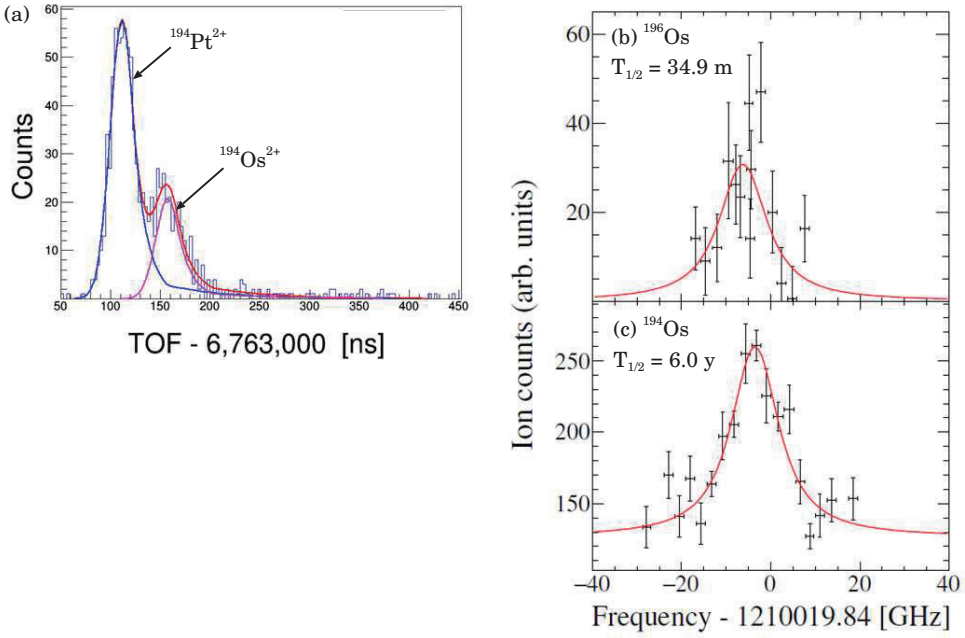

Figure 3: (a) Measured TOF spectrum of laser-induced $^{194}Os^{2+}$ (doubly charged in the MRTOF-MS system) with survived ion of non laser-resonant $^{194}Pt^{2+}$ emitted from the platinum production target. Measured laser resonance spectra of (b) ^{196}Os and (c) ^{194}Os.

To study the nuclear structures, we successfully measured the laser resonance spectra of ^{196}Os ($I^\pi = 0^+$, $T_{1/2} = 34.9$ m) and ^{194}Os ($I^\pi = 0^+$, $T_{1/2} = 6.0$ y), as shown in Figs. 3-(b) and (c) respectively, to determine the change in charge radii and the deformation parameters

by using the in-gas-cell laser ionization spectroscopy technique assisted by MRTOF-MS [17]. By comparing the evaluated deformation parameters with theoretical values, we found that ^{194}Os nucleus is oblately deformed and ^{196}Os nucleus would not be pure axially deformed rotor. Further systematic measurements of osmium isotopes are planed.

4 Summary

The KEK Isotope Separation System (KISS) was installed at RIKEN to perform nuclear spectroscopy of neutron-rich isotopes with neutron numbers around 126 for applications in astrophysics. We can successfully extract the neutron-rich isotopes produced by the MNT reactions from the KISS gas cell. We performed decay spectroscopy of ^{195,196,197,198}Os, ^{187}Ta, and ^{192}Re isotopes. By using in-gas-cell laser ionization spectroscopy technique, we measured the HFS spectra of ^{199g,199m}Pt, ^{196,197,198}Ir, and ^{194,196}Os isotopes. As the further spectroscopic studies at KISS, we plan to perform mass measurements by using MRTOF-MS and precise in-gas-jet laser ionization spectroscopy additionally.

Acknowledgments

This experiment was performed at the RI Beam Factory operated by RIKEN Nishina Center and CNS, University of Tokyo. The authors acknowledge the RIKEN accelerator staff for their support. This work was supported by JSPS KAKENHI Grant Nos. JP23244060, JP24740180, JP26247044, JP15H02096, JP17H01132, JP17H06090, and JP18H03711.

References

[1] Burbidge E.M. et al., Rev. Mod. Phys., 1957;29:547.
[2] Hirayama Y. et al., Nucl. Instrum. Method B, 2015;353:4.
[3] Hirayama Y. et al., Nucl. Instrum. Method B, 2017;412:11.
[4] Kudryavtsev Yu. et al., Nucl. Instrum. Method B, 1996;114:350.
[5] Dasso C.H. et al., Phys. Rev. Lett., 1994;73:1907.
[6] Watanabe Y.X. et al., Phys. Rev. Lett., 2015;115:172503.
[7] Mukai M. et al., Nucl. Instrum. Method A, 2018;884:1.
[8] Hirayama Y. et al., Nucl. Instrum. Method A, 2021;997:165152.
[9] Schury P. et al., Phys, Rev. C, 2017;95:011305(R).
[10] Hirayama Y. et al., Phys. Rev. C, 2018;98:014321.
[11] Watanabe Y.X et al., Phys. Rev. C, 2020;101:041305(R).
[12] Ahmed M. et al., Phys. Rev. C, 2021;103:054312.
[13] Walker P.M. et al., Phys. Rev. Lett, 2020;125:192505.
[14] Watanabe H. et al., submitted to Phys. Lett. B.
[15] Hirayama Y. et al., Phys. Rev. C, 2017;96:014307.
[16] Mukai M. et al., Phys. Rev. C, 2020;102:054307.
[17] Choi, H. et al., Phys. Rev. C, 2020;102:034309.
[18] Huyse H. et al., Nucl. Instrum. Method B, 2002;187:535.
[19] Kudryavtsev Yu. et al., Nucl. Instrum. Method B, 2013;297:7.
[20] Bohr A, Mottelson B.R., Nuclear structure:volume II Nuclear deformations. Massachusetts(US):W.A. Benjamin, Inc.;1975.

7. Production and applications of radioisotopes at RIKEN RI Beam Factory

– Chemistry of new elements through diagnosis and therapy of cancer –

Hiromitsu HABA*
Nishina Center for Accelerator-Based Science, RIKEN, Wako, Saitama 351-0198, Japan
*Email: haba@riken.jp

We are developing production technologies of radioisotopes (RIs) for application studies at RIKEN RI Beam Factory (RIBF). More than 100 RIs produced at the AVF cyclotron, RIKEN Linear Accelerator, and RIKEN Ring Cyclotron have been used in research fields of physics, chemistry, biology, engineering, medicine, pharmaceutical and environmental sciences. In this paper, RIs for superheavy element chemistry and targeted alpha therapy at RIBF are emphasized. Purified RIs such as ^{65}Zn, ^{67}Cu, and ^{109}Cd are delivered to universities and research institutes through Japan Radioisotope Association. Short-lived RIs such as ^{88}Zr, ^{175}Hf, and ^{211}At are also distributed to researchers through the platform for short-lived RI distribution, supported by JSPS KAKENHI.

1. Introduction

Due to its high sensitivity, the radioactive tracer technique has been successfully applied for investigations of the behavior of elements in the fields of physics, chemistry, biology, engineering, medicine, pharmaceutical and environmental sciences. At RIKEN RI Beam Factory (RIBF), we have been developing production technologies of radioisotopes (RIs) for application studies using the AVF cyclotron (AVF), RIKEN Linear Accelerator (RILAC), and RIKEN Ring Cyclotron (RRC). In this paper, the production and applications of RIs at RIBF are reported with focus on RIs for superheavy element chemistry and targeted alpha therapy. Distributions of RIs through Japan Radioisotope Association and Supply Platform of Short-lived Radioisotopes for Fundamental Research are introduced.

2. Production of RIs at RIBF

First of all, reliable excitation functions are necessary to effectively and quantitatively produce RIs of interest and to reduce contamination of undesired by-products. We have been systematically investigating the excitation functions especially for the d- and α-induced reactions on various targets at AVF in collaboration with Sunway University, Malaysia, International Atomic Energy Agency, Austria, Hokkaido University, and Institute for Nuclear Research (ATOMKI), Hungary. The excitation functions are compared in detail with the previous ones as well as the theoretical model calculations such as the TALYS code taken from the TENDL online database [1]. Then, we develop RI production apparatuses on the beam lines of AVF, RRC, and RILAC. We also develop chemical separation procedures to obtain RIs with high radionuclidic purity, specific radioactivity, and chemical purity. Finally, radioactivity and chemical purity of RIs are specified by γ-ray/α-particle spectrometry and Inductively Coupled Plasma

Mass Spectrometry (ICP-MS), respectively.

RIKEN RIs developed for application studies since 2002 are summarized in Table 1. With light- to heavy-ion beams from the AVF cyclotron, we produce more than 100 RIs from ^{7}Be (atomic number Z = 4) to ^{262}Db (Z = 105) [2,3]. RIs for superheavy element chemistry such as ^{265a,b}Sg (Z = 106) and ^{266}Bh (Z = 107) are produced using a gas-jet transport system coupled to the GAs-filled Recoil Ion Separator (GARIS) at RILAC [4]. On the other hand, RIs of a large number of elements, called multitracer, are simultaneously produced from metallic targets such as ^{nat}Ag and ^{197}Au irradiated with a 135 MeV/u ^{14}N beam from RRC [5].

3. Application studies with RIKEN RIs

The RIKEN RIs have been used in the application studies in collaboration with many researchers in the world as annually reported in RIKEN Accelerator Progress Reports [6] (See the section "Nuclear chemistry and Radiochemistry".) and the references therein. In this paper, we focus on RIs used in chemistry of superheavy elements and targeted alpha therapy.

3.1. Superheavy element chemistry

Chemical characterization of newly-discovered superheavy elements (SHEs, atomic numbers $Z \geq$ 104) is an extremely interesting and challenging subject in modern nuclear and radiochemistry [7]. To start up the SHE chemistry at RIBF, we installed a gas-jet transport system to the focal plane of GARIS [4]. This system is a promising approach for exploring new frontiers in the SHE chemistry: the background radiations from unwanted products are strongly suppressed, the intense primary heavy-ion beam is absent in the gas-jet chamber, and hence the high gas-jet extraction yield is attained. Furthermore, the beam-free condition makes it possible to investigate new chemical systems. Long-lived SHE RIs of ^{261a,b}Rf (Z = 104), ^{262}Db, ^{265a,b}Sg, and ^{266}Bh were produced in the ^{248}Cm(^{18}O,5n)^{261a,b}Rf, ^{248}Cm(^{19}F,5n)^{262}Db, ^{248}Cm(^{22}Ne,5n)^{265a,b}Sg, and ^{248}Cm(^{23}Na,5n)^{266}Bh reactions, respectively, and their decay properties were investigated in detail using a rotating wheel apparatus for α and SF spectrometry [8–11]. The decay properties determined for ^{261a,b}Rf, ^{262}Db, ^{265a,b}Sg, and ^{266}Bh are shown in Figure 1.

Using the GARIS gas-jet system, the first chemical synthesis and gas-chromatogrphic analysis of $Sg(CO)_6$ were successfully conducted under an international collaboration lead by GSI Helmholtzzentrum für Schwerionenforschung GmbH, Helmholtz Institute Mainz, and University of Mainz, Germany [12]. A detailed experiment to investigate the stability of the metal carbon bond in $Sg(CO)_6$ is in progress with a thermal decomposition setup developed by Paul Scherrer Institute, Switzerland [13]. Also, syntheses and properties of Tc, Ru, Rh, and Re carbonyls are under study at Institute of Modern Physics (IMP), China and RIBF for future studies on Bh, Hs (Z = 108), and Mt (Z = 109) carbonyls [14–16]. To realize aqueous chemistry studies of Sg and Bh, we have been developing a continuous and rapid solvent extraction apparatus which consists of a continuous dissolution apparatus Membrane DeGasser (MDG), a Flow Solvent Extractor (FSE), and a liquid scintillation detector for α/SF-spectrometry [17].

A conventional target/gas-jet system for the production of SHE RIs is also available at AVF [18]. The automated batch-type solid-liquid extraction apparatus for repetitive experiments of transactinides (AMBER) was developed by Osaka University, and distribution coefficients of Rf were determined in HCl [19]. Reversed-phase extraction behavior of Rf with thenoyltrifluoroacetone in HF/HNO_3 was investigated using Automated Rapid Chemistry Apparatus (ARCA) developed by Japan Atomic Energy Agency [20]. Recently, co-precipitation of Rf in basic solutions containing NH_3 or NaOH was

investigated in collaboration with Osaka University using a semiautomatic suction filtration apparatus, CHIN [21].

Table 1. List of radioisotopes developed for application studies at RIBF since 2002.

Nuclides	Z	$T_{1/2}$	Accelerator	Reactions
^{7}Be	4	53.29 d	AVF	^{nat}Li(p,xn)
^{24}Na	11	14.9590 h	AVF	^{nat}Mg(d,x)
^{28}Mg	12	20.91 h	AVF	^{27}Al(n,3p)
^{43,44}K	19	12.360 h, 22.3 h	AVF	^{nat,44,42}Ca(d,x)
^{44m,44}Sc	21	58.6 h, 3.927 h	AVF	^{nat}Ti(d,x)
^{44}Ti	22	49 y	AVF	^{nat}Ca(d,3n)
^{48}V	23	15.9735 d	AVF	^{nat}Ti(p,xn)
^{48,51}Cr	24	21.56 h, 27.702 d	AVF	^{nat}Ti(n,xn)
^{48}Cr	24	21.56 h	AVF	^{48}Ti(n,2n)
^{52g,54}Mn	25	5.591 d, 312.3 d	AVF	^{nat}Cr(p,xn)
^{56,57,58}Co	27	77.27 d, 271.79 d, 70.82 d	AVF	^{nat}Fe(d,xn)
^{61}Cu	29	3.333 h	AVF	^{nat}Zn(d,x)
^{65}Zn	30	244.26 d	AVF	^{nat}Cu(p,xn)
^{66,67}Ga	31	9.49 h, 3.2612 d	AVF	^{nat}Cu(d,xn)
^{67}Cu	29	61.83 h	AVF	^{nat}Zn(d,xn)
^{69m}Zn	30	13.76 h	AVF	^{70}Zn(p,α)
^{74}As	33	17.77 d	AVF	^{70}Zn(d,αn)
^{73}Sc	34	119.779 d	AVF	^{nat}Zn(d,x)
				^{nat}Ga(n,x)
				^{75}As(p,αx)
				^{75}As(d,2n)
				^{nat}Ge(n,xn)
^{83}Sr	38	64.84 d	AVF	^{nat}Rb(p,xn)
				^{nat}Rb(d,xn)
^{83}Zr*	40	7.86 min	AVF/RILAC	^{nat}Ge(^{18}O,xn)
^{88}Y	39	106.65 d	AVF	^{nat}Se(p,xn)
				^{nat}Se(d,xn)
				^{nat}Rb(α,xn)
^{88,89}Zr	40	83.4 d, 78.41 h	AVF	^{89}Y(p,xn)
				^{89}Y(d,xn)
				^{89}Y(n,p)
^{89m}Zr*	40	4.18 min	AVF	^{89}Y(d,2n)
				^{nat}Se(α,xn)
^{88m,89m}Nb*	41	7.8, 14.5 min	AVF/RILAC	^{nat}Ge(^{18}F,xn)
^{90m,89m}Nb*	41	18.81 s, 14.60 h	AVF	^{nat}Zr(p,xn)
				^{nat}Zr(d,xn)
^{90}Mo*	42	5.67 h	AVF/RILAC	^{nat}Ge(^{22}Ne,xn)
^{92m,90}Nb	41	10.15 d, 34.975 d	AVF	^{nat}Zr(p,xn)
				^{nat}Zr(d,xn)
^{92,99}Tc*	43	4.23 min, 293 min	AVF	^{nat}Mo(d,xn)
^{93m}Mo*	42	6.85 h	AVF	^{93}Nb(p,n)
				^{93}Nb(d,2n)
				^{nat}Zr(α,xn)
^{93g,99}Tc*	43	2.75 h, 293 min	AVF	^{93}Nb(n,xn)
^{95,96}Tc	43	20.0 h, 4.28 d	AVF	^{nat}Mo(d,xn)
^{93m}Tc	43	61 d	AVF	^{93}Mo(p,n)
				^{nat}Mo(d,xn)
				^{93}Nb(n,2n)
^{99}Mo	42	65.94 h	AVF	^{nat}Zr(α,xn)
^{99}Rh	45	16.1 d	AVF	^{99}Ru(p,n)
^{109m}Pd*	46	4.696 min	AVF	^{nat}Pd(d,x)
^{109m,}Ag*	47	33.5 min, 69.2 min	AVF	^{nat}Pd(d,xn)
^{111}Ag	47	7.45 d	AVF	^{nat}Pd(d,xn)
^{109}Cd	48	462.6 d	AVF	^{nat}Ag(p,xn)
				^{nat}Ag(d,xn)
^{124}Sb	51	60.20 d	AVF	^{nat}Sn(d,x)
^{121m}Te	52	154 d	AVF	^{nat}Sn(α,xn)
				^{nat}Sb(d,xn)
^{123}I	53	4.1760 d	AVF	^{124}Te(d,2n)
^{130m}Ba	56	28.7 h	AVF	^{133}Cs(n,x)
				^{nat}La(d,x)

Nuclides	Z	$T_{1/2}$	Accelerator	Reactions
^{139}Ce	58	137.640 d	AVF	^{nat}La(p,xn)
				^{nat}La(d,xn)
^{141}Ce	58	32.501 d	AVF	^{nat}Ba(n,x)
^{141m}Nd*	60	62.0 s	AVF	^{141}Pr(d,2n)
^{144}Pm	61	265 d	AVF	^{145}Pr(n,x)
^{145}Sm	62	66 s	AVF	^{148}Sm(d,α2n)
^{145,146}Eu*	63	2.63 min, 10.2 s	AVF	^{148}Sm(d,xn)
^{146}Gd	64	48.27 d	AVF	^{148}Sm(n,2n)
^{162,163}Yb*	70	18.87 min, 11.05 min	AVF	^{nat}Gd(^{12}C,xn)
^{163,164}W*	74	2.75 s, 6.0 s	RILAC	^{152}Sm(^{16}Mg,xn)
^{169}Hf*	72	3.24 min	AVF/RILAC	^{nat}Gd(^{16}O,xn)
^{170m}Ta*	73	6.76 min	AVF/RILAC	^{nat}Gd(^{19}F,xn)
^{170}Re*	75	9.2 s	RILAC	^{152}Gd(^{22}Ne,5n)
^{171}Hf*	72	23.6 h	AVF	^{nat}Yb(x,xn)
^{172}W*	74	7.6 min	AVF/RILAC	^{nat}Gd(^{22}Ne,xn)
^{176}Re*	75	2.40 min	RILAC	^{nat}Gd(^{22}Na,xn)
^{175}Hf	72	70 d	AVF	^{nat}Lu(p,xn)
				^{nat}Lu(d,xn)
^{177,178m,179m}Ta	73	56.56 h, 2.36 h, 1.82 y	AVF	^{nat}Hf(p,xn)
				^{nat}Hf(d,xn)
^{177}W*	74	135 min	AVF	^{nat}Hf(α,xn)
^{179m}Ta*	73	2.36 h	AVF	^{nat}Hf(d,xn)
^{179m}W*	74	6.40 min	AVF	^{nat}Ta(d,xn)
^{180}Re*	75	2.44 min	AVF	^{nat}Ta(α,xn)
^{181}W	74	121.2 d	AVF	^{nat}Ta(p,xn)
				^{nat}Ta(d,xn)
^{181}Re*	75	19.9 h	AVF	^{nat}W(d,xn)
^{182}Ta	73	114.43 d	AVF	^{nat}Hf(n,x)
^{182n,183,184m,184g}Re	75	12.7 h, 70.0 d, 169 d, 38.0 d	AVF	^{nat}W(d,xn)
^{183}Re	75	70.0 d	AVF	^{nat}Ta(n,xn)
^{187}Os	76	93.6 d	AVF	^{nat}Re(p,xn)
^{186}Re	75	90.64 h	AVF	^{186}W(d,2n)
^{188,189,191}Pt	78	10.2 d, 10.87 h, 2.802 d	AVF	^{nat}Os(α,xn)
				^{nat}Ir(d,xn)
^{203}Pb	82	51.873 h	AVF	^{203}Tl(p,n)
^{209}Bi	83	6.243 d	AVF	^{nat}Pb(p,xn)
				^{nat}Pb(d,xn)
^{209}Fr*	87	15.9 s	RILAC	^{209}Ra(^{4}He,3n)
^{207}Fr*	87	50.0 s	RILAC	^{197}Au(^{14}O,6n)
^{211}At	85	7.214 h	AVF	^{209}Bi(α,2n)
^{212}Fr*	87	20.0 min	AVF	^{206,207,208,nat}Pb(^{11}B,x)
^{214}Ac*	89	8.2 s	RILAC	^{197}Au(^{22}Ne,5n)
^{225}Ac	89	10.0 d	RRC	^{232}Th(^{14}N,xnyp)
^{229}Pa	91	1.50 d	AVF	^{232}Th(p,4n)
^{236}Np	93	1.54×10^{3} y	AVF	^{232}Th(^{7}Li,3n)
^{250}Fm*	100	4.2 s	RILAC	^{209}Bi(^{48}Ar,3n)
^{255}No*	102	3.1 min	AVF/RILAC AVF	^{249}Cf(^{12}C,5n) ^{248}Cm(^{11}C,5n)
^{255}Lr*	103	22 s	RILAC	^{209}Bi(^{48}Ca,2n)
^{253}Lr*	103	0.646 s	AVF	^{248}Cm(^{14}N,5n)
^{256}Lr*	103	6.3 s	AVF	^{248}Cm(^{14}N,4n)
^{261m}Rf*	104	68, 1.9 s	AVF/RILAC	^{248}Cm(^{18}O,5n)
^{261}Db*	105	34 s	AVF/RILAC	^{248}Cm(^{19}F,5n)
^{265m}Sg*	106	8.5, 14.4 s	RILAC	^{248}Cm(^{22}Ne,5n)
^{266}Bh*	107	10.0 s	RILAC	^{248}Cm(^{23}Na,5n)
Multitracer	<22		RRC	^{nat}Ti(^{14}N,xnyp)
Multitracer*	<29		RRC	^{nat}Cu(^{14}N,xnyp)
Multitracer	<47		RRC	^{nat}Ag(^{14}N,xnyp)
Multitracer	<72		RRC	^{nat}Hf(^{14}N,xnyp)
Multitracer*	<73		RRC	^{nat}Ta(^{14}N,xnyp)
Multitracer*	<79		RRC	^{197}Au(^{14}N,xnyp)
Multitracer*	<83		RRC	^{209}Bi(^{14}N,xnyp)
Multitracer	<90		RRC	^{232}Th(^{14}N,xnyp)

* RIs produced with the gas-jet system.

3.2. Production of ^{211}At for Targeted Alpha Therapy

In recent years, the needs for α-particle-emitting RIs for targeted alpha therapy (TAT) is rapidly increasing in the world. The α particles have a shorter range (40–100 μm) in living tissues than β particles (0.05–12 mm), and have a high linear energy transfer (~80 keV/μm), so they are highly cytotoxic. Thus, medicines labeled with α-particle-emitting RIs are considered to be effective in treating disseminated cancer, blood cancer, micrometastasis cancer, and microcancer remaining in a postoperative site. ^{211}At

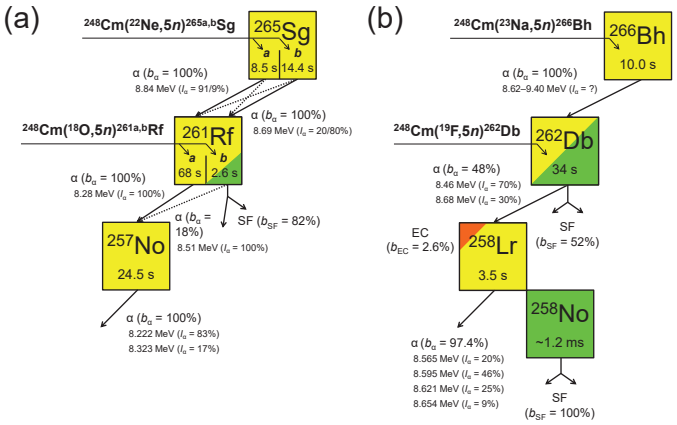

Figure 1. Decay pattern for the chains (a) ^{265a,b}Sg → ^{261a,b}Rf → ^{257}No → and (b) ^{266}Bh → ^{262}Db → ^{258}Lr → ^{258}No → [8–11].

decays to the stable nuclide ^{207}Pb by emitting an α particle with the half-life of 7.214 h. ^{211}At is produced in the ^{209}Bi(α,2n)^{211}At reaction by irradiating a metallic ^{209}Bi target with α particles accelerated by a cyclotron. The optimum incident beam energy for the production is ~28 MeV in order to minimalize the production of ^{210}At in the ^{209}Bi(α,3n)^{210}At reaction: ^{210}At decays to the long-lived and toxic ^{210}Po by an electron capture. Since the half-life of ^{211}At is very short, it is difficult to import ^{211}At from abroad and domestic production is essential. In order to realize the radionuclide therapy with ^{211}At in Japan, it is necessary to establish a platform for the production and supply of ^{211}At among domestic accelerator facilities that have large accelerators. Since 2015, we have been developing a production technology of ^{211}At at AVF and distributing it to 16 research groups in Japan [22].

Figure 2 shows a schematic and photos of the ^{211}At production system developed at RIBF. The metallic ^{209}Bi target is irradiated with α particles accelerated to 29.0 MeV by AVF. The beam energy is controlled with an accuracy of ±1% using a time-of-flight (TOF) beam energy measuring device. The metallic ^{209}Bi target in 20 mg/cm^2 thickness is prepared by a vacuum evaporation method on an Al plate. Since the melting point of the Bi metal is low (271.5 °C), the target placed at an angle of 15° with respect to the beam axis is effectively cooled by water (1.5 L/min) and He (30 L/min). In addition, the beam axis is rotated at 120 rpm by an electromagnet (beam wobbler) to reduce heat load on the target. The current setup can accept a beam intensity up to 40 μA to produce 2 GBq of ^{211}At in 1 h. After irradiation, as shown in Figure 2 (c), the Bi target is placed on a Cu boat in a quartz tube (i.d. 30 mm × L180 mm), and O_2 is passed through the tube (20 mL/min). The quart tube is heated up to 850 °C with an electric furnace. ^{211}At sublimated from the ^{209}Bi target is transported to a PFA tube (i.d. 1 mm×L1000 mm) bound in a spiral and cooled to –100 °C with a chiller. After collecting ^{211}At, the inside of the PFA tube is washed with a few hundred μL of pure water, methanol, chloroform, etc. to recover ^{211}At. The chemical yield is >80%. The purified ^{211}At is shipped to universities and research institutes in Japan to develop novel nuclear medicines for cancer therapy [23–25].

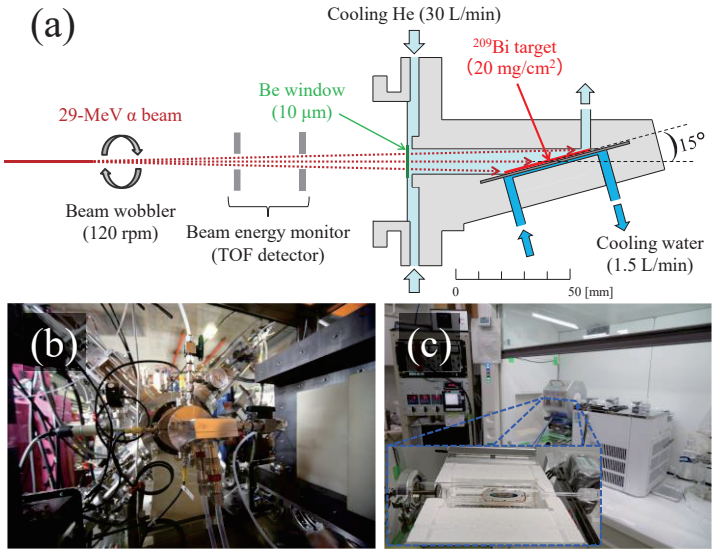

Figure 2. (a) Schematic of the target chamber for ^{211}At production. (b) Photo of the target chamber. (c) Photo of a dry distillation apparatus for ^{211}At separation.

^{225}Ac is also one of the most promising α-particle-emitting RIs for TAT. However, a stable supply

system of ^{225}Ac has not yet been established in Japan even at the basic research scale (~100 MBq). Thus, we started to develop the production technologies of ^{225}Ac in the ^{232}Th(^{14}N,xnyp)^{225}Ac and ^{226}Ra(p,2n)^{225}Ac reactions using RRC and AVF, respectively.

4. Distributions of RIKEN RIs

Since 2007, the purified RIs of ^{65}Zn, ^{67}Cu, ^{85}Sr, ^{88}Y, and ^{109}Cd are delivered to Japan Radioisotope Association for fee-based distribution to more than 40 universities, research institutes, and companies in Japan. More than 150 deliveries have been conducted until March, 2020. The RIKEN RIs such as ^{88}Zr, ^{95}Nb, ^{175}Hf, ^{179}Ta, and ^{211}At are also available under the JSPS KAKENHI program "Supply Platform of Short-lived Radioisotopes for Fundamental Research" in collaboration with Research Center for Nuclear Physics, Osaka University, Cyclotron and Radioisotope Center and Research Center for Electron Photon Science, Tohoku University, National Institute of Radiological Sciences and Takasaki Advanced Radiation Research Institute, National Institutes for Quantum and Radiological Science and Technology [26]. Until March, 2020, RIBF accepted a total of 99 orders for 23 research projects.

5. Summary

Present status of the production and applications of RIs at RIBF is briefly reviewed. RIs for SHE chemistry and TAT are highlighted. Very recently, the RILAC facility was upgraded as SRILAC with a 28 GHz superconducting ECR ion source, a super-conducting quarter-wavelength resonator, and a new gas-filled recoil ion separator (GARIS III) being installed. The SRILAC facility is expected to open the next generation RI applications at RIBF with an order of magnitude larger production yields. Using Superconducting Ring Cyclotron and the fragment separator BigRIPS, RIBF can generate more than 3,000 RI beams with the world's highest intensity. In near future, the RI beams will be used for application studies by implanting them into various materials such as water and pharmaceuticals.

References

[1] TALYS-based evaluated nuclear data library, https://tendl.web.psi.ch/tendl_2019/tendl2019.html (accessed 2021-02-25).

[2] Haba, H. et al., Tracer technique in Handbook of Nuclear Chemistry (2nd ed.), edited by A. Vértes, S. Nagy, Z. Klencsár, R. G. Lovas, and F. Roesch, vol. 3, Springer, 2010, pp. 1761–1792.

[3] Haba, H., Production of radioisotopes for application studies at RIKEN RI Beam Factory, J. Part. Accel. Soc. Jpn., 2015; 12: 206–212 (in Japanese).

[4] Haba, H. et al., RIKEN gas-filled recoil ion separator GARIS as a promising interface for superheavy element chemistry –Production of element 104, ^{261}Rf, using the GARIS/gas-jet system–, Chem. Lett., 2009; 38: 426–427.

[5] Haba, H. et al., Development of a gas-jet-coupled multitarget system for multitracer production, Radiochim. Acta, 2005; 93: 539–542.

[6] RIKEN Accel. Prog. Rep., https://www.nishina.riken.jp/researcher/APR/index_e.html (accessed 2021-02-25).

[7] Haba, H., A new period in superheavy-element hunting, Nat. Chem., 2019; 11: 10–13.

[8] Haba, H. et al., Production and decay properties of the 1.9-s isomeric state in ^{261}Rf, Phys. Rev. C, 2011; 83: 034602.

[9] Haba, H. et al., Production of ^{265}Sg in the ^{248}Cm(^{22}Ne,5n)^{265}Sg reaction and decay properties of two isomeric states in ^{265}Sg, Phys. Rev. C, 2012; 85: 024611.

[10] Haba, H. et al., Production of ^{262}Db in the ^{248}Cm(^{19}F,5n)^{262}Db reaction and decay properties of ^{262}Db and ^{258}Lr, Phys. Rev. C, 2014; 89: 024618.

[11] Haba, H. et al., Production of ^{266}Bh in the ^{248}Cm(^{23}Na,5n)^{266}Bh reaction and its decay properties, Phys. Rev. C, 2020, 102: 024625.

[12] Even, J. et al., Synthesis and detection of a seaborgium carbonyl complex, Science, 2014; 345: 1491–1493.

[13] Usoltsev, I., Decomposition studies of group 6 hexacarbonyl complexes. Part 1: Production and decomposition of $Mo(CO)_6$ and $W(CO)_6$, Radiochim. Acta, 2016; 104: 141–151.

[14] Wang, Y. et al., Gas-phase chemistry of technetium carbonyl complexes, Phys. Chem. Chem. Phys., 2015; 17: 13228–13234.

[15] Cao, S. et al., Gas-phase chemistry of ruthenium and rhodium carbonyl complexes, Phys. Chem. Chem. Phys., 2016; 18: 119–125.

[16] Wang, Y. et al., The study of rhenium pentacarbonyl complexes using single-atom chemistry in gas phase, Phys. Chem. Chem. Phys., 2019; 21: 7147–7154.

[17] Haba, H., Superheavy element chemistry at GARIS, EPJ Web Conf., 2016; 131: 07006.

[18] Haba, H., Startup of superheavy element chemistry at RIKEN, Eur. Phys. J. D, 2007; 45: 81–86.

[19] Yokokita, T., Observation of the chemical reaction equilibria of element 104, rutherfordium: Solid-liquid extraction of Rf, Zr, Hf and Th with Aliquat 336 resin from HCl, Dalton Trans., 2016; 45: 18827–18831.

[20] Yokoyama, A. et al., Extraction behavior of rutherfordium as a cationic fluoride complex with a TTA chelate extractant from HF/HNO_3 acidic solutions, Radiochim. Acta, 2019; 107: 27–32.

[21] Kasamatsu, Y. et al., Co-precipitation behaviour of single atoms of rutherfordium in basic solutions, Nat. Chem., 2021, DOI: 10.1038/s41557-020-00634-6.

[22] Haba, H., Production of radioisotopes for targeted radionuclide therapy at RIKEN, Drug Delivery Syst., 2020; 35: 114–120 (in Japanese).

[23] Fujiki, K. et al., ^{211}At-labeled immunoconjugate via a one-pot three-component double click strategy: Practical access to α-emission cancer radiotherapeutics, Chem. Sci., 2019; 10: 1936–1944.

[24] Ohshima, Y. et al., Preclinical evaluation of new α-radionuclide therapy targeting LAT1: 2-[^{211}At]astato-α-methyl-L-phenylalanine in tumor-bearing model, Nucl. Med. Biol., 2020; 90-91:15–22.

[25] Takashima, H. et al., Radioimmunotherapy with an ^{211}At-labeled anti-tissue factor antibody protected by sodium ascorbate, Cancer Sci. (in press).

[26] Supply Platform of Short-lived Radioisotopes for Fundamental Research (in Japanese), https://www.rcnp.osaka-u.ac.jp/~ripf/, (accessed 2021-02-25).

8. Measurements of production cross sections of medical radioisotopes via charged-particle-induced reactions

Masayuki AIKAWA[1*]
[1]Faculty of Science, Hokkaido University
N10W8, Kita-ku, Sapporo 060-0810, Japan
[*]Email: aikawa@sci.hokudai.ac.jp

Production reactions of medical radioisotopes are studied for nuclear medicine. One of such radioisotopes is ^{169}Yb and its production cross sections of four charged-particle-induced reactions were experimentally determined. Physical yields were derived from the measured cross sections. The comparison of the physical yields indicates that the deuteron-induced reaction on ^{169}Tm is preferable for the ^{169}Yb production.

1. Introduction

Radioisotopes can be used for a variety of applications, e.g., radiotherapy and diagnosis in nuclear medicine. There are basically several reactions on stable nuclei to produce each radioisotope. Investigations of such reactions are necessary to find better reactions with less byproducts and with higher cost effectiveness. Production cross sections of the radioisotopes are thus important nuclear data. However, there still exist a lack of data and data with large errors [1]. It is indispensable to obtain more accurate and reliable data for the application. Recent technical development of accelerators and detectors enables us to reach such data.

We study charged-particle-induced reactions among the possible reactions for the production. The charged-particle-induced reactions have an advantage to be able to produce radioisotopes with atomic numbers different from those of targets. We expect chemical separation of the products from the targets and obtain the objective radioisotopes with high specific activity.

One of the medical radioisotopes we focused on is ^{169}Yb ($T_{1/2}$ = 32.018 d, EC = 100%). It is an Auger electron and X-ray emitter and suitable for brachytherapy [2]. To produce ^{169}Yb, there are several reactions, such as proton-, deuteron- and alpha-induced reactions on thulium and alpha-induced reaction on erbium (Fig. 1). We performed experiments to determine cross sections of the four reactions [3–5]. The production cross sections were compared with previous studies and theoretical model calculation in the TENDL library [6]. Physical yields of the products for practical use

^{167}Yb 17.5 min	^{168}Yb Stable	**^{169}Yb 32.0 d**	^{170}Yb Stable
^{166}Tm 7.70 h	^{167}Tm 9.25 d	^{168}Tm 93.1 d	^{169}Tm Stable
^{165}Er 10.4 h	^{166}Er Stable	^{167}Er Stable	^{168}Er Stable

Fig. 1. Nuclear chart around ^{169}Yb.

were also derived from the measured cross sections. The results are expected to contribute to nuclear medicine.

2. Method

The experiments were performed at RIKEN, Japan and ATOMKI, Hungary. The well-developed methods, stacked-foil activation technique and high-resolution gamma-ray spectrometry, were adopted. The targets consisted of thin metallic foils for objective and monitor reactions. The stacked targets were irradiated with beams of the charged particles. The beam intensities were measured by a Faraday cup. Gamma rays emitted from the irradiated foils without chemical separation were measured by HPGe detectors. Nuclear data required for deduction of cross sections were retrieved from online databases [7,8].

The cross sections of the monitor reactions were compared with the IAEA recommended values [9] to assess the beam parameters and target thicknesses. According to the comparison of the monitor reactions, only the beam intensities were corrected within the uncertainties. The corrected intensities and measured thicknesses were used to deduce the production cross sections of ^{169}Yb.

The production cross sections of ^{169}Yb were derived from measured net counts of the 177.21-keV gamma line (I_γ = 22.28%). The more intense gamma lines at 63.12 (I_γ = 43.62%) and 197.96 keV (I_γ = 35.93%) were unselected because of possible interference with X rays and the 198.25-keV gamma line from the ^{168}Tm decay ($T_{1/2}$ = 93.1 d).

3. Result and discussion

We measured cross sections of the four reactions, proton- [3], deuteron- [5] and alpha-induced reactions on ^{169}Tm and alpha-induced reaction on ^{nat}Er [4]. Physical yields were derived from the measured cross sections and compared with each other. The most appropriate reaction for the ^{169}Yb production among them was discussed based on the comparison.

3.1. ^{169}Tm(p,n)^{169}Yb reaction

The cross sections of the ^{169}Tm(p,n)^{169}Yb reaction were determined as shown in Fig. 2 [3]. The result is compared with the previous experimental data [10–12] and the TENDL-2019 values [6]. The peak amplitude and position are consistent with Birattari et al. [10]. The data of Spahn et al. [11] are two times larger than ours. The shape of the TENDL-2019 data is different from the experimental data.

3.2. ^{169}Tm(d,2n)^{169}Yb reaction

The excitation function of the ^{169}Tm(d,2n)^{169}Yb reaction was measured [5]. The result is shown in Fig. 3 together with the earlier measured experimental data [13,14] and the TENDL-2019 values [6]. The peak position is in good agreement with the previous experimental data and theoretical calculation although our result shows slightly higher than the other experimental data.

3.3. ^{169}Tm(α,x)^{169}Yb reaction

We performed two experiments to measure the cross sections of the ^{169}Tm(α,x)^{169}Yb reaction. The cooling times were longer than 86.9 d and 36.5 d for the first and the second experiments. During the cooling times, the co-produced parent nucleus ^{169}Lu ($T_{1/2}$ = 34.06 h) had entirely decayed to ^{169}Yb.

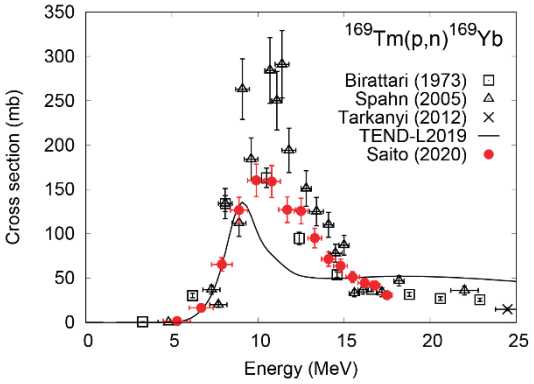

Fig. 2. Excitation function of the ^{169}Tm(p,n)^{169}Yb reaction with the previous data [13,14] and the TENDL-2019 values [6].

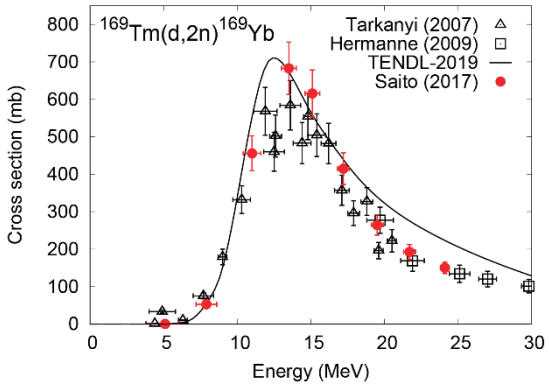

Fig. 3. Excitation function of the ^{169}Tm(d,2n)^{169}Yb reaction with the previous data [13,14] and the TENDL-2019 values [6].

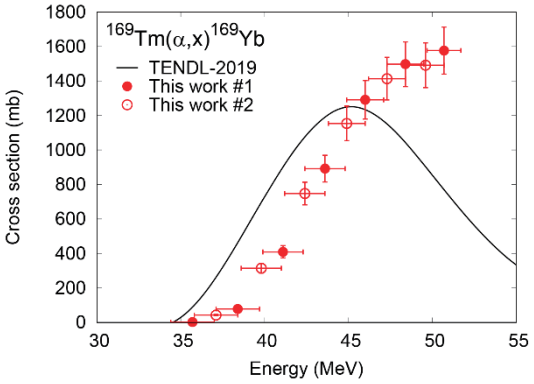

Fig. 4. Excitation function of the ^{169}Tm(α,x)^{169}Yb reaction with the TENDL-2019 values [6].

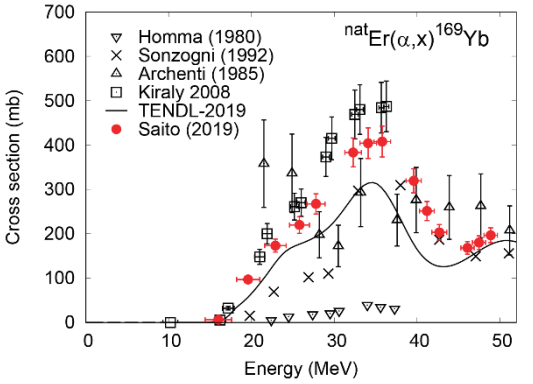

Fig. 5. Excitation function of the ^{nat}Er(α,x)^{169}Yb reaction with the previous data [15–18] and the TENDL-2019 values [6].

Therefore, the cumulative cross sections could be obtained. The results are shown in Fig. 4 with the TENDL-2019 values [6]. The TENDL-2019 values are very different from our result. There is no previous study found in a literature survey.

3.4. ^{nat}Er(α,x)^{169}Yb reaction

The cross sections of the ^{nat}Er(α,x)^{169}Yb reaction were experimentally determined [4]. The result is shown in Fig. 5 in comparison with the previous studies [15–18] and the TENDL-2019 values [6]. Both data of Király et al. [17] and TENDL-2019 have nearly the same peak position as ours at around 35 MeV while the amplitudes are different. The other experimental data differ significantly in both the shape and amplitude from our results.

3.5. Physical yield of ^{169}Yb

Physical yields of ^{169}Yb in the proton-, deuteron-, alpha-induced reactions on ^{169}Tm and alpha-induced reaction on ^{nat}Er were derived from the measured cross sections. The results are shown in Fig. 6 and found that the deuteron-induced reaction on ^{169}Tm is preferable to produce ^{169}Yb. We can obtain ^{169}Yb without any radioactive impurities using chemical separation because co-produced ^{168}Yb and ^{170}Yb are stable.

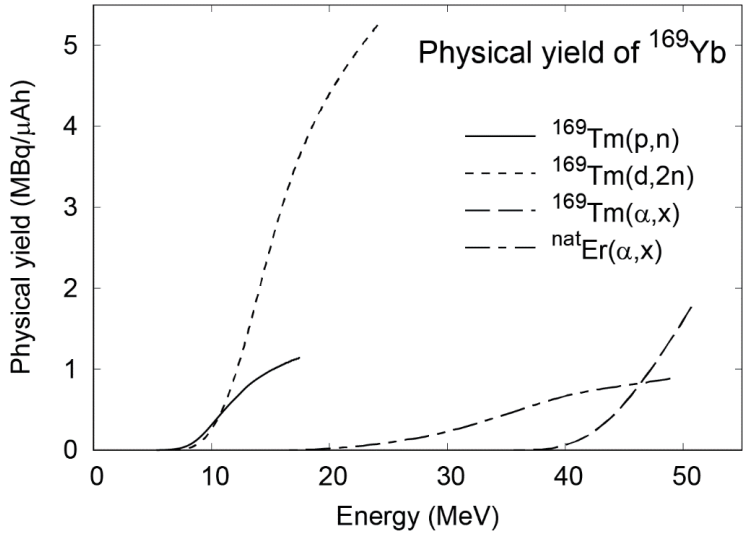

Fig. 6. Physical yields derived from the measured cross sections.

4. Conclusion

The production reactions of the medical radioisotope ^{169}Yb were investigated. The cross sections of four charged-particle-induced reactions were measured in RIKEN, Japan and ATOMKI, Hungary. Physical yields were determined from the measured cross sections and compared with each other. According to the comparison, the deuteron-induced reaction on ^{169}Tm is the most appropriate for the production.

References

1) Capote R, Nichols AL, Nortier FM, et al., IAEA coordinated research project on nuclear data for charged-particle monitor reactions and medical isotope production, EPJ Web Conf. 2017;146:08007.
2) Leonard KL, DiPetrillo TA, Munro JJ, et al., A novel ytterbium-169 brachytherapy source and delivery system for use in conjunction with minimally invasive wedge resection of early-stage lung cancer, Brachytherapy, 2011;10:163–169.
3) Saito M, Aikawa M, Murata T, et al., Production cross sections of ^{169}Yb by the proton-induced reaction on ^{169}Tm, Nucl Instruments Methods Phys Res Sect B, 2020;471:13–16.
4) Saito M, Aikawa M, Sakaguchi M, et al., Production cross sections of ytterbium and thulium radioisotopes in alpha-induced nuclear reactions on natural erbium, Appl Radiat Isot, 2019;154:108874.
5) Saito M, Aikawa M, Komori Y, et al., Production cross sections of ^{169}Yb and Tm isotopes in deuteron-induced reactions on ^{169}Tm, Appl Radiat Isot, 2017;125:23–26.
6) Koning AJ, Rochman D, Sublet J, et al., TENDL: Complete Nuclear Data Library for Innovative Nuclear Science and Technology, Nucl Data Sheets, 2019;155:1–55.
7) International Atomic Energy Agency, LiveChart of Nuclides [Internet], 2009, Available from: https://www-nds.iaea.org/livechart/ [cited 2021 Jan 10].
8) National Nuclear Data Center, Nuclear structure and decay data on-line library, Nudat 2.8

[Internet]. 2019, Available from: http://www.nndc.bnl.gov/nudat2/ [cited 2021 Jan 10].

9) Hermanne A, Ignatyuk A V., Capote R, et al., Reference Cross Sections for Charged-particle Monitor Reactions, Nucl Data Sheets, 2018;148:338–382.
10) Birattari C, Gadioli E, Gadioli Erba E, et al., PRE-EQUILIBRIUM PROCESSES IN (p,n) REACTIONS, Nucl Phys A, 1973;201:579–592.
11) Spahn I, Takács S, Shubin YN, et al., Cross-section measurement of the ^{169}Tm(p,n) reaction for the production of the therapeutic radionuclide ^{169}Yb and comparison with its reactor-based generation, Appl Radiat Isot, 2005;63:235–239.
12) Tárkányi F, Hermanne A, Takács S, et al., Activation cross-sections of proton induced nuclear reactions on thulium in the 20-45MeV energy range, Appl Radiat Isot, 2012;70:309–314.
13) Hermanne A, Tárkányi F, Takács S, et al., Excitation functions for production of medically relevant radioisotopes in deuteron irradiations of Pr and Tm targets, Nucl Instruments Methods Phys Res Sect B, 2009;267:727–736.
14) Tárkányi F, Hermanne A, Takács S, et al., Activation cross sections of the ^{169}Tm(d,2n) reaction for production of the therapeutic radionuclide ^{169}Yb, Appl Radiat Isot, 2007;65:663–668.
15) Homma Y, Sugitani Y, Matsui Y, et al., Cyclotron production of ^{167}Tm from natural erbium and natural holmium, Appl Radiat Isot, 1980;31:505–508.
16) Sonzogni AA, Romo ASMA, Ozafran MJ, et al., Alpha-induced reactions on natural erbium, J Radioanal Nucl Chem Lett, 1992;165:295–303.
17) Király B, Tárkányi F, Takács S, et al., Excitation functions of alpha-induced nuclear reactions on natural erbium, Nucl Instruments Methods Phys Res Sect B, 2008;266:549–554.
18) Archenti A, Wasilevsky C, De La Vega Vedoya M, et al., (α,xn) Reactions on Natural Erbium, Radiochim Acta, 1985;38:65–68.

Acknowledgements

This work was carried out at RI Beam Factory operated by RIKEN Nishina Center and CNS, University of Tokyo, Japan. A part of this work was supported by JSPS KAKENHI Grant Number 17K07004.

9. Development of Radioisotopes Production Method by Accelerator-based Neutron

-Activity at Kyushu University 2020 -

Tadahiro KIN[1*]
[1]Department of Advanced Energy Engineering Science, Kyushu University
1-6 Kasuga-koen Kasuga-shi., Fukuoka-ken, 816-8580, Japan

Radioisotopes (RIs) production using deuteron accelerator-based neutrons has been studying at Kyushu University. We primarily focus on neutrons generated via the C or Be(d, n) reactions in a target whose thickness is thicker than the deuteron range. These reactions are selected because (1) high intense neutrons having high kinetic energy can generate by the elastic and non-elastic breakup reaction of deuterons, and (2) neutron energy spectrum has a maximum of around a half incident deuteron energy, i.e., varying deuteron energy guides the spectrum shape adjustment. The two approaches have conducted the study: proposal of new production routes and new RIs with the accelerator-based neutron method and systematic measurements of double-differential thick-target neutron yields (DDTTNYs) up to 40 MeV. The present paper shows some examples of past works (^{92}Y production for biodistribution assessment and ^{132}Cs production for alternative environment tracer as ^{137}Cs), and current status (systematic DDTTNY measurement results) of our project.

1. Introduction

Recently, the accelerator-based neutron has been widely applied in various fields. In this decade, medical radioisotopes (RIs) production using the neutron has been proposed by Nagai et al. First in the research, the production method of ^{99}Mo, which is the mother nuclide of the most used medical RI, ^{99m}Tc, was proposed [1,2]. In the study, deuterons are accelerated to around 100 keV and bombarded on a tritium target to obtain neutrons by DT fusion reactions. Generated neutrons have nearly monoenergetic around 14 MeV, where the ^{99}Mo production reaction ^{100}Mo(n,2n) has a large cross section. The study reveals that the production method can generate a sufficient amount of ^{99}Mo of the world demand. We have also proposed the ^{64}Cu and ^{67}Cu production methods for other applications by using accelerator-based neutron via the C(d,n) reaction [3]. These copper RIs are new promising candidates of theranostics, which means combining therapy and diagnosis. In the proposed route, 40-MeV deuterons are used to generate accelerator-based neutrons to obtain intense flux. The amount of the RIs is estimated to be sufficient for clinical use (a few hundreds of MBq for diagnosis, a few GBq for therapy). The accelerator-based neutron method by deuterons was summarized as a GRAND system in Ref.[4].

We started studying the RI production method by the accelerator-based neutron in 2012 when I moved from Prof. Nagai's group at JAEA to Prof. Watanabe's laboratory at Kyushu University. At that

time, Kyushu University already gets started a nuclear data study on deuteron-induced reactions[5,6]. Thus, our research has not only been a part of the GRAND project but also combined with the nuclear data study[7–12].

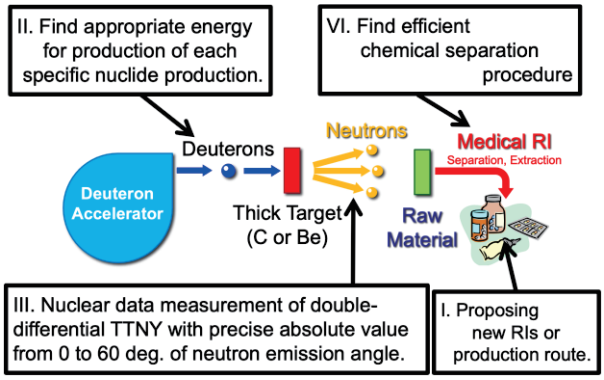

Fig. 1 Objectives of radioisotopes production by the accelerator-based neutron method.

In our study, the C or Be(d,n) reactions have been used to produce the accelerator-based neutron because the neutron energy distribution can be adjusted by incident deuteron energy. It means users can roughly control the radioactive and isotopic purity of produced RIs. Some of RIs have been investigated to find the appropriate deuteron energy to obtain sufficient quantity with high purity. Moreover, for clinical use, the chemical separation process has also been studied. In this paper, first, two RI (^{92}Y and ^{132}Cs) production routes proposed in our study are reviewed[7,12].

Second, I introduce the latest publication of systematic measurement of thick-target neutron-yield of C(d,n) [10]. Third, the preliminary result of uncertainty propagation in neutron spectra [13]. Finally, I summarize the paper and show prospects.

2. New Route to Produce ^{92}Y and ^{132}Cs

2.1. Yttrium-92 production for Assessment of Biodistribution of ^{90}Y-labeled ibritumomab tiuxetan

This section reviews a proposal of ^{92}Y to improve the precision of assessment for metabolic distribution of ^{90}Y ibritumomab tiuxetan (see Ref. [7] for detail).

Yttrium-90 ibritumomab tiuxetan is the first radio immune therapy agent approved by the US Food and Drug Administration (USFDA) and followed by more than 40 other countries, including Japan. Until November 2011, biodistribution is assessed using a single photo emission computed tomography (SPECT) scan by administering ^{111}In-ibritumomab tiuxetan before ^{90}Y-ibritumomab tiuxetan therapy was required in the United States, Japan, and Switzerland to predict radiation dose to normal tissues and organs. The FDA, however, removed this procedure based on a clinical study. The main reason was “analysis of data in 253 patients showed that the In-111 imaging was not a reliable predictor of altered Y-90 Zevalin (the trade name of ibritumomab tiuxetan) bio-distribution”. Suppose a yttrium isotope that emits gamma rays labels the ibritumomab tiuxetan that emits positron or suitable gamma rays. In that case, such a procedure will constitute a reliable monitor by the adoption of positron emission tomography (PET) or gamma-ray imaging. Two radioactive yttrium isotopes have been proposed by Rösche et al. [14] and Nagai et al. [15]. In the present study, we have proposed gamma-emitter, ^{92}Y, which can be produced only by accelerator-based neutrons, for precise assessment of biodistribution (see Fig. 2).

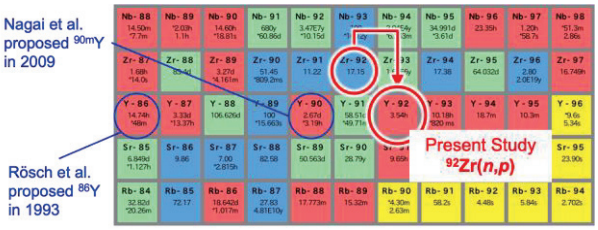

Fig. 2 Production routes of radioactive yttrium isotopes. The ^{92}Y proposed in the present study can only be produced via the fast neutron-induced method.

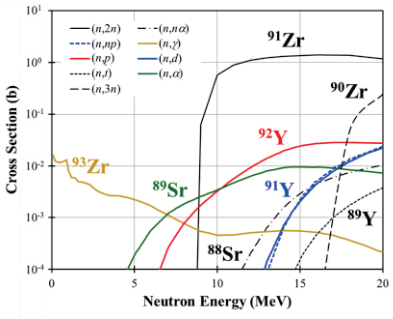

Fig. 3 Neutron excitation functions of ^{92}Zr stored in JENDL-4.0u.

The production route is ^{92}Zr(n,p) reactions, and its theoretical neutron excitation function is shown in Fig. 3 together with other ones of byproduct for ^{92}Zr (note that the functions are available in JENDL-4.0u [16]). We have conducted a thick-target neutron yield (TTNY) measurement of C(d,n) reactions for 20-MeV deuterons at Cyclotron and Radioisotope Center (CYRIC) at Tohoku University to estimate the production amount and isotopic purity of ^{92}Y product. We adopted the multiple foils activation methods to derive the TTND. As shown in Fig. 4, deuterons were accelerated up to 20 MeV by AVF930 cyclotron and guided to the thick carbon target installed in the 32 course to irradiate multiple foils made of Al, Fe, Co, Ni, Zn, Zr, Mo at the irradiation point for 19 hours. The average beam current on the carbon target was 2 μA.

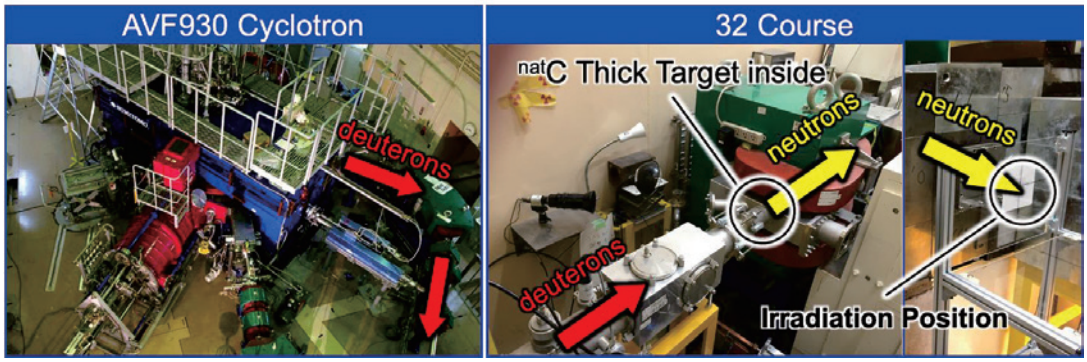

Fig. 4 AVF930 type accelerator used to measure the thick-target neutron yield of C(d,n) reactions using the multiple foils activation methods at the 32 course. Neutrons emitted around 0 degrees concerning the beam axis were collimated and bombarded on the multiple foils at the irradiation point.

The TTNY was derived from activities induced by the neutron irradiation by unfolding process using GRAVEL code [17]. For the next step, using the derived TTNY, a production simulation was conducted for 20 g of enriched ^{92}Zr target irradiation to estimate the production amount and purity. As a result, we found 1.32 GBq of high isotopic purity (94.9%) ^{92}Y can be produced by a 2-mA deuteron beam on the carbon target for 7.5-h irradiation. This amount can be used for around ten patients of biodistribution assessments.

2.2. Environment tracer Cs-132, the alternative of Cs-137

In the environment study of radioactive cesium, ^{137}Cs ($T_{1/2}$ = 30 y) has been well used to know

environmental dynamics even if some studies are focused on the short period (around from a few days to a few weeks) dynamics. The half-life is too long for the task, and management of the tracer after an experiment has been a heavy load of research works. To improve this situation, we have proposed ^{132}Cs as an alternative tracer of ^{137}Cs for studies of the short period dynamics, e.g., a few days dynamics (dominant period for absorption into the soil) of radioactive cesium released by the Fukushima Daiichi Nuclear Power Plant Accident. The radioactive material management is straightforward because it has a drastically shorter half-life (6.5 d) than ^{137}Cs. In the present study, we conducted a production experiment of the ^{132}Cs using an accelerator-based neutron method to investigate production amount and radioactive purity. The accelerator-based neutron irradiated a 12-g Cs_2CO_3 sample via the C(*d*,*n*) reactions by 1.2 μA of 30-MeV deuterons as a similar irradiation system in Fig. 4. As a result, 102 kBq/g of ^{132}Cs was obtained with higher than 98.5% radioactive purity. Following that, a feasibility study of cesium distribution measurement in andosol soil, which is a typical species of soil in Japan, was performed. The NaI(Tl) detector was placed through a lead collimator having a 1-cm window, as shown in Fig. 5 (left). First, we flow cesium aqueous into the soil and measure the initial distribution (the blue line in Fig. 5 (right)). After 8-h adsorption time, distilled water was flowed to remove free cesium. Finally, adsorbed distribution was measured as shown in the red line in Fig. 5 (right). We found almost all of the cesium is adsorbed in andosol soil in a short period, 8 hours. The property is well known, but we concluded the produced ^{132}Cs tracer could be an alternative to environment tracer ^{137}Cs.

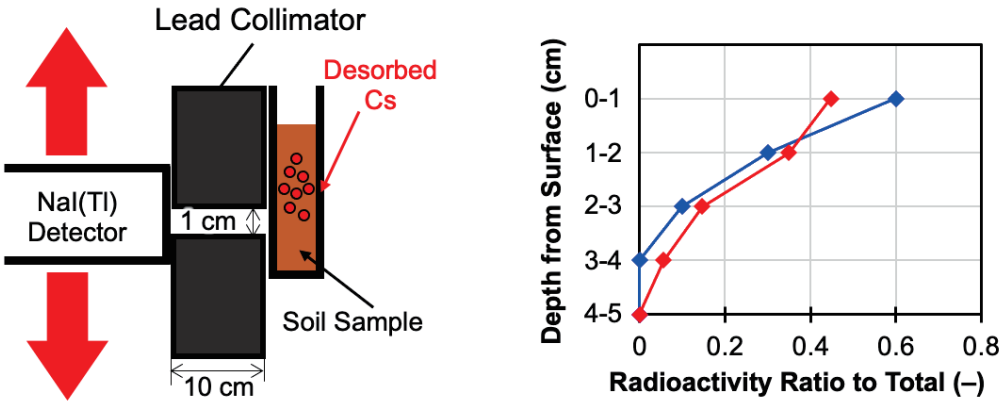

Fig. 5 Setup of measurement of radioactive cesium distribution (left) and its results. The blue line shows the initial allocation, and the red line shows the distribution after water flow with an 8-hour adsorption time.

3. Systematic Measurement of Double-differential Thick-target Neutron Yield of C(*d*,*n*) reaction

The neutron generation by the C(*d*,*n*) reaction on a thick target is promising for radioisotope production by accelerator-based neutron method. As mentioned above, an intense neutron field is possible coincidently with adjustment of neutron energy distribution by incident deuteron energy. For this application, the thick-target neutron yield of wide neutron emission angles (0-90degs) from 10 to 40-MeV incident deuterons is necessary to estimate production amount and isotopic purity. However, the

nuclear data has not been systematically measured by a single facility with the same irradiation conditions. To improve this situation, we have conducted a series of double-differential thick-target neutron yield measurements for C(*d*,*n*) reaction at 12, 20, and 30 MeV deuterons for neutron emission angles 0, 10, 20, 30, and 45 degrees at Tandem accelerator facility of JAEA. The experimental results are compared with close deuteron energy and neutron emission angles. See Ref. [10] for the results and details.

4. Summary

We have proposed new radioisotopes (RIs) or new production routes possible by accelerator-based neutron methods. Experiments of RIs production to know production amounts and find appropriate chemical separation methods. Also, double-differential thick-target neutron yields (DDTTNYs) of the proposed route have been measured to estimate isotopic purity, including stable isotope byproducts.

Furthermore, the DDTTNYs have been systematically (in neutron emission angle and incident deuteron energy) measured for storing nuclear data of deuteron-induced reactions. The experiments have been conducted at Cyclotron and Radioisotope Center at Tohoku University and Tandem accelerator at Japan Atomic Energy Agency. At this moment, we conclude the DEURACS model [18] gives precise DDTTNYs for C(*d*,*n*) reactions in the measured incident energy range from 12 to 35 MeV, especially at around 0 degrees.

The effort to find the new route or RIs will be continued in the future. Moreover, we will analyze nuclear data uncertainty contributions in the unfolding process by random sampling method using covariance for worthful nuclear data measurement.

References

[1] Nagai Y, Hatsukawa Y., Production of ^{99}Mo for nuclear medicine by ^{100}Mo(n, 2n) ^{99}Mo, J Phys Soc Japan, 2009;78:12–15.

[2] Nagai Y, Hatsukawa Y, Kin T, et al., Successful labeling of ^{99m}Tc-MDP using ^{99m}Tc separated from ^{99}Mo produced by ^{100}Mo(n,2n)^{99}Mo, J Phys Soc Japan. 2011;80:4–7.

[3] Kin T, Nagai Y, Iwamoto N, et al., New production routes for medical isotopes ^{64}Cu and ^{67}Cu using accelerator neutrons, J Phys Soc Japan. 2013;82:1–8.

[4] Nagai Y, Hashimoto K, Hatsukawa Y, et al., Generation of radioisotopes with accelerator neutrons by deuterons, J Phys Soc Japan, 2013;82:1–7.

[5] Araki S, Watanabe Y, Kitajima M, et al., Systematic measurement of double-differential neutron production cross sections for deuteron-induced reactions at an incident energy of 102 MeV, Nucl Instruments Methods Phys Res Sect A Accel Spectrometers, Detect Assoc Equip [Internet], 2017;842:62–70, Available from: https://doi.org/10.1016/j.nima.2016.10.043.

[6] Nakayama S, Kouno H, Watanabe Y, et al., Theoretical model analysis of (d,xn) reactions on ^{9}Be and ^{12}C at incident energies up to 50 MeV, Phys Rev C, 94, 014618.

[7] Kin T, Sanzen Y, Kamida M, et al., Production of ^{92}Y via the ^{92}Zr(n, p) reaction using the C(d, n) accelerator neutron source, EPJ Web Conf, 2017;146:0–3.

[8] Kin T, Kawagoe T, Araki S, et al., Production of high-purity medical radio isotope ^{64}Cu with accelerator-based neutrons generated with 9 and 12 MeV deuterons, J Nucl Sci Technol, 2017; 54: 1123–1130.

[9] Watanabe Y, Kin T, Araki S, et al., Deuteron nuclear data for the design of accelerator-based

neutron sources: Measurement, model analysis, evaluation, and application, EPJ Web Conf, 2017.

[10] Patwary MKA, Kin T, Aoki K, et al., Measurement of double-differential thick-target neutron yields of the C(d,n) reaction at 12, 20, and 30 MeV, J Nucl Sci Technol, 2021;58:252–258 Available from: https://doi.org/10.1080/00223131.2020.1819908.

[11] Patwary MKA, Kin T, Araki N, et al., Feasibility study of radioisotope ^{132}Cs production using accelerator- based neutrons, Evergreen, 2019;6.

[12] Kin T, Araki N, Patwary MKA, et al., Production method of environmental tracer ^{132}Cs by accelerator-based neutron,. EPJ Web Conf, 2020;239:20002.

[13] Aoki K, Kin T, Patwary MKA, et al., Development of MC-based uncertainty estimation technique of unfolded neutron spectrum by multiple-foil activation method, EPJ Web Conf, 2020;239:01021.

[14] Rösch F, Qaim SM, Stöcklin G, Production of the positron emitting radioisotope ^{86}Y for nuclear medical application, Appl Radiat Isot, 1993;44:677–681.

[15] Nagai Y, Iwamoto O, Iwamoto N, et al., Production of an isomeric state of ^{90}Y by fast neutrons for nuclear diagnostics, J Phys Soc Japan, 2009;78:113201.

[16] Shibata K, Iwamoto O, Nakagawa T, et al., JENDL-4.0: A new library for nuclear science and engineering, J Nucl Sci Technol, 2011;48:1–30.

[17] Matzke M, Unfolding of Pulse Height Spectra: The HEPRO Program System, Rep PTB-MN-19, 1994;

[18] Nakayama S, Kouno H, Watanabe Y, et al., Development of a code system DEURACS for theoretical analysis and prediction of deuteron-induced reactions, EPJ Web Conf, 2017;146:100–103.

10. Isotope production in spallation reaction of ^{93}Zr and ^{93}Nb induced by proton and deuteron

Keita NAKANO[†1]

[1]J-PARC Center, Japan Atomic Energy Agency, Tokai-mura, Ibaraki 319-1195, Japan
[†]Email: nakano.keita@jaea.go.jp

Nuclear transmutation technology has been attracting attention as a method for treating high-level radioactive waste. One of the candidates is the spallation reaction using high-energy particles, especially for the nuclides with relatively small neutron-capture cross sections such as long-lived fission product (LLFP) ^{93}Zr. The accumulation of nuclear reaction data and the development of nuclear reaction models based on the data are indispensable for the accurate prediction of the amount of conversion of ^{93}Zr to stable nuclides and/or short-lived nuclides and residual long-lived nuclides after the transmutation. Therefore, under the ImPACT program (Period: 2014 − 2018), we have measured isotope-production cross sections in proton- and deuteron-induced spallation reactions on LLFP ^{93}Zr and adjacent nuclide ^{93}Nb at RIKEN RIBF. In the experiment, a ^{93}Zr beam at 50 MeV/nucleon and a ^{93}Nb beam at 113 MeV/nucleon were produced by inflight-fission of ^{238}U. These beams were irradiated to secondary targets containing hydrogen and deuterium to induce spallation reactions, and the product yields were analyzed by ZeroDegree Spectrometer to determine the product cross sections. The results are compared with the nuclear reaction models.

1 Introduction

The problem of the high-level radioactive waste disposal is one of the most important issues in the nuclear energy field. In order to reduce the long-term risk of the high-level radioactive waste, research and development of transmutation technologies have been carried out. However, while the transmutation of minor actinoids has been studied by fast reactors and accelerator-driven nuclear transmutation systems [1], the transmutation of long-lived fission products (LLFPs), which also have a long-term risk, has not been widely studied. Therefore, transmutation studies of the LLFPs with half-lives longer than 100,000 years were conducted in the ImPACT program [2]. Among the LLFPs, ^{93}Zr has a very long half-life of 1.5 million years and a relatively high fission yield of approximately 6%. On the other hand, since ^{93}Zr has a relatively smaller neutron-capture cross section than other long-lived fission products [3], it was necessary to explore a new method other than transmutation using a nuclear reactor. Therefore, transmutation of ^{93}Zr by spallation reactions using high-energy protons and deuterons has been proposed. In order to evaluate the performance of this method, isotope-production cross sections for proton- and deuteron-induced reactions on ^{93}Zr, which are the most important data to estimate the amount of transmutation and the radioactivity after irradiation activity, are required.

In this study, we measured the isotope-production cross sections of 50 MeV/nucleon proton and deuteron bombardment on ^{93}Zr in order to improve nuclear reaction models which will be used for the study of the LLFP transmutation. The newly measured data are also useful to discuss the energy dependence of the isotope-production cross sections by combining with

experimental data at 105 and 209 MeV/nucleon [4, 5]. In addition, we measured the isotope-production cross sections in 113-MeV/nucleon proton- and deuteron-induced reactions on ^{93}Nb. The proton and neutron numbers in ^{93}Nb are $Z = 41$ and $N = 52$, respectively, whereas they are $Z = 40$ and $N = 53$ in ^{93}Zr. It is interesting to see how the difference of a single nucleon in the initial proton and neutron numbers influences the reproducibility of the nuclear reaction models by comparing the results with the previous ^{93}Zr data at 105 MeV/nucleon [4].

2 Experiment

Both the ^{93}Zr and ^{93}Nb experiments were performed at the RIKEN Radioactive Isotope Beam Factory (RIBF) using a cocktail beam containing secondary beams of ^{93}Zr and ^{93}Nb. Since the experimental procedures and setups for the ^{93}Zr and ^{93}Nb experiments were similar, only the details of the ^{93}Zr experiments will be described here.

In the ^{93}Zr experiment, the BigRIPS [6] and the ZeroDegree Spectrometer (ZDS) [6] were used to analyze secondary beams and reaction products, respectively. First, a ^{238}U primary beam accelerated up to 345 MeV/nucleon impinged onto a 7-mm-thick ^{9}Be primary target installed at the entrance of BigRIPS. The secondary beam containing ^{93}Zr ions was produced through inflight-fission of the ^{238}U primary beam. The secondary beam was identified using beamline detectors placed in the second-half of the BigRIPS. Then the secondary beam impinged onto a secondary target, cooled gaseous H_2 and D_2 [7], at the entrance of the ZDS. The residual nuclei produced in the nuclear reactions with the secondary targets were also identified by beamline detectors at ZDS. Seven different magnetic-field settings $\Delta(B\rho)/B\rho = -6\%$, -4%, -2%, 0%, $+2\%$, $+4\%$, and $+6\%$ were adopted to measure wide ranges of mass numbers and charge states of the reaction products. The typical current of the primary beam was approximately 400 enA.

3 Data Analysis

Same as the experimental procedure, since the main procedures of the data analysis of the ^{93}Zr and ^{93}Nb experiments are almost the same, the data analysis only for the ^{93}Zr will be presented here.

Particle identification of the secondary beam was performed based on the TOF$-B\rho-\Delta E$ method [8] using signals from the beamline detectors. Left panel of Figure 1 shows a two-dimensional identification plot of the secondary beam by the atomic number Z and the mass-to-charge ratio A/Q. As shown in the left panel of Figure 1, the secondary beam contains only isotones of ^{93}Zr. Each nuclide was clearly separated with resolutions of 0.45 (FWHM) in Z and 0.28 (FWHM) in A, which are sufficient to identify the ^{93}Zr beam. The events in the ranges $39.6 \leq Z \leq 40.4$ and $2.319 \leq A/Q \leq 2.333$ were selected as the ^{93}Zr beam. The purity, which is calculated as a ratio of the number of ^{93}Zr beam in the above-mentioned ranges to the number of total events, and the typical count rate of ^{93}Zr were 57.8% and 980 counts per second, respectively. The energy of the ^{93}Zr beam were 51 and 52 MeV/nucleon at the centers of the H_2 and D_2 targets, respectively, calculated from the magnetic rigidity of the secondary beam before the secondary target considering the energy loss in beamline materials using the LISE++ code [9]. The energy spreads in the secondary targets were calculated as $\pm$10 MeV/nucleon.

Same as the particle identification of secondary beam, that of the reaction products was performed based on the TOF$-B\rho-\Delta E$ method. Right panel of Figure 1 indicates the identification plot of the reaction products from the H_2 secondary target at the 0% ZDS $B\rho$ setting after selecting the ^{93}Zr beam.

The isotope-production cross sections were determined from the number of incident ^{93}Zr ions and the number of each isotope. A systematic uncertainty was estimated to be 4.6% including

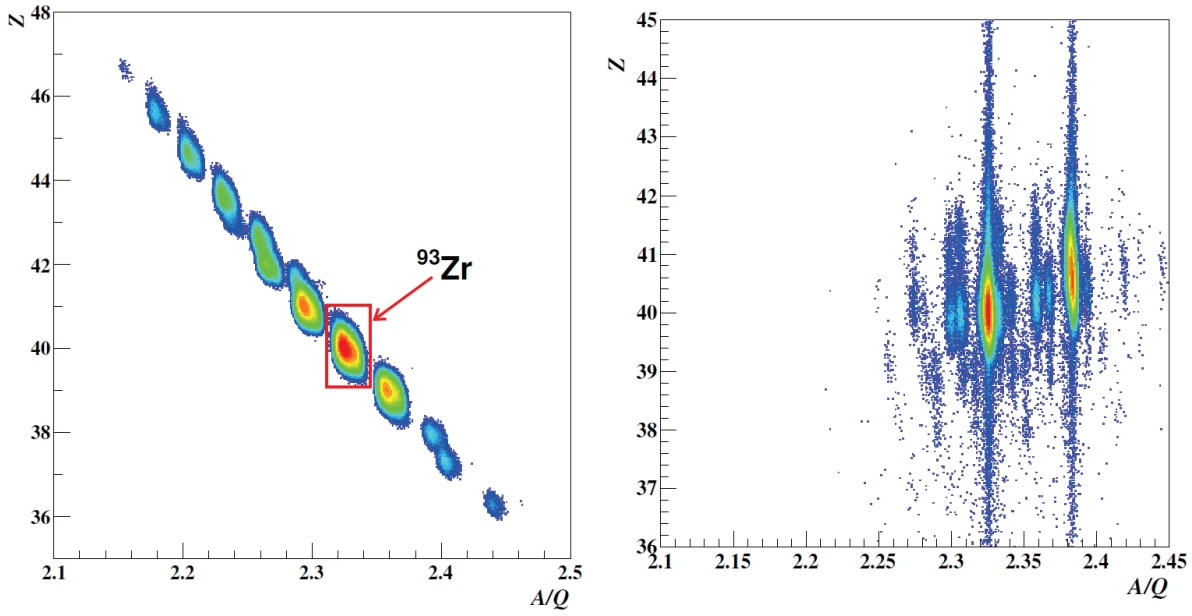

Figure 1: Left: Particle identification plot of the secondary beam by the atomic number Z and the mass-to-charge ratio A/Q in the ^{93}Zr experiment. Right: Particle identification plot of the reaction product from the H_2 secondary target after selecting the ^{93}Zr beam in the 0% $B\rho$ setting.

uncertainties of the thickness of the secondary target, multiple reactions in the secondary target, and the energy spread in the secondary target.

4 Results and Discussion on ^{93}Zr data

Figure 2 shows the measured isotope-production cross sections in the proton- and deuteron-induced reactions on ^{93}Zr at 50 MeV/nucleon together with those at 105 and 209 MeV/nucleon [4, 5]. The black circles are the measured isotope-production cross sections in the proton case, and the red triangles in deuteron case. The black solid and red dashed lines correspond to calculated cross sections by PHITS [10] in the proton- and deuteron-induced reactions, respectively. The upper, middle, and lower panels show the data at 209, 105, and approximately 50 MeV/nucleon, respectively. The error bars include only the statistical uncertainties. Jumps at the neutron magic number $N = 50$, which is pointed out in the previous works [4, 5], are seen in the Zr-isotopic chain for both the proton- and deuteron-induced reactions and in the Y-isotopic chain for the deuteron-induced reaction even in the data at 50 MeV/nucleon. In the Y-isotopic chain, ^{87}Y has a noticeble large production cross section. This corresponds to the first peak of an excitation function of the ^{93}Zr$(p, x)^{87}$Y reaction around 50 MeV/nucleon.

The PHITS calculations are in good agreement with the measured data even with the newly measured data. In particular, the trend around ^{87}Y in the 51-MeV proton-induced reaction was successfully reproduced by the PHITS calculation. However, discrepancies as seen in the previous works are still observed in the data at 50 MeV/nucleon: one-mass-shifts to the heavy side in the distribution of the Nb-isotopic chain, underestimations of the production cross sections in the neutron-deficient region of Nb- and Y-isotopic chains, overestimations of the production cross sections near the target nucleus ^{93}Zr, and an exaggerated even-odd staggering in the Sr-isotopic chain. In terms of the energy dependence of the reproducibility of the PHITS calculations, the ratio of calculation to experimental (C/E) of the ^{92}Zr and ^{92}Y production cross

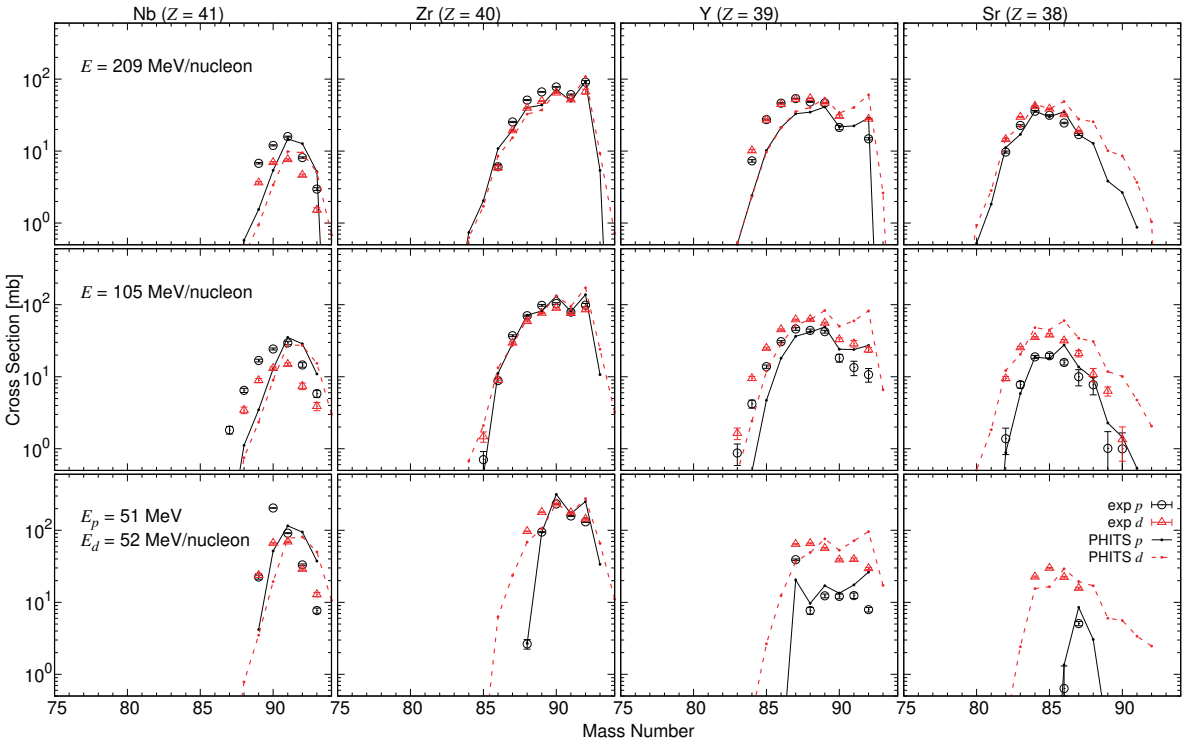

Figure 2: Isotope-production cross sections for the proton- and deuteron-induced reactions on ^{93}Zr.

sections are getting worse as the decrease of the incident energy in the proton-induced cases. In the deuteron-induced cases, on the other hand, the C/E of those have the largest value in the data at 105 MeV.

5 Results and Discussion on ^{93}Nb data

Figure 3 shows the measured isotope-production cross sections in the proton- and deuteron-induced reactions on ^{93}Nb at 113 MeV/nucleon. The black circles and red triangles correspond to the measured data in the proton- and deuteron-induced reactions, respectively. The PHITS calculations are also plotted by the black solid lines for the proton-induced case and by the red dashed lines for the deuteron-induced case. Although discontinuous jumps at the neutron magic number $N = 50$ are observed in the Zr-isotopic chains for both the proton- and deuteron-induced reactions because of the closed-shell structure, no clear jump appeared in the Nb-isotopic chain.

The PHITS calculations well reproduce the measured isotope-production cross sections as does the ^{93}Zr data. Also, the four discrepancies seen in the ^{93}Zr data are also found in the ^{93}Nb data. In particular, the underestimations of the production cross sections in the neutron-deficient region of the Nb- and Y-isotopic chains are observed for the both ^{93}Zr and ^{93}Nb data. If the atomic number of the target nuclide increases by one, it might be expected that the atomic number of the underestimated nuclide also increases by one, that is, cross sections of the Mo- and Zr-isotopic chains are expected to be underestimated in ^{93}Nb data. However, the underestimated isotopic chains remained the same for both ^{93}Nb and ^{93}Zr targets. This demonstrates that the reproducibility of the calculation is largely influenced by the final nuclides rather than the reaction.

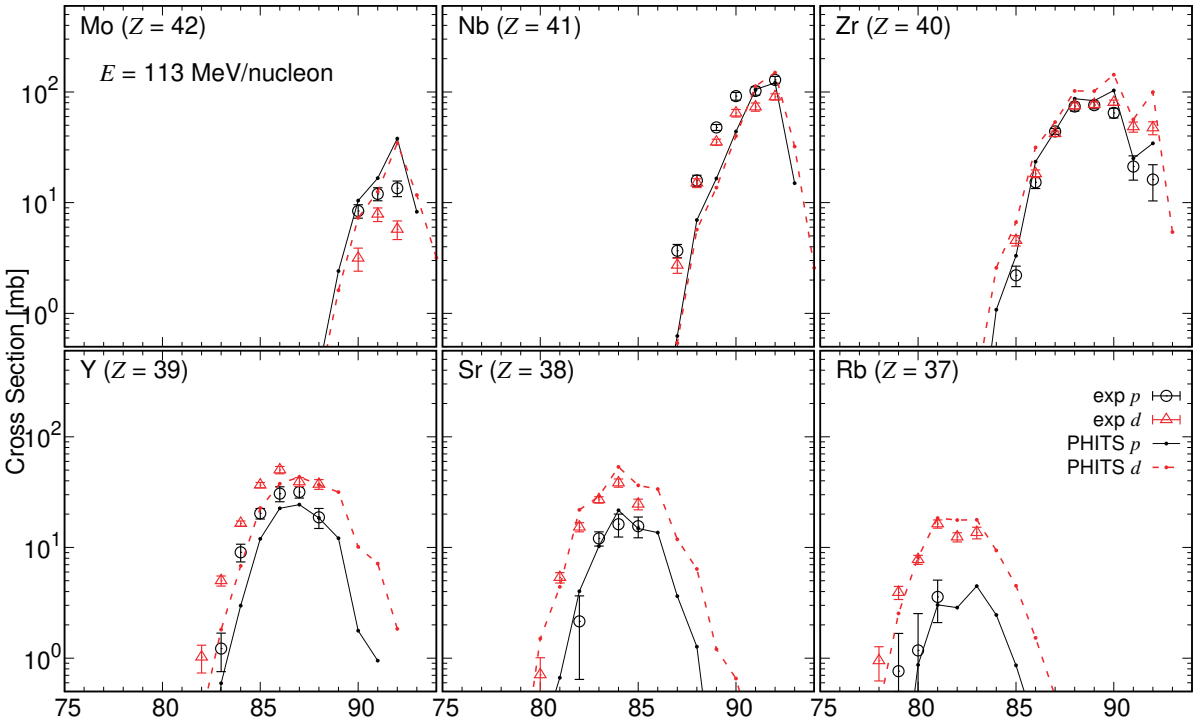

Figure 3: Isotope-production cross sections for the proton- and deuteron-induced reactions on ^{93}Nb.

6 Summary

Isotope-production cross sections for the proton- and deuteron-induced reactions on ^{93}Zr at approximately 50 MeV/nucleon and ^{93}Nb at 113 MeV/nucleon were measured at RIKEN RIBF. The measured data are useful to discuss the reaction energy and target nucleus dependences of the isotope-production cross sections. The comparison of the ^{93}Zr data at the three different reaction energies with the PHITS calculations revealed that the four discrepancies are identically seen in the isotope-production cross sections at the reaction energies ranging from 50 to 200 MeV/nucleon. In particular, the overestimations of the production cross sections near the target nucleus become more serious at the lower reaction energy. The comparison between the measred ^{93}Nb data and the PHITS calculations demonstrates that the discrepancies are observed despite the changes of the atomic and mass number by one. Also, the underestimations in the neutron deficient-region are seen in the Nb- and Y-isotopic chains for the both ^{93}Zr and ^{93}Nb data regardless of the difference of the atomic number of the target nuclei ^{93}Zr and ^{93}Nb.

References

[1] Tsujimoto K, Oigawa H, Ouchi N, et al., Research and Development Program on Accelerator Driven Subcritical System in JAEA, J Nucl Sci Technol, 2007;44(3):483-490.

[2] ImPACT Program, https://www.jst.go.jp/impact/program/08.html (accessed:2021-11-17).

[3] Shibata K, Iwamoto O, Nakagawa T, et al., JENDL-4.0: A New Library for Nuclear Science and Engineering, J Nucl Sci Technol, 2011;48(1):1-30.

[4] Kawase S, Nakano K, Watanabe Y, et al., Study of proton- and deuteron-induced spallation reactions on the long-lived fission product ^{93}Zr at 105 MeV/nucleon in inverse kinematics, Prog Theor Exp Phys, 2017;2017:093D03.

[5] Kawase S, Watanabe Y, Nakano K, et al., Measurement of isotopic production cross sections of proton- and deuteron-indued reactions on ^{93}Zr at 200 MeV/nucleon, JAEA-Conf 2018-001. 2018;2018:111.

[6] Kubo T, Kameda D, Suzuki H, et al., BigRIPS separator and ZeroDegree spectrometer at RIKEN RI Beam Factory, Prog Theor Exp Phys, 2012;2012:03C003.

[7] Ryuto H, Kunibu M, Minemura T, et al., Liquid hydrogen and helium targets for radioisotope beams at RIKEN, Nucl Instrum Meth A, 2005;555:1-5.

[8] Fukuda N, Kubo T, Ohnishi T, et al., Identification and separation of radioactive isotope beams by the BigRIPS separator at the RIKEN RI Beam Factory, Nucl Instrum Meth B, 2013;317:323-332.

[9] Tarasov OB and Bazin D, LISE++: Exotic beam production with fragment separators and their design, Nucl Instrum Meth B, 2016;376:185-187.

[10] Sato T, Features of Particle and Heavy Ion Transport code System (PHITS) version 3.02, J Nucl Sci Technol, 2018;55:684-690.

Acknowledgments

I would like to thank ImPACT-RIBF collaborators for their contributions to the experiment, advice on data analysis, and fruitful discussion. I would like to thank the accelerator staff of the RIKEN Nishina center for providing high-quality ^{238}U primary beam. This works was funded by ImPACT Program of Council for Science, Technology and Innovation (Cabinet Office, Government of Japan).

11. Development of energy-degraded RI beam and expansion of nuclear reaction studies

– Recent results obtained by the OEDO-SHARAQ system –

Shin'ichiro MICHIMASA[1*]
[1]Center for Nuclear Study, the University of Tokyo
2-1 Hirosawa, Wako, Saitama 351-0198, Japan
[*]Email: mitimasa@cns.s.u-tokyo.ac.jp

The OEDO beamline was developed to promote measurements of nuclear reactions induced by radioactive isotope beams at several tens of MeV/u and to clarify the properties of radioactive nuclei with respect to their structures and reactions. This report introduces the performance of the OEDO beamline to produce energy-degraded RI beams and recent experimental studies using the OEDO-SHARAQ system. In the last section, planned experiments at OEDO are discussed.

1. Introduction

Radioactive isotope (RI) beams are an essential tool to explore the properties of short-lived nuclei. Recent developments of the RI production are strongly promoting the progress of modern nuclear physics and especially providing various opportunities to obtain nuclear data of RI's. Such intense RI beams are mainly provided by two types of RI production schemes: isotope separator on-line (ISOL) method and in-flight method. With the ISOL method, RIs are produced from fission or spallation of a target of heavy elements induced by electron, proton, or deuteron beams; once produced, the RIs are extracted from the production target and re-accelerated ready for the nuclear reaction studies. In contrast, the in-flight method produces an RI beam by using the fragments ejected from the production target. One major difference between these methods is the beam energy provided for the measurements. Figure 1 illustrates the characteristics of RI produced by ISOL or in-flight methods on the mass-and-energy plane. While these two methods widely cover the mass-and-energy region, there exists a blank spot of medium mass nuclei and several tens of MeV/u.

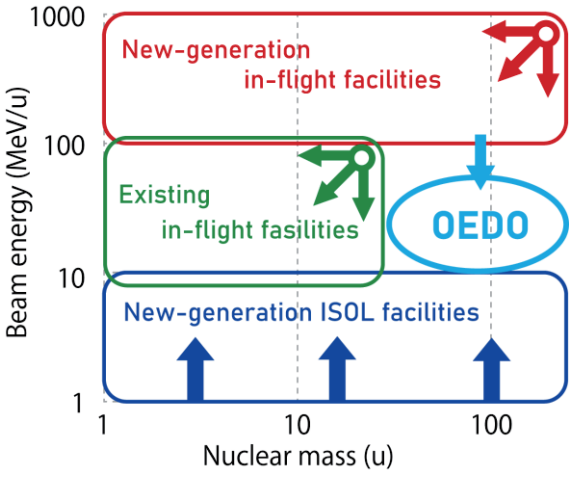

Figure 1: Characteristics of RI production methods on the mass-and-energy plane.

The OEDO beamline [1] was designed to access to this blank region. The energy range of several tens of MeV/u is attractive because nuclear transfer and/or energy-dissipation reactions at this energy range are powerful tools to make clear the structures in exotic nuclei. This article describes the outline of the OEDO device, involved experiments, and physics topics expected to be explored by OEDO.

1.1. OEDO beamline

Coupled with an in-flight RI separator the OEDO beamline enables us to produce energy-degraded RI beams. For low-energy reaction studies with short-lived nuclei, beamlines should provide good beam focusing, improved energy compression, and efficient transmission. The OEDO beamline balances these properties by exploiting a time-dependent radiofrequency (RF) ion-optical element installed into the beamline. At the secondary target OEDO achieved a focus of about 30-mm diameter, a beam energy spread of 10%, and a good transmission (~30%). This performance of OEDO is appropriate for nuclear reaction studies with exotic nuclei far from the β-decay stability line.

A schematic layout of the OEDO beamline from BigRIPS to the SHARAQ spectrometer is shown in Fig. 2. The inset photograph displays the main components of the OEDO beamline, where a RF deflector (RFD) and two superconducting triplet quadrupole (STQ) magnets were recently installed. The BigRIPS and upstream section of the OEDO beamline are used to produce and purify the RI beam of interest. The section from FE9 to FE11 in the OEDO beamline serves to degrade the energy of the RI beam. The section from FE11 to S0 serves to tag the beam for RI-induced reactions.

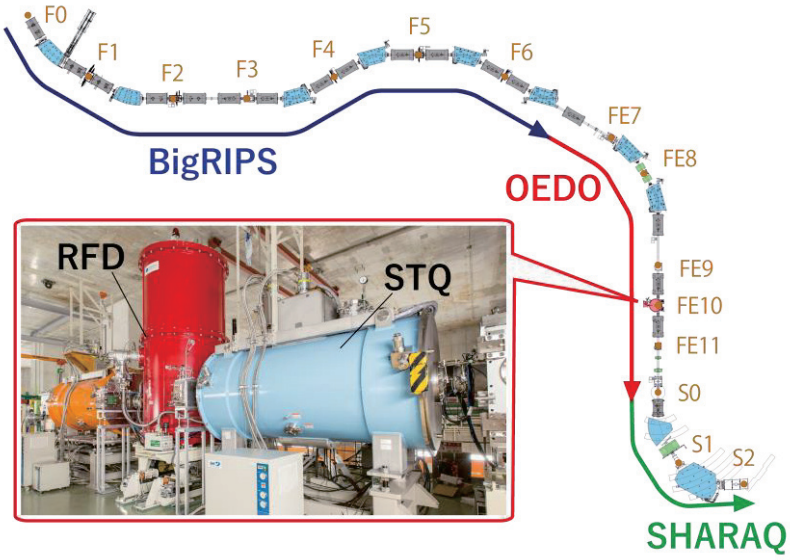

Figure 2: Schematic layout of the OEDO beamline with the BigRIPS and SHARAQ Spectrometer.

In the energy-degrading section, the beam is tuned to a moderate momentum dispersion of about 15 mm/% at the FE9 focus. At this location a recently developed angle-tunable wedge degrader [2] is installed as a monoenergetic degrader, which serves two primary functions The first is to control the beam energy by selecting a suitable degrader thickness, the second is to minimize the energy spread of outgoing RI particles by utilizing a position-energy correlation of the dispersive focus. The system consists of two aligned aluminum plates with quadratically changing thicknesses of the same magnitude, but one concave the other convex. In the overlapping region, the quadratic component of the total thickness is canceled. To achieve the monoenergetic condition, the remaining linear component is tuned by adjusting the

overlapping region. The ion optics in the FE9-FE10 and FE10-FE11 sections are designed to be point-to-parallel and parallel-to-point transport modes, respectively. The RFD, installed at FE10, uses an RF electric field to provide time-dependent focusing of the beam at FE11 or S0 depending on experimental requirements. The applied RF high voltage deflects the beam in the horizontal direction. The phase of the RFD is synchronized with the acceleration phase of the superconducting ring cyclotron (the final stage of the RIBF sequence of accelerators). A secondary target for reaction measurements can be installed at FE11 or S0. However, during previous experiments, all magnets in the FE10-S0 section were used to establish point-to-parallel ion-optics to achieve acceptance matching with the SHARAQ spectrometer. The SHARAQ spectrometer analyses reaction products at the reaction target and identifies beam-like particles outgoing from the target. The reaction channel at the target is determined by coupling particle identification of incoming and outgoing nuclei on an event-by-event basis.

The performance of OEDO beamline was demonstrated through experimental studies. Figure 3 shows a typical performance in energy compression and beam focusing of the OEDO beamline. Figure 3(a)

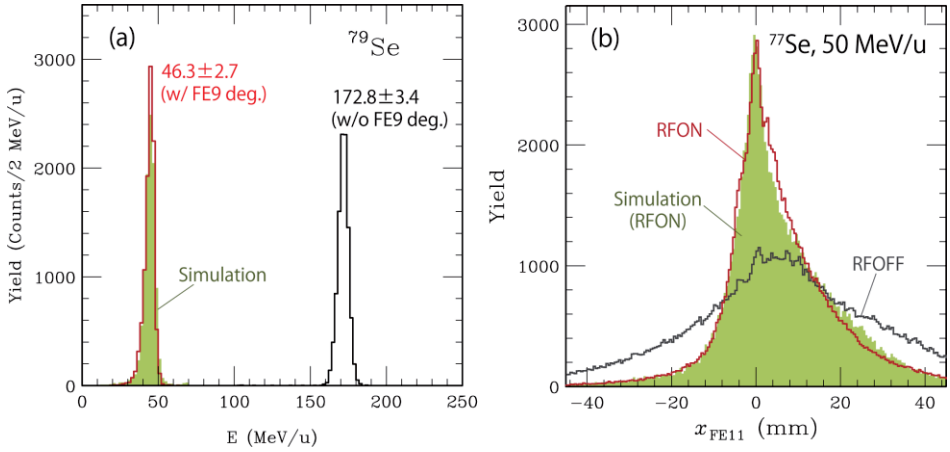

Figure 3: Demonstration of (a) energy compression and (b) beam focusing in the OEDO beamline.

demonstrates the energy compression from 173 MeV/u to 46 MeV/u by using the angle-tunable wedge degrader system at FE9. The system successfully reduces the beam energy spread from 3.4 MeV/u to 2.7 MeV/u. Figure 3(b) shows position distributions of a 50-MeV/u ^{77}Se beam at FE11 when the OEDO RFD is on (off) as a red (black) histogram. This demonstrates the excellent focusing potential of the OEDO beamline. The colored histograms shown in Fig. 3(a) and (b) are from simulations of a beam transport along the beamline. The consistency between simulated and experimental distributions shows the OEDO beamline is performing to the designed capability.

1.2. Experimental opportunities with the OEDO-SHARAQ system.

The low-energy RI beams produced by the OEDO beamline are used to induce a nuclear reaction on a secondary target located at FE11 or S0 (see Fig. 2). Beam energies of a few tens of MeV/u are suitable to populate nucleon- and/or alpha-transfer reactions. Additionally, in this energy range of the beams, the mechanism of nuclear reactions smoothly changes from a direct process to pre-equilibrium process, and thus many-quasiparticle states will be produced via inelastic channels. By using such features, OEDO provides various experimental opportunities to research nuclear structure on short-lived nuclei.

In preparation for reaction measurements, the FE11 and S0 focal planes feature open spaces of approximately 1.5 m along the beam axis. These spaces accommodate not only the location of the

secondary target but also installation of particle detector arrays to surround the secondary target. The standard experimental setup is designed for inverse-kinematics reaction measurements on an event-by-event basis. The secondary reaction target is a probe for the interested reaction. For example, solid foils, confined gases, or confined liquid target are used frequently. For RI beams produced by the OEDO beamline, a set of tracking detectors installed upstream of the secondary target measures an incident trajectory. Downstream of the reaction target the beam-like reaction products are analyzed by the SHARAQ spectrometer to determine their momentum vectors. At the final focal plane of SHARAQ, a *ΔE-E* detector array is installed by default to identify the nuclear species. In each reaction event, the data set of momentum vectors and nuclear species of both incident and outgoing particles enable us to identify the induced reaction channel and to measure the scattering angle of the reaction products. In addition to the default detector setup, one may install additional detectors to measure recoil particles around the secondary target position. As an example of a performed experiment, a particle detector array was installed to surround the target and it successfully determined excitation energies of the outgoing particles using the missing-mass spectroscopic technique [4].

2. Recent achievements by using the OEDO-SHARAQ system

This section describes two recent achievements at OEDO, the first being proton-induced reaction measurements on ^{93}Zr and ^{107}Pd at ~25 MeV/u [5,6], and the second a surrogate (*d,p*) measurement to estimate (n,γ) cross sections on ^{79}Se [4].

2.1. Proton-induced reactions on ^{107}Pd and ^{93}Zr

A series of proton-induced reaction studies at around 25 MeV/u were performed by using ^{107}Pd and ^{93}Zr beams. Through the JST-ImPACT program [7], the transmutation cross sections of these nuclei for the proton- and deuteron-induced reaction cross sections were measured at various incident energies [8-11]. The cross sections were measured at the lowest incident energy to date and contributed to the systematic data set. The detector setup was similar to that described in the section 1.1, where the reaction target was a cooled hydrogen gas target of 5-8 mg/cm^2 thickness. Figure 4 shows the energy dependence of transmutation cross sections of the proton-induced reactions on ^{107}Pd. The present experiments provided the data in between 20 and 30 MeV/u. In the figure, each color represents a different isotope of Ag or Pd. The solid lines show theoretical estimations of the production cross sections for each isotope. The predictions reproduce the data within 1 sigma. The enhancement of Ag production is noticeable in the energy region of 20 MeV/u and the Ag production amounts to 80% of the total cross section. The enhancement is considered to be caused by compound nuclear decay of ^{108}Ag* produced by a proton and ^{107}Pd. A similar trend was observed in proton-induced reactions on ^{93}Zr, the detailed reports of which will be available soon.

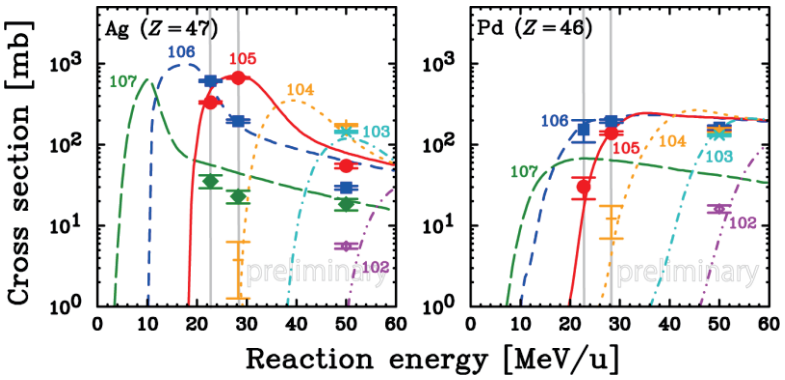

Figure 4: Systematics of transmutation cross sections for Ag and Pd isotopes.

2.2. Evaluation of the neutron-capture reaction on ^{79}Se by using the (d,p) reaction

We measured the (d,p) reactions on ^{77,79}Se to evaluate the ^{79}Se(n,γ) cross section by the surrogate ratio method [12,13]. For the reaction measurement, a deuterated-polyethylene film of 4 mg/cm^2 was selected as the reaction target. A Si-CsI(Tl) array named TiNA was installed in a geometry surrounding the target to measure recoil protons. The populated excitation energy of ^{78,80}Se was determined from the proton momenta on an event-by-event basis, and therefore the γ-emission probability distributions were determined as a function of the excitation energy. The surrogate ratio method enabled estimation of neutron-capture cross sections of ^{79}Se from the previously measured (n,γ) cross sections of ^{77}Se [14], the measured γ-emission distributions, and the formation cross sections of the ^{78,80}Se compound nuclei. The formation cross sections of ^{78,80}Se were obtained using the optical model calculations. The (n,γ) cross sections on ^{79}Se evaluated by the present γ-emission probability are shown in Fig. 5. The lines in the figure show several of the nuclear data evaluations. The ENDF/B-VII can reproduce the current results within the experimental errors. The report on this experiment is in the final stage for publication and will be available soon [15].

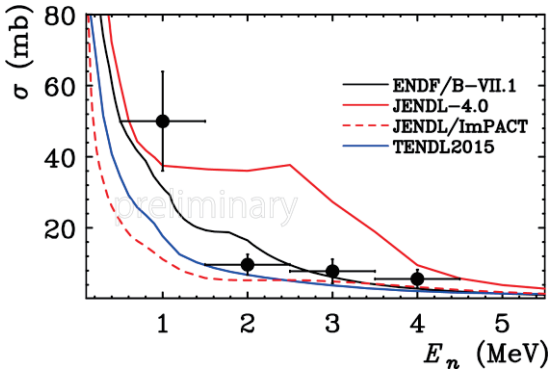

Figure 5: Evaluated (n,γ) cross sections on ^{79}Se by the surrogated ^{79}Se(d,p) reaction at 20 MeV/u.

3. Future program

The production of low-energy RI beams in the range of 10-50 MeV/u has the unique opportunity to excite bombarded nuclei into multi-quasiparticle states. This feature can possibly enable a new type of nuclear measurement to investigate reaction mechanisms and nuclear structures. We are planning new experimental studies via such pre-equilibrium and/or compound nuclear reactions. Since compound nuclear reactions can provide various nucleon configurations, this method may be useful for experimental studies on shape evolutions including shape coexistence in RI's far from the beta stability. Also, we plan to apply the surrogate ratio method used in previous experimental studies to improve quantitative evaluations of astrophysical (n,γ) reaction rates which strongly affect nucleosynthesis in astrophysical sites [16].

4. Summary

The new beamline OEDO successfully provides suitable energy-degraded RI beams around 20-50 MeV/u for inverse-kinematics reaction measurements by using a new ion-optical scheme. The beam spot size at FE11 is typically 15 mm (FWHM).

Two series of experiments were performed using the OEDO-SHARAQ system. In the measurement of the proton-induced transmutation cross sections, new nuclear data on radioactive nuclei ^{107}Pd and ^{93}Zr at 20-30 MeV/u were provided for the first time. ^{77,79}Se beams at 20 MeV/u were used for neutron-transfer reaction measurements via the (d,p) transfer reaction, and consequently the first experimental evaluation of neutron-capture cross sections on ^{79}Se was provided.

References

[1] Michimasa, S., Hwang, J.W., Yamada, K., et al.: OEDO, the energy-degrading beamline at RI Beam Facility, Prog. Theo. Exp. Phys. 2019, 043D01 (2019).

[2] Hwang, J.W., Michimasa, S., Ota, S., et al.: Angle-tunable wedge degrader for an energy-degrading RI beamline, Prog. Theo. Exp. Phys. 2019, 043D02 (2019).

[3] Michimasa, S., Imai, N., Dozono, M., et al.: New energy-degrading beamline for in-flight RI beams, OEDO, Nucl. Instrum. Methods Phys. Res. B 463, 143 (2020).

[4] Imai, N.: Nuclear reaction data of low-energy LLFP produced by OEDO, Proc. 2017 Symp. On Nuclear Data, JAEA-Conf 2018-001, 39-44 (2018).

[5] Dozono, M., Imai, N., Michimasa, S. et al.: Proton- and deuteron-induced reactions on ^{107}Pd and ^{93}Zr at 20 – 30 MeV/nucleon, RIKEN Accel. Prog. Rep. 52 (2019).

[6] Hwang, J.W., Iribe, K., Dozono, M. et al.: Proton/deuteron-induced reactions of ^{93}Zr using the slow RI beam, CNS annual report 2018, CNS-REP-98, 17 (2020).

[7] ImPACT program “Reduction and Resource Recycling of High-level Radioactive Wastes through Nuclear Transmutation”, http://www.jst.go.jp/impact/en/program/08.html (accessed:2021-11-17).

[8] Wang, H., Otsu, H., Sakurai, H., et al.: Spallation reaction study for the long-lived fission product ^{107}Pd, Prog. Theo. Exp. Phys. 2017, 021D01 (2017).

[9] Wang, H., Otsu, H., Chiga, N., et al.: Enhancement of element production by incomplete fusion reaction with weakly bound deuteron, Commun. Phys. 2, 78 (2019).

[10] Kawase, S., Nakano, K., Watanabe, Y., et al.: Study of proton- and deuteron-induced spallation reactions on the long-lived fission product ^{93}Zr at 105 MeV/nucleon in inverse kinematics, Prog. Theo., Exp., Phys., 2017, 093D03 (2017).

[11] Nakano, K., Watanabe, Y., Kawase S., et al.: Isotope-production cross sections of residual nuclei in proton- and deuteron-induced reactions on ^{93}Zr at 50 MeV/u, EPJ Web Conf., 239, 20006 (2020).

[12] Chiba, S., Iwamoto, O.: Verification of the surrogate ratio method, Phys. Rev. C 81, 044604 (2010).

[13] Escher, J.E., Dietrich, F.S: Cross sections for neutron capture from surrogate measurements: An examination of Weisskopf-Ewing and ratio approximations, Phys. Rev. C 81, 024612 (2010).

[14] Kawada, S., Igarashi, M., Katabuchi T., et al.: Measurements of keV-Neutron Capture Cross Sections and Capture Gamma-Ray Spectra of ^{77}Se, J. Nucl. Sci. Tech. 47, 643 (2010).

[15] Imai, N., Dozono, M., Michimasa, S. et al.: to be submitted.

[16] Mumpower, M.R., Surman, R., McLaughlin, G.C., et al.: The impact of individual nuclear properties on r-process nucleosynthesis, Prog. Part. and Nucl. Phys. 86, 86 (2016).

Acknowledgements

We thank the RIKEN Nishina Center and the CNS, the University of Tokyo accelerator staff for the excellent beam delivery. The work was funded by ImPACT Program of Council for Science, Technology and Innovation (Cabinet Office, Government of Japan).

12. Theoretical analysis of deuteron-induced reactions and development of deuteron nuclear database

Shinsuke NAKAYAMA
Nuclear Data Center, Japan Atomic Energy Agency
2-4 Shirakata, Tokai-mura, Naka-gun, Ibaraki 319-1195, Japan
Email: nakayama.shinsuke@jaea.go.jp

Intensive fast neutron sources using deuteron accelerators have been proposed for various applications. Toward evaluation of deuteron nuclear data, we have developed a code system dedicated for deuteron-induced reactions, named DEURACS. In this paper, we present the results of theoretical analysis for (*d,xn*) reactions with DEURACS and discuss how important it is to consider the breakup processes for accurate prediction of deuteron-induced reaction cross sections. Moreover, we have recently developed deuteron nuclear database JENDL/DEU-2020 by employing DEURACS. The validation results of JENDL/DEU-2020 are also presented.

1. Introduction

Since deuteron is a weakly bound system whose binding energy is 2.225 MeV, it easily breaks up and emits a neutron through interaction with a target nucleus. Utilizing this property, intensive fast neutron sources using deuteron accelerators have been proposed for not only science and engineering fields [1, 2] but also medical applications [3]. In the above-mentioned accelerator-based neutron sources, (*d,xn*) reactions on Li, Be, or C are employed to generate neutron beams. Thus, for design studies of such neutron sources, accurate and comprehensive nuclear data of deuteron-induced reactions especially on Li, Be, and C isotopes are indispensable.

Under these circumstances, we have developed a code system dedicated for deuteron-induced reactions toward deuteron nuclear data evaluation. The code system was named DEURACS, and it was so far successfully applied to analyses of production of nucleons [4, 5], composite particles up to $A = 4$ [6, 7], and residual nuclei [8]. From these results, it is expected that DEURACS describes the mechanism of deuteron-induced reaction well and is suitable for completing deuteron nuclear data through interpolation and extrapolation of available experimental values. Thus, we have recently developed a deuteron nuclear database up to 200 MeV for ^{6,7}Li, ^{9}Be, and $^{12, 13}$C by employing DEURACS. The new database was named JENDL/DEU-2020 [9] as one of the series of JENDL special-purpose files.

In this paper, we first present the brief overview of DEURACS and the results of analysis for the Li(*d,xn*) reactions as an example of the theoretical analysis with DEURACS. Through the analysis, we discuss how important it is to consider the breakup processes of incident deuteron. Next, the outline of JENDL/DEU-2020 is given and then the validation results of JENDL/DEU-2020 through comparison with experimental data are presented.

2. Theoretical analysis of deuteron-induced reactions

2.1. Overview of DEURACS

DEURACS consists of several calculation codes based on theoretical models to describe each

reaction process characteristic of deuteron-induced reactions. In the following, we briefly outline the theoretical models and methods in DEURACS to calculate the double differential cross section (DDX) of (*d,xn*) reaction that is a fundamental quantity in terms of neutron production. More details about the models and methods in DEURACS are described for (*d,xn*) reaction in Ref. [9] and for other reactions in Refs. [6-8].

In DEURACS, the DDXs of (*d,xn*) reactions are expressed by incoherent summation of the following components:

$$\frac{d^2\sigma_{(d,xn)}}{dEd\Omega} = \frac{d^2\sigma_{\mathrm{EB}}}{dEd\Omega} + \frac{d^2\sigma_{\mathrm{NEB}}}{dEd\Omega} + \frac{d^2\sigma_{\mathrm{PE+CN}}}{dEd\Omega}, \quad (1)$$

where $d^2\sigma_{\mathrm{EB}}/(dEd\Omega)$, $d^2\sigma_{\mathrm{NEB}}/(dEd\Omega)$, and $d^2\sigma_{\mathrm{PE+CN}}/(dEd\Omega)$ correspond to the DDXs for elastic breakup, nonelastic breakup, and pre-equilibrium and compound nucleus processes, respectively.

First, the elastic breakup component is directly calculated by the continuum-discretized coupled-channels (CDCC) method [10]. Next, the nonelastic breakup component is calculated by the Glauber model with the noneikonal approach described in Ref. [11]. In this approach, the eikonal *S* matrices used in the Glauber model are replaced by the quantum *S* matrices given by the optical model calculations. However, the Glauber model cannot properly calculate the (*d,n*) transfer reactions to the specific bound states in the residual nucleus, which is a part of nonelastic breakup. To deal with this problem, we separately calculate the transfer reaction by a conventional zero-range distorted wave Born approximation (DWBA) using the DWUCK4 code [12].

In addition to the breakup processes, the pre-equilibrium and the compound nucleus processes are calculated using the two-component exciton model and the Hauser-Feshbach model implemented in the CCONE code [13]. In deuteron-induced reactions, three types of composite nuclei can be formed by the absorption of either neutron or proton in the incident deuteron or the incident deuteron itself. In DEURACS, a calculation taking these effects into account is performed by combining the Glauber model and the models in CCONE. Moreover, DEURACS was recently modified to take into account the contribution of sequential particle decay from discrete levels in residual light nuclei [e.g., ^{9}Be(*Ex* = 2.43 MeV)] and unstable ones (e.g., ^{5}He) [9].

2.2. Theoretical analysis of (*d,xn*) reactions

To understand the relations among the reaction processes, we first perform a component-by-component analysis of DDXs of (*d,xn*) reactions. The results for the Li(*d,xn*) reactions at 40 MeV are presented in Figure 1. The DDXs of the ^{7}Li(*d,xn*) reactions calculated with DEURACS are decomposed into three components as expressed in the right-hand side of Equation (1). To make the analysis clearer, the target in the calculation is assumed to be 100% ^{7}Li. In the figure, each component and the sum of the three components are shown and compared with the experimental data [14]. Note that the experimental data are those for natural lithium (92.5% ^{7}Li and 7.5% ^{6}Li). As presented in the figure, the sums of the three components well reproduce both the shape and magnitude of the experimental data regardless of the emission angles.

The sharp peak observed around 50 MeV at 0° is attributed to the (*d,n*) transfer reaction, which is a part of nonelastic breakup. The experimental small peak seen around 40 MeV at 0° is a contribution from the ^{6}Li(*d,n*)^{7}Be transfer reaction, which is not considered in the calculation presented in Figure 1. As for the broad peaks seen around half the deuteron incident energy at forward angles, they are formed by the breakup processes, namely, elastic and nonelastic breakup. The nonelastic breakup component is

dominant at 0° but it has a stronger angle dependence than the elastic breakup component, and consequently the former is smaller than the latter at 30°. This result demonstrates that it is necessary to consider the two breakup components for the accurate prediction of the DDXs of the (*d,xn*) reaction at various angles.

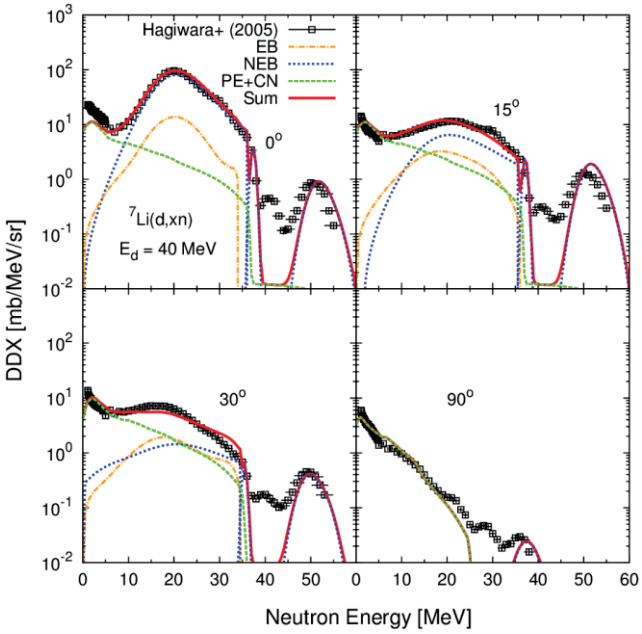

Figure 1. Calculated and experimental DDXs for the Li(*d,xn*) reactions at 40 MeV.
The number at the top of each plot denotes the emission angle.
The target in the calculation is ^{7}Li but that in the experiment is natural lithium.

On the other hand, almost all of low-energy components below 10 MeV are due to the pre-equilibrium and compound nucleus processes. Especially at 90°, the breakup components become very small and almost all spectra are explained by the contributions from the pre-equilibrium and compound nucleus processes. This indicates that the calculation method taking into account the formation of three types of composite nuclei and the particle decay from discrete levels works well.

3. Development of deuteron nuclear database

3.1. Outline of JENDL/DEU-2020

Based on the evaluation results employing DEURACS, we have developed JENDL/DEU-2020, the deuteron nuclear database for ^{6,7}Li, ^{9}Be, and ^{12,13}C at incident energies up to 200 MeV [9]. JENDL/DEU-2020 is compiled according to the ENDF-6 format. In addition to the original ENDF-6 formatted files, we have developed application libraries based on JENDL/DEU-2020 for use in the Monte Carlo transport calculation codes such as MCNP [15] and PHITS [16]. An ACE format file is available in MCNP but the present version of PHITS (version 3.20) cannot treat the ACE file for deuteron. To deal with this problem, we have developed ACE formatted files for MCNP and "Frag-Data" formatted ones for PHITS, respectively. Frag-Data is the format uniquely defined in the PHITS code. The details about the two application libraries are described in Ref. [9].

3.2. Validation results of JENDL/DEU-2020

As an example of the validation results of JENDL/DEU-2020, those for the DDXs of the (*d,xn*)

reactions on natural lithium are illustrated in Figure 2. In the figure, the calculated and experimental DDXs at 0° are compared for the incident energies up to 200 MeV. Experimental data are taken from Refs. [14, 17-19]. As for JENDL/DEU-2020, we obtained the DDXs from the MCNP calculation for a thin lithium target using the ACE file of JENDL/DEU-2020. This is because the effect of deuteron energy loss in the target is seen in the experimental data. The thickness of the target is set to be the same as that used in each experiment. For comparison, we also present the calculation results with the models implemented in the PHITS code. In the PHITS calculation, the approach combining the Intra-Nuclear Cascade of Liège (INCL) [20] and DWBA proposed by Hashimoto et al. [21] is adopted. The values stored in the deuteron sub-library of TENDL-2017 [22] are also plotted.

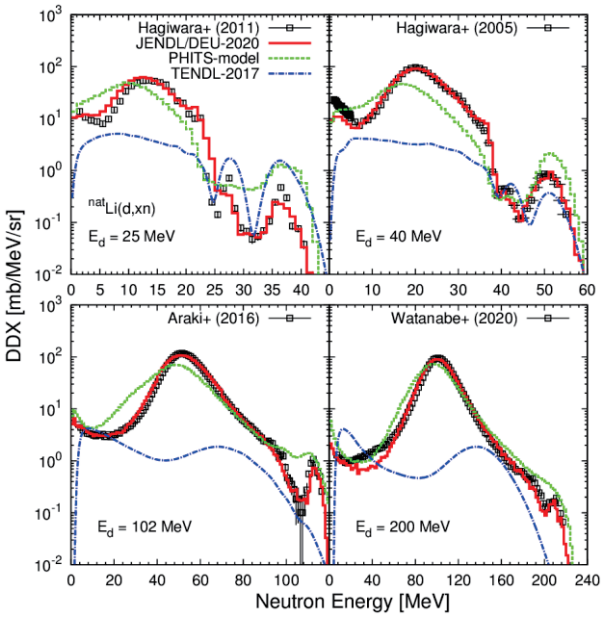

Figure 2. Calculated and experimental DDXs at 0° for the ^{nat}Li(*d,xn*) reactions. Incident energies are 25, 40, 102, and 200 MeV.

As shown in the figure, the calculation results based on JENDL/DEU-2020 reproduce experimental data better than the results with the models in PHITS and the values of TENDL-2017 in a wide range of incident energies. As for the calculation with the models in PHITS, the magnitudes and positions of the broad peaks around half the deuteron incident energies are different from the experimental ones especially in the low incident energies. On the other hand, TENDL-2017 underestimates the experimental values considerably at all incident energies. This indicates that the empirical model by Kalbach [23] adopted in TENDL to evaluate the breakup components does not work well for light target such as lithium.

To evaluate the results in Figure 2 more quantitatively, we calculate a relative deviation from experimental value by the following equation:

$$s = \frac{\sum \left| \sigma_i^{exp.} - \sigma_i^{calc.} \right| \Delta E_i}{\sum \sigma_i^{exp.} \Delta E_i}, \tag{2}$$

where $\sigma_i^{exp.}$ is experimental DDX at i-th neutron energy point, $\sigma_i^{calc.}$ is calculated DDX at the energy point corresponding to $\sigma_i^{exp.}$, and ΔE_i is energy bin of $\sigma_i^{exp.}$. Figure 3 illustrates the deviations obtained from the three calculations presented in Figure 2.

Since TENDL-2017 significantly underestimates the experimental DDXs, the deviations are almost 100% in each incident energy. As for the models in PHITS, the deviations become smaller as the incident

energy increases. This is because the picture of the INC model becomes more appropriate as the incident energy increases. The deviations obtained from JENDL/DEU-2020 are less than 15% for all incident energies. In addition to that, we have confirmed that the prediction accuracy of JENDL/DEU-2020 for beryllium and carbon targets is as good as that for lithium target [9]. From these results, it is expected that neutron production data of JENDL/DEU-2020 are reliable and it makes a large contribution to design studies of neutron sources with deuteron accelerator.

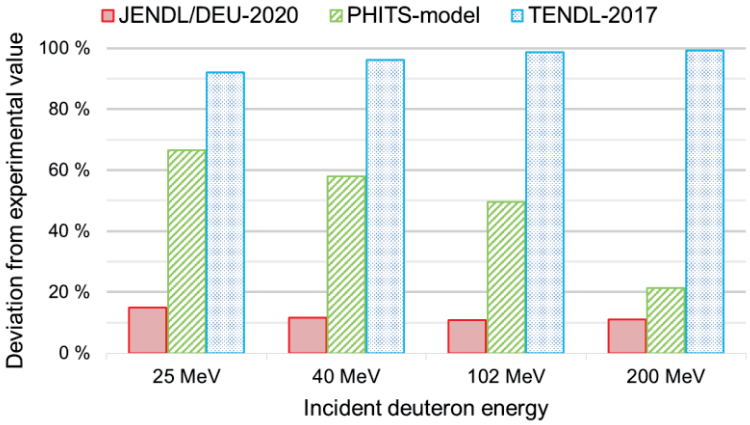

Figure 3. Relative deviations from experimental values defined by Equation (2) in terms of DDXs at 0° for the ^{nat}Li(*d,xn*) reactions.

4. Summary

We have presented the results of theoretical analysis for the Li(*d,xn*) reactions with DEURACS, which is the code system dedicated for deuteron-induced reaction we have developed. From the analysis, it has been shown that consideration of the breakup processes is essentially important for accurate prediction of deuteron-induced reaction cross sections. Based on the evaluation results employing DEURACS, we have developed JENDL/DEU-2020, the deuteron nuclear database for ^{6,7}Li, ^{9}Be, and ^{12,13}C at incident energies up to 200 MeV. From the comparison with experimental data, it has been demonstrated that the calculation results based on JENDL/DEU-2020 reproduces the measured neutron production data well at incident energies from a few tens of MeV to 200 MeV. JENDL/DEU-2020 is expected to make a large contribution to diverse design studies of deuteron accelerator neutron sources.

References

1) Ledoux X, Aiche M, Avrigeanu M, et al., The neutrons for science facility at SPIRAL-2, Nucl Data Sheets, 2014;119:353-356.
2) Moeslang A, Heinzel V, Matsui H, et al., The IFMIF test facilities design, Fusion Eng Des, 2006;81:863-871.
3) Nagai Y, Hashimoto K, Hatsukawa Y, et al., Generation of radioisotopes with accelerator neutrons by deuterons, J Phys Soc Jpn, 2013;82:064201.
4) Nakayama S, Watanabe Y, Systematic investigation of spectroscopic factors from (*d,p*) reactions for deuteron nuclear data evaluation, J Nucl Sci Technol, 2016;53:89-101.
5) Nakayama S, Kouno H, Watanabe Y, et al., Theoretical model analysis of (*d,xn*) reactions on ^{9}Be and ^{12}C at incident energies up to 50 MeV, Phys Rev C, 2016;94:014618.
6) Nakayama S, Kouno H, Watanabe Y, et al., Development of a code system DEURACS for

theoretical analysis and prediction of deuteron-induced reactions, EPJ Web Conf, 2017;146:12025.
7) Nakayama S, Iwamoto O, Watanabe Y, Consistent description of light composite particle emission in deuteron-induced reactions, Phys Rev C, 2019;100:044603.
8) Nakayama S, Furutachi N, Iwamoto O, et al., Role of breakup processes in deuteron-induced spallation reactions at 100–200 MeV/nucleon, Phys Rev C, 2018;98:044606.
9) Nakayama S, Iwamoto. O, Watanabe Y, et al., JENDL/DEU-2020: deuteron nuclear data library for design studies of accelerator-based neutron sources, J Nucl Sci Technol, 2021;DOI: 10.1080/00223131.2020.1870010.
10) Yahiro M, Ogata K, Matsumoto T, et al., The continuum discretized coupled-channels method and its applications, Prog Theor Exp Phys, 2012;2012:01A206.
11) Ye T, Hashimoto S, Watanabe Y, et al., Analysis of inclusive (*d*,*xp*) reactions on nuclei from ^{9}Be to ^{238}U at 100 MeV, Phys Rev C, 2011;84:054606.
12) Kunz P, Rost E, The distorted-wave Born approximation. In: Computational nuclear physics 2, Springer; 1993. p. 88-107.
13) Iwamoto O, Iwamoto N, Kunieda S, et al., The CCONE code system and its application to nuclear data evaluation for fission and other reactions, Nucl Data Sheets, 2016;131:259-288.
14) Hagiwara M, Itoga T, Kawata N, et al., Measurement of neutron emission spectra in Li(*d*,*xn*) reaction with thick and thin targets for 40-MeV deuterons, Fusion Sci Technol, 2005;48:1320-1328.
15) Goorley T, James M, Booth T, et al., Initial MCNP6 release overview, Nucl Technol, 2012;180:298-315.
16) Sato T, Iwamoto Y, Hashimoto S, et al., Features of particle and heavy ion transport code system (PHITS) version 3.02, J Nucl Sci Technol, 2018;55:684-690.
17) Hagiwara M, Itoga T, Oishi T, et al., Experimental studies of neutron emission spectra in Li(d,xn) reactions for IFMIF, J Nucl Mater, 2011;417:1284-1287.
18) Araki S, Watanabe Y, Kitajima M, et al., Systematic measurement of double-differential neutron production cross sections for deuteron-induced reactions at an incident energy of 102 MeV, Nucl Instrum Methods A, 2017;842:62-70.
19) Watanabe Y, Sadamatsu H, Araki S, et al., Study of the Li(*d*,*xn*) reaction for the development of accelerator-based neutron sources, EPJ Web Conf, 2020;239:20012.
20) Boudard A, Cugnon J, David JC, et al., New potentialities of the Liège intranuclear cascade model for reactions induced by nucleons and light charged particles, Phys Rev C, 2013;87:014606.
21) Hashimoto S, Iwamoto Y, Sato T, et al., New approach to description of (*d*,*xn*) spectra at energies below 50 MeV in Monte Carlo simulation by intra-nuclear cascade code with distorted wave Born approximation, Nucl Instrum Methods B, 2014;333:27-41.
22) Koning A, Rochman D, Sublet JC, et al., TENDL: complete nuclear data library for innovative nuclear science and technology, Nucl Data Sheets, 2019;155:1-55.
23) Kalbach C, Preequilibrium reactions with complex particle channels, Phys Rev C, 2005;71:034606.

Acknowledgements

The author is grateful to O. Iwamoto, Y. Watanabe, and K. Ogata for fruitful discussions. This work was partially funded by JSPS KAKENHI Grant Number 19K15483.

13. Roles and Current Status on Reactor Physics Experiment in Research Reactors

Cheol Ho PYEON
Institute for Integrated Radiation and Nuclear Science, Kyoto University
Asashiro-nishi, Kumatori-cho, Sennan-gun, Osaka 590-0494, Japan
Email: pyeon.cheolho.4z@kyoto-u.ac.jp

Nuclear reactors are mainly categorized as a commercial power reactor and a test and research reactor for generating electric power and conducting research of radiation utilization, respectively. Main roles of the test and research reactor are to conduct the research and development of nuclear engineering and radiation detection fields with the use of radiation, including neutron and γ-ray, and to contribute to the education of young generation. Another part of this paper is to contain the feasibility study on the accelerator-driven system (ADS) conducted for nuclear transmutation analyses with the combined use of the solid-moderated and solid-reflected core and the fixed-field alternating gradient accelerator, at the Kyoto University Critical Assembly (KUCA). Through the experimental analyses, static and kinetic parameters of reactor physics are interestingly revealed for nuclear transmutation of minor actinides (^{237}Np and ^{241}Am) and uncertainty quantification of a coolant material (lead and bismuth), with respect to ADS. Additionally, experimental education programs for domestic and overseas students conducted at KUCA are introduced in the paper.

1. Introduction

Nuclear reactors are mainly categorized as two parts: a commercial power reactor; a test and research reactor for generating electric power and conducting research of radiation utilization, respectively. Of two reactors, main roles of the test and research reactor are to conduct the research and development of nuclear engineering and radiation detection fields with the use of radiation, including neutron and γ-ray, and to contribute to the education of young generation. Many research reactors are importantly equipped with experimental facilities to research objectives, including irradiation holes, neutron beams and spectrum shift changers, although the commercial reactors insufficiently meet the items. An index of classification of research reactors is to provide a wide range of neutron spectrum and thermal reactor power, with the combined use of nuclear fuel, moderators, reflectors and coolant materials by varying the kinds, the geometries, the configurations and the utilization purposes.

The experimental studies on the accelerator-driven system (ADS) were conducted for nuclear transmutation analyses with the combined use of the Kyoto University Critical Assembly [1]-[3] (KUCA; A-core: solid-moderated and -reflected core) and the fixed-field alternating gradient (FFAG) [4] accelerator. The ADS experiments with 100 MeV protons obtained from the FFAG accelerator had been carried out to investigate the neutronic characteristics of ADS, and the static and kinetic parameters were accurately analyzed

through both the measurements and the Monte Carlo simulations of reactor physics parameters, including the reaction rates, the neutron spectrum, the neutron multiplication, the neutron decay constants and the subcriticality. The neutronic characteristics of Pb-Bi are considered importantly and analyzed experimentally from the viewpoint of reactor physics: neutron yield and neutron spectrum by the Pb-Bi target; uncertainties of Pb-Bi cross sections in the core. Furthermore, irradiation experiments of the minor actinides (^{237}Np and ^{241}Am) was conducted in hard spectrum core at KUCA to examine the feasibility of reaction rate analyses (^{237}Np and ^{241}Am fission and capture reactions) of nuclear transmutation. Finally, in this paper, the joint laboratory course for students in the KUCA C-core was mentioned with a short history of the course and textbooks by multi languages (Japanese, English and Korean).

2. Roles of Test and Research Reactors

Test and research reactors are designed for generating neutrons with a wide variety of energy, including new type power reactors and critical assemblies in research and development phase. Basically, utilization targets are focused on the research of nuclear science and engineering, the development of industrial application and training and education for young generation of students and engineers. Main role of test and research reactors is to conduct the research and development of basic, industrial and educational utilizations by neutrons with a wide variety of energy, and main objectives of these are categorized by several reactor components, including the neutron energy, reactor power, nuclear fuel, moderator, reflector and coolant material. Domestic test and research reactors are listed as shown in Table 1.

Table 1 List of domestic test and research reactors

Reactor	Power	Fuel	Moderator	Coolant	Objective
JRR-3 (JAEA)	20 MW	U_3Si_2-Al	H_2O	H_2O	Beam utilization
NSRR (JAEA)	300 kW	U-ZrH	H_2O	H_2O	Accident research
Joyo (JAEA)	140 MW	U-Pu	-	Liquid Na	Fast reactor
JMTR (JAEA)	50 MW	U_3Si_2-Al	H_2O	H_2O	Material test
HTTR (JAEA)	30 MW	UO_2	Graphite	He gas	R&D of High-temp. reactor
KUR (Kyoto U.)	5 MW	U_3Si_2-Al	H_2O	H_2O	Multi purposes
UTR-KINKI (Kindai)	1 W	U-Al	H_2O	-	Training and education
KUCA (Kyoto U.)	100 W	U-Al	H_2O (Poly.)	-	Basic research of reactor physics

3. Kyoto University Critical Assembly

A critical assembly is a nuclear facility for conducting mock-up and benchmark experiments in the field of nuclear reactor physics field, such as KUCA shown in Figure 1. It is also one of the most effective facilities for the education related to nuclear engineering and technology, especially that students and engineers grasp the basic concepts of nuclear reactors by conducting experiments on and operating the reactor in person. Current computation technology of reactor simulator systems for reactor operation has made rapid progress, and most reactor operators at nuclear power stations have been trained through simulators, all of which contribute to safe operation of reactors. It follows, therefore, that for the education of students majoring in nuclear engineering,

conducting experiments on actual reactors is a prerequisite to understanding the reactor itself. Furthermore, experiments on a critical assembly provide students and engineers valuable opportunities to appreciate safety regulations related to reactor facilities and the handling of nuclear materials.

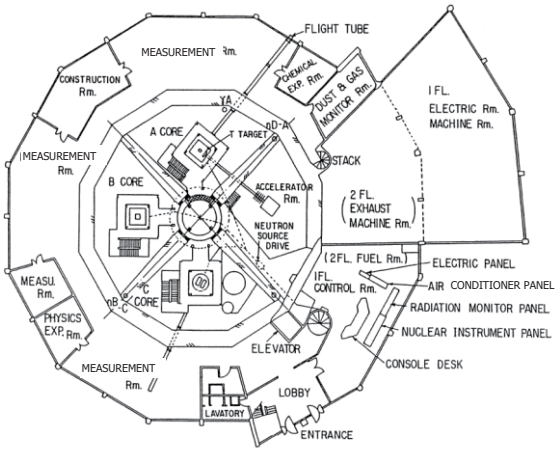

Figure 1 Horizontal cross section of the KUCA (Ref. [1])

3.1. Accelerator-Driven System

At KUCA, A and B are polyethylene-moderated and -reflected cores, and C is a light water-moderated and -reflected one. The three cores are operated at a low mW power in the normal operating state, whereas the maximum power is 100 W. The accelerator-driven system (ADS) experiments were carried out in the A-core (Figure 2) composed of the HEU fuel and polyethylene reflector rods, with the combined use of the FFAG accelerator (high-energy proton accelerator; Figure 3) that has the main characteristics: 100 MeV energy, 0.1 nA intensity (at most), 20 Hz repetition rate, 100 ns pulsed width and 1.0×10^7 1/s neutron yield.

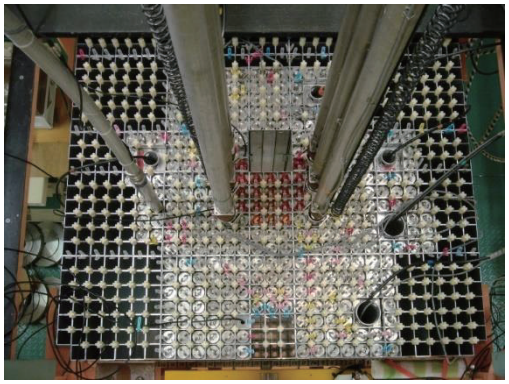

Figure 2 KUCA A-core (Ref. [1])

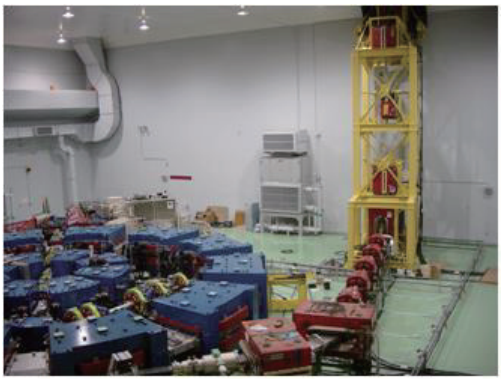

Figure 3 FFAG accelerator (Ref. [4])

To investigate the neutron characteristics of external neutron sources, ADS experiments with 100 MeV protons was carried out by varying a heavy metal target at the location of target. As unique attempt, the combination of materials tungsten (W) and beryllium (Be) was selected as plural targets for the aim for accomplishment of the neutron spectrum in high-energy region and the neutron yield of high-energy neutrons in the core. The combined use of the heavy- (W, Pb and Bi) and the light-nuclide (Be and lithium) was considered useful for accomplishment of the research objectives relating the neutron spectrum and the neutron

yield. Here, the plural targets with the combined use of heavy- and light-nuclide were called “two-layer target” in this study. From the numerical results (Figure 4) by MCNP calculations, the neutron spectrum was observed high in high-energy region with the combined use of W and Be. In the design of two-layer target, the proton beams could be actually penetrated into Be target, and inversely stopped inside W target, and the dimensions of two-layer target were determined to be in W (50 mm diameter and 9 mm thick) and Be (50 mm diameter and 6 mm thick). Also, the effects of specific target (two-layer target) were confirmed through the measured results of ^{115}In(n, γ)^{116m}In reaction rate distributions in the core, as shown in Figure 5.

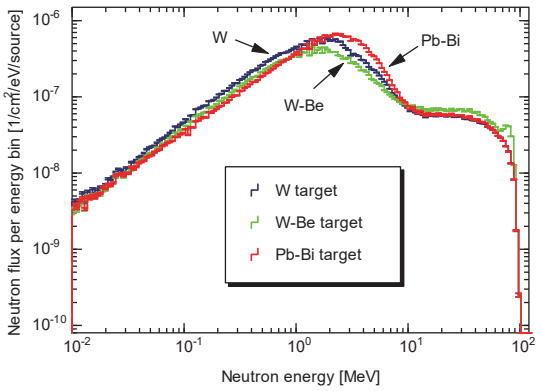

Figure 4 Neutron spectra of external neutron sources by varying heavy metal target in ADS experiments (Ref. [5])

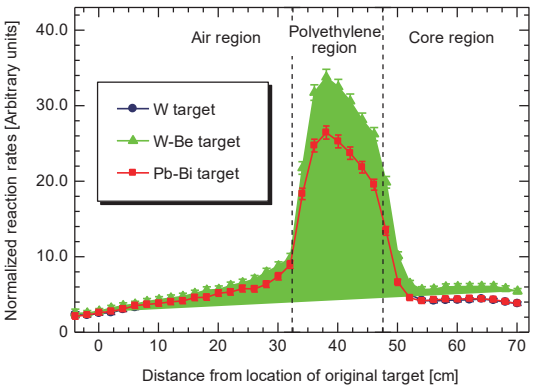

Figure 5 Comparison between measured reaction rate distributions in ADS experiments (Ref. [5])

Furthermore, nuclear transmutation of ^{237}Np and ^{241}Am by ADS soundly implemented by combining the subcritical core and the 100 MeV proton accelerator, and the use of a Pb-Bi target, was demonstrated through the experimental results of fission and capture reaction events, as shown in Figures 6 and 7, when irradiation experiments were conducted in hard spectrum core at KUCA.

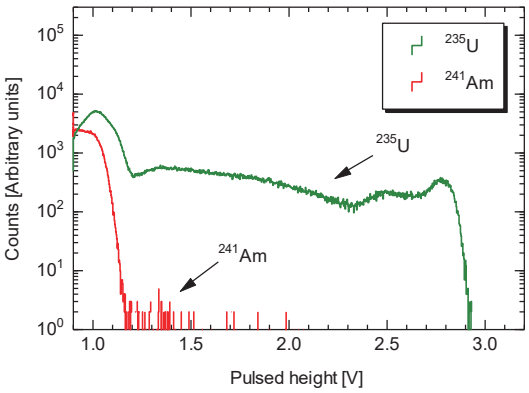

Figure 6 Measured pulsed-height signals of ^{241}Am and ^{235}U fission reaction events by the ADS irradiation (Ref. [6])

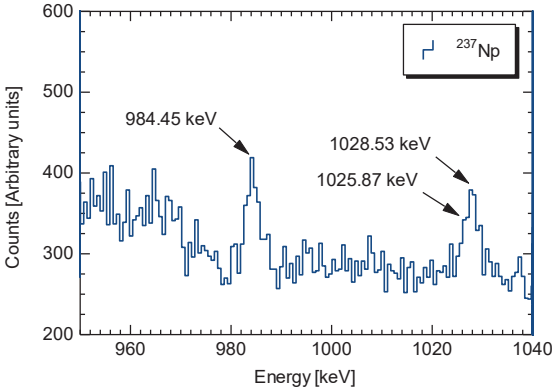

Figure 7 Measured γ-ray spectrum of ^{237}Np capture reaction events by the ADS irradiation (Ref. [6])

3.2 Training and Education Programs

The joint reactor-laboratory course [1]-[3] for Japanese and overseas students at KUCA was launched in 1975 and various experiments on reactor physics have been conducted since: approach to criticality, control rod calibration, measurement of neutron flux and power calibration, subcriticality measurements by the Feynman-α and the pulsed neutron methods, and instruction in reactor operation. These experiments were conducted in the KUCA C-core, which is a water-moderated- and -reflected-core with a plate-type fuel consisted of U-Al alloy. Until fiscal year 2019, over three thousand and six hundred undergraduate and graduate students all over Japan attended this course. The same course for Korean undergraduate students in the Kyoto University Critical Assembly (KUGSiKUCA) program was launched from 2003 to 2009 and founded by the Korean government. In addition to the Swedish students ranging between 2007 and 2009, the Reactor Physics Asia Experiment Program (RPHA-XP) was launched newly in 2012 for graduate students in Korea and China. From 2003 to 2019, a total of three hundred foreign students in overseas, including Korea, Sweden and China, took part in this program.

For the foreign students, in April 2010, Kyoto University Press published a textbook in English [2], which was transcribed from the Japanese course work [1] comprising lectures, experiments, discussions and reports that had been prepared from English textbooks on nuclear reactor physics, as shown in Figure 8. Preceding that publication, a textbook translated into Korean [3] was published in Korea on March 2010.

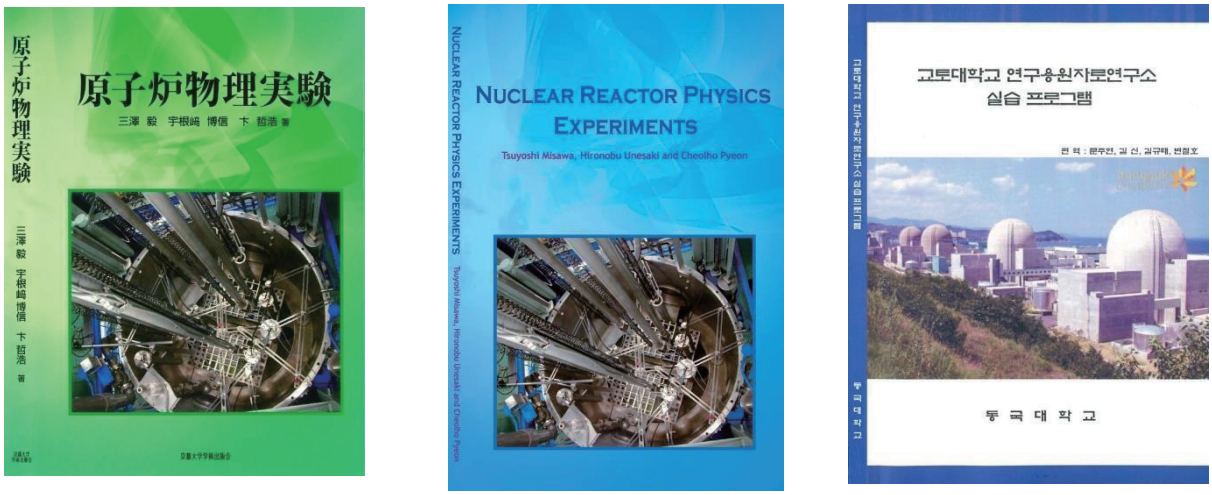

Figure 8　Textbooks by multi languages (Japanese, English and Korean) of the joint reactor-laboratory course conducted at KUCA

4. Summary

Main role and objectives of test and research reactors were described in this paper, indicating the kind, reactor power and core components in domestic. Also, another part with respect to the critical assembly as one of test and research reactors was contained, such as the ADS experiments with 100 MeV protons carried out with the combined use of the KUCA A-core and the FFAG accelerator. In the ADS experiments, the effects of two-layer target composed of W and Be were found apparently well on the neutron multiplication. Furthermore, nuclear transmutation of ^{237}Np and ^{241}Am by ADS soundly implemented by combining the subcritical core and the 100 MeV proton accelerator, and the use of a Pb-Bi target, was demonstrated through the experimental results of fission and capture reaction events. Finally, as important utilization of the KUCA facility, the joint reactor-laboratory course for Japanese and overseas students at KUCA launched in 1975 was introduced, containing interestingly the experimental textbooks with the multi languages.

References

[1] Misawa T, Unesaki H and Pyeon CH, Nuclear Reactor Physics Experiments, Kyoto University Press, Kyoto, Japan 2010.

[2] Misawa T, Unesaki H and Pyeon CH, Nuclear Reactor Physics Experiments, Kyoto University Press, Kyoto, Japan 2010. [in Japanese]

[3] Moon JH, Kim S, Kim GT and Pyeon CH, Nuclear Reactor Physics Experiments, Dongguk University Press, Gyeongju, Korea 2010. [in Korean]

[4] Lagrange JB, Planche T, Yamakawa E, et al., Straight scaling FFAG beam line. Nucl. Instrum, Methods A. 2013; 691: 55-63.

[5] Pyeon CH, Nakano H, Yamanaka M, et al., Neutron characteristics of solid targets in accelerator-driven system with 100 MeV protons at Kyoto University Critical Assembly, Nucl. Technol. 2015; 192: 181-190.

[6] Pyeon CH, Yamanaka M, Oizumi A, et al., First nuclear transmutation of ^{237}Np and ^{241}Am by accelerator-driven system at Kyoto University Critical Assembly, J. Nucl. Sci. Technol, 2019; 56: 684-689.

14. Data-driven approaches in nuclear shell-model calculations

Noritaka SHIMIZU[†1], Sota YOSHIDA[2], and Takahiro MIZUSAKI[3]

[1]Center for Nuclear Study, the University of Tokyo, Hongo, Bunkyo-ku, Tokyo 113-0033, Japan
[2]Institute for Promotion of Higher Academic Education, Utsunomiya University, Tochigi, Japan
[3]Institute of Natural Sciences, Senshu University, 3-8-1 Kanda-Jinbocho, Chiyoda-ku, Tokyo 101-8425, Japan
[†]Email: shimizu@cns.s.u-tokyo.ac.jp

We briefly review some applications of machine learning and its related techniques to nuclear shell-model calculations. As an example, we quantified uncertainty caused by the parameters of the shell-model Hamiltonian utilizing Bayesian statistics. It enables us to quantify the uncertainty of the theoretical predictions and their agreement with experimental data in a statistical manner. Moreover, we point out that a large deviation of the confidence interval for the energy in shell-model calculations from the corresponding experimental data can be used as an indicator of some exotic property, *e.g.*, alpha clustering. Besides, we briefly introduce a recent effort to use the restricted Boltzmann machine to describe nuclear shell-model wave functions.

1 Introduction

As computational power has been increasing recently, machine learning and its peripheral techniques are intensively developed in the prevalence of artificial-intelligence (AI) techniques. The applications of these techniques are expected to accelerate the progress of natural science, including nuclear structure physics. Among the theoretical models in nuclear structure physics, nuclear shell model calculation is one of the most powerful tools to investigate the ground and low-lying excited states of nuclei, since it can describe any many-body correlations inside the valence shell on equal footing by configuration mixing. In this paper, we briefly review two applications of these techniques to the shell-model calculations as follows. The uncertainty quantification utilizing the Bayesian statistics in shell-model calculations [1] is discussed in Sect. 2. The introduction of the restricted Boltzmann machine (RBM) to the Variational Monte Carlo (VMC) formulation in shell-model calculations is discussed in Sect. 3. This paper is summarized and some other applications are mentioned in Sect. 4.

2 Uncertainty quantification by Bayesian analysis

2.1 Bayesian analysis

We here show the uncertainty quantification of the shell-model study of p-shell nuclei by applying the Bayesian analysis. In this study, we take the $0p_{3/2}$ and $0p_{1/2}$ single-particle orbits with ^{4}He

being an inert core. While the traditional shell-model Hamiltonian by S. Cohen and D. Kurath [2] is well-known for this model space, we construct the ensemble of the parameters of the Hamiltonian to estimate the uncertainty.

We consider the probability distribution of the interaction parameters which reproduce the experimental data with reasonable uncertainty. In the Bayesian analysis, it is described by the posterior distribution, *i.e.*, the conditional probability under the observation of data. This posterior probability is obtained exploiting Bayes' theorem,

$$P(\theta|D) \quad = \quad \frac{P(D|\theta)P(\theta)}{P(D)} \propto P(d|\theta)P(\theta). \tag{1}$$

In this work, θ is a set of 17 parameters, which consist of the 2 single-particle energies and 15 two-body matrix elements and defines the shell-model Hamiltonian in the p-shell model space. The D is a set of the physical observables, which are taken as 33 data of energies and excitation energies in this work. In the present work, the likelihood function is taken as

$$P(D|\theta) \quad = \quad \exp[-\chi^2(\theta)/2] \tag{2}$$

with the squared errors,

$$\chi^2(\theta) \quad = \quad \sum_{n=1}^{N_D} \left(\frac{\mathcal{O}_n^{\rm expt} - \mathcal{O}_n^{\rm th}[\theta]}{\Delta\mathcal{O}} \right)^2 . \tag{3}$$

where the $\mathcal{O}_n^{\rm expt}$ and $\mathcal{O}_n^{\rm th}$ denote the n-th experimental data and theoretical data, respectively. The N_D is the number of data and, in this case, we take $N_D = 33$ binding and excitation energies of the p-shell nuclei. $\Delta\mathcal{O}$ denotes the typical error, 0.35 MeV, containing experimental and theoretical ones although the experimental error is negligible for these energies.

For simplicity, the prior probability is taken as the uniform distribution, namely $P(\theta) \propto 1$. In this case, the maximum a posteriori (MAP) estimation becomes with the minimization of the χ^2 fit. Note that the denominator in Eq.(1) is absorbed to the normalization factor and does not need to be considered.

We generate sets of the Hamiltonian parameters θ whose frequency distribution obeys the probability $P(D|\theta)$ to estimate the uncertainty of the theoretical results caused by the parameter fitting. For that purpose, we adopted the Laplace approximation [1], since we found it numerically difficult to obtain the parameter sets using the Markov Chain Monte Carlo method without this approximation.

2.2 Results

We prepared 50,000 samples of θ whose frequency distribution obeys the posterior probability, Eq.(1), and performed shell-model calculations to estimate the uncertainty of the shell-model results. Figures 1(a) and (b) show the excitation energies and energy expectation values and their uncertainties of the low-lying states of ^{12}C. In the figures, the violin plots with error bars show the theoretical results and their uncertainties. The shell-model results well reproduce the experimental values, which means that the experimental values are inside the 1σ uncertainty ranges except for the 0_2^+ state. It indicates that the 0_2^+ state cannot be described by p-shell shell-model calculation, which is reasonable since this state is known as three α-cluster state, or called the Hoyle state and its structure is considered to be far from shell-model wave functions. The result of the valence-shell in-medium similarity renormalization group (VS-IMSRG), in which the effective interaction is given in an *ab initio* way, is also shown for comparison.

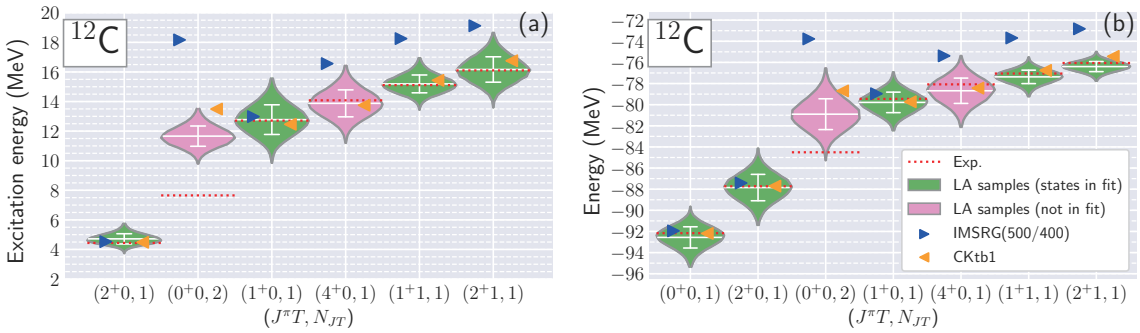

Figure 1: (a) Excitation energies and (b) energy expectation values of the ground and low-lying states of ^{12}C. The labels (J^π, T, N_{JT}) denote the total angular-momentum and parity J^π, isospin T, and N-th lowest state of (J^π, T). The violin plots with error bars show the theoretical values and their uncertainties. Red dotted lines, orange triangles, and blue triangles denote the experimental values, the traditional shell-model results [2], and the VS-IMSRG results [3]. Taken from Ref. [1].

3 Variational Monte Carlo in nuclear shell-model calculations and the restricted Boltzmann machine

In general, the shell-model calculation is difficult to be applied to heavy-mass nuclei since the dimension of the Hamiltonian matrix often becomes too huge to be diagonalized. As an attempt to solve this problem, we propose to introduce the Restricted Boltzmann Machine (RBM), one of the artificial neural networks, to the Variational Monte Carlo (VMC) framework. The introduction of the artificial neural network to solve quantum many-body problems was firstly succeeded in condensed matter physics [4, 5].

3.1 Formulation

We start with the framework of the VMC in shell-model calculations [6]. The VMC trial wave function with even A particles, $|\phi\rangle$, is defined as

$$\langle m|\phi\rangle \quad = \quad N(m)\langle m|\left(f_{ij}c_i^\dagger c_j^\dagger\right)^{A/2}|-\rangle \tag{4}$$

where i and j denote single-particle states, and f_{ij} is a set of variational parameters to describe pair correlation. $|m\rangle = c_{m_1}^\dagger c_{m_2}^\dagger \cdots c_{m_A}^\dagger|-\rangle$ is the M-scheme configuration [6, 7] specified by the A-particle occupation of the single-particle states $m = (m_1, m_2, \cdots m_A)$.

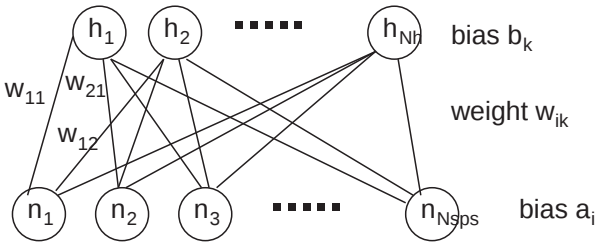

Figure 2: Schematic view of the restricted Boltzmann machine.

The $N(m)$ is given by the RBM and defined as [5]

$$\begin{aligned} N(m) &= \sum_{\{h_k=\pm 1\}} \exp\left(\sum_i a_i n_i + \sum_{i,k} w_{ik} n_i h_k + \sum_k b_k h_k\right) \\ &= \prod_k 2\cosh(b_k + \sum_i w_{ik} n_i) \exp(\sum_i a_i n_i) \end{aligned} \tag{5}$$

where a_i, b_k, and w_{ik} denote the bias of visible nodes, the bias of hidden nodes, and weights between the visible node i and the hidden node k, respectively. $n_i = 1$ for the occupied states ($n_{m_a} = 1$ for $a = 1, 2, ..., A$) and $n_i = 0$ for the unoccupied states. The schematic view of the RBM is shown in Fig. 2. Note that the weights of the RBM are restricted only between the visible and hidden nodes, from which the second line of Eq.(5) is deduced.

The energy expectation values of this trial wave function is evaluated statistically by

$$\frac{\langle\psi|H|\psi\rangle}{\langle\psi|\psi\rangle} = \frac{1}{\sum_m |\langle m|\psi\rangle|^2} \sum_m |\langle m|\psi\rangle|^2 \frac{\langle m|H|\psi\rangle}{\langle m|\psi\rangle} = \sum_m p(m) E_l(m), \tag{6}$$

where the local energy is defined as $E_l(m) = \langle m|H|\psi\rangle/\langle m|\psi\rangle$. The summation $\sum_m p(m)$ in Eq. (6) is computed statistically by preparing a set of the M-scheme configurations $|m\rangle$ whose frequency distribution obeys the probability $p(m) \propto |\langle m|\psi\rangle|^2$ exploiting the Markov Chain Monte Carlo method [6]. Thus, we avoid to store the whole possible $|m\rangle$, the number of which may be too huge. The variational parameters, f_{ij}, a_i, b_k and w_{ik} are determined to minimize the energy expectation value by the stochastic reconfiguration method [8], which can be considered as one of the machine-learning techniques.

3.2 Benchmark test

As a benchmark test, we performed the VMC calculation to evaluate the ground-state energy of ^{28}Si with the *sd*-shell model space and the USD interaction [9]. In this case, 24 visible nodes are used to describe each occupation of the single-particle states in *sd* shell for the RBM.

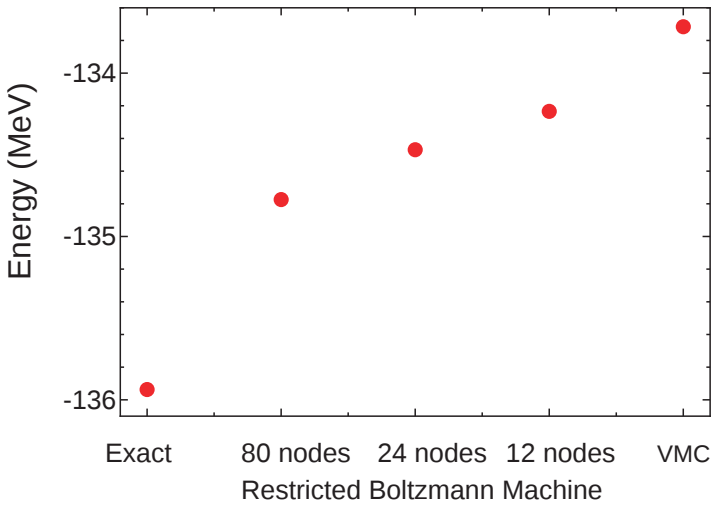

Figure 3: Shell-model energies of the ground state of ^{28}Si obtained by the exact diagonalization, the VMC results with the 80 RBM hidden nodes, 24 RBM hidden nodes, 12 RBM hidden nodes, and the VMC result without the RBM.

Figure 3 shows the shell-model energies obtained by the VMC without the RBM, with the RBM 12 hidden nodes, the 24 hidden nodes, the 80 hidden nodes. The exact energy is also shown in the left-hand side of Fig. 3. The statistical errors of the VMC are small enough and not shown in the figure. While the VMC without the RBM shows 2.2-MeV deviation from the exact one, the introduction of the RBM factor fills this gap to some extent. As increasing the number of the RBM hidden nodes, the description power of the RBM is enhanced and the energy approaches the exact value, although the 1-MeV gap remains even with the 80 hidden nodes. Further study is expected to fill this gap by applying the angular-momentum projection [6].

4 Summary and perspectives

We briefly reviewed some applications of the machine-learning techniques to nuclear shell-model calculations. Bayesian analysis was applied to the shell-model calculations and we demonstrated that uncertainty quantification is feasible with p-shell nuclei as an example. The statistical analysis of the sd-shell nuclei is found in Ref. [10]. As another application, we introduced the RBM to the VMC approach in the framework of the shell-model calculations and performed the benchmark test, which shows promising features to overcome the numerical difficulty in shell-model calculations.

Many more promising attempts have been done to apply the AI-related methods to shell-model calculations, which cannot be described in this paper. For example, we exploit a clustering algorithm to divide the basis states of the no-core Monte Carlo shell model [11] into a small number of groups in order to discuss the α-clustering structure of ^{12}C. Besides, Gaussian Process and artificial neural network are exploited to the extrapolation of the energy eigenvalue to infinite model space in the no-core shell model approach [12, 13]. We expect that such AI-related approaches will drastically open the frontiers of nuclear structure physics.

Acknowledgment

Numerical calculations were performed on Oakforest-PACS supercomputer (hp200130, hp190160, hp180179, hp170230, hp160146, xg18i035) and CX400 supercomputer of Nagoya University (hp160146). NS acknowledge valuable supports by “Priority Issue on post-K computer” (Elucidation of the Fundamental Laws and Evolution of the Universe) and “Program for Promoting Researches on the Supercomputer Fugaku” (Simulation for basic science: from fundamental laws of particles to creation of nuclei), MEXT, Japan.

NS and SY acknowledge T. Togashi and T. Otsuka for our collaboration about the uncertainty quantification of shell-model studies.

References

[1] S. Yoshida, N. Shimizu, T. Togashi, and T. Otsuka, Phys. Rev. C **98**, 061301(R) (2018).

[2] S. Cohen and D. Kurath, Nucl. Phys. **73**, 1 (1965).

[3] S. R. Stroberg, A. Calci, H. Hergert, J. D. Holt, S. K. Bogner, R. Roth, and A. Schwenk, Phys. Rev. Lett. **118**, 032502 (2017).

[4] G. Carleo and M. Troyer, Science **355**, 602 (2017)

[5] Y. Nomura, A. S. Darmawan, Y. Yamaji, and M. Imada, Phys. Rev. B **96**, 205152 (2017); L. Huang, and L. Wang, Phys. Rev. B **95**, 035105 (2017); G. Carleo, Y. Nomura, and M. Imada, Nat. Comm. **9**, 5322 (2018).

[6] T. Mizusaki and N. Shimizu, Phys. Rev. C **85**, 021301(R) (2012); N. Shimizu and T. Mizusaki, Phys. Rev. C **98**, 054309 (2018).

[7] N. Shimizu, T. Mizusaki, Y. Utsuno, and Y. Tsunoda, Comp. Phys. Comm. **244**, 372 (2019).

[8] S. Sorella, Phys. Rev. B **64**, 024512 (2001).

[9] B. A. Brown and B. H. Wildenthal, Ann. Rev. Nucl. Part. Sci. **38**, 29 (1988).

[10] J. M. R. Fox, C. Johnson, and R. N. Perez, Phys. Rev. C **101**, 054308 (2020).

[11] T. Yoshida, N. Shimizu, T. Abe and T. Otsuka, J. Phys.: Conf. Ser. **569**, 012063 (2014).

[12] S. Yoshida, Phys. Rev. C **102**, 024305 (2020)

[13] W. G. Jiang, G. Hagen, and T. Papenbrock, Phys. Rev. C **100**, 054326 (2019) G. A. Negoita et al., Phys. Rev. C **99**, 054308 (2019).

15. Nuclear data generation using machine learning

Hiroki IWAMOTO[†1]

[1]Nuclear Science and Engineering Center, Japan Atomic Energy Agency
[†]Email: iwamoto.hiroki@jaea.go.jp

Gaussian processes are used as a Bayesian machine learning technique to solve regression and classification problems. This paper reviews this technique, and presents some merits and issues for the nuclear data generation.

1 Introduction

Gaussian processes [1, 2] are used as a Bayesian machine learning technique to solve the regression and classification problems. Because a regression model based on Gaussian processes (GPR) gives predictive distributions for regression problems, this technique may be a powerful tool not only for evaluating nuclear data but also for determining the corresponding uncertainty. In the previous study, a method to generate nuclear data from experimental data was proposed based on GPR [3], and it was demonstrated that our method can generate reasonable regression curves and their uncertainties from experimental data. This paper reviews this technique, and some merits and issues for the nuclear data generation are presented.

2 Gaussian process regression

Suppose that we have N measured data points (measurement energy points $\boldsymbol{x}_N \in \mathbb{R}^N$ and corresponding cross sections with uncertainties [one standard deviation, 1σ], $\boldsymbol{t}_N \pm \delta\boldsymbol{t}_N \in \mathbb{R}^N$) for a certain nuclear reaction and that we aim to generate a set of cross-sections for certain M energy points $\boldsymbol{x}_M \in \mathbb{R}^M$. GPR expresses the conditional probability distribution of $\boldsymbol{t}_M \in \mathbb{R}^M$ given by $\boldsymbol{t}_N$, $p(\boldsymbol{t}_M|\boldsymbol{t}_N)$, as a Gaussian distribution with mean $\boldsymbol{\mu}_M$ and covariance $\boldsymbol{\Sigma}_{M,M}$:

$$p(\boldsymbol{t}_M|\boldsymbol{t}_N) = \mathcal{N}(\boldsymbol{t}_M \mid \boldsymbol{\mu}_M, \boldsymbol{\Sigma}_{M,M}), \tag{1}$$

$$\boldsymbol{\mu}_M = \mathbf{C}_{NM}^{\top}\mathbf{C}_{NN}^{-1}\boldsymbol{t}_N, \tag{2}$$

$$\boldsymbol{\Sigma}_{MM} = \mathbf{C}_{MM} - \mathbf{C}_{NM}^{\top}\mathbf{C}_{NN}^{-1}\mathbf{C}_{NM}. \tag{3}$$

The (i, j)-th element of the covariance $\mathbf{C}_{NN}$ is expressed as

$$C(\boldsymbol{x}_i, \boldsymbol{x}_j) = k(\boldsymbol{x}_i, \boldsymbol{x}_j) + \delta t_i \delta_{ij} \delta t_j, \tag{4}$$

where $k(\boldsymbol{x}_i, \boldsymbol{x}_j)$ represents the kernel function, and the δ_{ij} is the Kronecker delta. The (i, j)-th elements of $N \times M$ matrix $\mathbf{C}_{NM}$, $M \times N$ matrix $\mathbf{C}_{MN}(= \mathbf{C}_{NM}^{\top})$, and $M \times M$ matrix $\mathbf{C}_{MM}$ are of the form:

$$C(\boldsymbol{x}_i, \boldsymbol{x}_j) = k(\boldsymbol{x}_i, \boldsymbol{x}_j). \tag{5}$$

For the kernel function, this study used the following radial basis function:

$$k(\boldsymbol{x}_i, \boldsymbol{x}_j) = \theta_1 \exp\left(-\frac{\theta_2}{2}||\boldsymbol{x}_i - \boldsymbol{x}_j||^2\right), \tag{6}$$

where $\boldsymbol{\Theta} = (\theta_1, \theta_2)$ is a set of hyperparameters, which is optimized by finding a solution that maximizes the marginal log likelihood $p(\boldsymbol{t}_N|\mathbf{C}_{NN}, \boldsymbol{\Theta})$:

$$\boldsymbol{\Theta}_{\rm opt} = \underset{\boldsymbol{\Theta}}{\rm argmax} \ln p(\boldsymbol{t}_N|\mathbf{C}_{NN}, \boldsymbol{\Theta}) \tag{7}$$

$$= \underset{\boldsymbol{\Theta}}{\rm argmax} \left(-\frac{1}{2}\ln|\mathbf{C}_{NN}| - \frac{1}{2}\boldsymbol{t}_N\mathbf{C}_{NN}^{-1}\boldsymbol{t}_N^\top - \frac{N}{2}\ln(2\pi)\right). \tag{8}$$

3 Generated cross-sections

3.1 Nuclide-production cross-sections

Figure 1 compares the generated nuclide production cross-sections for the ^{27}Al$(p, X)^4$He and ^{27}Al$(p, X)^{10}$Be reactions with physics models of INCL++/ABLA07 [4, 5] and INCL4.6/GEM [6, 7] and evaluated nuclear data libraries of ENDF/B-VIII.0 [8], JENDL-4.0/HE [9], and TENDL-2019 [10]. The experimental data, which were measured with the activation method, were taken from the experimental nuclear database, EXFOR [11]. The blue dashed line with uncertainty band indicates the cross-sections generated by GPR. Although the physics models and evaluated nuclear data account for the trends of the production cross-sections as a function of incident energy, it fails to agree with the experimental data. These discrepancies would be solved by improving the phyicis model or model parameters. In contrast, since GPR draws smooth curves to fit the experimental data without the need for physics models, the curves agree in principle with the experiments.

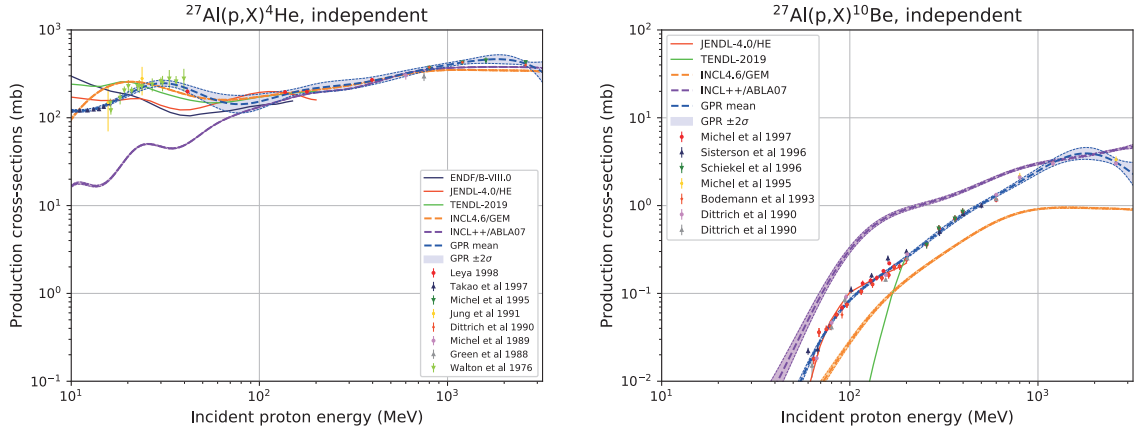

Figure 1: Comparisons of nuclide production cross-sections for the ^{27}Al$(p, X)^4$He reaction (left panel) and the ^{27}Al$(p, X)^{10}$Be reaction (right panel) with physics models of INCL++/ABLA07 [4, 5] and INCL4.6/GEM [6, 7] and evaluated nuclear data libraries of ENDF/B-VIII.0 [8], JENDL-4.0/HE [9], and TENDL-2019 [10]. The dashed blue line and the light blue band present the mean of the generated predictive distribution and $\pm 2\sigma$ about the mean, respectively. The experimental data were taken from EXFOR [11].

3.2 GPR as a random sampler

Figure 2 shows generated nuclide-production cross-section for the $^{\mathrm{nat}}\mathrm{N}(p, X)^{10}\mathrm{Be}$ reaction and the generated correlation matrix. In the left panel of Figure 2, the 10 colored lines indicate random samples of the cross sections, which can be easily generated according $\boldsymbol{t}_M|\boldsymbol{t}_N \sim \mathcal{N}(\boldsymbol{t}_M \mid \boldsymbol{\mu}_M, \boldsymbol{\Sigma}_{MM})$. These random samples would be of significant benefit to subsequent uncertainty propagation analyses by the random sampling technique in research fields such as neutronics, reactor physics, and shielding analyses.

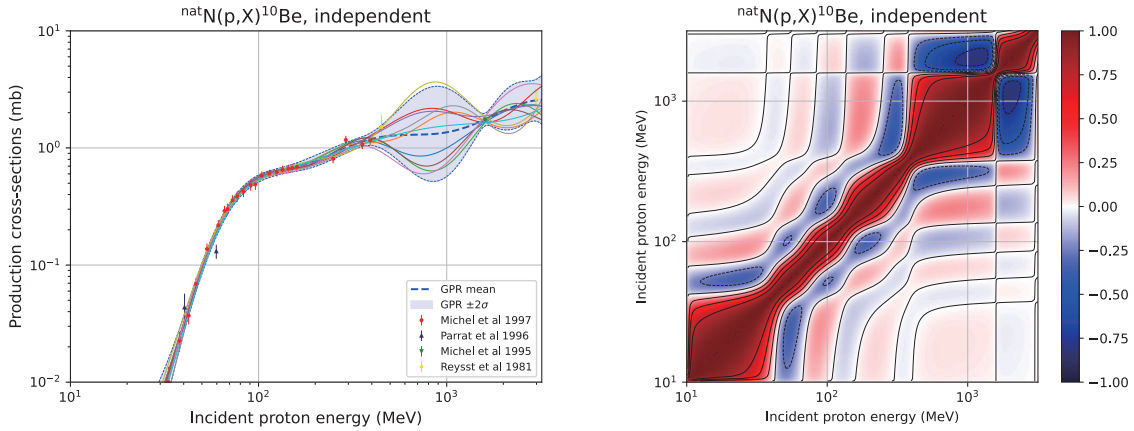

Figure 2: Generated nuclide-production cross-section (left panel) and the generated correlation matrix (right panel) for the $^{\mathrm{nat}}\mathrm{N}(p, X)^{10}\mathrm{Be}$ reaction. For the left panel, the dashed blue line and the light blue band present the mean of the generated predictive distribution and $\pm 2\sigma$ about the mean, respectively. The 10 colored lines present random samples generated according to $\boldsymbol{t}_M|\boldsymbol{t}_N \sim \mathcal{N}(\boldsymbol{t}_M \mid \boldsymbol{\mu}_M, \boldsymbol{\Sigma}_{MM})$. The experimental data were taken from EXFOR.

3.3 Case of small experimental dataset

Figure 3 illustrates the nuclide-production cross-section for the $^{27}\mathrm{Al}(p, pn)^{26}\mathrm{Al}$ reaction. In the left panel, the cross-section was generated from the experimental data by Sisterson, et al. [12] and Schneider, et al. [13]. Here, since the threshold energy can be deduced from the mass of the reaction system ($x_{\mathrm{th}} = 11.3$ MeV), it was considered as training data (i.e. $\{x_{\mathrm{th}}, t_{\mathrm{th}}, \delta t_{\mathrm{th}}\} = \{11.3\ \mathrm{MeV}, 10^{-3}\ \mathrm{mb}, 10^{-4}\ \mathrm{mb}\}$). Although its exact position including its uncertainty cannot be determined, a reasonable curve in this energy range seems to be obtained, and we confirmed that the generated uncertainty did not strongly depend on the additional training data. However, an unacceptably large uncertainty band is still observed at the GeV range, which is owing to the lack of experimental data. Such uncertainty information would be useful for motivating to conduct new experiments in terms of enhancing the prediction acuracy.

As one possible way to resolve such problems, it may be necessary to give some physical knowledge as training data. In this case, from the total proton-neutron cross-section systematics [14], the (p, pn) cross-sections in the GeV range is expected to be constant. In the right panel of Figure 3, auxiliary constant cross-section value points are added in the GeV range to take into account this knowledge. However, this ad hoc solution need to be improved in future.

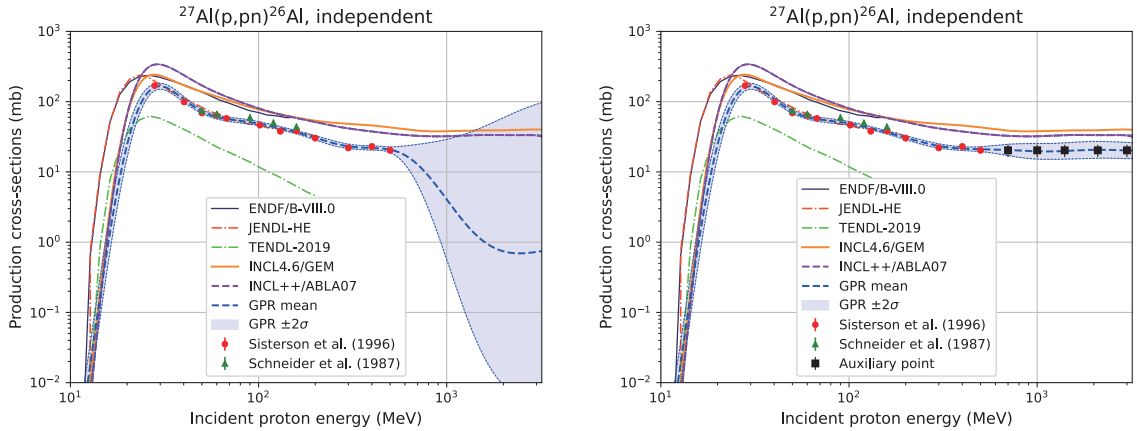

Figure 3: Left panel: nuclide production cross-section for the $^{27}\mathrm{Al}(p, pn)^{26}\mathrm{Al}$ reaction generated from the experimental data. Right panel: same as the left panel but with the inclusion of auxiliary points infered from the total proton-neutron cross-section systematics at the GeV range.

4 Summary

We have applied the GPR technique to generate nuclear data, focusing on proton-induced nuclide production cross-sections. Reasonable curves with corresponding uncertainties were obtained and the results indicate that this approach is effective for generating nuclear data.

References

[1] Rasmussen, C.F., Williams, C.K.I., Gaussian process for machine learning, The MIT press, Cambridge, 2006.

[2] Bishop, C.M., Pattern recognition and machine learning, Springer, New York, 2006.

[3] Iwamoto, H., Generation of nuclear data using Gaussian process regression, J. Nucl. Sci. Technol., vol.57, no.8, 2020, pp.932–938.

[4] Leray, S., et al., Extension of the Liège Intra Nuclear Cascade model to light ion-induced collisions for medical and space applications. J. Phys.: Conf. Series, vol.420, 2013, pp. 012065.

[5] Kelić, A., et al., ABLA07 – Towards a complete description of the decay channel of a nuclear system from spontaneous fission to multifragmentation. INDC(NDS)-0530, IAEA, 2008, pp.181–221.

[6] Boudard, A., et al., New potentialities of the Liège intranuclear cascade model for reactions induced by nucleons and light charged particles. Phys. Rev. C, 2013, 014606.

[7] Furihata, S., Statistical analysis of light fragment production from medium energy proton-induced reactions. Nucl. Instrum. Meth. B, vol.171, 2000, pp.251–258.

[8] Brown, D.A., ENDF/B-VIII.0: The 8$^{\mathrm{th}}$ major release of the nuclear reaction data library with CIELO-project cross sections, new standards and thermal scattering data. Nucl. Data Seets, vol.148, 2018, pp.1–142.

[9] Kunieda, S., et al., Overview of JENDL-4.0/HE and benchmark calculations. Proceedings of the 2015 Symposium on Nuclear Data, Tokai-mura, 2015, JAEA-Conf 2016-004, 2016, pp.44–46.

[10] Koning, A.J., et al., TENDL: Complete nuclear data library for innovative nuclear science and technology. Nucl. Data Sheets, vol.155, 2019, pp.1–55.

[11] Otuka, N., et al., Towards a more complete and accurate experimental nuclear reaction data library (EXFOR): International collaboration between nuclear reaction data centres (NRDC). Nucl. Data Sheets, vol.120, 2014, pp.272–276.

[12] Sisterson, J.M., et al., Measuring excitation functions needed to interpret cosmogenic nuclide production in lunar rocks. Conf. on Appl. of Accel. in Res. and Ind., Denton, USA, 1996, pp.811.

[13] Schneider, R.J., et al., Measurement of cross sections for aluminum-26 and sodium-24 induced by protons in aluminum. Nucl. Instrum. Meth. B, vol.29, 1987, pp.271–274.

[14] Cugnon, J., et al., Simple parametrization of cross-sections for nuclear transport studies up to the GeV range Nucl. Instrum. Meth. B, vol.111, 1996, pp.215–220.

16. Exploration of automated data processing for mass production of nuclear data at RIBF

Shoichiro KAWASE[1,2]
[1]Interdisciplinary Graduate School of Engineering Sciences, Kyushu University
6-1 Kasuga-koen, Kasuga, Fukuoka 816-8580, Japan
[2]RIKEN Nishina Center for Accelerator-Based Science
Email: kawase@aees.kyushu-u.ac.jp

Since the secondary beam produced by the RIBF generally contains various nuclides, it is possible to acquire data on non-rare events systematically. However, systematic nuclear data acquisition at RIBF has not been realized due to the lack of data acquisition capability and workforce for data analysis. If data calibration can be automated, the latter will be solved. For the automation of data calibration, advanced statistical inference methods could be used. In this study, the Markov chain Monte Carlo method was employed for a part of particle identification analysis in a secondary beam experiment, and the results were comparable to those of the conventional analysis method.

1. Introduction

Data-intensive science has been proposed as the fourth paradigm of scientific research following experimental, theoretical, and computational sciences. In data-intensive science, a large amount of data, obtained by advanced data acquisition and processing and simulation techniques, are aggregated, and statistical inference is used to develop data-driven scientific research.

The RI beam experiment at RIBF[1)] has the advantage of developing such a data-intensive science. The secondary beam used in RIBF generally contains many different nuclides. Therefore, in principle, it is possible in an experiment at RIBF to obtain rare events that the experimental proposer aims for and systematically obtain non-rare nuclear reaction data simultaneously. Such non-rare data may include isotope production and elastic scattering cross sections. The systematic acquisition of such data and the development of scientific research based on the aggregated data is consistent with the direction of data-intensive science.

However, in practice, the data acquisition and data processing capacity of RIBF is limited in two aspects: data acquisition systems and workforce. First, to measure rare events efficiently, data from non-rare events are usually excluded from the acquisition at the trigger level. Also, data on common events that cannot be excluded are rarely published because the data alone have little academic impact, despite the effort required to analyze it. Even if a non-collaborator would like to analyze the data and extract systematic features from them, it is not easy to actually analyze the data because of the need for detailed information on the experimental conditions, such as the operating conditions of the detector and the magnetic field settings of the electromagnets, which vary from experiment to experiment.

The latter of these two limitations can be overcome by automating the data calibration. In order to realize the automation of data calibration in RIBF, modern statistical inference methods could be applied.

In this report, an attempt to apply the Markov chain Monte Carlo method (MCMC) to the particle identification analysis for secondary beams is introduced.

2. Data Analysis

At the BigRIPS particle separator[2] at RIBF, secondary beam particles are identified on an event-by-event basis from time-of-flight (TOF), magnetic rigidity ($B\rho$), and energy loss (ΔE) information obtained by using beamline detectors (the TOF-$B\rho$-ΔE method)[2]. In this study, MCMC was applied to the determination of ion-optical transfer matrix elements, which is the part of the $B\rho$ analysis. The first-order ion-optical transformation between two focal planes is given by

$$\begin{pmatrix} x_f \\ a_f \\ \delta \end{pmatrix} = \begin{pmatrix} (x|x) & (x|a) & (x|\delta) \\ (a|x) & (a|a) & (a|\delta) \\ 0 & 0 & 1 \end{pmatrix} \begin{pmatrix} x_i \\ a_i \\ \delta \end{pmatrix}. \quad (1)$$

Here, (x_i, a_i) and (x_f, a_f) are the positions and angles in the horizontal plane at the initial and the final focal planes, and δ is the deviation of $B\rho$ from the central value $B\rho_0$ and defined by the following equation:

$$B\rho = \left(1 + \frac{\delta}{100}\right) B\rho_0. \quad (2)$$

The coefficients $(x|x), (x|a), (x|\delta), (a|x)$, $(a|a)$, and $(a|\delta)$ are referred to as first-order transfer matrix elements. In the conventional method, first-order transfer matrix elements are determined by linear fitting procedure, and the effect of higher-order transfer matrix elements are adjusted by the empirical method so as to improve the resolution of mass-to-charge ratio (A/Q). On the other hand, the new method using MCMC has the potential to determine higher-order transfer matrix elements directly from measurement data.

In this study, a dataset taken in the spallation reaction measurement on ^{93}Zr was used for the analysis. In this dataset, beam particles distribute only in limited phase-space. At first, x_{F5} and TOF_{35}

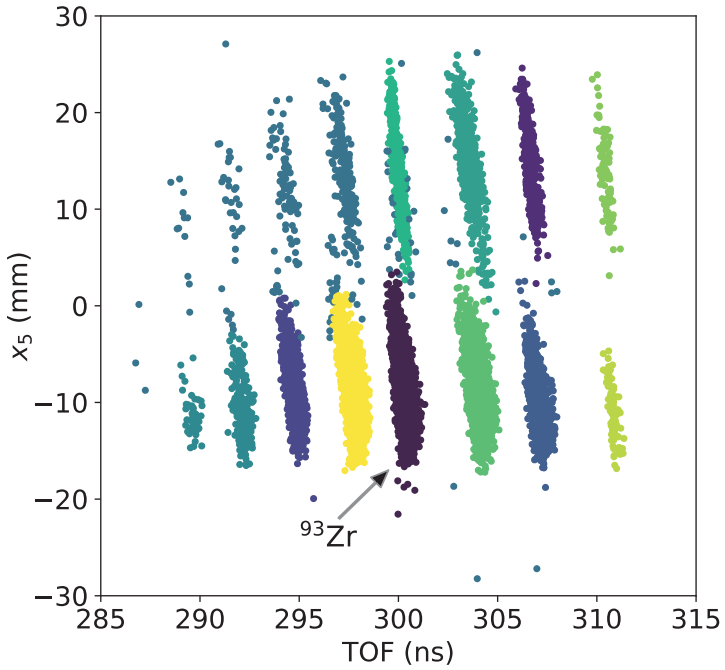

Figure 1 Correlation between x_5 and TOF and clustering result using GMM.

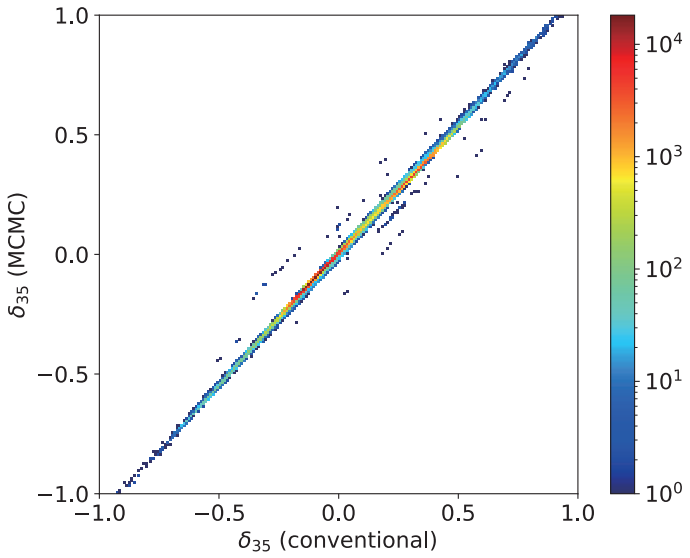

Figure 2 Correlation of δ obtained using MCMC (vertical axis) and a conventional analysis method (horizontal axis).

distributions were fitted with the Gaussian mixture model (GMM) implemented in *scikit-learn*[3], an open-source machine learning library, and the events corresponding to ^{93}Zr was extracted. Figure 1 shows the clustering result using GMM. Then, the first-order matrix elements were estimated using MCMC with a probabilistic programming language *Stan*[4]. Finally, δ's for all events in the dataset were calculated using the estimated matrix elements. Figure 2 shows the correlation of δ's obtained using MCMC to that obtained in a conventional analysis method.

3. Summary

An analysis method employing MCMC was applied to the $B\rho$ analysis with a limited dataset, and similar results to the conventional analysis method were obtained. In the future, further development, such as the introduction of higher-order matrix elements and application to more general datasets, will be done to achieve automated data calibration.

References

1) Yano, Y., The RIKEN RI Beam Factory Project: A status report, Nucl. Instrum. Meth. Phys. Res. B, vol.261, 2007, pp.1009-1013.
2) Fukuda, N., Kubo, T., Ohnishi, T., Inabe, N., Takeda, H., Kameda, D., Suzuki, H., Identification and separation of radioactive isotope beams by the BigRIPS separator at the RIKEN RI Beam Factory, Nucl. Instrum. Meth. Phys. Res. B, vol.317, 2013, pp.323-332.
3) Pedregosa, F., et al, Scikit-learn: Machine Learning in Python, J. Mach. Learn. Res., vol.12, 2011, pp.2825-2830.
4) Stan Development Team, Stan Modeling Language Users Guide and Reference Manual, 2.25, https://mc-stan.org

Acknowledgments

This work is supported in part by the Education and Research Support Program on Mathematical and Data Science funded by Education and Research Center for Mathematical and Data Science, Kyushu University.

17. Study of the fission path energy of U-236 using microscopic mean-field model

Kazuki FUJIO[†1], Shuichiro EBATA[2], Tsunenori INAKURA[1], and Satoshi CHIBA[1]

[1] *Tokyo Institute of Technology, Ookayama2-12-1, Meguro, Tokyo, 152-8850, Japan*
[2] *Saitama University, Shimo-Okubo255, Sakura-ku, Saitama, 338-8570, Japan*
[†] *E-mail: fujio.k.aa@m.titech.ac.jp*

Abstract

To study a fission path, we investigated the potential energy surface of U-236 with respect to its quadrupole and octupole deformations, using the microscopic theoretical model with Skyrme-type effective interactions. We divided the potential energy surface into 7 terms to investigate their contributions to the fission barrier height. Although the height is decided from the competition among the terms, we found the Coulomb term and a combination of others excluding the spin-orbit and pairing energy terms have a relatively small interaction dependence. It indicates that the amplitudes of spin-orbit and pairing energy will affect the barrier height.

1 Introduction

Minor Actinides (MA) are produced through a sequence of neutron-capture, β-, and α-decays in nuclear reactors. The MAs affect the performance of nuclear reactors and the composition of nuclei in the radioactive waste. Therefore, nuclear data such as the fission product yield of MA is necessary for reactor technology and to deal with the radioactive waste effectively. However, the data is insufficient and its uncertainty is large, due to the difficulty of experiments using highly radioactive materials. A theoretical approach is one of the effective techniques to prepare unmeasured data or to predict unmeasurable data. The macro-micro models [1, 2] that consist of the liquid drop model [3] and a quantum correction have been employed widely for the fission study. The liquid drop model is employed to describe the bulk property of the nucleus, and the quantum correction is introduced for the nuclear shell effects. The parameters in the model and correction are phenomenologically determined to reproduce the nuclear properties well. Although the model works well to explain and reproduce the known data, its prediction power might be small for unknown data. To supply and predict the data of MA or unmeasured, we should have a more fundamental approach in which the empirical methods are excluded as far as possible. Therefore we employ a microscopic mean-field model that can describe nuclei from the degree of freedom of nucleon to investigate the fission phenomena. Our model employs the Skyrme effective interaction [4], which has been developed to describe the basic nuclear properties in the vicinity of ground states: nuclear binding energy, nuclear matter parameters, radius, deformation, and shell structure. We should investigate carefully the applicability of these effective interactions to be applied to nuclear fission because the nuclei become much deformed in the way to scission hence they are far from their ground states. In this study, we calculate the potential energy surface (PES) of the U-236 assuming the compound nucleus of n + U-235 reaction, and investigate the difference among the PES given by existing Skyrme effective interactions.

2 Method

We employ the Skyrme-Hartree-Fock+BCS model [5] and impose constraints on the nuclear shape [6] of U-236. To describe any nuclear deformation in this work, the wave function is represented in the three-dimensional coordinate space. The three Skyrme effective interactions (SkM*, SLy4, SkI3) are employed. The Skyrme effective interaction is written with the delta function of a space r, as follows:

$$\begin{aligned}\hat{v}(i,j) &= t_0\left(1+x_0P_\sigma\right)\delta\left(\boldsymbol{r}\right)+\frac{1}{2}t_1\left(1+x_1P_\sigma\right)\left(\boldsymbol{k}^2\delta\left(\boldsymbol{r}\right)+\delta\left(\boldsymbol{r}\right)\boldsymbol{k}^{'2}\right)+t_2\left(1+x_2P_\sigma\right)\boldsymbol{k}\cdot\delta\left(\boldsymbol{r}\right)\boldsymbol{k}^{'} \\ &\quad +\frac{1}{6}t_3\left(1+x_3P_\sigma\right)\rho^\alpha\left(\frac{\boldsymbol{r}_i+\boldsymbol{r}_j}{2}\right)\delta\left(\boldsymbol{r}\right)+iW\left(\boldsymbol{\sigma}_i+\boldsymbol{\sigma}_j\right)\cdot\boldsymbol{k}\times\delta\left(\boldsymbol{r}\right)\boldsymbol{k}^{'}, \qquad (1)\end{aligned}$$

where t_0, x_0, t_1, x_1, t_2, x_2, t_3, x_3, α, W are parameters, $\boldsymbol{\sigma}$ is the Pauli matrix, P_σ is the spin exchange operator, $\boldsymbol{k}$ and $\boldsymbol{k}^{'}$ are relative momentums. The $\boldsymbol{k}$ ($\boldsymbol{k}^{'}$) is formed $(\overrightarrow{\nabla}_i-\overrightarrow{\nabla}_j)/2i$ $((\overleftarrow{\nabla}_i-\overleftarrow{\nabla}_j)/2i)$ which acts on the right (left) side. These parameters are adjusted to reproduce nuclear properties according to the protocol of each parameter set. The SkM* parameter set is to reproduce the fission barrier height of the Pu-240 [7], the SLy4 is designed to deduce the nucleon matter properties [8], and the SkI3 is prepared to reproduce the single-particle states of Pb-208 which the relativistic mean-field model deduces [9]. We can calculate the energy of a system from the expectation value of the Skyrme interaction by the many-body wave function. Normally, Skyrme interaction is divided into the central force and spin-orbit force. However, it is divided into the four forces because we want to investigate the behavior of each term in detail. The first term in Eq.(1) is named volume term which works as the attractive force, the second and third terms are reflected the nuclear surface properties due to including the differential operators. The fourth term is named density-dependent term which works as a repulsive force. The last term means the spin-orbit force. The many-body wave function formed as BCS-type [10] is employed in which the single-particle states and the pairing correlation are determined self-consistently. We calculate the PES of U-236 in which the fission reaction of U-235 induced a thermal neutron is assumed. The constraints on nuclear shape are expressed with the radial direction r and the spherical harmonics Y_{lm}. The quadrupole $\hat{Q}_{20}$ and octupole $\hat{Q}_{30}$ operators are applied to express the elongation and mass asymmetry of the nucleus, respectively. Their forms are:

$$\begin{aligned}\hat{Q}_{20} &= r^2Y_{20}=\sqrt{\frac{5}{16\pi}}r^2(3\cos^2\theta-1), \\ \hat{Q}_{30} &= r^3Y_{30}=\sqrt{\frac{7}{16\pi}}r^3(5\cos^3\theta-3\cos\theta). \qquad (2)\end{aligned}$$

For the investigation of the fission path, the PES is calculated with these constraints. The constraints are introduced to the Hamiltonian $\hat{H}$, such as Lagrange multiplier:

$$\hat{H}^{'}=\hat{H}-\sum_{l=2,3}\lambda_{l0}\left(\hat{Q}_{l0}-Q_{l0}\right)^2, \qquad (3)$$

where λ_{l0} is the Lagrange multiplier and Q_{l0} is the expectation value $\langle\hat{Q}_{l0}\rangle$ with the many-body wave function. The procedure to calculate the PES is 1) to prepare the ground state, 2) to elongate the nucleus with using $\hat{Q}_{20}$, and 3) to add the octupole moment using $\hat{Q}_{30}$ for the expression of mass asymmetry.

3 Results and discussion

Figure 1 shows the PES with respect to Q_{20} and Q_{30} using SkI3 parameter set. The PES dE can be calculated as the difference between the ground state energy $E_{G.S.}$ and the energy at the

Table 1: Calculation results for $E_{G.S.}$, $B_{\rm inner}$, $B_{\rm outer}\,(Q_{30}=0)$ and $B_{\rm outer}\,(Q_{30}\neq 0)$ using different Skyrme interactions together with experimental values

Force	SkM*	SLy4	SkI3	exp.
$E_{\rm G.S.}$ (MeV)	-1796.97	-1796.46	-1799.85	-1790.41
$B_{\rm inner}$ (MeV)	8.4	10.4	8.7	4.9
$B_{\rm outer}\,(Q_{30}=0)$ (MeV)	13.1	18.1	14.2	-
$B_{\rm outer}\,(Q_{30}\neq 0)$ (MeV)	7.2	10.2	6.3	5.8

each point $E(Q_{20}, Q_{30})$, and as follows;

$$dE = E(Q_{20}, Q_{30}) - E_{G.S.}. \tag{4}$$

The dashed line shows the symmetry fission path corresponding to $Q_{30}=0$, and the solid line shows a path following a valley of the PES in Figure 1. Nucleon densities at some important points are given in this figure, additionally, it is clear that the path written by the solid line is easier to undergo fission than the dashed one. Figure 2 shows the results of dE along the two fission paths. The dashed and the solid line are the same as in Figure 1. All of interactions have the ground state, the 2$^{\rm nd}$ minimum, the inner fission barrier $B_{\rm inner}$ and the outer fission barrier $B_{\rm outer}$. The two-humped barrier structure can be seen for the three effective interactions and the mass asymmetric deformation allows the decreasing the $B_{\rm outer}$. Our results and the experimental data for $E_{G.S.}$ [12] and for the fission barrier heights are shown in Table 1. This result reveals that our calculation overestimates the experimental data of the fission barrier height [11]. To elucidate the reason for this overestimation, we investigate which terms contribute to and which manner to the fission barrier in the following. The total binding energy E_{tot} of each interaction

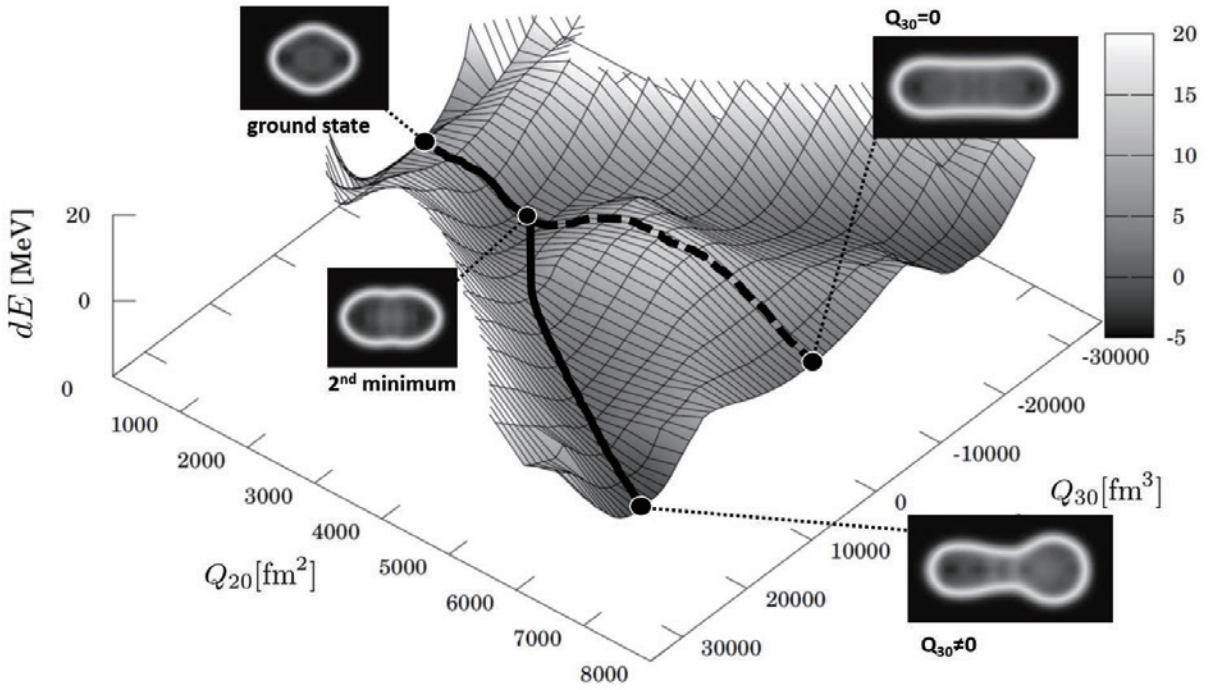

Figure 1: The PES of SkI3 with respect to Q_{20} and Q_{30}

can be divided into 7 terms which are $E_{\rm t0}$, $E_{\rm t1,t2}$, $E_{\rm t3}$, $E_{\rm ls}$, the kinetic energy $E_{\rm kinetic}$, the

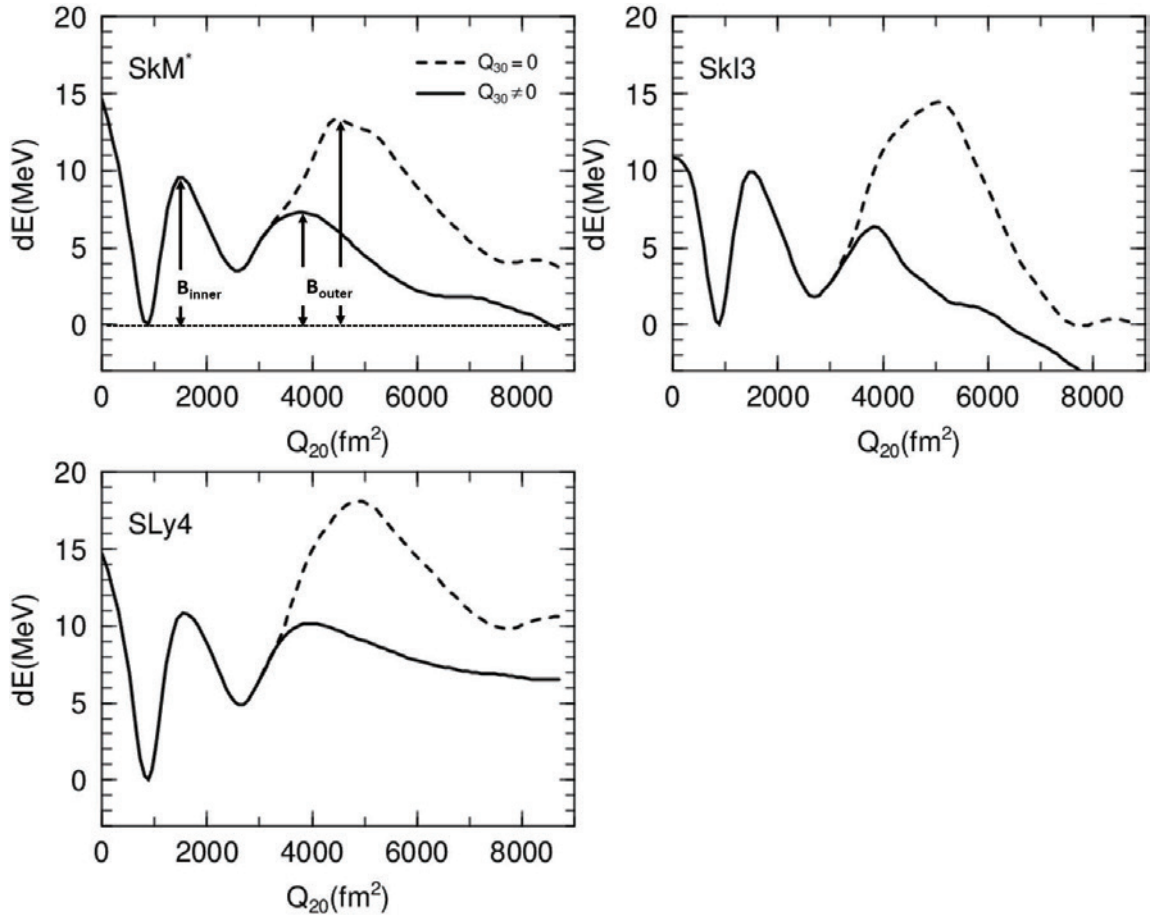

Figure 2: The fission path with respect to Q_{20}

Coulomb energy $E_{\rm Coulomb}$, and the pairing energy $E_{\rm pair}$:

$$\begin{aligned} E_{tot} &= E_{\rm t0} + E_{\rm t1,t2} + E_{\rm t3} + E_{\rm ls} + E_{\rm kinetic} + E_{\rm Coulomb} + E_{\rm pair} \\ &= E_{\rm Skyrme} + E_{\rm kinetic} + E_{\rm Coulomb} + E_{\rm pair}. \end{aligned} \tag{5}$$

The Skyrme energy $E_{\rm Skyrme}$ is composed of the volume energy $E_{\rm t0}$, the surface energy $E_{\rm t1,t2}$, the density dependence energy $E_{\rm t3}$, and the spin-orbit energy $E_{\rm ls}$. It is difficult to specify their contributions to the fission barrier because they have a complicated competition. To extract the major characterizing the barrier, we search a combination of the energy terms which have a small interaction-dependence, namely, the non-characteristic parts of the PES on all interactions.

Figure 3 shows the result of them. These energies is calculated as the same way of Eq.(4). The solid line shows SkM*, the dashed one is SLy4 and the dotted one is SkI3. The left panel represents the sum of $E_{\rm t0} + E_{\rm t1,t2} + E_{\rm t3} + E_{\rm kinetic}$. This summation increases with increasing Q_{20} for the three effective interactions. On the other hand, $E_{\rm Coulomb}$ decreases with increasing Q_{20}, because the Coulomb force is inversely proportional to the distance of the charge. There are small interaction dependences on the sum of $E_{\rm t0} + E_{\rm t1,t2} + E_{\rm t3} + E_{\rm kinetic}$ and $E_{\rm Coulomb}$, which indicates that the $E_{\rm ls}$ and $E_{\rm pair}$ have a very important role to form the fission barrier. The behavior of the $E_{\rm ls}$ and $E_{\rm pair}$ are compared with the fission path in Figure 4. The upper left (right) shows $E_{\rm ls}$ ($E_{\rm pair}$) and the lower left shows the fission path. The solid (dotted) arrow indicates a bump (valley) of the fission path. These results show that $E_{\rm ls}$ has in-phase and, $E_{\rm pair}$ has the out-of-phase with the fission path. The phase relationship between the spin-orbit force

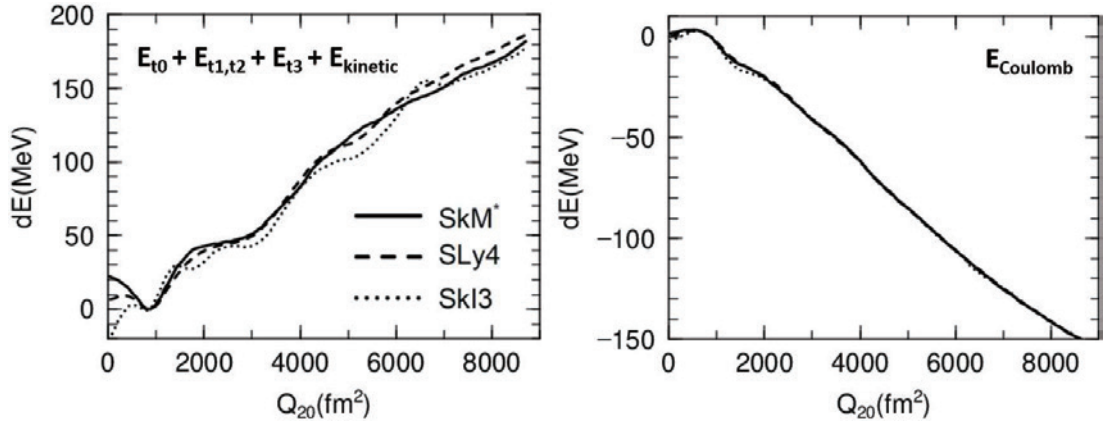

Figure 3: The contributions for dE: (left) $E_{\rm t0} + E_{\rm t1,t2} + E_{\rm t3} + E_{\rm kinetic}$, and (right) $E_{\rm Coulomb}$

and the pairing correlation has been known for the previous nuclear structure study [13]. We point out that there are small interaction dependences on the sum of $E_{\rm t0} + E_{\rm t1,t2} + E_{\rm t3} + E_{\rm kinetic}$ and $E_{\rm Coulomb}$. Therefore, the $E_{\rm ls}$ and $E_{\rm pair}$ might have an important role to decide the fission barrier height.

4 Conclusion

We investigate the PES of U-236 by the constraint Skyrme-Hartree-Fock+BCS with respect to the quadrupole Q_{20} and octupole Q_{30} momentums. Our calculation reproduces the two-humped barrier structure on the fission path, shows also that the degree of freedom for the mass asymmetry on fission products, namely, Q_{30} effects, allows the decreasing the outer barrier height. The calculated fission barriers overestimate the experimental data. In order to elucidate the reason for the overestimation, the fission path is decomposed into 7 terms. The sum of $E_{\rm t0} + E_{\rm t1,t2} + E_{\rm t3} + E_{\rm kinetic}$, and the $E_{\rm Coulomb}$ have a small interaction-dependence. Thus, the $E_{\rm ls}$ and $E_{\rm pair}$ might affect the fission barrier height.

Acknowledgement

This work is supported by the Leading initiative for Excellent Young Researchers, MEXT, Japan, and by the Japan Society for the Promotion of Science (JSPS) KAKENHI Grant Number JP20K03943.

References

[1] V. M. Strutinsky, Shell effects in nuclear masses and deformation energies, Nucl. Phys. **A95**, 1967, pp.420–442.

[2] V. M. Strutinsky, “Shells” in deformed nuclei, Nucl. Phys. **A122**, 1968, pp.1–33.

[3] N. Bohr and J. A. Wheeler, The Mechanism of Nuclear Fission, Phys. Rev. **56**, 1939, pp.426–450.

[4] D. Vautherin and D. M. Brink, Hartree-Fock Calculations with Skyrme’s Interaction. 1. Spherical Nuclei, Phys. Rev. **C5**, 1972, pp.626-647.

[5] S. Ebata and T. Nakatsukasa, Octupole deformation in the nuclear chart based on the 3D Skyrme HartreeFock plus BCS model, Phy. Scr. **92**, 2017 pp.064005

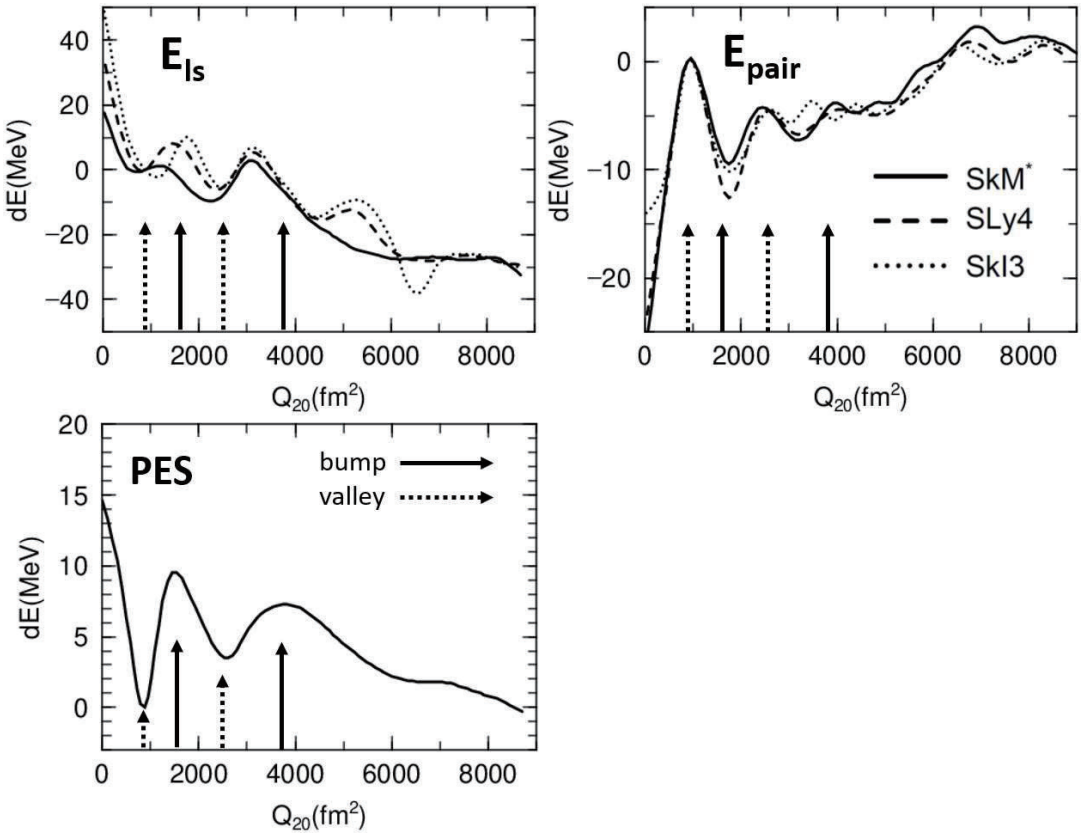

Figure 4: The behavior of the $E_{\rm ls}$ and $E_{\rm pair}$

[6] G. Scamps and C. Simenel, Impact of pear-shaped fission fragments on mass-asymmetric fission in actinides, Nature. 564, 2018, 382385.

[7] J. Barrel et al., Towards a better parametrisation of Skyrme-like effective forces: A critical study of the SkM force, Nucl. Phys. **A386**, 1982, 79-100.

[8] E. Chabanat et al., A Skyrme parametrization from subnuclear to neutron star densities Part 2. Nuclei far from stabilities, Nucl. Phys. **A635**, 1998, 231-256.

[9] P.-G. Reinhard and H. Flocard, Nuclear effective forces and isotope shifts, Nucl. Phys. **A584**, 1995, 467-488.

[10] Bardeen et al., Theory of Superconductivity, Phys. Rev. **108**, 1957, 1175-1204.

[11] T. Belgya et al., Handbook for Calculations of Nuclear Reaction Data RIPL-2, IAEA TECDOC-1506., 2006.

[12] AMDC-Atomic Mass Data Center -IAEA-NDS https://www-nds.iaea.org/amdc/ (accessed:2021-11-17).

[13] S. G. Nilsson and I. Ragnarsson, SHAPES AND SHELLS IN NUCLEAR STRUCTURE, CAMBRIDGE UNIVERSITY PRESS, 1995.

18. Three fission modes in ^{258}Md studied by Langevin model

Shoma Ishizaki [†1], Yoshihiro Aritomo[1], Mizuki Okubayashi[1], Katsuhisa Nishio[2], and Kentarou Hirose[2]

[1]Faculty of Science and Engineering, Kindai University Higashi-Osaka, Osaka 577-8502, Japan
[2]Advanced Science Research Center, Japan Atomic Energy Agency Tokai, Ibaraki 319-1195, Japan
[†]Email: uthorium232@gmail.com

Abstract

Recently, fission-fragment mass properties of ^{258}Md was measured in JAEA. The data indicates a mixture of fission modes. We tried to calculate the fission properties of ^{258}Md using the Langevin model.

1 Introduction

It has been shown that fission has multiple modes, characterized by mass asymmetric fission and mass symmetric fission [1-7]. In neutron-rich heavy element region, it is argued that several fission modes coexist, with a significant change of their yields in accordance with the number of neutrons contained in the fissionig nucleus. A typical example is found in the fermium isotopes. The dominant mode transition is from the asymmetric splitting for ^{257}Fm to the shape symmetric one for ^{258}Fm [8]. This transitions was interpreted as due to the lowering of the fission barrier for symmetric fission toward heavier mass isotopes. Its important to know the potential energy surface structure and nuclear's deformation process to understand fission mechanism in neutron-rich heavy element region [9].

At the JAEA tandem facility, fission of an exited compound nucleus ^{258}Md was studied in the reaction of ^{4}He+^{254}Es. Based on the systematics of the spontaneous fission [8], the nucleus are located in the region where mass-symmetric fission dominates.

For the discussion of the experimental data, we made a calculation of fission using the Langevin model. For the later discussion, we define three types of fission paths (modes); mass-asymmetric fission (standard mode), symmetric fission with high total kinetic energy TKE (supershort), and symmetric fission with low TKE (superlong).

2 Framwork

We use the fluctuation-dissipation model and employ the Langevin equations[10] to investigate the fission process. The nuclear shape is defined by the two-center parametrization [11,12], which has three deformation parameters, z_0, δ, and α to serve as collective coordinates: z_0 is the distance between two potential centers, α is a mass-asymmetry parameter defined by $(A_1\text{-}A_2)/(A_1+A_2)$ using fragment masses, A_1 and A_2. The symbol δ denotes the deformation of the

fragments defined as $\delta = 3(R_{\parallel}R_{\perp})/(2R_{\parallel}+R_{\perp})$, where $R_{\parallel}$ and $R_{\perp}$ are the half length of the axes of an ellipse in the z_0 and ρ directions of the cylindrical coordinate, respectively, as shown in Figure 1 in Ref. [10].

We adopted the neck parameter ε=0.55 following the empirical relation in Ref. [9]. The three collective coordinates are abbreviated as q, $q = z,\delta,\alpha$. For a given value of a temperature of a system T, the potential energy is defined as a sum of the liquid-drop (LD) part, a rotational energy and a microscopic (SH) part:

$$V(q,l,T) = V_{LD}(q) + \frac{\hbar^2 l(l+1)}{2I(q)} + V_{SH}(q,T), \tag{1}$$

$$V_{LD}(q) = E_s(q) + E_c(q), \tag{2}$$

$$V_{SH}(q,T) = E^0_{shell}(q)\Phi(T), \tag{3}$$

$$\Phi(T) = \exp\left(-\frac{aT^2}{E_d}\right). \tag{4}$$

Here, V_{LD} is the potential energy calculated with the finite-range liquid drop model, given as a sum of the surface energy E_S [12] and the Coulomb energy E_C. V_{SH} is the shell correction energy evaluated by the Strutinski method from the single-particle levels of the two-center shell model. The shell correction has a temperature dependence expressed by a factor Φ(T), in which E_d is the shell damping energy chosen to be 20 MeV [13] and a is the level density parameter. At the zero temperature ($T = 0$), the shell correction energy reduces to that of the two-center shell model values E^0_{shell}. The second term on the right-hand side of Eq. (1) is the rotational energy for an angular momentum l [10], with a moment of inertia at q, $I(q)$.

The multidimensional Langevin equations [10] are given as

$$\frac{dq_i}{dt} = \left(m^{-1}\right)_{ij} p_i, \tag{5}$$

$$\frac{dp_i}{dt} = -\frac{\partial V}{\partial q_i} - \frac{1}{2}\frac{\partial}{\partial q_i}\left(m^{-1}\right)_{jk} p_j p_k - \gamma_{ij}\left(m^{-1}\right)_{jk} p_k + g_{ij}R_j(t), \tag{6}$$

where i =$\{z,\delta,\alpha\}$ and $p_i = m_{ij}dq_j/dt$ is a momentum conjugate to coordinate q_i . The summation is performed over repeated indices. In the Langevin equation, m_{ij} and γ_{ij} are the shape-dependent collective inertia and the friction tensors, respectively. The wall-and-window one-body dissipation [14-16] is adopted for the friction tensor which can describe the pre-scission neutron multiplicities and total kinetic energy of fragments simultaneously [17]. A hydrodynamical inertia tensor is adopted with the Werner-Wheeler approximation for the velocity field [18]. The normalized random force R_i(t) is assumed to be that of white noise, i.e., $R_i(t)$=0 and $R_i(t)R_j(t)$=$2\delta_{ij}\delta(t_1 - t_2)$. The strength of the random force g_{ij} is given by the Einstein relation $\gamma_{ij}T = \sum_k g_{ij}g_{jk}$.

3 Results and discussion

Figure 1 shows the calculated results of the FFMDs and TKE distributions of ^{258}Md. FFMDs show mass symmetric splitting. The peak of the TKE distribution is about 235 MeV. From features, the supershort mode was dominant in the calculation results.

Figure 2 shows the evolution of each fission modes as a function of excitation energy of ^{258}Md (in this work, fission modes was defined in the range of mass numbers and TKE in Table 1). Here, the count as the vertical axis means the number of events in the Langevin calculation. The calculation shows that the standard mode decreases with excitation energy. It is considered

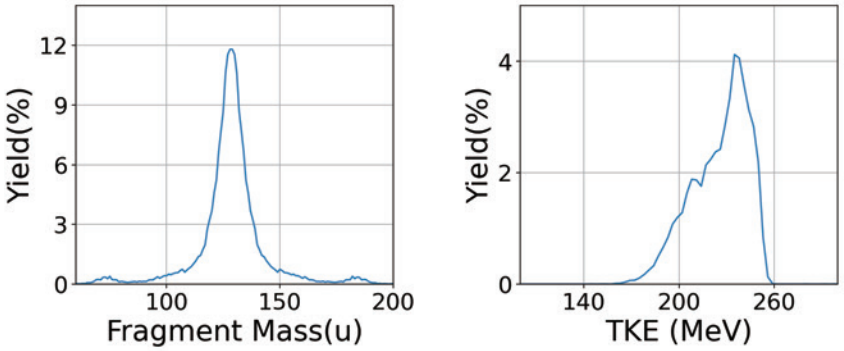

Figure 1: Calculation result of FFMDs(left) and TKE distribution(right) at excitation energy $E^* = 18MeV$

that this is because the shell structure responsible for mass-asymmetry decreases with excitation energy.

Figure 3 shows the fission pathways of each mode in the $z - \delta$ plane. From the 1st local minimum(around $\{z,\delta\}\sim\{0.0,0.2\}$) to the 2nd local minimum(around $\{z,\delta\}\sim\{1.0,0.2\}$), the three modes behave very similarly. But it can be seen that the standard mode branches first at $z \approx 1.3$ and then the superlong mode branches at $z \approx 1.8$.

Figure 4 shows the energy of the fissioning nucleus at each shape plotted as a function of z. In Figure 4, the saddle point is located at $z \approx 1.3$ in the standard mode, $z \approx 1.8$ in the superlong mode, and $z \approx 2.0$ in the supershort mode, so it was found that the branch point shown in Figure 3 is located at the saddle point. In particular, the saddle point of superlong mode is close to that of supershort mode, the trajectory is very similar up to the saddle point of superlong mode.

Table 1: Mass and TKE region of each mode

mode	Mass	TKE
supershort	114≦Mass≦144	TKE>220MeV
superlong	114≦Mass≦144	TKE≦220MeV
standard	114>Mass,144<Mass	TKE≦220MeV

4 Conclusion

In this work, the fission mode of ^{258}Md was studied by trajectory calculation using a Langevin equations. As a result, it was found that the investigated three modes bifurcate around the exit point of the 2nd local minimum on potential energy surface. Also, since the saddle point of superlong mode is close to that of supershort mode, the trajectory is very similar up to the saddle point of superlong mode.

Acknowledgements

The Langevin calculations were performed using the cluster computer system (Kindai-VOSTOK) which is supported by Research funds for External Fund Introduction by Kindai University.

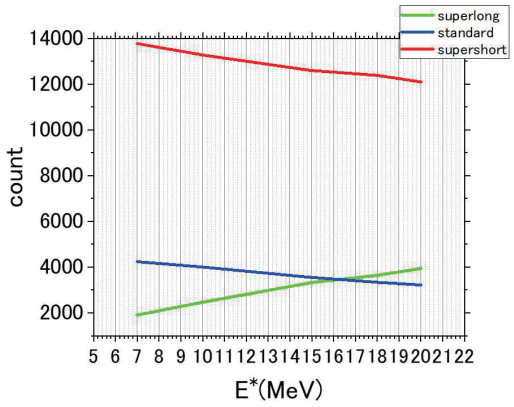

Figure 2: The counts of each mode as a function excitation energy E^*

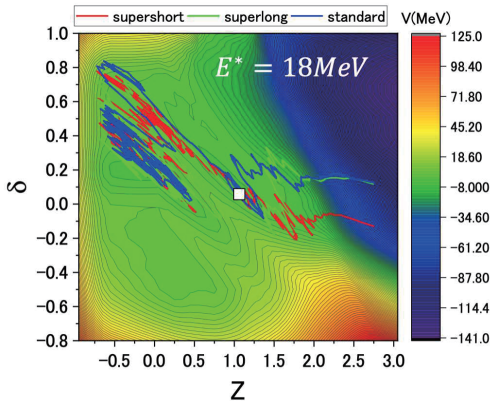

Figure 3: Each mode trajectory in $z - \delta$ plane on $\alpha = 0$ potential energy surface (The white square in the figure indicates the second minimum point)

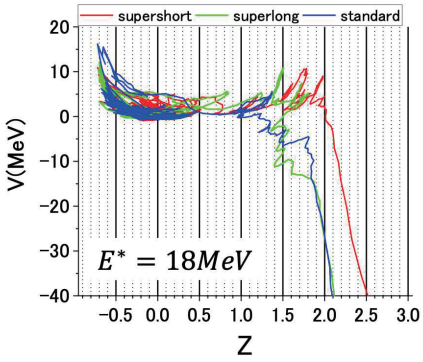

Figure 4: Each mode trajectory in $z - V$ plane

References

[1] E. K. Hulet, J. F. Wild, R. J. Dougan, R. W. Lougheed, J. H. Landrum, A. D. Dougan, et al., Phys. Rev. Lett., 56, 313 (1986).

[2] P. A. Baisden, C. M. Henderson, R. J. Dupzyk, R. L. Hahn, M. Schdel, K. Smmerer, and G. R. Bethune, Phys. Rev. C, 40, 770 (1989).

[3] V. Pokrovsky, L. Calabretta, M. G. Itkis, et al., Phys. Rev. C, 60, 041304

[4] E. K. Hulet, R. W. Lougheed, J. H. Landrum, J. F. Wild, D. C. Hoffman, J. Weber, and J. B. Wilhelmy, Phys. Rev. C, 21, 966 (1980).

[5] J.F. Wild, J. van Aarle, W. Westmeier, R. Lougheed, E.K. Hulet, K.J. Moody, R.J. Dougan, E.-A. Koop, R.E. Glaser, R. Brandt and P. Patzelt, Phys. Rev. C, 41, 640 (1990).

[6] S. Cwiok P. Rozmej, A. Sobiczewski, and Z. Patyk, Nucl. Phys. A, 491, 281 (1989).

[7] U. Brosa, S. Grossmann, and A. Muller, Phys. Rep., 197,167 (1990).

[8] D.C. Hoffman et al., Phys. Rev. C, 21, 637 (1980).

[9] Y. Miyamoto et al., Phys. Rev. C, 99, 051601(R) (2019).

[10] Y. Aritomo and M. Ohta, Nucl. Phys. A, 744, 3 (2004).
[11] K. Sato, A. Iwamoto, K. Harada, S. Yamaji, and S. Yoshida, Z. Phys. A, 288, 383 (1978).
[12] H. J. Krappe, J. R. Nix, and A. J. Sierk, Phys. Rev. C, 20, 992(1979).
[13] A. V. Ignatyuk, G. N. Smirenkin, and A. S. Tishin, Sov. J. Nucl. Phys., 21, 255 (1975).
[14] J. Blocki, Y. Boneh, J. R. Nix, J. Randrup, M. Robel, A. J. Sierk, and W. J. Swiatecki, Ann. Phys., 113, 330 (1978).
[15] J. R. Nix and A. J. Sierk, Nucl. Phys. A, 428, 161c (1984).
[16] H. Feldmeier, Rep. Prog. Phys., 50, 915 (1987).
[17] T.Wada,Y.Abe, and N. Carjen,Phys. Rev. Lett., 70, 3538 (1993).
[18] K. T. R. Davies, A. J. Sierk, and J. R. Nix, Phys. Rev. C 13, 2385 (1976).

19. The origin of correlation between mass and angle in quasi-fission

S. Amano†, Y. Aritomo, S. Ishizaki, M. Okubayashi, and S. Okugawa

Kindai University 3-4-1 Kowakae, Higashi-Osaka, Osaka-hu 577-8502, Japan

†Email: amano_shota@kindai.ac.jp

Mass-angle distribution (MAD) measurement of heavy and superheavy element fragmentation reactions is one of the powerful tools for investigating the mechanism of fission and fusion process. MAD shows a strong correlation between mass and angle when the quasi-fission event is dominant. It has characteristic that appears diagonal correlation as long as the quasi-fission event is dominant. This diagonal correlation could not be reproduced in previous our model before the introduction of the parameters.

In this study, we systematically evaluate the unknown model parameters contained in our model and clarify those model parameters to reproduce the diagonal correlation that appears in MAD. Using a dynamical model based on the fluctuation dissipation theorem that employs Langevin equations, we calculate MADs of two reaction systems ^{48}Ti+^{186}W and ^{34}S+^{232}Th which are dominated by quasi-fission. We were able to clarify the effects of unknown model parameters on the MAD. In addition, we identified the values of model parameters that can reproduce the correlation between mass and angle. As a result, it was found that the balance of tangential friction and moment of inertia values is important for the correlation between mass and angle.

1 Introduction

Currently, superheavy element synthesis is limited to the success of element Z = 118. The production of new superheavy elements will foot in the 8th period of the periodic table, and will provide insight into the existence of island of stability. In addition, neutron-rich nuclei far from the valley of stability are important for understanding the r-process in astronomical nuclear physics. The supernova explosion is one of the origins of the elements along with the evolution of the stars. During a supernova explosion, a large amount of new elements are created and spread around. After those elements create the new star, the new star eventually die, leading to an explosion again. The elements in the universe and the solar system is created through such an evolution cycle of stars and elements. Superheavy elements and neutron-rich nuclei create in the process of that element synthesis scenario. Production of those nuclei are significant to elucidate element synthesis scenario but, extremely difficult. In recent years, the method using the nucleon transfer reaction for the synthesis of new superheavy elements and neutron-rich nuclei has been proposed [1, 2], but a quantitative prediction model has not been established. The mechanism of the nucleon transfer reaction has been studied for many years in many models, including semiclassical models such as GRAZING [3] and Langevin [1], and microscopic models such as time-depent Hartree-Fock (TDHF) [4]. In this study, we analyze the relationship between mass and angle obtained by the nucleon transfer reaction. Mass-angle

distribution (MAD) is the emission angle on the vertical axis and the mass ratio M_R on the horizontal axis. M_R is represented by $M_R = \frac{A_{i=1,2}}{A_1+A_2}$. A_1 and A_2 represent the mass number of the projectile-like fragment and the target-like fragment, respectively. When the projectile nucleus collides with the target nucleus, the projectile nucleus receives nucleons from the target nucleus while rubbing around the target nucleus, increases the mass number, and finally leaves from the target nucleus in a certain direction. There is a correlation between the number of nucleon transferred (mass) and the emission angle, and the characteristic is depends on the projectile nucleus and the target nucleus. By analyzing this correlation, we are trying to elucidate the fusion process. MAD shows a strong correlation between mass and angle when the quasi-fission reaction is dominant [5]. This correlation could not be reproduced with the dynamical model developed in the previous research. In this study, we evaluated MADs of the two reaction systems ^{48}Ti + ^{186}W and ^{34}S + ^{232}Th dominated quasi-fission using a dynamical model. This paper contain as follows Sec. 2 describes the details of the model framework. Sec. 3 discusses the parameter dependence of MAD. The last section describes conclusion.

2 Framework

2.1 Potential energy surface

We adopt the dynamical model which similar to unified model [7]. First, the initial stage of the nucleon transfer reactions consists of two parts: (1) the system is placed in the ground state of the projectile and target because the reaction proceeds is too fast for nucleons to reconfigure a single particle state (2) The part where the system relaxes to the ground state of the entire composite system which changes the potential energy surface to an adiabatic one. Therefore, we consider the time evolution of potential energy from the diabatic one $V_{diab}(q)$ to adiabatic one $V_{adiab}(q)$. Here, q denotes a set of collective coordinates representing nuclear deformation. The diabatic potential is calculated by a folding procedure using effective nucleon-nucleon interaction [6–8]. However, the adiabatic potential energy of the system is calculated using an extended two-center shell model [8]. Then, we connect the diabatic and the adiabatic potentials with a time-dependent weighting function as follows:

$$\begin{aligned} V &= V_{diab}(q) f(t) + V_{adiab}(q) [1 - f(t)], \\ f(t) &= \exp\left(-\frac{t}{\tau}\right). \end{aligned} \tag{1}$$

Where t is the interaction time and $f(t)$ is the weighting function included the relaxation time τ. We use the relaxation time $\tau = 10^{-21}s$ proposed in [9–11]. We use the two-center parameterization [12,13] as coordinates to represent nuclear deformation. To solve the dynamical equation numerically and avoid the huge computation time, we strictly limited the number of degrees of freedom and employ three parameters as follows: z_0 (distance between the centers of two potentials), δ (deformation of fragment), and α (mass asymmetry of colliding nuclei); $\alpha = \frac{(A_1-A_2)}{(A_1+A_2)}$, where A_1 and A_2 not only stand for the mass numbers of the target and projectile, respectively [6,14] but also are then used to indicate mass numbers of the two fission fragments. As shown in Fig. 1 in Ref. [12], the parameter δ is defined as $\delta = \frac{3(a-b)}{(2a+b)}$, where a and b represent the half length of the ellipse axes in the z_0 and ρ directions, respectively. We assume that each fragment has the same deformation as a first step. In addition, we use scaling to save computation time and use the coordinate z defined as $z = \frac{z_0}{(R_{CN}B)}$, where R_{CN} denotes the radius of the spherical compound nucleus and the parameter B is defined as $B = \frac{(3+\delta)}{(3-2\delta)}$.

2.2 Dynamical equations

We perform trajectory calculations of the time-dependent unified potential energy [6, 7, 14] by Langevin equation. We start trajectory calculations from a sufficiently long distance between both nuclei [14]. So, we use the model which takes into account the nucleon transfer for slightly separated nuclei [6]. Process for the separated nucleon transfer use the procedure described in Refs. [6, 7]. When both nuclei has been changed the mononucleus state that window of the contact nuclei is sufficiently opened, the evolution process of the mass asymmetry parameter α switches from the master equation to Langevin equation according to the procedure described in Ref. [14]. We use the multidimensional Langevin equation [6, 14, 15] unified following:

$$\begin{aligned}
\frac{dq_i}{dt} &= \left(m^{-1}\right)_{ij} p_j, \\
\frac{dp_i}{dt} &= -\frac{\partial V}{\partial q_i} - \frac{1}{2}\frac{\partial}{\partial q_i}\left(m^{-1}\right)_{jk} p_j p_k \gamma \ -_{ij} \left(m^{-1}\right)_{jk} p_k + g_{ij} R_j\left(t\right), \\
\frac{d\theta}{dt} &= \frac{\ell}{\mu_R R^2}, \\
\frac{d\varphi_1}{dt} &= \frac{L_1}{\Im_1}, \\
\frac{d\varphi_2}{dt} &= \frac{L_2}{\Im_2}, \\
\frac{d\ell}{dt} &= -\frac{\partial V}{\partial \theta} - \gamma_{tan}\left(\frac{\ell}{\mu_R R^2} - \frac{L_1}{\Im_1}a_1 - \frac{L_2}{\Im_2}a_2\right) R + R g_{tan} R_{tan}\left(t\right), \\
\frac{dL_1}{dt} &= -\frac{\partial V}{\partial \varphi_1} - \gamma_{tan}\left(\frac{\ell}{\mu_R R^2} - \frac{L_1}{\Im_1}a_1 - \frac{L_2}{\Im_2}a_2\right) a_1 - a_1 g_{tan} R_{tan}\left(t\right), \\
\frac{dL_2}{dt} &= -\frac{\partial V}{\partial \varphi_2} + \gamma_{tan}\left(\frac{\ell}{\mu_R R^2} - \frac{L_1}{\Im_1}a_1 - \frac{L_2}{\Im_2}a_2\right) a_2 - a_2 g_{tan} R_{tan}\left(t\right).
\end{aligned} \tag{2}$$

The collective coordinates q_i represent z, δ, and α, the symbol p_i denotes momentum conjugated to q_i, and V is the multidimensional potential energy. : The symbols θ and ℓ indicates the relative orientation of nuclei and relative angular momentum respectively. φ_1 and φ_2 stand for the rotation angles of the nuclei in the reaction plane (their moment of inertia and angular momenta are $\Im_{1,2}$ and $L_{1,2}$, respectively), $a_{1,2} = \frac{R}{2} \pm \frac{(R_1 - R_2)}{2}$ is the distance from the center of the fragment to the middle point between the nuclear surfaces, and $R_{1,2}$ is the nuclear radii. The symbol R is distance between the nuclear centers. The total angular momentum $L = \ell + L_1 + L_2$ is preserved. The symbol μ_R is reduced mass, and γ_{tan} is the tangential friction force of the colliding nuclei. Here, it is called sliding friction. The phenomenological nuclear friction forces for separated nuclei are expressed in terms of γ^F_{tan} for sliding friction using the Woods-Saxon radial form factor described in Refs. [6, 7]. The sliding friction are described as $\gamma_{tan} = \gamma^0_t F\left(\zeta\right)$, where the radial form factor $F\left(\zeta\right) = \left(1 + \exp^{\zeta}\right)^{-1}, \zeta = \frac{(\xi - \rho_F)}{a_F}$. γ^0_t denote the strength of the tangential friction, respectively. $\rho_F \sim 2$ fm and $a_F \sim 0.6$ fm are the model parameters, and ξ is the distance between the nuclear surfaces $\xi = R - R_{contact}$, where $R_{contact} = R_1 + R_2$ [6]. The symbols separated by m_{ij} and γ_{ij} stand for the shape-dependent collective inertia and friction tensors elements, respectively. We adoped the hydrodynamic inertia tensor m_{ij} in Werner-Wheeler approximation for the velocity field [24]. The normalized random force $R_i\left(t\right)$ is assumed to be white noise: $\langle R_i(t)\rangle$=0 and $\langle R_i(t_1) R_j(t_2)\rangle = 2\delta_{ij}\delta(t_1 - t2)$. According to Einstein relation, the strength of the random force g_{ij} is given $\gamma_{ij} T = \sum_k g_{ij} g_{jk}$, where T is the temperature of the compound nucleus calculated from the intrinstic energy of the composite system. The adiabatic potential energy is defined as

$$\begin{aligned}
V_{\text{adiab}}\left(q, L, T\right) &= V_{LD}\left(q\right) + \frac{\hbar^2 L(L+1)}{2\mathcal{I}(q)} + V_{SH}\left(q, T\right), \\
V_{LD}\left(q\right) &= E_S\left(q\right) + E_C\left(q\right), \\
V_{SH}\left(q, T\right) &= E^0_{shell}\left(q\right)\Phi\left(T\right), \\
\Phi\left(T\right) &= \exp\left(-E^* E_d\right).
\end{aligned} \tag{3}$$

Here, $\mathcal{I}(q)$ represents the moment of inertia of the rigid body with deformation q. The centrifugal energy generated from the angular momentum L of the rigid body is also taken into account. V_{LD} and V_{SH} are the potential energy of the finite range liquid drop model and the shell correction energy that takes into account temperature dependence, respectively. The symbol E^0_{shell} indicates the shell correction energy at T=0. The temperature dependence factor $\Phi(T)$ is explained in Ref. [14], where E^* indicates the excitation energy of the compound nucleus. E^* is given $E^* = aT^2$, where a is the level density parameter. The shell damping energy E_d is selected as 20 MeV. This value is given by Ignatyuk et al. [25]. The symbols E_S and E_C stand for generalized surface energy [26] and Coulomb energy, respectively.

In this study, the calculation MADs was performed by changing two parameters (γ^0_t and f_{ina}). γ^0_t is the tangential friction correction factor, f_{ina} is shown the correction factor in the form of $\frac{\hbar^2 L(L+1)}{2\mathcal{I}(q) f_{ina}}$. $\mathcal{I}(q)$ represents the moment of inertia of a rigid body.

3 Results

Figure 1 shows the calculation MADs for ^{48}Ti+^{186}W at E$_{\mathrm{c.m.}}$=187.87MeV and their dependence on f_{ina} and γ^0_t parameters in the range of f_{ina} =1.5-5.0 and γ^0_t=0.5-10.

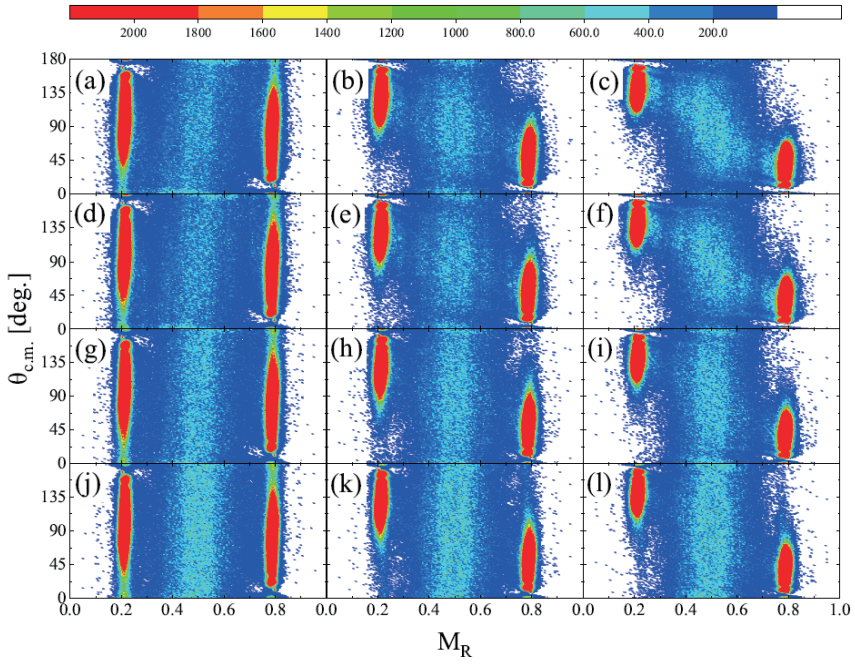

Figure 1: The calculation MADs for ^{48}Ti+^{186}W at E$_{\mathrm{c.m.}}$=187.87MeV and their dependence on f_{ina} and γ^0_t parameters in the range of f_{ina} =1.5-5.0 and γ^0_t=0.5-10. The result of (a)(d)(g)(j), (b)(e)(h)(k) and (c)(f)(i)(l) adopt f_{ina} =1.5, and f_{ina} =3.0 and f_{ina} =5.0, respectively. (a)-(c), (d)-(f), (g)-(i) and (j)-(l) adopt γ^0_t=0.5, γ^0_t=1.0, γ^0_t=5.0 and γ^0_t=10, respectively.

For example, in Fig. 1(k), there is no correlation in MAD, which means that the emitted nuclei are emitted in all directions of 360 degrees, which is characteristic of the dominant fusion-fission process. Moreover, it is considered that the situation of quasi-fission process is reproduce because Fig. 1(a) has a correlation between angle and mass. Fig. 1(a) and 1(d) can reproduce the characteristics of the experimental values [5] well. When f_{ina} was large, the two bodies after contact tended to be difficult to move. It was found that when γ^0_t is large, the correlation

between mass and angle is lost. It is considered that this is because the emission angle overs 2 and is fragments are emitted in all directions due to the dominant fusion-fission reaction.

Next, Figure 2 shows the calculation results of ^{34}S+^{232}Th MAD at E$_{c.m.}$=168.75MeV when γ_t^0 and f_{ina} are changed. For instance, in Fig. 2(j), there is no correlation between mass and angle to dominate fusion-fission. On the other hand, since Fig. 2(l) has a correlation between angle and mass, it is considered that we reproduce the situation of quasi-fission process. Fig. 2(i) and 2(l) can reproduce the characteristics of the experimental values [5] well. The influence for MAD does not change even if the moment of inertia for rigid body and the tangential friction change respectively. But, the correlation originated from quasi-fission between mass and angle show when both γ_t^0 and f_{ina} are large. This is unlike ^{48}Ti+^{186}W case.

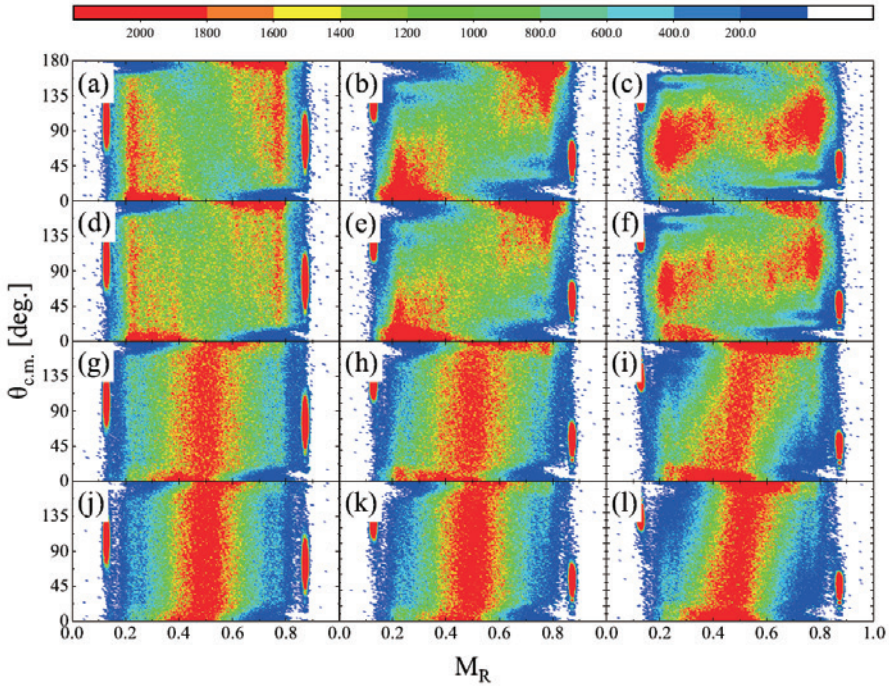

Figure 2: The calculation MADs for ^{34}S+^{232}Th at E$_{c.m.}$=168.75MeV and their dependence on f_{ina} and γ_t^0 parameters in the range of f_{ina} =1.5-5.0 and γ_t^0=0.5-10. The result of (a)(d)(g)(j), (b)(e)(h)(k) and (c)(f)(i)(l) adopt f_{ina} =1.5, and f_{ina} =3.0 and f_{ina} =5.0, respectively. (a)-(c), (d)-(f), (g)-(i) and (j)-(l) adopt γ_t^0=0.5, γ_t^0=1.0, γ_t^0=5.0 and γ_t^0=10, respectively.

In this study, it was found that the tangential friction and the moment of inertia for rigid body that can reproduce the correlation between mass and angle depends on the reaction system. In the reaction system with a small mass asymmetry of the incident system such as ^{48}Ti+^{186}W, the calculation result could reproduce the correlation originated quasi-fission like the experimental values by the small value of the tangential friction and the moment of inertia for the rigid body. On the other hand, the calculation result could reproduce the characteristic originate from quasi-fission when the value of the tangential friction and the moment of inertia for the rigid body large in the reaction system that the initial mass asymmetry is large such as ^{34}S+^{232}Th. From these results, it is considered that the value of the tangential friction and the moment of inertia for reproducing the experimental value depend on the initial mass asymmetry.

4 Conclusion

It was found that the tangential friction and the moment of inertia for the rigid body are strongly relate to the correlation which originates from quasi-fission in the heavy element region. It was also found that the balance of these physical quantities shows the characteristic whether quasi-fission is dominant or fusion-fission reaction is dominant. It was possible to reproduce the characteristics of the experimental results which quasi-fission is dominant by changing the unknown model parameters. We need to calculate systematically to specify what unkown model parameters depend on. Furthermore, it is necessary to find the correlation between the values of these unknown model parameters and other physical quantities to reduce unknown parameters. In the future, we will investigate the dependence of tangential friction and the moment of inertia for the rigid body on mass asymmetry.

References

[1] A.V. Karpov and V.V. Saiko, Phys. Rev. C **96**, 024618 (2017).
[2] V.I. Zagrebaev, et al., Phys. Rev. C **73**, 122701 (2008).
[3] A. Winther, Phys. A **572**, 191 (1994).
[4] S. Ayik, et al., Phys. Rev. C **96**, 024611 (2017).
[5] R.du Riez, et al., Phys. Rev. C **88**, 054618 (2013).
[6] V. Zagrebaev and W. Greiner, J. Phys. G **31**, 7, 825 (2005).
[7] V. Zagrebaev and W. Greiner, J. Phys. G **34**, 11, 2265 (2007).
[8] V.I. Zagrebaev, et al., Phys. Part. Nuclei **38**, 469 (2007).
[9] G.F. Bertsch, Z. Phys. A **289**, 103 (1978).
[10] W. Cassing and W. Nörenberg, Nucl. Phys. A **401**, 467 (1983).
[11] A. Diaz-Torres, Phys. Rev. C **69**, 021603 (2004).
[12] J. Maruhn and W. Greiner, Z. Phys **251**, 431 (1972).
[13] K. Sato, A. Iwamoto, K. Harada, S. Yamaji and S. Yoshida, Z. Phys. A **288**, 383 (1978).
[14] Y. Aritomo and M. Ohta, Nucl. Phys. A **744**, 4 (2004)
[15] Y. Aritomo, Phys. Rev. C **80**, 064604 (2009)
[16] J. Blocki, et al., Ann. Phys **113**, 330 (1978).
[17] J.R. Nix and A.J. Sierk, Nucl. Phys. A **428**, 161c (1984).
[18] J. Randrup and W.J. Swiatecki, Nucl. Phys. A **429**, 105 (1984).
[19] H. Feldmeier, Rep. Prog. Phys **50**, 915 (1987).
[20] N. Carjan, A.J. Sierk, and J.R. Nix, Nucl. Phys. A **452**, 381 (1986).
[21] M. Carjan, et al., AIP Conference Proceeding No.250 (AIP, New York, 1992).
[22] T. Wada, Y. Abe and N. Carjan, Phys. Rev. Lett **70**, 3538 (1993).
[23] T. Asano, T. Wada, M. Ohta, S. Yamaji and H. Nakahara, J. Nucl. Radio Sci **7**, 7 (2006).
[24] K.T.R Davies, A.J. Sierk and J.R. Nix, Phys. Rev. C **13**, 2385 (1976).
[25] A.N. Ignatyuk, G.N. Smirenkin and A.S. Tishin, Sov. J. Nucl. Phys **21**, 255 (1975).
[26] H.J. Krappe, J.R. Nix and A.J. Sierk, Phys. Rev. C **20**, 992 (1979).

Acknowledgments

The Langevin calculation were perfomed using the cluster computer system (Kindai-VOSTOK) which is supported by JSPS KAKENHI Grant Number 20K04003.

20. Neutron emission during fission process by dynamical model

R.Yamasaki[1], S.Tanaka[1,3], Y.Aritomo[1,2], K.Nishio[3]
[1]Graduate School of Science and Engineering, Kindai University
[2]Faculty of Science and Engineering, Kindai University
Higashi-Osaka, Osaka 577-8502, Japan
[3]Advanced Science Research Center, Japan Atomic Energy Agency
Tokai, Ibaraki 319-1195, Japan
e-mail: ryoutayamasaki.dia0101@gmail.com

Through joint research by the Japan Atomic Energy Agency and Kindai University, it has revealed that the yield distribution of fission products (fission fragments) changes significantly depending on the neutrons emitted from the compound nucleus. This multichance fission (MCF) effect is particularly important to treat high energy fissions, such as transmutation of long lived minor actinide nucleus by fission using ADS. In this work, we have introduced the neutron evaporation during fission process in the Langevin model and aimed to describe the entire reaction process in a unified manner. The calculated results also reproduced experimental data of the fission-fragment mass distribution.

1. Introduction and Background

Since Japan's energy self-sufficiency rate is as low as 8%, energy diversification is being promoted at each electric power company, and it is expected that the nuclear power generation will continue to play a part of power sources. Long lived minor actinides accumulated in a reactor, is one of the important issues in the nuclear power generation. Therefore, a method of transmuting the long lived minor actinides to short lived minor actinides using Accelerator-driven System (ADS) is considered as a feasible option. ADS applies a proton beam generated by a proton accelerator to a spallation target such as lead and bismuth to generate spallation neutrons. This spallation neutron is used to transmute the long lived minor actinides by fission from highly excited states. From these things, it is important to understand fission from highly excited states.

From the above, through joint research by the Japan Atomic Energy Agency (JAEA) and Kindai University, it has become clear that fission fragment mass distributions (FFMDs) change significantly depending on the neutrons emitted from the compound nucleus. In the so-called multichance fission (MCF) concept, fission takes place after emitting several neutrons. Because

the emitted neutrons bring out excitation energy corresponding to neutron binding energy and its kinetic energy, this revives the shell structure of a nucleus responsible for mass-asymmetric fission, thus change the FFMDs. The effect of MCF is particularly important to treat high energy fissions, such as fission process in ADS. Until now, the MCF calculation was performed by combining a fission model calculation (Langevin equation) and a statistical model using a code such as GEF [1,2]. However, this method does not introduce neutron emission during the fission process.

In the conventional method using the GEF code, only neutron emission from the compound nucleus was considered as shown in Fig. 1. Therefore, in this work, we have introduced the neutron evaporation during fission process in the Langevin model as shown in Fig. 2. For this, a change of the potential energy in each neutron evaporation step is treated.

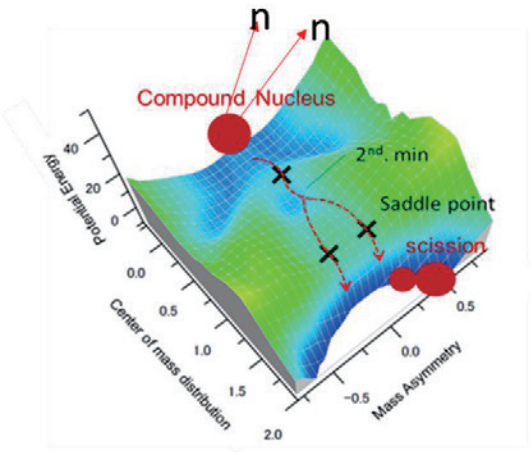

Figure 1 It is a diagram that considers only neutron emission from the compound nucleus, and is a diagram in which a fission path is projected on the potential energy surface. The saddle points are marked by the symbol “+”.

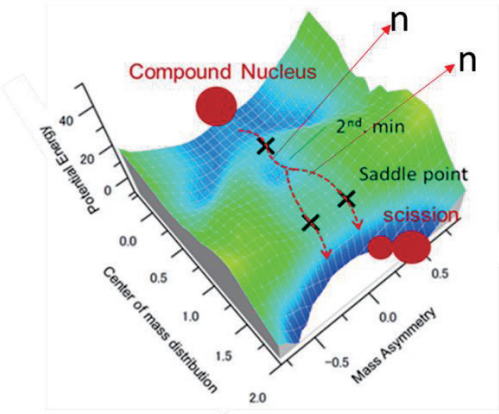

Figure 2 It is a diagram that considers neutron emission in all the processes of fission, and is a diagram in which a fission path is projected on the potential energy surface. The saddle points are marked by the symbol “+”.

2. Theory and Method

A simple neutron decay width Γ_n based on detailed balance is adopted, and the Gilbert and Cameron equation is used for the level density ρ [3-5]. The Γ_n and ρ are given as

$$\Gamma_n^J = \frac{1}{2\pi\rho(E_{CN}^*,J)}\int_0^{E_f}\sum_{l'}\sum_{s'}T_l(\varepsilon)\rho\big(E_f-\varepsilon,I'\big)d\varepsilon \tag{1}$$

$$\rho(U^*,J) = \frac{\sqrt{\pi}}{12a^{1/4}U^{*5/4}}\exp\big(2\sqrt{aU^*}\big)\times\frac{2J+1}{2\sqrt{2\pi}\sigma^3}exp\left[-\frac{(J+1/2)^2}{2\sigma^2}\right] \tag{2}$$

where E_{CN}^* and U^* are the excitation energy of the compound nucleus and the effective excitation energy of the compound nucleus, respectively. The effective excitation energy of the intermediate nucleus E_f can be expressed by $E_f = E_{CN}^* - B_n - E_k$ (B_n: neutron binding energy, E_k: emitted neutron kinetic energy). σ is the spin cut-off parameter. The level density parameter *a* is given as

$$a = a_0\left\{1+\frac{E_{shell}}{E^*}\big(1-e^{-rE^*}\big)\right\},\ \ r = r_0A^{-1/3} \tag{3}$$

where E_{shell} is the shell correction energy at temperature of the compound nucleus *T=0*. In the Langevin model adopted in this study, random number determines the ratio of the Langevin's time step to the neutron decay width.

In this work, the three-dimensional two-center parametrization was adopted to describe nuclear shape. *z* is the distance between two potential centers, δ is the deformation of the fragment, α is the mass asymmetry of the two fragments. The advantage of this model is that it can represent both the fusion and the fission with a relatively small number of parameters. The two-center parametrization is described using two harmonic oscillators. z_1 and z_2 are the distances from the origin of contact of the harmonic oscillator to the center of each harmonic oscillator. The z_0, δ and α are given as

$$z_0 = |z_1| + |z_2| \tag{4}$$

$$\delta = \frac{3(a-b)}{2a-b} \tag{5}$$

$$\alpha = \frac{A_1-A_2}{A_1+A_2} \tag{6}$$

where A_1 and A_2 is the mass numbers of heavy and light fragments, and *a* and *b* are the half length of the axes of an ellipse in the z_0 and ρ directions of the cylindrical coordinate, respectively. In order to shorten the calculation time of the computer when solving the equation of motion, we introduce *z* as

$$z = \frac{z_0}{R_{CN}B}\quad ,\ B = (3+\delta)/(3-2\delta) \tag{7}$$

where R_{CN} is the radius of the compound nucleus.

In the two-center parametrization, the size of the connecting cross section (neck size) of each fragment is described by the neck parameter ε. The ε is givens as

$$\varepsilon(A_c) = 0.01007A_c - 1.94 \tag{8}$$

where A_c is the mass number of the compound nucleus [6].

In the fission process, the nuclear potential is described by the adiabatic potential $V_{adiab}(q)$. In this case, density of a nucleus is constant. The adiabatic potential is described by the sum of the potential of the liquid drop model and the shell correction energy as

$$V_{adiab}(q, L, T) = V_{LD}(q) + \frac{\hbar^2 L(L+1)}{2I(q)} + V_{SH}(q, T) \tag{9}$$

$$V_{LD}(q) = E_S(q) + E_C(q) \tag{10}$$

$$V_{SH}(q, T) = E_{shell}(q)\Phi(T) \tag{11}$$

$$\Phi(\mathrm{T}) = \exp\left(-\frac{aT^2}{E_d}\right) \tag{12}$$

where *I(q)* is the inertial mass from a rigid body, and V_{LD} is the potential of the liquid drop model. The excitation energy can be expressed by $E^* = aT^2$(a: level density parameter). V_{SH} is shell correction energy considering temperature dependence. The shell damping energy E_d of 20 MeV was used in this work. E_S and E_C are the surface and coulomb energy, respectively. At the high energy, the shell correction energy becomes extremely small, and the internal structure of the nucleus disappears, resulting in mass symmetric fission.

In this work, the time evolution nuclear shape is described by the Langevin equation. The Langevin equation is given as

$$\frac{dq_i}{dt} = (m^{-1})_{ij}p_j \tag{13}$$

$$\frac{dp_i}{dt} = -\frac{\partial V}{\partial q_i} - \frac{1}{2}\frac{\partial}{\partial q_i}(m^{-1})_{ik}p_j p_k - \gamma_{ij}(m^{-1})_{jk}p_k + g_{ij}R_j(t) \tag{14}$$

where $q_i = \{z, \delta, \alpha\}$ and p_i is the conjugate momentum of q_i. m_{ij} and γ_{ij} are the inertial mass and the friction coefficient that depend on the shape of the nucleus, respectively, R is a normalized random variable according to the Gaussian distribution, and g_{ij} is the dimension of the random force.

3. Result and Discussion

In this work, FFMDs of $^{236\text{-}238}$U, $^{238\text{-}240}$Np, and $^{240\text{-}242}$Pu are calculated in the initial excitation energy range of E^*=15-55 MeV. Fig. 3 shows a comparison between the calculated results and the experimental data measured at JAEA's tandem accelerator [7-9]. From Fig. 3, the calculation results when neutron emission was taken into consideration in the fission process showed that the mass asymmetric shape of FFMDs was maintained even at high excitation energies. The

calculation results can reproduce the experimental data well.

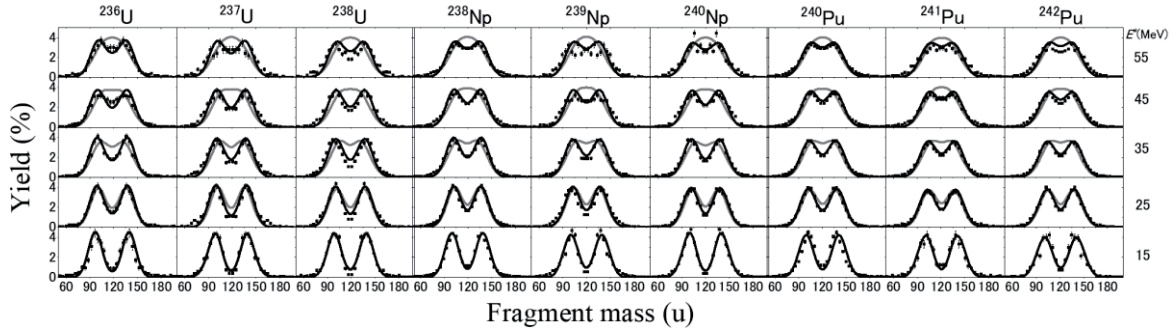

Figure 3 Calculation results of FFMDs without (gray curves) and with (black curves) neutron emission in the fission of $^{236\text{-}238}$U, $^{238\text{-}240}$Np, and $^{240\text{-}242}$Pu. Dependence on the excitation energy of the initial compound nucleus (E^*=15-55 MeV, see right hand side of the figure) is shown. The calculation FFMDs are compared with the experimental data (points with error bars) [7-9].

The average number of neutron emissions of $^{236\text{-}238}$U, $^{238\text{-}240}$Np, and $^{240\text{-}242}$Pu was calculated, and the results are compared to the calculated neutron-emission before fission in the GEF code [1,2]. Looking at the results in Table 1-3, our calculation agrees well with the GEF calculation at high excitation energies. In addition, our calculation does not show any isotope dependence, in contrast to the GEF code, which exhibit a increasing trend of the neutron emission number with the mass of isotope. In addition, at low excitation energies, the average number of neutron emissions calculated by the present Langevin calculation is larger than the GEF result. In the conventional method, only the emission of the excitation energy of 15 MeV from the compound nucleus shape was considered. In the model of this work, the initial value of excitation energy of 15 MeV changes from moment to moment, which may cause a difference. We need to investigate this difference in detail in the future.

Table 1 Average number of neutron emissions of $^{236\text{-}238}$U [1,2]

E^*	^{236}U		^{237}U		^{238}U	
	Present (during fission)	GEF code (before fission)	Present (during fission)	GEF code (before fission)	Present (during fission)	GEF code (before fission)
15MeV	0.01	0.26	0.02	0.41	0.03	0.26
25MeV	0.54	0.92	0.60	1.14	0.71	0.99
35MeV	1.34	1.61	1.41	1.85	1.43	1.97
45MeV	2.10	2.21	2.13	2.49	2.10	2.61
55MeV	2.45	2.75	2.60	3.06	2.53	3.25

Table 2 Average number of neutron emissions of $^{238\text{-}240}$Np [1,2]

E^*	^{238}Np		^{239}Np		^{240}Np	
	Present (during fission)	GEF code (before fission)	Present (during fission)	GEF code (before fission)	Present (during fission)	GEF code (before fission)
15MeV	0.00	0.29	0.03	0.14	0.03	0.25
25MeV	0.54	0.83	0.66	0.78	0.66	0.94
35MeV	1.36	1.42	1.40	1.51	1.44	1.62
45MeV	1.98	1.97	2.06	2.10	1.99	2.30
55MeV	2.52	2.48	2.52	2.66	2.48	2.90

Table 3 Average number of neutron emissions of $^{240\text{-}242}$Pu [1,2]

E^*	^{240}Pu		^{241}Pu		^{242}Pu	
	Present (during fission)	GEF code (before fission)	Present (during fission)	GEF code (before fission)	Present (during fission)	GEF code (before fission)
15MeV	0.01	0.12	0.01	0.22	0.01	0.14
25MeV	0.48	0.61	0.54	0.75	0.59	0.73
35MeV	1.12	1.19	1.22	1.37	1.32	1.43
45MeV	1.77	1.74	1.79	1.96	1.90	2.06
55MeV	2.25	2.26	2.27	2.51	2.37	2.65

4. Summary and Perspectives

We performed the fission calculation including neutron emission during fission process. The calculated results reproduce well the experimental data of FFMDs. It was shown that the method of this work can evaluate neutron emission during fission process. However, the change in the number of neutron emission due to the mass number of the compound nucleus could not be confirmed. We plan to improve the model. We will investigate the shape of the compound nucleus when neutrons are emitted. Also we plan to calculate the fission probability as a function of excitation energy to see if the step-like structure of the reaction cross-section appears at the energy that multi-chance fission emerges.

References

[1] S. Tanaka, Y. Aritomo, Y. Miyamoto, *et al*., Phys. Rev. C **100**, 064605 (2019).
[2] K.-H. Schmidt, B. Jurado, C. Amouroux, and C. Schmitt, Nucl. Data Sheets **131**, 107 (2016).
[3] A. Gilbert and A.G.W. Cameron, Can.J.Phys. **43**, 269 (1965).
[4] V. Weisskopf, Phys. Rev. **52**, 295 (1937).
[5] N. Bohr and J.A. Wheeler, Phys. Rev. **56**, 426 (1939).
[6] Y. Miyamoto, Y. Aritomo, S. Tanaka, *et al*., Phys. Rev. C **99**, 051601 (2019).
[7] R. Leguillon, K. Nishio, K. Hirose, *et al*., Phys. Lett. B **761**, 125 (2016).
[8] K. Hirose, K. Nishio, S. Tanaka, *et al*., Phys. Rev. Lett. **119**, 222501 (2017).
[9] M. Vermeulen, K. Nishio, K. Hirose, *et al*., Phys. Rev. C **102**, 054610 (2020).

21. Fission fragment distributions of neutron-rich nuclei based on Langevin calculations: r-process nucleosynthesis simulations

Mizuki OKUBAYASHI*[1], Shoya TANAKA[1,2], Yoshihiro ARITOMO[1], Shoma ISHIZAKI[1], Shota AMANO[1], and Nobuya NISHIMURA†[3,4]

[1]Graduate School of Science and Engineering Research, Kindai University, Higashi-Osaka 577-8502, Japan
[2]Advanced Science Research Center, JAEA, Tokai 319-1195, Japan
[3]Astrophysical Big Bang Laboratory, CPR, RIKEN, Wako 351-0198, Japan [4]Division of Science, NAOJ, Mitaka, Tokyo 181-8588 Japan
*Email: m.okubayashi39@gmail.com
†Email: nobuya.nishimura@riken.jp

Abstract

The nuclear fission of very neuron-rich nuclei related the r-process are important for the termination of nucleosynthesis flows on the nuclear chart and the formation of final abundances. Nevertheless, most of available fission data for the r-process calculations are based on the theory predictions, including phenomenological treatments. In this study, we calculated a series of nuclear fission distribution for neutron-rich nuclei away from the β-stability line. As most of these nuclei are experimentally unknown, we are based on theory calculations based on the dynamical fission model with the Langevin method. We performed fission distribution calculations for neutron-rich actinoid nuclei, which are important in the r-process. In the present paper, we compared the obtained mass and charge distributions with experimental data. We also show the results of the systematic behaviour of mass distribution for neutron-rich U and Fm isotopes.

1 Introduction

Nucleosynthesis by the rapid-neutron-capture process, *r-process*, represents for cosmic origin of the heaviest elements (e.g., gold and uranium) beyond the iron-group peak. Although several astrophysical scenarios have been proposed, the mechanism of the r-process is not completely understood (for a recent review, see [1, 2, 3]). One of main reasons is a large uncertainty in the nuclear-physics properties of very neutron-rich nuclei, e.g., neutron captures rates and several decay half-lives. To determine nucleosynthesis flows on the r-process "path", the β-decay and the neutron capture (strongly depending on theoretical mass prediction) are significant. The nuclear fission is a key ingredient of the termination of and the final abundance distribution if r-processing is strong enough to reach actinoids.

Nuclear fission, therefore, plays an essential role under certain r-process conditions [4, 5, 6, 7], in particular, in very neutron-rich environments, e.g., neutron star mergers. The nucleosynthesis path goes into the very neutron-rich trans-uranium region. The effects of fission are significant to shape the r-process abundances due to fission recycling, of which fission products become seed nuclei ($A < 200$) for the next r-processing during a single nucleosynthesis process. Besides

the abundance prediction, fission is also a key role as the heating source of kilonovae at late times ($\sim$ 10 days to months) [8, 9], electromagnetic transients of neutron star mergers. A sign of fission heating may have been observed in the light curve of the kilonova associated with the gravitational wave, GW170817. The precise understanding of fission becomes much crucial in the era of gravitational astronomy.

In this study, we calculate the fission-fragment mass distributions of very neutron-rich nuclei. Fission product distributions are important for the r-process, but experimental data are not available. We adopt the Langevin method [10, 11], widely adopted in the study of low-energy fission. We found that the calculated fission mass distributions for uranium, of which the charge (Z) distribution is obtained by the UCD (unchanged charge distribution assumption), can well reproduce experimental data in JENDL (^{232}U to ^{232}U). We also found that the fission fragment distribution changes from the two peak feature (asymmetric fission) to the one-peak (symmetric fission) with increasing the neutron number.

The present paper is structured as follows. In Section 2, we briefly describe the basics of the Langevin calculations and the UCD assumption. The results of the mass and charge distribution are shown in Section 3. Section 4 is dedicated to the conclusion.

2 Method

2.1 Dynamical fission calculations by the Langevin method

We calculate fission fragment distributions (FFD) following fission dynamics by solving the Langevin equations, based on the fluctuation-dissipation model [11, 10]. In the fission calculations, deformation and fission processes are represented by the "motion" of trajectories on the multi-dimensional deformation space. For the nuclear shape, we adopt the two-centre-shell model with three parameters (see, [11, 10] for the details), i.e., the distance of two nuclei (z_0), the degree of deformation of a fragment (δ), and the mass asymmetry (α).

We calculate the dynamical process of fission by solving the multi-dimensional Langevin equations of motion, which are expressed as follows:

$$\frac{dq_i}{dt} = (m^{-1})_{ji} P_j \tag{1}$$

$$\frac{dp_i}{dt} = -\frac{\partial V}{\partial q_i} - \frac{1}{2}\frac{\partial}{\partial q_i}(m^{-1})_{jk} P_j P_k - \gamma_{ij}(m^{-1})_{jk} P_k + g_{ij} R_j(t) \ , \tag{2}$$

where $q_i = \{z, \sigma, \alpha\}$ and their momentum conjugate, $p_i = m_{ij} dq_i/dt$. V is the potential, and m_{ij} and γ_{ij} are the inertia mass and friction coefficient depending on the shape of the nucleus.

The last term of Eq. 2 corresponds to the random force with the normalized white noise $R_j(t)$. The g_{ji} is the strength of the random force, which is related with the friction tensor γ_{ji} by the classical Einstein relation,

$$\gamma_{ji} T = \sum_k g_{ij} g_{jk} \tag{3}$$

where T is the temperature of the nucleus. Following this random property in the momentum equation (Eq. 2), each event shows a different trajectory on the potential energy space. We repeat fission dynamics calculations to find the convergence of fission distributions, e.g., the FFD.

2.2 Charge distributions

Although the time evolution and the FFD are determined in our Langevin calculations, the charge distribution of fission fragments cannot be obtained. However, the charge distribution

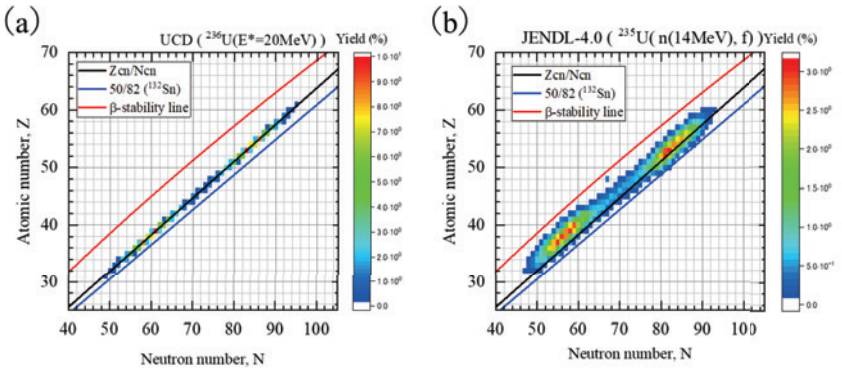

Figure 1: (a) The calculated FFD on the N-Z plane for ^{236}U with the excitation energy: $E^* =$ 20MeV. (b) The experimental FFD (JENDL-4.0 [12]) for ^{235}U by the neutron-induced fission. The N/Z line of compound nucleus (black), the $N/Z = 50/82$ line of a double-magic nucleus ^{132}Sn (blue), and the β-stability line (red) are plotted.

of fission products is a fundamental quantity for the determination of the production rate of individual isotopes. Thus, it is an essential nuclear data for the comparison of experiments and r-process nucleosynthesis calculations. We calculate the charge distribution based on the assumption of unchanged charge distribution (UCD), where the charge distribution (charge density) remains unchanged during the whole fission process, i.e., the charge density of the compound nucleus is maintained.

Based on the UCD assumption, we can only calculate the charge (Z) distribution along to the N/Z line, i.e., "projection" to the N/Z axis. For example, the calculated charge distribution of ^{236}U is shown in Fig. 1a. However, the distribution must be width on this line, as shown in the experimental data (Fig. 1b) of the FFD for neutron-included fission of ^{236}U (the compound nucleus is ^{236}U). Therefore, we adopt Gaussian distribution to calculated the width of FFD with $\sigma = 0.01$, which is relatively well reproduce available experimental data in JENDL-4.0 [12].

3 Results

In this section, we show the fission fragment mass and charge distributions for ^{236}U, of which experimental data are available (Section 3.1). We see our fission model can reproduce experi-

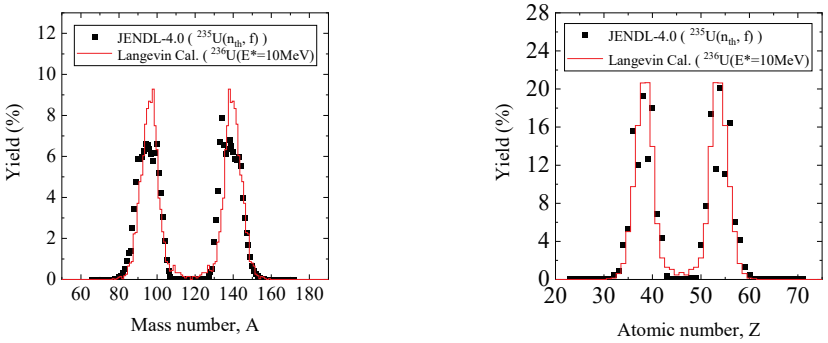

Figure 2: The calculated mass distribution *(left)* and the charge distribution *(right)* of ^{236}U, compared with the experimental data in JENDL-4.0 [12].

ments well at least in the less neutron-rich U isotopes. Then, the results of fission calculations for series of U and Fm isotopes are shown in Section 3.2.

3.1 Fission fragment mass and charge distributions

For the application to the r-process simulations, we need fission properties for very neutron-rich nuclei far from the β-stability line. However, experimental data in such region are not available yet. Therefore, we firstly carry out fission calculations for U isotopes near the β-stability line.

Fig. 2 shows the results of the mass and charge distribution of fission fragments for ^{236}U. The fission calculation is performed with the excitation energy, $E^* = 10$ MeV. The distributions are compared with experimental data in JENDL-4.0 [12]. The calculated mass distribution, a fundamental variable of the Langevin equations, shows good agreement with experimental data. The charge distribution with the current simple treatment, based on the UCD, also reproduce the experiment.

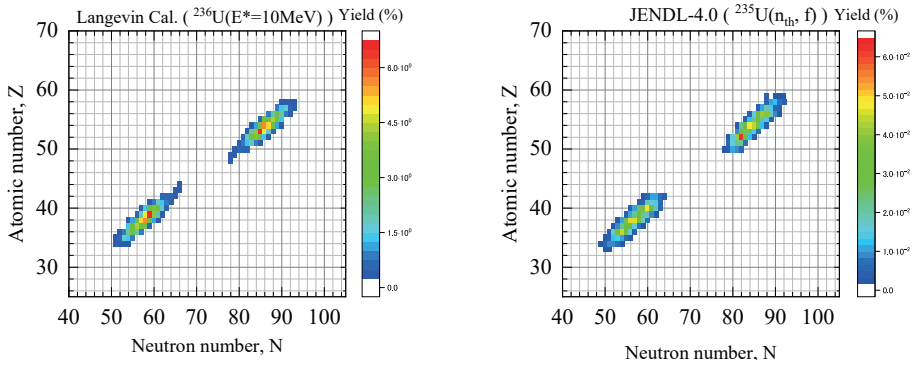

Figure 3: The fission fragment distribution on the N–Z plane. The calculation (*left*) and experimental data (*right*) are plotted.

Fig. 3 shows the fission fragment distribution on the N-Z plane for ^{236}U. The calculation is compared to the neutron-induced fission with the same compound nucleus. The width along the N/Z line is our systematic Gaussian fitting (Section 2.2). As expected by Fig. 2, calculated values reproduce basic properties of the JENDL data.

3.2 Neutron-rich isotopes for U and Fm

We perform a series of fission calculations for the neutron-rich actinoid nuclei. We show the results of U ($Z = 92$) and Fm ($Z = 100$) isotopes with 10–20 more neutron rich from the β-stability line. It is experimentally known for Fm isotopes that the fission fragmentation becomes

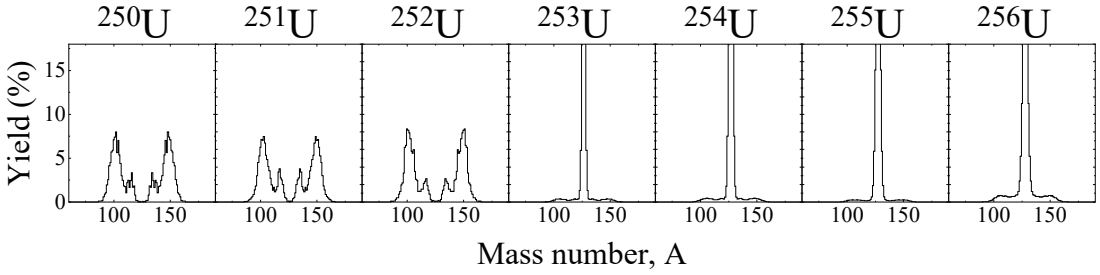

Figure 4: The calculated FFD for neutron-rich U ($Z = 92$) isotopes, ^{250}U to ^{256}U.

the asymmetric to symmetric as the neutron number increases. Thus, the number of peaks in FFD changes from two to one in the neutron-rich nuclei.

We adopt lower excitation energy, $E^* = 7$ MeV, corresponding to low energy environments the r-process occurs. The calculated FFD for ^{250}U to ^{256}U are shown in Fig. 5. We find the distribution changes between ^{252}U and ^{253}U. The number of peaks reduced from two to one, i.e., the FFD becomes symmetric from asymmetric.

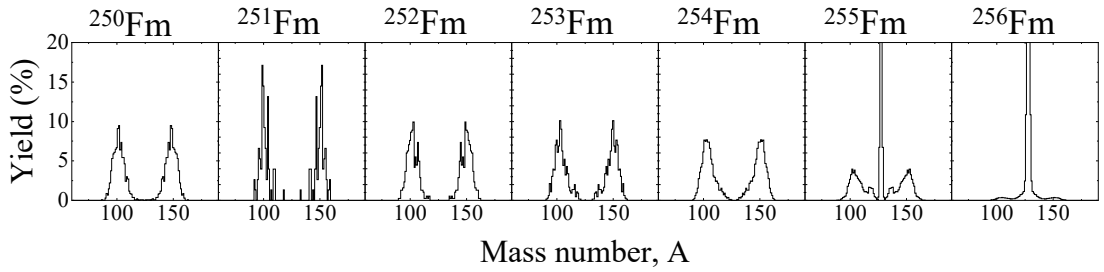

Figure 5: Same as Fig. 4, but for Fm ($Z = 100$) isotopes.

We also find the transition of the symmetry in FFD for Fm isotopes. Fig. 5 shows mass distributions of $^{250-256}$Fm. A drastic change in the FFD is found between ^{254}Fm and ^{255}Fm. As this set of Fm nuclei is less neutron-rich compared to U, this feature has been suggested by previous experiments.

This transition was found by previous works in the trans-uranium region (see, [11] and references therein), but suggested boundary is $A = 257$ line. This disagreement may cause uncertainties in the Langevin models (model parameters) and the difference of initial conditions. Note that Langevin calculations, based on the same numerical code as the current study, can reproduce the experiments of Fm with specific input physical parameters [11].

The transition is commonly found in our calculations for U to Db isotopes (Tanaka et al., in prep.). Such systematic behaviour can be significant to shape the final abundances of r-process calculations. Conversely, the comparison of r-process calculations with fission distributions can restrict the fission mechanism. In previous studies, such discussions have been done with simplified fission models. Based on dynamical fission calculation, our approach can shed light on the microscopic features of heavy nuclei.

4 Conclusion

In the present work, we have performed fission calculations of neutron-rich nuclei using a kinetic model for application to r-process simulations, and have shown the unique property that the mass number distribution changes dramatically with one or two different mass numbers. Such a change in the distribution affects the production of elements in the synthesis of elements in space, and our results, including further improvements, are expected to contribute to the understanding of the r-process.

As for the Fm region and the neutron-rich nuclides in the U region, experimental data have been obtained by domestic research institutes including Japan Atomic Energy Agency and RIKEN. It is expected to verify the theoretical calculations. As for the Fm region and the neutron-rich nuclides in the U region, experimental data have been obtained by domestic research institutes, including Japan Atomic Energy Agency and RIKEN RIBF. It is expected to verify the theoretical calculations. To develop a complete theoretical set of fission data, the supporters of such future experiments are desirable.

Acknowledgments

This study is financially supported by JSPS KAKENHI (19H00693, 20K04003, 20H05648). The parts of computations are performed by computer facilities in CfCA, NAOJ and YITP, Kyoto University.

References

[1] C. J. Horowitz, A. Arcones, B. Côté, and et al.: Journal of Physics G Nuclear Physics **46** (2019) 083001.

[2] M. Arnould and S. Goriely: Progress in Particle and Nuclear Physics **112** (2020) 103766.

[3] J. J. Cowan, C. Sneden, J. E. Lawler, A. Aprahamian, M. Wiescher, K. Langanke, G. Martínez-Pinedo, and F.-K. Thielemann: Rev. Mod. Phys. **93** (2021) 015002.

[4] S. Goriely, J. L. Sida, J. F. Lemaître, S. Panebianco, N. Dubray, S. Hilaire, A. Bauswein, and H. T. Janka: Phys. Rev. Lett.**111** (2013) 242502.

[5] M. Eichler, A. Arcones, A. Kelic, O. Korobkin, K. Langanke, T. Marketin, G. Martinez-Pinedo, I. Panov, T. Rauscher, S. Rosswog, C. Winteler, N. T. Zinner, and F. K. Thielemann: Astrophys. J. **808** (2015) 30.

[6] S. Shibagaki, T. Kajino, G. J. Mathews, S. Chiba, S. Nishimura, and G. Lorusso: Astrophys. J. **816** (2016) 79.

[7] N. Vassh, M. R. Mumpower, G. C. McLaughlin, T. M. Sprouse, and R. Surman: Astrophys. J. **896** (2020) 28.

[8] S. Wanajo: Astrophys. J. **868** (2018) 65.

[9] Y. Zhu, R. T. Wollaeger, N. Vassh, R. Surman, T. M. Sprouse, M. R. Mumpower, P. Möller, G. C. McLaughlin, O. Korobkin, T. Kawano, P. J. Jaffke, E. M. Holmbeck, C. L. Fryer, W. P. Even, A. J. Couture, and J. Barnes: Astrophys. J. Lett.**863** (2018) L23.

[10] S. Tanaka, Y. Aritomo, Y. Miyamoto, K. Hirose, and K. Nishio: Phys. Rev. C**100** (2019) 064605.

[11] Y. Miyamoto, Y. Aritomo, S. Tanaka, K. Hirose, and K. Nishio: Phys. Rev. C**99** (2019) 051601.

[12] K. Shibata, O. Iwamoto, T. Nakagawa, N. Iwamoto, A. Ichihara, S. Kunieda, S. Chiba, J. Katakura, and N. Otuka: Journal of Korean Physical Society **59** (2011) 1046.

22. Extended Migdal-Watson formula to evaluate background strength in binary breakup reactions

Riu NAKAMOTO[1], Makoto ITO [†1], Akito SAITO[2], and Susumu SHIMOURA[3]

[1]Department of Pure and Applied Physics, Kansai University, Yamatecho, 3-3-35, Suita 564-8680, Japan
[2]Department of Radiation Oncology, Hiroshima University Hospital 1-2-3 Kasumi, Minami, Hiroshima, Hiroshima 734-8551, Japan
[3]Center for Nuclear Study, School of Science, The University of Tokyo, 7-3-1, Hongo, Bunkyo-ku, Tokyo, 113-0033, Japan
[†]Email: itomk@kansai-u.ac.jp

New formula to describe the background strength in the binary breakup, which is induced by the direct breakup process, is considered on the basis of the Migdal-Watson (MW) formula. The strength of the direct breakup is calculated by the complex scaling method. We have found that the extended MW formula, which is proposed in the present study, nicely reproduces the strength of the direct breakup calculated by Complex Scaling Method.

1 Introduction

Inelastic scattering is a useful tool to explore the intrinsic structure of the excited states of nuclei. In particular, the inelastic excitation of the nucleus to the resonant states above the threshold for the particle decay, which is often called the breakup reaction, is very important because we can pin down the intrinsic nuclear structure in the resonances by controlling the detection of the exit channels, which are the combination of the emitted fragments. A typical and good example about the inelastic scattering to the continuum can be seen in the breakup reaction of ^{12}Be into the α + ^{8}He and ^{6}He + ^{6}He channels [1]. In this experiment, the careful multi-pole decomposition analysis (MDA) was performed, and the MDA analysis elucidates that many resonant states with a sharp width of $\Gamma_R \leq 1$ MeV exist in the spins from $J^\pi = 0^+$ to 8^+ [1]. The resonances in these channels appear in a close energy spacing with $\Delta E \sim 0.5$ MeV in the lower energy region below $E_x \leq 15$ MeV.

In determining the resonance parameters, such as the resonance energies and the decay widths, the evaluation of the non-resonant background strength is indispensable because the resonant enhancements, which have a strong energy dependence, are embedded in the non-resonant background contribution.

In order to extract the information about the resonance parameters precisely, it is quite important to propose the appropriate analytic function for describing the non-resonant background contribution in the breakup reaction. In this article, we investigate the structure of the non-resonant background strength in the binary system, which is generated by the direct breakup process, and propose a new formula to evaluate the background contribution by extending the Migdal-Watson (MW) formula [2, 3, 4]. In the calculation of the strength for the direct breakup, we employ the complex scaling method (CSM) [6], which is a powerful tool to

describe the few-body continuum states. From the CSM calculation, we check the applicability of the extended MW formula to the evaluation of the background contribution for the binary breakup. Here we consider the breakup of ^{20}Ne into $\alpha + {}^{16}$O because the ^{20}Ne nucleus is known to be a typical example of the binary cluster system [7, 8]

The organization of this article is the following. In section 2, theoretical formulation is explained. This section contains the explanation of CSM, the definition of the direct breakup and the details of the computational setting. The original Migdal-Watson theory and its extension are explained in section 3. In section 4, the strength function calculated by CSM is analyzed, and the validity of the extended MW formula is discussed. The final section is devoted to summary.

2 Theoretical framework

2.1 Complex scaling method

In the present study, the direct breakup is defined by the one step transition from the initial ground state to the final excited state embedded in the continuum. The background strength generated by the direct breakup process is evaluated by the complex scaling method (CSM) [6]. In CSM, the transformation of the complex rotation with the rotation angle θ

$$\hat{U}(\theta)f(\mathbf{r}) \;=\; e^{\frac{3}{2}i\theta}f(e^{i\theta}\mathbf{r}) \;=\; f^{\theta} \tag{1}$$

is introduced for the arbitrary function of $f(\mathbf{r})$. Here the rotation on $\mathbf{r}$ should be read as the transformation on the radial part of the coordinate and hence, $r \rightarrow re^{i\theta}$. The Schrödinger equation transformed by this complex rotation becomes

$$\hat{H}^{\theta}\Psi^{\theta} \;=\; E^{\theta}\Psi^{\theta} \;\;, \tag{2}$$

where Ψ^{θ} is defined by equation (1) and $\hat{H}^{\theta} = \hat{U}(\theta)\hat{H}\hat{U}(\theta)^{-1}$. In the rotated Hamiltonian $\hat{H}_{\theta}$, the dynamical coordinates of $\mathbf{r}$ contained in $\hat{H}$ is complex rotated like $\hat{H}^{\theta} = \hat{H}(e^{i\theta}\mathbf{r})$. The amplitude of the resonant wave function, which originally diverges in the asymptotic region, is damped in the large distant region by this complex rotation and hence, the usual computation technique for the bound state problem, such as the basis expansion method, is possible to apply. The energy eigenvalues calculated from the CSM plus basis expansion technique become the discrete and complex eigenvalue, $E^{\theta} \rightarrow E^{\theta}_{\nu}$ labeled by the eigenvalue number ν. According to the ABC theorem [6], the energy eigenvalues for the bound state are invariant, and the energy eigenvalues for the resonances are clearly separated from the non-resonant continuum states in the complex energy plane [6].

The CSM is possible to apply to the calculation of the strength function, which represents the transition strength of the initial ground state (Ψ_i) induced by the external field of $\hat{O}_{\lambda}$ with the multi-polarity λ [8]. The definition of the strength function of $S_{\lambda}(E)$ is given by

$$S_{\lambda}(E) \;=\; \sum_{f} |<\Psi_f|\hat{O}_{\lambda}|\Psi_i>|^2\delta(E-E_f) \;\;, \tag{3}$$

where Ψ_f denotes the final state belonging to the f-th eigenstate excited by the external field of $\hat{O}_{\lambda}$. By introducing the complex rotation given by equation (1) and the extended completeness relation [6], the strength function is rewritten like

$$S_{\lambda}(E) \;= -\frac{1}{\pi}\,\Im\, R_{\lambda}(E) \tag{4}$$

with the response function of $R_{\lambda}(E)$ defined by

$$R_{\lambda}(E) \;=\; \sum_{\nu} \frac{<\tilde{\Psi}^{\theta}_i|(\hat{O}^{\dagger}_{\lambda})^{\theta}|\Psi^{\theta}_{\nu}><\tilde{\Psi}^{\theta}_{\nu}|\hat{O}^{\theta}_{\lambda}|\Psi^{\theta}_i>}{E-E^{\theta}_{\nu}} \;\;. \tag{5}$$

Here the Ψ^θ is the solution of CSM, and the tilde in the bra-state means that the complex conjugate is not taken for the radial part of the wave function [6].

2.2 Setting of theoretical calculation

In the present study, the direct breakup of ^{20}Ne into $\alpha + {}^{16}$O is considered because the ^{20}Ne is a typical example of the binary cluster system [9]. In the calculation of the $\alpha + {}^{16}$O system, the computational setting is the same as the setting in reference [7]. The interaction potential V is composed of the nuclear (V_N) and Coulomb (V_C) potentials, and their explicit form is given by

$$V(R) = V_N(R) + V_C(R) \quad (6)$$

$$V_N(R) = -154 \cdot \exp(-0.1102R^2) \quad (7)$$

$$V_C(R) = 16 \cdot \frac{e^2}{R} \cdot \mathrm{erf}(0.4805R) \quad (8)$$

with the definition of the error function of

$$\mathrm{erf}(x) = \frac{2}{\sqrt{\pi}} \int_0^x \exp(-t^2)dt \ . \quad (9)$$

The computational process to prepare the initial wave function (Ψ_i) and the final one (Ψ_f) for the $\alpha - {}^{16}$O relative motion is also the same as those in reference [7]. The pseudo potential with the harmonic oscillator wave function is included to exclude the Pauli's forbidden states in solving the Schrödinger equation with the potentials shown in equations (6), (7) and (8) [7, 8].

2.2.1 Operators for direct breakup

In the present analysis, the standard operator with the multi-polarity of $\lambda = 2$ is used as the external field inducing the direct breakup. Namely, in the calculation of the matrix element in equation (3), we use $\hat{O}_{\lambda=2}$ exciting the relative wave function of two clusters, such as

$$\hat{O}_{\lambda=2} = \sqrt{4\pi} R^2 Y_{2,0}(\hat{\mathbf{R}}) \ , \quad (10)$$

where $\mathbf{R}$ denotes the relative coordinate of two clusters. In addition, we consider the higher order operator for the monopole excitation, which is given by

$$\hat{O}_{\lambda=0} = \sqrt{4\pi} R^2 Y_{0,0}(\hat{\mathbf{R}}) \ . \quad (11)$$

The importance of the cluster excitation by this higher order operator has recently been pointed out in references [12, 13].

A special treatment is required in the calculation of the monopole transition using equation (11). In the matrix element for the direct breakup in equation (3), the operation of the monopole operator on the initial wave function in the ground state generates the superposition of a series of the wave functions, which contains both of the ground and excited states. Thus, the ground state component must be extracted from the product of the monopole operator and the initial wave function, which is called the initial wave packet [2]. This exclusion can be achieved by the replacement in the radial operator of $R^2 \to R^2 - < R^2 >$, in which $< R^2 >$ denotes the expectation value of R^2 with the ground wave function.

3 Migdal-Watson theory and its extension

In the s-wave breakup of the binary system composed of the charge neutral particles, the strength function can be expressed by the closed formula in the case of the short range limit of the initial state. This formula is called the Migdal-Watson (MW) theory [3, 4], which expresses the strength function in terms of the effective range theory [5]. The detailed explanation of the MW formula and its application to the breakup of the di-neutron system is reported in reference [2]. Here we explain the essence of the MW formula and extend the formula to the case of the binary breakup reaction including the effects of the the finite charge, the finite spin and the finite size.

In the MW theory, the monopole strength of the direct breakup with the relative energy E for the binary fragments ($S_{\lambda=0}(E)$) is given by

$$S_0(E) \propto \frac{\sqrt{E}}{AE^2 + BE + C} , \tag{12}$$

where the constants of A, B and C are function of the scattering length and the effective range [2, 3, 4]. The MW formula in equation (12) must be valid for the breakup from the initial wave packet strongly localized inside of the nuclear interaction.

The MW formula shown in equation (12) is valid for the s-wave breakup from the initial wave packet localized inside of the nuclear interaction, which corresponds to the tightly binding system composed of the charge neutral fragments. Here we try to extend equation (12) so as to describe the direct breakup reaction of the general binary systems, which have the finite charge, the finite spin in the final scattering state ($S_{\lambda\neq0}(E)$) and the finite size of the initial wave packet.

We extend equation (12) to the following function:

$$S_\lambda(E) \propto \frac{P_\lambda(ka)e^{-\beta E}}{AE^2 + BE + C} . \tag{13}$$

In this function, $P_\lambda(ka)$ denotes the penetration factor with the momentum k for the binary decaying fragments and the channel radius a. P_λ corresponds to the extension of the factor of $\sqrt{E}$ in equation (12). If we consider the limit of $k \to 0$ and $\lambda = 0$, $P_\lambda(ka)$ is reduced to $\sqrt{E}$.

On the contrary, β in the exponential term simulates the effect of the finite size of the initial packet. β should be small in the case of the limit of the strong binding system, and vice versa. We try to reproduce the background strength generated by the direct breakup by controlling the five fitting parameters: A, B, C, a, β.

4 Results

The fitting result using the extended MW formula in equation (13) is shown in the two panels of figure 1. The quadrupole and monopole strengths for $^{20}\mathrm{Ne} \to \alpha + {}^{16}\mathrm{O}$ are shown in the left and right panels, respectively. The calculated strength functions (solid curves) are nicely reproduced by the extended MW formula (open circles). In both the panels, the solid circle with the error bar means the resonance energy ($\mathcal{E}_R$) with the decay width (Γ_R) of the potential resonance in the final state. The peak structure in the strength function nicely corresponds to the resonance energy and the width and hence, the enhancement is originated from the resonance formation.

In the fitting analysis of the quadrupole transition, we do not use the original resonance parameter ($\mathcal{E}_R = 4.2$ MeV and $\Gamma_R = 2.8$ MeV) but the tuned parameters for the Breit-Wigner part: $A = 0.025$, $B = -0.21$, $C = 0.48$, $a = 5.5$ fm and $\beta = 0.015$ MeV^{-1} in equation (13). In the monopole transition,

the resonance parameter of the 0^+ resonance is $\mathcal{E}_R = 3.3$ MeV and $\Gamma_R = 2.0$ MeV. The parameters used for the fitting to the monopole transition are $A = 0.029$, $B = -0.19$, $C = 0.33$,

$a = 5.0$ fm and $\beta = 0.015$ MeV^{-1}, in which (A, B, C) are modified from the original resonance parameters.

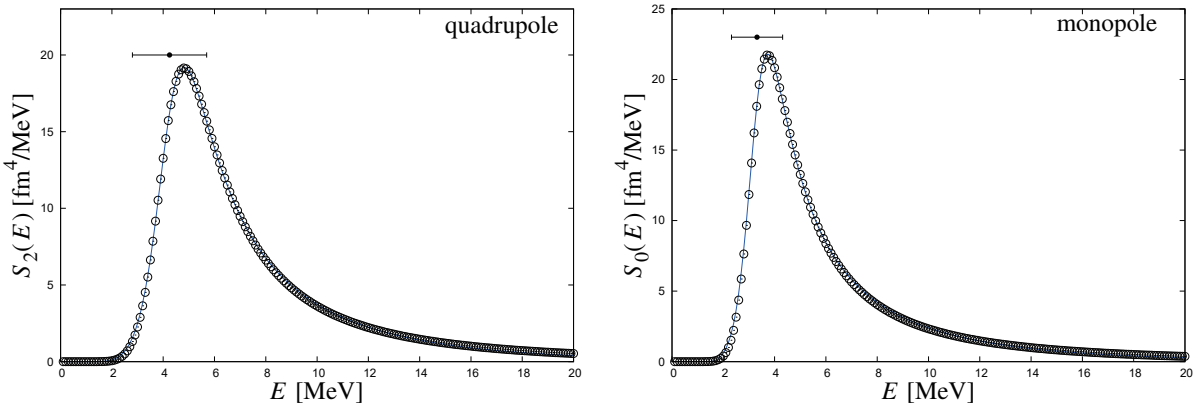

Figure 1: Comparison of the strength function of $^{20}\mathrm{Ne} \rightarrow \alpha + {}^{16}\mathrm{O}$ with fitting results by the extended Migdal-Watson formula in equation (13). The left panel shows the quadrupole ($S_2(E)$) transition, while the right one shows the monopole ($S_0(E)$) transitions. The α threshold energy is set to the zero point in the abscissa. In both of the panels, the solid curve and the open circles represent the strength function calculated from CSM and fitting results by equation (13), respectively. The solid circle with the error bar shows the resonance energy with the decay width.

In the monopole transition, the excitation energy of the peak position corresponds to about 10 MeV, and this energy is much lower than the excitation energy of the monopole single particle excitation, which reaches about 30 MeV in this mass region [10]. One of the characteristic feature in the α cluster excitation is that the strong monopole strength appears at the lower excitation energy region as pointed out in the previous calculations [10, 11]. Therefore, the extended MW formula, which is developed by the present analysis, is important in the evaluation of the low-lying strength of the monopole transition induced by the α cluster excitation.

5 Summary

In summary, we have investigated the feature of the strength function for the direct breakup process, in which a bound nucleus dissociates into the binary fragments. The direct breakup process is defined by the direct and one-step transition from the specific component of the binary channel in the many-body bound state to the distorted wave for this channel, which is generated by the nuclear and Coulomb potentials in the final scattering state. The transition strength of the direct breakup is considered to be the main component of the non-resonant background strength in the realistic breakup experiment.

In order to describe the background strength in the simple manner, we have considered the analytic function by extending the Migdal-Watson (MW) formula [3, 4, 5], which has recently been discussed in the s-wave breakup of the di-neutron system [2]. The MW formula gives the function of the quadratic energy denominator times the square root of energy, such as $\sqrt{E}/(AE^2 + BE + C)$. This formula is valid for the s-wave binary breakup of the charge neutral system, and the initial wave function is assumed to be strongly confined inside of the short range nuclear interaction.

We have extended the MW formula so as to include the effects of the finite spins, the finite charge and the finite size of the initial wave packet. First, the numerator of $\sqrt{E}$ is replaced by

the penetration factor of $P_\lambda(ka)$ to take into account the effects of the finite spin (λ) and finite charge.

Furthermore, we have introduced the exponential damping factor, $\exp(-\beta E)$, which is originated from the tunneling tail of the initial wave packet outside of the nuclear interaction.

The extended MW formula proposed for the direct breakup is

$$\frac{P_\lambda(ka)\cdot\exp(-\beta E)}{AE^2+BE+C} \quad . \tag{14}$$

We have tested the extended MW formula by fitting the strength function obtained from the theoretical calculation of the direct breakup. Here we have evaluated the strength by the direct breakup in $^{20}\mathrm{Ne} \rightarrow \alpha + {}^{16}\mathrm{O}$ [7] on the basis of the formulation of the complex scaling method (CSM) [6]. In the CSM calculation of the monopole and quadrupole transitions, we have confirmed that the resonant peak appears around $E \sim 5$ MeV above the α threshold energy, and the strength functions are nicely reproduced by the extended MW formula. Since we have confirmed the availability of the MW formula in the direct breakup in the binary system, it is important to apply the formula to other binary breakup reactions, such as $^{12}\mathrm{Be} \rightarrow \alpha + {}^{8}\mathrm{He}$ [1]. The application to ^{12}Be is now under progress.

Acknowledgments

We would like to thank Ms. N. Nishida, Mr. R. Ikegawa, Mr. M. Matsushita, Mr. H. Yamada and all the members of the Quantum Many-body Physics Laboratory at Kansai University for their useful discussions and kind support. One of the authors (M. I.) thanks Prof. H. Otsu at RIKEN for kind support and encouragement.

References

[1] A. Saito *et al.*, Mod. Phys. Lett. A, Vol. 25, No. 21−23, 2010, pp. 1858-1861.

[2] S. Shimoura, Eur. Phys. Jour. Plus **133**, 2018, 463.

[3] A. Migdal, Sov. Phys. JETP **1**, 1955, 2.

[4] K. Watson, Phys. Rev. C**88**, 1952, 1163.

[5] N. Austern, Nucl. Phys. **7**, 1958, 195.

[6] S. Aoyama, T. Myo, K. Katō and K. Ikeda, Prog. Theor. Phys. **116**, 2006, and references therein, pp.1-35.

[7] A. T. Kruppa and K. Katō, Prog. Theor. Phys. **84**, 1990, 1145.

[8] T. Myo, A. Ohnishi and K. Katō, Prog. Theor. Phys. **99**, 1998, 801.

[9] H. Horiuchi *et al.*, Prog. Theor. Phys. Suppl. 2012 Jan; **192**: 1-238 , and references therein.

[10] T. Yamada, Y. Funaki, H. Horiuchi, K. Ikeda, and A. Tohsaki, Prog. Theor. Phys. **120**, 2008, 1139.

[11] T. Yamada, Y. Funaki, T. Myo, H. Horiuchi, K. Ikeda, G. Röpke, P. Schuck, and A. Thosaki, Phys. Rev. C**85**, 2012, 034315.

[12] Y. Chiba, M. Kimura, Y. Taniguchi, Phys. Rev. C**93**, 2016, 034319.

[13] Y. Chiba, Y. Taniguchi, M. Kimura, Phys. Rev. C**95**, 2017, 044328.

23. Evaluation of Neutron Nuclear Data on Cobalt-59 for JENDL-5

Nobuyuki Iwamoto
Nuclear Data Center, Nuclear Science and Engineering Center, Japan Atomic Energy Agency, Tokai, Ibaraki 319-1195, Japan
e-mail: iwamoto.nobuyuki@jaea.go.jp

The neutron nuclear data of ^{59}Co were evaluated in the energy region of 10^{-5} eV to 20 MeV for the development of JENDL-5. The resonance parameters and total cross sections were taken from the measurement by de Saussure et al. in the resolved and unresolved resonance regions, respectively. The thermal capture cross section was evaluated using available measured data. The present data were consistent with the values in major evaluated libraries. In the fast neutron energy region the evaluation was made with various types of measured data by the nuclear reaction calculation code CCONE. It is found that the present results well reproduce the measured data.

1 Introduction

Cobalt is a monoisotope element, and the stable isotope is ^{59}Co. Cobalt is one of the important structural materials and is contained in carbon steel and concrete as well as SUS304. Therefore, the accurate nuclear data of ^{59}Co are requisite for analyses in nuclear and accelerator facilities; specifically radioactivity estimation of ^{59}Fe (half-life 44.5 d), ^{58}Co (70.9 d) and ^{60}Co (5.27 y) related to decommissioning of the facilities.

The nuclear data of ^{59}Co [1] in the general purpose library JENDL-4.0 are based on the evaluation in 1988. Since the early evaluation, a partial revision was made at the JENDL-3.3 evaluation in 2001 [2]. After the release of JENDL-3.3, many measurements have been done for, e.g., capture, $(n, 2n)$, (n, p), and (n, α) reactions. Therefore, the reconsideration of nuclear data is required for the development of JENDL-5.

2 Evaluation methods and results

The evaluation of ^{59}Co was divided into three energy regions: resolved resonance region, unresolved resonance region and fast neutron energy region. Evaluation details and obtained results will be explained below.

2.1 Resolved resonance region

The resonance parameters and scattering radius were taken from the data of de Saussure et al. [3], who made the detailed analysis of resonance parameters, using neutron transmission data with different sample thicknesses measured at ORNL. Figures 1 and 2 illustrate the present total cross sections and the data of JENDL-4.0, together with the measured data with sample thicknesses of 0.021, 0.075 and 0.301 atoms/barn and sample temperature of 293 K in the energy range of 10^{-5} eV to 100 keV.

The capture cross sections calculated by the resonance parameters were compared with the data of Spencer & Macklin [4] in Figures 3 and 4. JENDL-4.0 has more resonances than the present result. They come from the resonance data [4, 5, 6], in which Spencer & Macklin [4] provided only capture kernel data for many resonances. The capture kernel data might be useful, if average values of radiation widths, for example, were assumed. Nevertheless, the use of their data was finally rejected because reasonable values of neutron width were not obtained for many resonances, assuming the average radiation width of 0.36 eV for p-wave resonances [3].

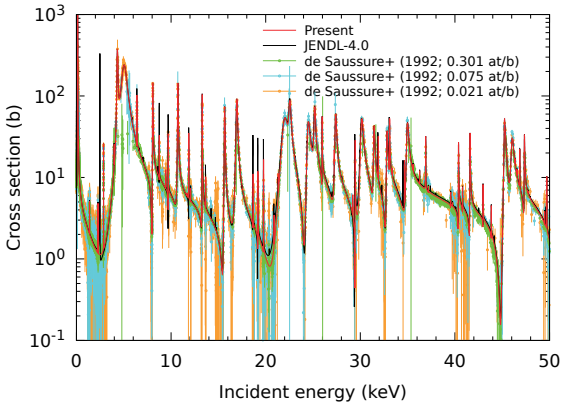

Figure 1: Comparison of the present total cross section with measured data, together with JENDL-4.0, in the energy region of 10^{-5} eV to 50 keV.

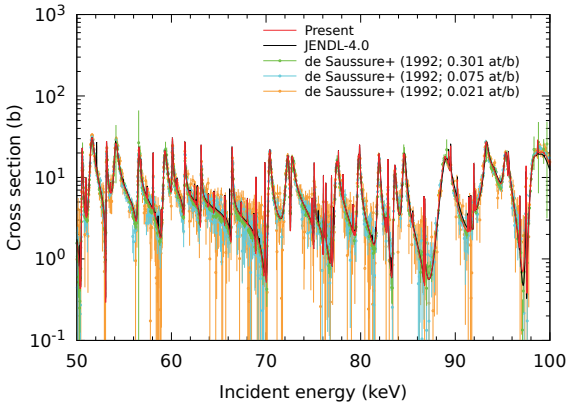

Figure 2: Same as Figure 1, but in the energy region of 50 to 100 keV.

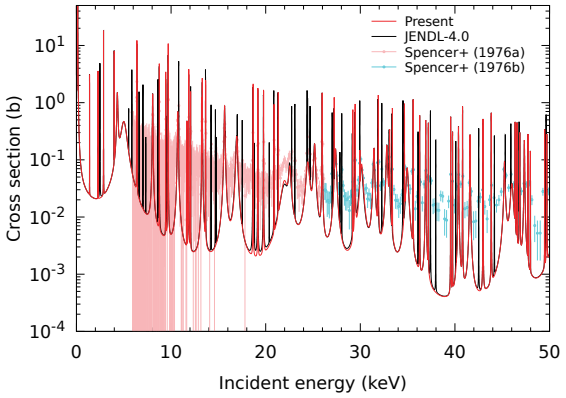

Figure 3: Comparison of the present capture cross section with measured data, together with JENDL-4.0, in the energy region of 10^{-5} eV to 50 keV.

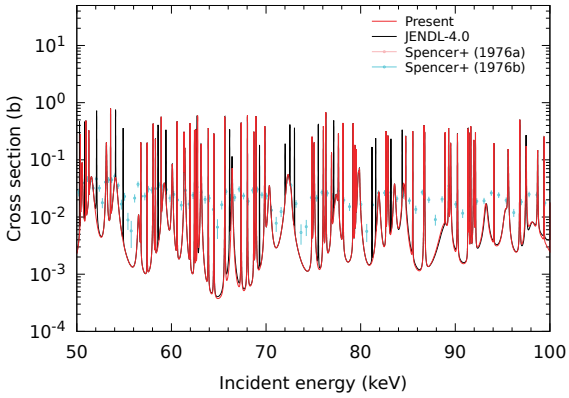

Figure 4: Same as Figure 3, but in the energy region of 50 to 100 keV.

Thermal capture cross section was evaluated with measured data. Most of the measurements was made, based on the absorption cross section of natural boron, and capture cross section of gold as a monitor cross section. In the present evaluation, the two monitor cross section values adapted in the published data were corrected with the IAEA Neutron Data Standards [7]. In addition, uncertainty estimation was made by the method in the report [8]. The obtained result of capture cross section was 37.31(21) b. This value is almost consistent with the data of JENDL-4.0 (37.20(524) b), ENDF/B-VIII.0 (37.17 b) [9] and JEFF-3.3 (37.17 b) [10] as shown in Figure 5. The neutron and radiation widths of negative resonance at −226 eV were revised to reproduce the present value.

2.2 Unresolved resonance region

Resonances are hard to be resolved one by one due to physical nature of resonances and/or experimental conditions as an incident energy increases. This region is called as unresolved resonance region, where cross sections fluctuate and are not smooth, in general. To keep these shapes is important for shielding calculations in nuclear and accelerator facilities. In the present evaluation, the data of thick sample (0.301 atoms/barn) of de Saussure et al. [3] were adopted

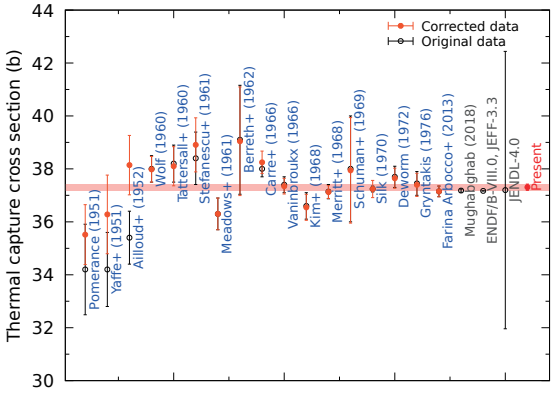

Figure 5: Comparison of capture cross section at thermal energy with measured data, together with evaluated data. The black open circles indicate the original values by the authors; the orange filled circles stand for the values corrected with the latest standard cross sections.

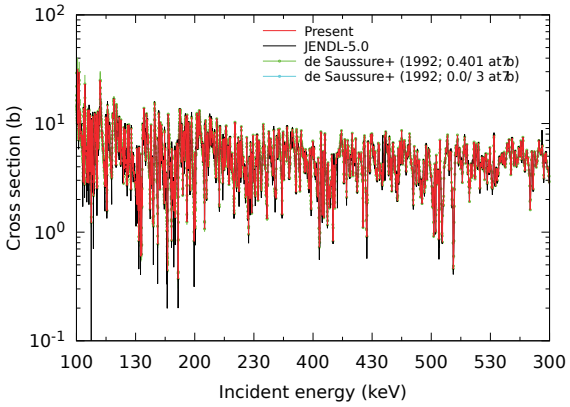

Figure 6: Comparison of total cross section with measured data, together with JENDL-4.0, in the energy region of 100 to 500 keV.

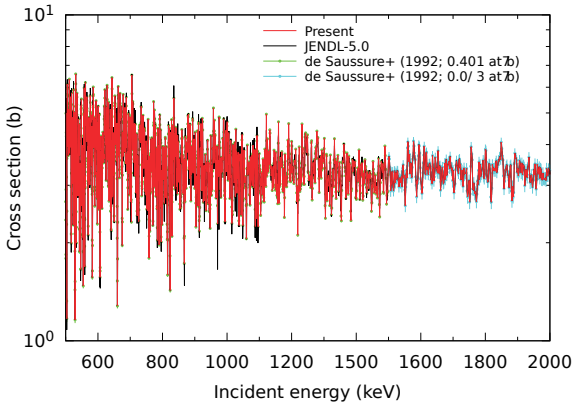

Figure 7: Same as Figure 6, but in the energy region of 500 to 2000 keV.

from 100 keV to 1.5 MeV, above which the data of thin sample (0.075 atoms/barn) were taken up to 5 MeV. The direct use of measured data have disadvantages because experimental effects of multiple-scattering and resolution function are not corrected. Nevertheless, the measured data were adopted without any changes, since we do not have proper ways to derive perfect cross sections in this region. The same choices were made in the past JENDL evaluation. The present result is thus similar to JENDL-4.0 as shown in Figures 6 and 7. The difference can be seen as deep valley of the resonances in JENDL-4.0. This might be due to improper interpolation of measured data.

2.3 Fast neutron energy region

In the fast neutron energy region, neutron cross sections were calculated by using the nuclear reaction calculation code CCONE [11], which composes of the coupled channels optical model code CCOM and the Hauser-Feshbach statistical model code CCSM.

The CCOM code was used to calculate neutron transmission coefficients of ^{59}Co. The optical model potential was taken from a functional form of Kunieda et al. [12]. The coupled levels were ground state (J^π=7/2$^-$) and two excited levels (E_x, J^π)=(1.19, 9/2$^-$) and (1.46, 11/2$^-$), where J^π is the spin-parity and E_x is the excitation energy in MeV. The potential parameters were modified to reproduce the total cross section and elastic scattering angular distributions. In the use of total cross sections, the data of Abfalterer et al. [13] were taken into account up to 200 MeV, up to which the nuclear data will also be included in JENDL-5 with the form of the production cross sections of residual nuclides.

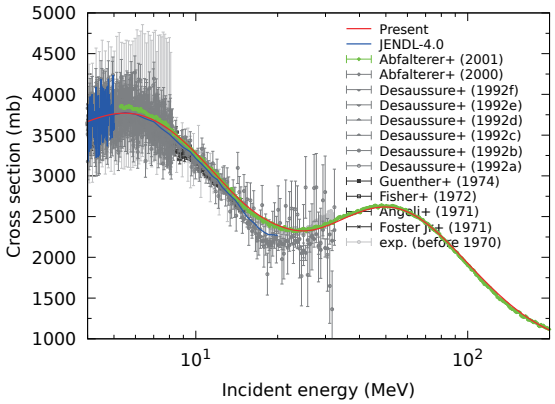

Figure 8: Comparison of the present total cross section with measured data, together with JENDL-4.0.

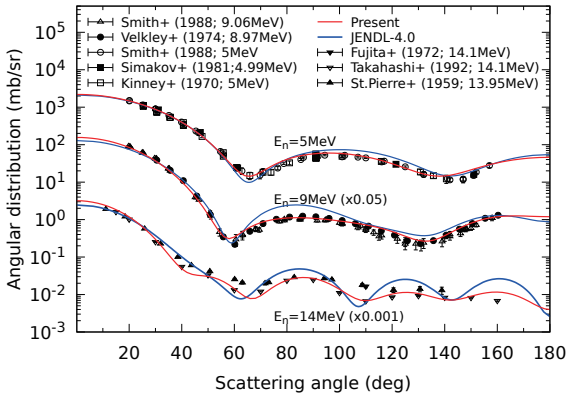

Figure 9: Comparison of the present elastic scattering angular distribution with measured data, together with JENDL-4.0.

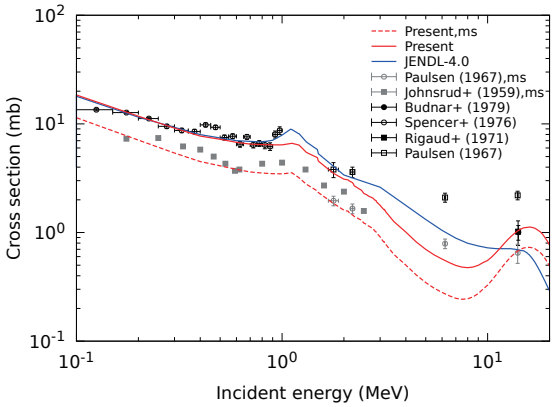

Figure 10: Comparison of the present capture cross section with measured data, together with JENDL-4.0. The evaluated production cross section of meta state of ^{60}Co is added.

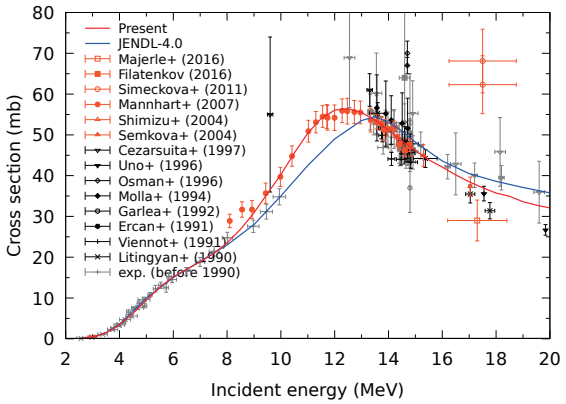

Figure 11: Comparison of the present (n, p) reaction cross section with measured data, together with JENDL-4.0.

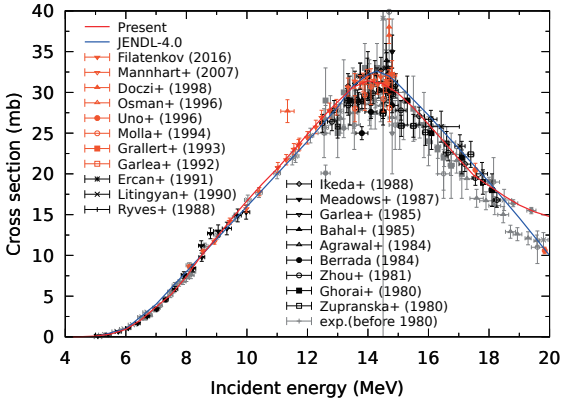

Figure 12: Comparison of the present (n, α) reaction cross section with measured data, together with JENDL-4.0.

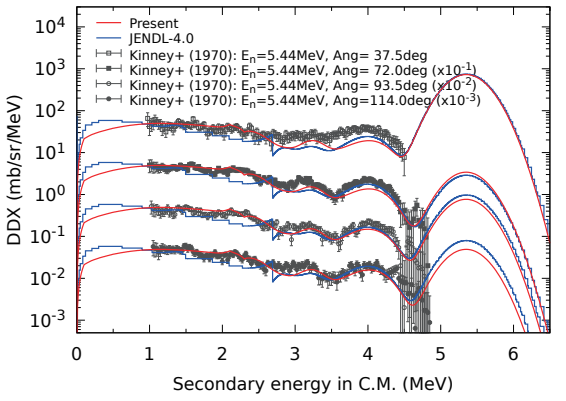

Figure 13: Comparison of the present neutron emission double differential cross section with measured data, together with JENDL-4.0.

The CCSM code is employed to calculate the compound, pre-equilibrium and direct processes in nuclear reaction. The pre-equilibrium and direct processes were considered by two-component exciton and DWBA models, respectively. The contribution from the direct process to inelastic scattering cross sections was determined to reproduce corresponding measured data.

Figure 8 shows the present total cross sections compared with measured data, together with JENDL-4.0 given by averaged values of de Saussure et al. [3] and Cierjacks [14]. The data of JENDL-4.0 has cross sections smaller than the present results above 6 MeV. The calculated total cross sections were illustrated below 5 MeV, for checking the reproducibility of the measured cross sections by the optical model. Figure 9 shows the angular distributions of neutron elastic scattering at incident energies of 5, 9 and 14 MeV, where the contribution of compound elastic scattering has negligible. The present data were in good agreement with measured data. It is found that JENDL-4.0 has larger cross sections at the scattering angles between 60 and 180 degrees, compared to the measured data.

The present capture cross sections are compared with measured data and JENDL-4.0 in Figure 10. The result was obtained to reproduce the data of Spencer & Macklin [4] below 1 MeV. The adjustment of direct/semi-direct capture contribution was done to reproduce the data of Rigaud et al. [15] and Budnar et al. [16]. The evaluated production cross section for meta state ($E_x = 58.59$ keV) of ^{60}Co populated by capture reaction was also shown in Figure 10 and will be included in JENDL-5. The gamma-ray strength function (in unit of 10^{-4}) of s-wave resonances in the present evaluation is 2.53, which is small in comparison with 3.88(35) [17] and 3.83 [3]. This fact might indicate that the radiation width (or resonance spacing) is smaller (or larger) than that ever known in resonance analyses.

The present (n, p) reaction cross sections are illustrated in Figure 11. The result is different from the data of JENDL-4.0 above 8 MeV, especially, in the energy range between 8 and 14 MeV, due to incorporation of new data measured by activation method [18].

Figure 12 represents the comparison of the present (n, α) reaction cross sections with the several measurements and JENDL-4.0. The present evaluation followed the data of Mannhart et al. [18] and Filatenkov [19] between 8 and 15 MeV, supplemented with the data published after 1980 above and below the energy region. JENDL-4.0 has a little bit higher cross sections than the present result above 13 MeV.

The comparisons of the present data with the data of Kinney et al. [20] were made for double differential cross sections of secondary neutrons at incident energy of 5.44 MeV and emission angles of 37.5, 72, 93.5 and 114 deg. in Figure 13. These secondary neutrons come from inelastic and elastic scattering. A discrepancy is evident when the present data below 1 MeV are compared to JENDL-4.0 in Figure 13. The small contribution of low energy neutrons in the present evaluation may be attributed to low level density, characteristic of structural materials.

3 Summary

The evaluation of neutron induced reaction data of ^{59}Co was made in the energy range of 10^{-5} eV to 20 MeV. The evaluation was separately done in the three energy regions: resolved and unresolved resonance regions and fast neutron energy region. For the resolved and unresolved resonance regions the data derived by de Saussure et al. were adopted without including extra resonances appeared in JENDL-4.0. The thermal capture cross section was evaluated using available cross section data, which were corrected, based on the latest standard cross sections. The obtained value reasonably matches the data of ENDF/B-VIII.0 and JEFF-3.3. In the fast neutron energy region, the evaluations were performed for various types of nuclear data by using the nuclear reaction calculation code CCONE. The potential parameters of the optical model were fixed with the measured total cross sections up to 200 MeV and elastic scattering angular distribution. The evaluated results show good agreement with the measured data. These data will be compiled into the next general purpose library JENDL-5.

References

[1] Shibata K, Iwamoto O, Nakagawa T, et al. JENDL-4.0: A New Library for Nuclear Science and Engineering. J. Nucl. Sci. Technol. 2010; 48:1-30.

[2] Shibata K, Kawano T, Nakagawa T, et al. Japanese Evaluated Nuclear Data Library Version 3 Revision-3: JENDL-3.3, J. Nucl. Sci. Technol. 2002;39:1125.

[3] De Saussure G, Larson NM, Harvey JA, et al. Multilevel resonance analysis of ^{59}Co neutron transmission measurements, ORNL/TM-11762 (1991).

[4] Spencer RR, Macklin RL. Neutron Capture Cross Section of Cobalt-59 in the Energy Range 2.5 to 1000 keV, Nuclear Science and Engineering 1976;61:346-355.

[5] Garg JB, Rainwater J, Havens WW. Jr. Nucl. Sci. Eng. 1978;65:76.

[6] Mughabghab SF. Atlas of Neutron Resonances - Resonance Parameters and Thermal Cross Sections $Z = 1 - 100$. Elsevier (2006).

[7] Carlson AD, Pronyaev VG, Capote R, et al. Evaluation of the Neutron Data Standards, Nuclear Data Sheets, 2018;148:143-188.

[8] Improving Nuclear Data Accuracy of the ^{241}Am Capture Cross-section, NEA/WPEC SG-41 (NEA/NSC/R(2020)2) (2020).

[9] Brown DA, Chadwick MB, Capote R, et al. ENDF/B-VIII.0: The 8th major release of the nuclear reaction data library with CIELO-project cross sections, new standards and thermal scattering data, Nucl. Data Sheets 2018;148:1-142.

[10] Plompen AJM, Cabellos O, De Saint Jean C, et al. The joint evaluated fission and fusion nuclear data library, JEFF-3.3, Eur. Phys. J. 2020;A56:181.

[11] Iwamoto O, Iwamoto N, Kunieda S, et al. The CCONE code system and its application to nuclear data evaluation for fission and other reactions. Nucl. Data Sheets 2016;131:259-288.

[12] Kunieda S, Chiba S, Shibata K, et al. Coupled-channels Optical Model Analyses of Nucleon-induced Reactions for Medium and Heavy Nuclei in the Energy Region from 1keV to 200 MeV. J. Nucl. Sci. Technol. 2007;44:838-852.

[13] Abfalterer WP, Bateman FB, Dietrich FS, et al. Measurement of neutron total cross sections up to 560 MeV, Phys. Rev. 2001;C63:044608.

[14] Cierjacks S, Forti P, Kopsch D, et al. High resolution total neutron cross sections for Na, Cl, K, V, Mn and Co between 0.5 and 30 MeV, Kernforschungszentrum Karlsruhe Reports No.1000, Vol.(SUPP.2) (1969).

[15] Rigaud F, Irigaray JL, Petit GY, et al. Gamma-ray spectra following the capture of 14 MeV neutrons by Co-59, Nb-93 and Rh-103, Nuclear Physics, 1971:A173:551-560.

[16] Budnar M, Cvelbar F, Hodgson E, et al. Prompt gamma-ray spectra and integrated cross sections for the radiative capture of 14 MeV neutrons for 28 natural targets in the mass region from 12 to 208, INDC(YUG)-6 (1976).

[17] Mughabghab SF. Atlas of Neutron Resonances (Sixth edition), Elsevier (2018).

[18] Mannhart W, Schmidt D. Measurement of Neutron Activation Cross Sections in the Energy Range from 8 MeV to 15 MeV, PTB-N-53 (2007).

[19] Filatenkov AA. Neutron activation cross sections measured at KRI in neutron energy region 13.4-14.9 MeV, INDC(CCP)-0460 (2016).

[20] Kinney WE, Perey FG. Neutron elastic- and inelastic-scattering cross sections for Co in the energy range 4.19 to 8.56 MeV, Oak Ridge National Lab. Reports No.4549 (1970).

24. SCALE6.2 ORIGEN library produced from JENDL/AD-2017

Chikara KONNO*, Mami KOCHIYAMA and Hirokazu HAYASHI
Japan Atomic Energy Agency
2-4 Shirakata, Tokai-mura, Naka-gun, Ibaraki-ken 319-1195, Japan
*Email: konno.chikara@jaea.go.jp

A SCALE6.2 ORIGEN library was produced from JENDL Activation Cross Section File for Nuclear Decommissioning 2017 (JENDL/AD-2017) with the AMPX-6 code in order to popularize JENDL/AD-2017 widely. The produced ORIGEN library of JENDL/AD-2017 was tested with the JPDR decommissioning data, which demonstrated that the library had no problems.

1. Introduction

The SCALE code system is a modeling and simulation tool complex for nuclear safety analyses and designs. The SCALE6.2 code system [1] was released in 2016 (the latest version is SCALE6.2.4). The ORIGEN code [1] in SCALE6.2 used for activation calculations in decommissioning is completely different from the previous ORIGEN-S code [2] until SCALE6.0 [2] and has the following features.

1) The input format of ORIGEN is easy to use and understand.
2) It is expected that the calculation accuracy is improved because ORIGEN uses one group cross section data generated from multigroup neutron spectra in all calculation points with the COUPLE code [1] in SCALE6.2, while the ORIGEN-S code uses three group cross section data generated with a multigroup neutron spectrum in a typical pressurized-water reactor.
3) The calculation time of ORIGEN including COUPLE is at most about twice of that of ORIGEN-S even for 200 groups.

We expect that ORIGEN in SCALE6.2 will be mainly used for activation calculations in nuclear facility decommissioning. JAEA released JENDL Activation Cross Section File for Nuclear Decommissioning 2017 (JENDL/AD-2017) [3] in 2018. Thus we have produced a SCALE6.2 ORIGEN library from JENDL/AD-2017 in order to popularize JENDL/AD-2017 widely.

2. Method

The nuclear data processing code AMPX-6 [4] in SCALE6.2.4 was used to produce the SCALE6.2 ORIGEN library of JENDL/AD-2017 because the format of SCALE6.2 ORIGEN library was not open. The processing conditions are as follows.

- Group structure : 200 groups (the same as one of the ORIGEN libraries attached in SCALE6.2)

- ✓ We assume transport calculations with the multigroup library MATXSLIB-J40 (neutron : 199 groups) [5].
- ✓ The 200 group structure is the same as the 199 group structure except for its first group.

- Temperature : 300 K
  - ✓ We assume activation calculations for bio-shield concrete.
- Weight function : Maxwell+1/*E*+Fission spectrum + 1/*E* (above 10 MeV)
- Infinite dilution cross sections

Input data of AMPX-6 are very complicated. We used the ExSite code [4] in SCALE6.2.4 in order to generate a typical template input file for AMPX-6. We produced an ORIGEN library from each file of JENDL/AD-2017 with AMPX-6 and the template input and combined all the ORIGEN libraries to one ORIGEN library with AMPX-6.

We encountered several problems during the processing of JENDL/AD-2017 with AMPX-6. Thus we adopted the following coping strategies.

- We used the 0K MF10 version of JENDL/AD-2017 because AMPX-6 could not process the 0K MF9 version.
- We modified a metastable state level based on the decay data of SCALE6.2 (ex. ^{134m}Cs level : 3 in JENDL/AD-2017, 1 in decay data of SCALE6.2).
- JENDL/AD-2017 includes resonance data which should not be used to re-construct cross section data. However AMPX-6 re-constructs and adds cross section data with the resonance data in JENDL/AD-2017 as shown in Fig. 1. Thus we removed the resonance data in JENDL/AD-2017.

3. Comparison with Continuous Energy Cross Section

Two hundred group cross sections of typical nuclei and reactions in the produced ORIGEN library of JENDL/AD-2017 were extracted with the graphical user interface code Fulcrum [1] for visualizing SCALE libraries in SCALE6.2.4 because the format of the ORIGEN libraries is not open. Figures 1 to 4 plot them with continuous energy ones produced with the nuclear data processing code NJOY [6]. The figures show that the processing of the modified JENDL/AD-2017 with AMPX-6 is adequate.

4. Test with JPDR Activation Calculation

We calculated radioactive inventories in bio-shield concrete of JAEA JPDR (Japan Power Demonstration Reactor) [7], whose decommissioning completed in 1996, for validating the produced ORIGEN library of JENDL/AD-2017. Neutron spectra inside the concrete are calculated with the Sn DORT code [8], a 199 group library including up-scattering data from MATXSLIB-J40 and a partial JPDR model shown in Fig. 5. Radioactive inventories were calculated in the concrete with COUPLE and ORIGEN in SCALE6.2.4 and the calculated neutron spectra, where two activation libraries were used; the 200 group library produced from JENDL/AD-2017 and the 200 group library [1] attached in SCALE6.2 (produced from JEFF-3.1/A [9]). “0.0” was added before 199 group neutron spectra because the first group value of the 200 group structure was lack in the 199 group structure and negligibly small. The elapsed time for 161 ORIGEN and COUPLE calculations was 4 minutes, which is not so long compared with 2.5 minutes of 161 ORIGEN-S calculations. Figure 6 shows the calculated radioactivity distribution at Z=340 cm (cooling time : 15 years). The calculation results with two libraries are almost the same, which suggests that the ORIGEN library from JENDL/AD-2017 has no problems. The

calculated results are different from the measured ones. This is considered to be due to reinforced steel in the bio-shield concrete, which was not included in the calculations.

5. Summary

A 200 group SCALE6.2 ORIGEN library from JENDL/AD-2017 was produced with AMPX-6. Radioactive inventories in bio-shield concrete of JAEA JPDR were calculated with ORIGEN in SCALE6.2.4 for testing the library. As a result, it was demonstrated that the produced library had no problems. The produced library will be released from JAEA.

References

[1] Wieselquist, W.A., Lefebvre, R.A., Jessee, M.A., SCALE Code System, ORNL/TM-2005/39 Version 6.2.4, 2020.

[2] ORNL, SCALE: A Modular Code System for Performing Standardized Computer Analyses for Licensing Evaluation, ORNL/TM-2005/39 Version 6, 2009.

[3] https://wwwndc.jaea.go.jp/ftpnd/jendl/jendl-ad-2017.html (accessed 2021-01-08).

[4] Wiarda, D., Dunn, M.E., Greene, N.M., Williams, M.L., Celik, C., Petrie, L.M., AMPX-6: A Modular Code System for Processing ENDF/B, ORNL/TM-2016/43, 2016.

[5] https://rpg.jaea.go.jp/main/ja/library_matxslibj40/ [in Japanese] (accessed 2021-01-08).

[6] MacFarlane, R.E., Muir, D.W., Boicourt, R.M., Kahler, A.C., Conlin, J.L., The NJOY Nuclear Data Processing System, Version 2016, LA-UR-17-20093, 2016.

[7] Kocherov, N.P. (Ed.), International benchmark calculations of radioactive inventory for fission reactor decommissioning, INDC(NDS)-355, 1996.

[8] ORNL RSICC, DOORS3.2a: One, two- and three-dimensional discrete ordinates neutron/photon transport code system, CODE PACKAGE CCC-650, 2007.

[9] Sublet, J-Ch., Koning, A.J., Forrest, R.A., Kopecky, J., The JEFF-3.0/A Neutron Activation File—New Features, Validation, and Usage, AIP Conference Proceedings, vol. 769, 2005, pp.203-206.

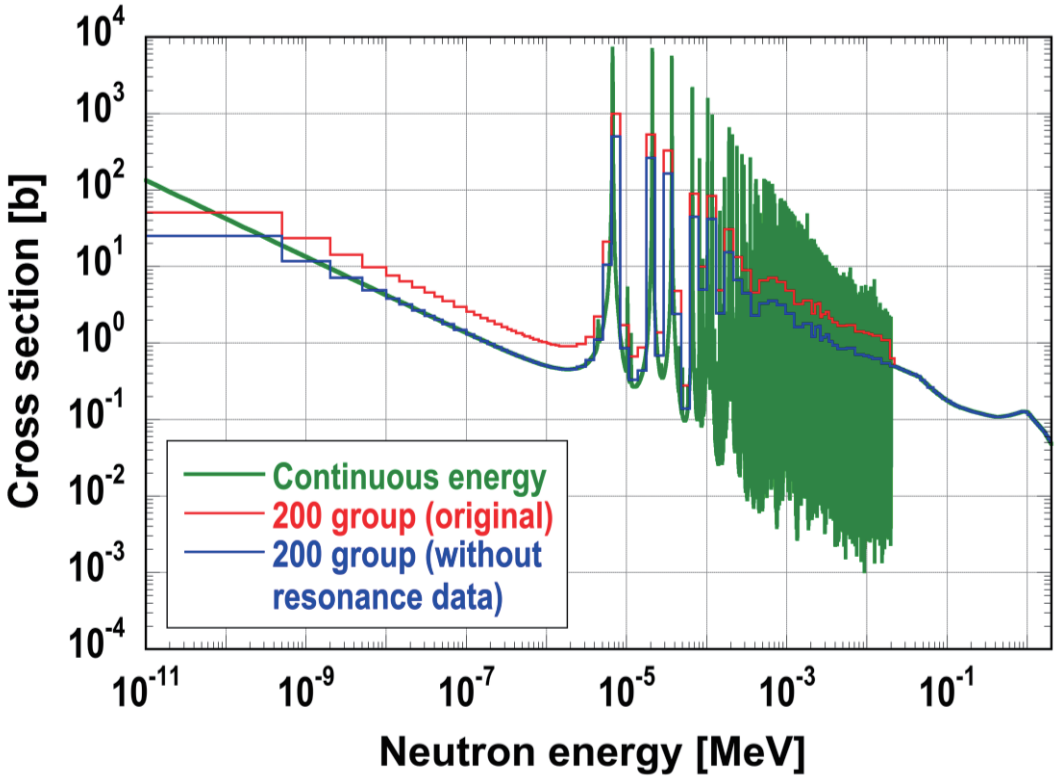

Fig. 1 Capture cross section of ^{238}U in JENDL/AD-2017.

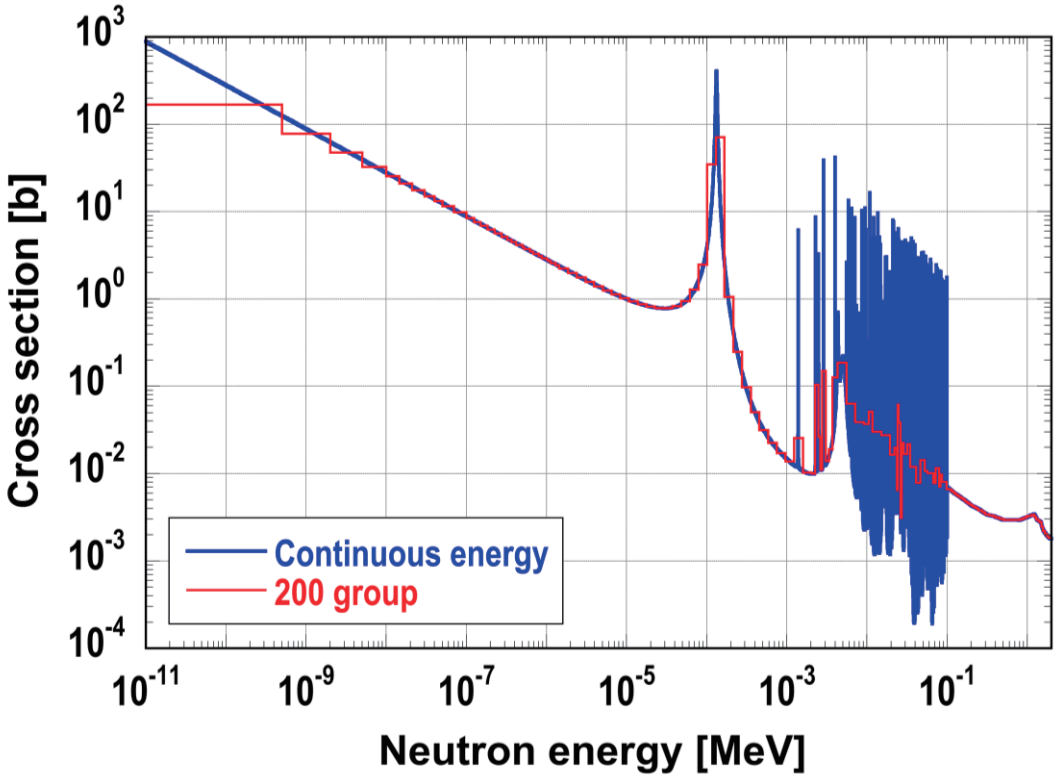

Fig. 2 Cross section of ^{59}Co(n,γ)^{60g}Co in JENDL/AD-2017.

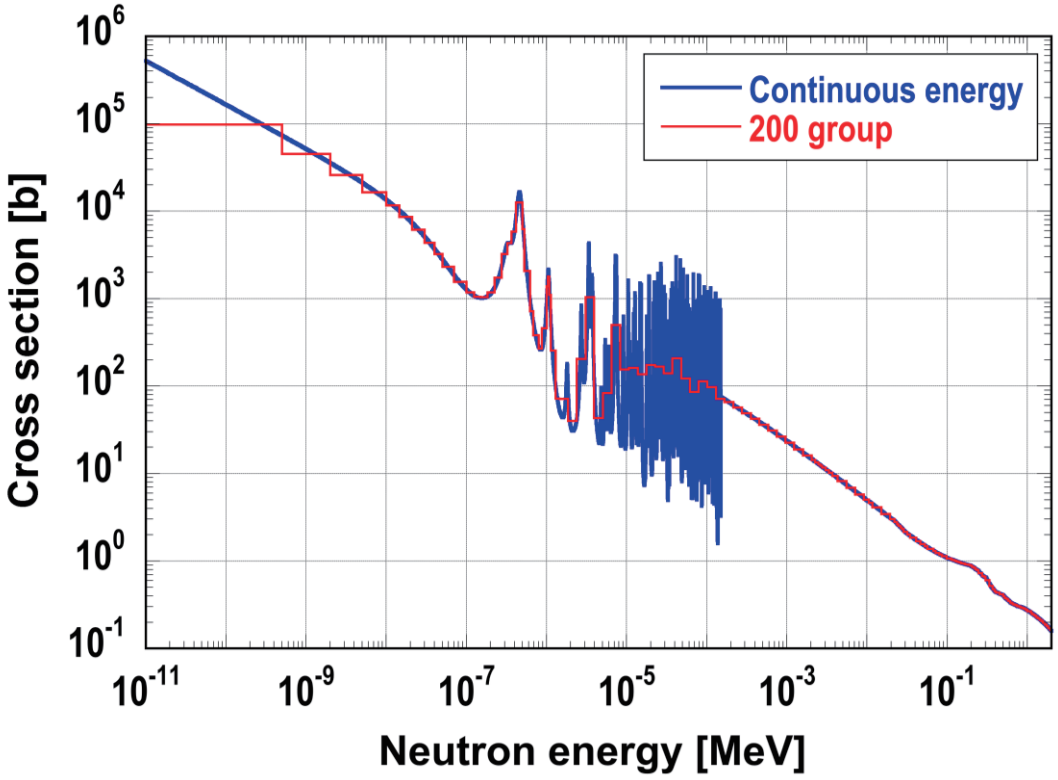

Fig. 3 Cross section of ^{151}Eu(n,γ)^{152g}Eu in JENDL/AD-2017.

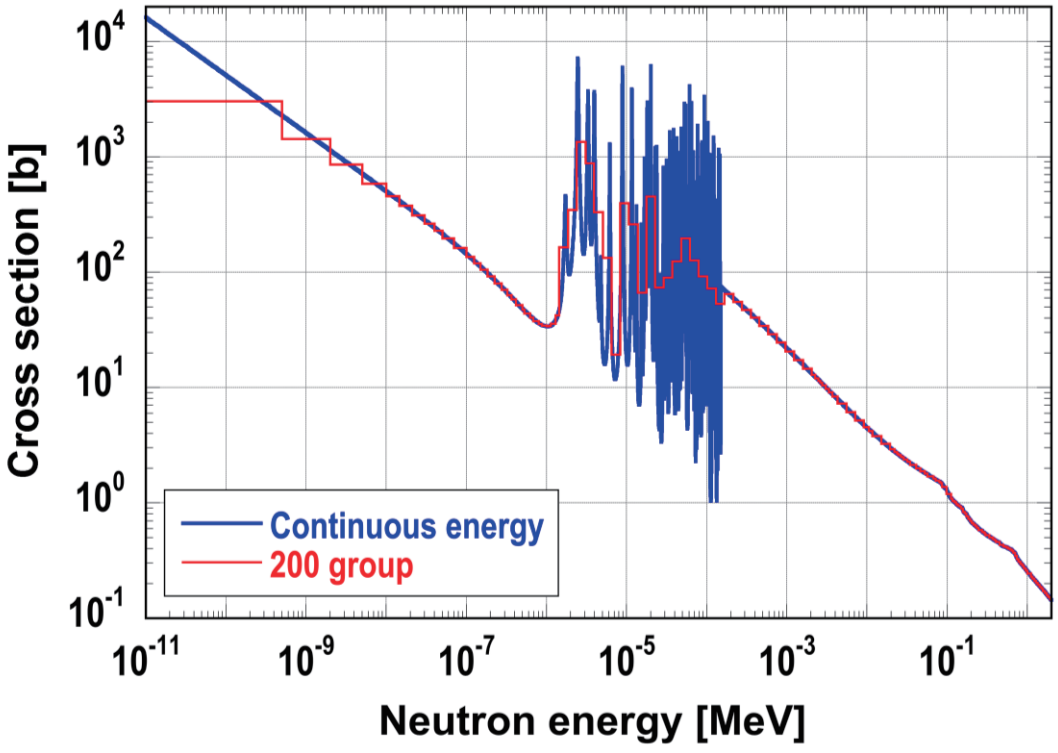

Fig. 4 Cross section of ^{153}Eu(n,γ)^{154g}Eu in JENDL/AD-2017.

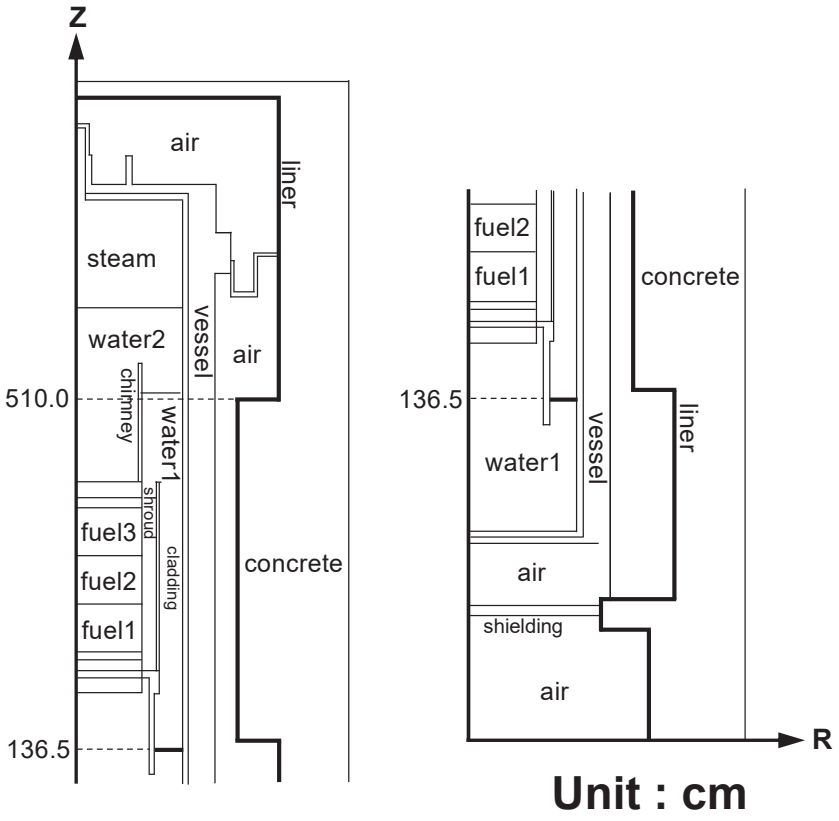

Fig. 5 Two-dimensional JPDR calculation model. Only the colored region was used in DORT calculation.

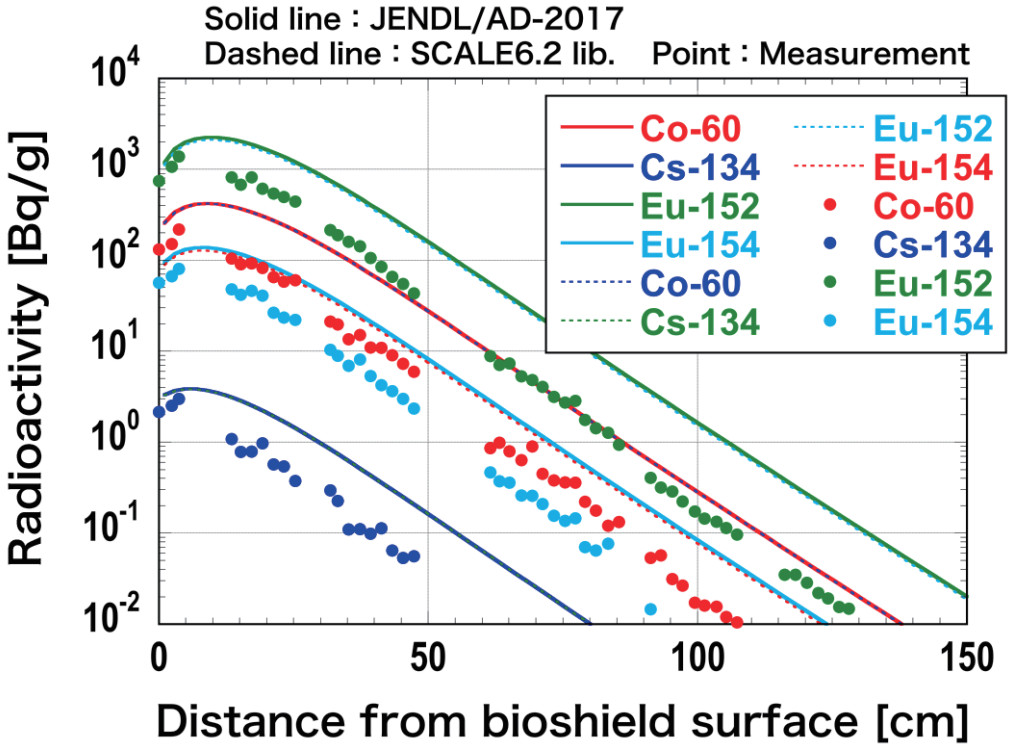

Fig. 6 Radioactivity distribution at Z=340 cm (cooling : 15 years).

25. Experimental plan for displacement damage cross sections using 120-GeV protons at Fermi National Accelerator Laboratory

Yosuke IWAMOTO[1,2*], Makoto YOSHIDA[3], Shin-ichiro MEIGO[2], Katsuya YONEHARA[4], Taku ISHIDA[3], Keita NAKANO[2], Shin-ichiro ABE[1], Hiroki IWAMOTO[1,2], T. SPINA[4], K. AMMIGAN[4], N. MOKHOV[4], Atsushi YABUUCHI[5], and Toshimasa YOSHIIE[5]

[1]Nuclear Science and Engineering Center, Japan Atomic Energy Agency
2-4 Shirakata, Tokai, Naka, Ibaraki 319-1195, Japan

[2]J-PARC Center, Japan Atomic Energy Agency
2-4 Shirakata, Tokai, Naka, Ibaraki 319-1195, Japan

[3]J-PARC Center, High Energy Accelerator Research Organization
1-1 Oho, Tsukuba, Ibaraki 305-0801, Japan

[4]Fermi National Accelerator Laboratory
Batavia IL 60510-5011, U.S.

[5]Institute for Integrated Radiation and Nuclear Science, Kyoto University
2, Asashiro-Nishi, Kumatori, Sennan, Osaka 590-0494, Japan

[*]Email: iwamoto.yosuke@jaea.go.jp

For the validation of the number of displacements per atom (dpa) calculated by Monte Carlo codes, an experimental program has been launched to measure displacement cross sections of metals with 120-GeV protons at Fermilab Test Beam Facility (FTBF) in Fermi National Accelerator Laboratory (FNAL). Experiments will be performed at the M03 beam line high-rate tracking area in FTBF in the US fiscal year 2022 (October 2021 – September 2022). For the preparation of experiments, the sample assembly with four-wire samples of aluminum, copper, niobium and tungsten with 250-μm diameter have been developed. The sample assembly will be maintained at around 4 K by using a Gifford–McMahon (GM) cryocooler in a vacuum chamber. Then, changes in the electrical resistivity of samples will be obtained under 120-GeV proton irradiation. To obtain a sufficient resistance increase under the beam irradiation, approximately 40 hours is needed for all samples. Recovery of the accumulated defects through isochronal annealing, which is related to the defect concentration in the sample, will also be measured after the cryogenic irradiation.

1. Introduction

To predict the operating lifetime of materials in high-energy radiation environment at accelerator facilities, Monte Carlo codes such as PHITS[1,2,3], MARS[4], and FLUKA[5] are used to calculate the number of displacements per atom (dpa) related to the number of Frenkel pairs. The Norgertt–Robinson–Torrens (NRT) model has been widely used to predict the number of the "initial" Frenkel pairs (NRT-

dpa) [6]. For more accurate estimation of the actual damage production, athermal-recombination-corrected displacement damage (arc-dpa) was proposed [7]. For the validation of codes, it is necessary to measure displacement cross-sections of metals in relation to changes in electrical resistivity at cryogenic temperature (around 4 K) where the recombination of Frenkel pairs by thermal motion is well suppressed.

To validate the code, we developed the cryogenic irradiation chamber and measured displacement cross section of copper with 125 MeV protons [8], data of aluminum, copper and tungsten with 200 and 389 MeV protons [9,10], and data of copper and iron with 0.4 – 3 GeV protons [11], respectively. The comparison of displacement cross sections between the data and calculated results indicates that the arc-dpa results are in a good agreement with the data while the NRT-dpa results are larger than the data by about a factor of three. The measurement of aluminum, copper, iron and tungsten with 30-GeV protons will be performed at J-PARC. Since there is no experimental data with energy over 30 GeV, we have launched an experimental program to measure displacement cross sections of metals with 120-GeV protons at Fermilab Test Beam Facility (FTBF) in Fermi National Accelerator Laboratory (FNAL). In this paper, we introduce the experimental plan and the progress of the preparation.

2. Experimental plan and progress of the preparation

2.1. Experimental device

Experiments will be performed at the M03 beam line high-rate tracking area in FTBF in the US fiscal year 2022 (October 2021 – September 2022). The beam consists of 120 GeV protons. The length of spill is 4.2 seconds and approximate repetition is 60 seconds. Figure 1 shows the layout of the experimental area at M03 and picture of the irradiation chamber with the cold head of the Gifford-McMahon (GM) cooler (RDK-408D2, Sumitomo Heavy Industries, Ltd.) with 1.0 W cooling capacity at 4.2 K.

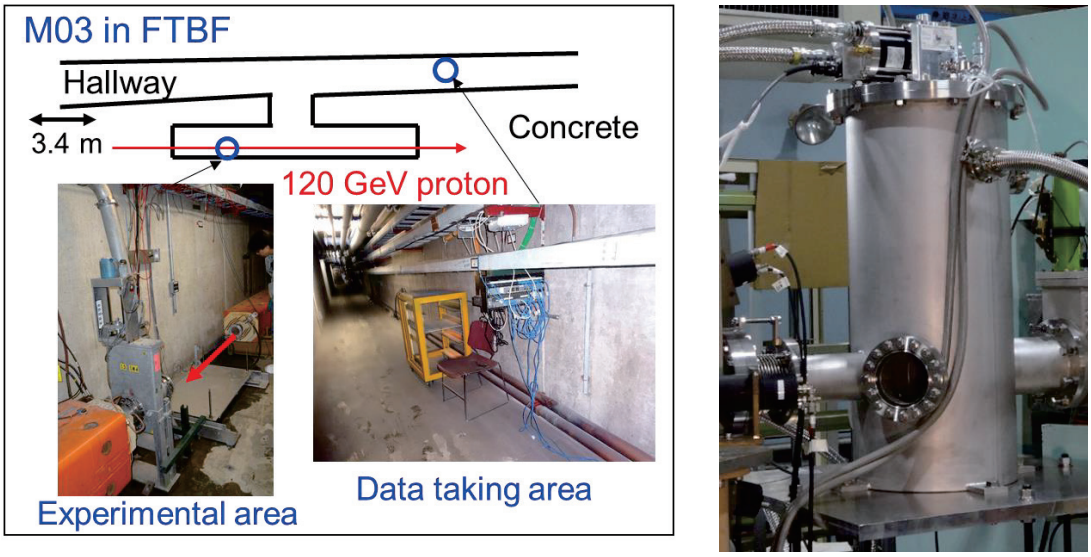

Figure 1: The experimental area at M03 (left) and an irradiation chamber with the GM cooler (right).

The irradiation chamber developed in our previous study [9,10] will be put on the beam line in the experimental area. A data taking system and the helium gas compressor for the operation of the GM cryocooler will be set at the data taking area. A segmented wire ionization chamber (SWIC) will be installed for the beam profile at front and back of the irradiation chamber. Beam scan is possible in

horizontal and vertical directions with SWIC. An ion chamber operational in the upstream enclosure in the same beamline will be used for the beam current measurement. Figure 2 shows layout of the irradiation chamber drawn by PHITS.

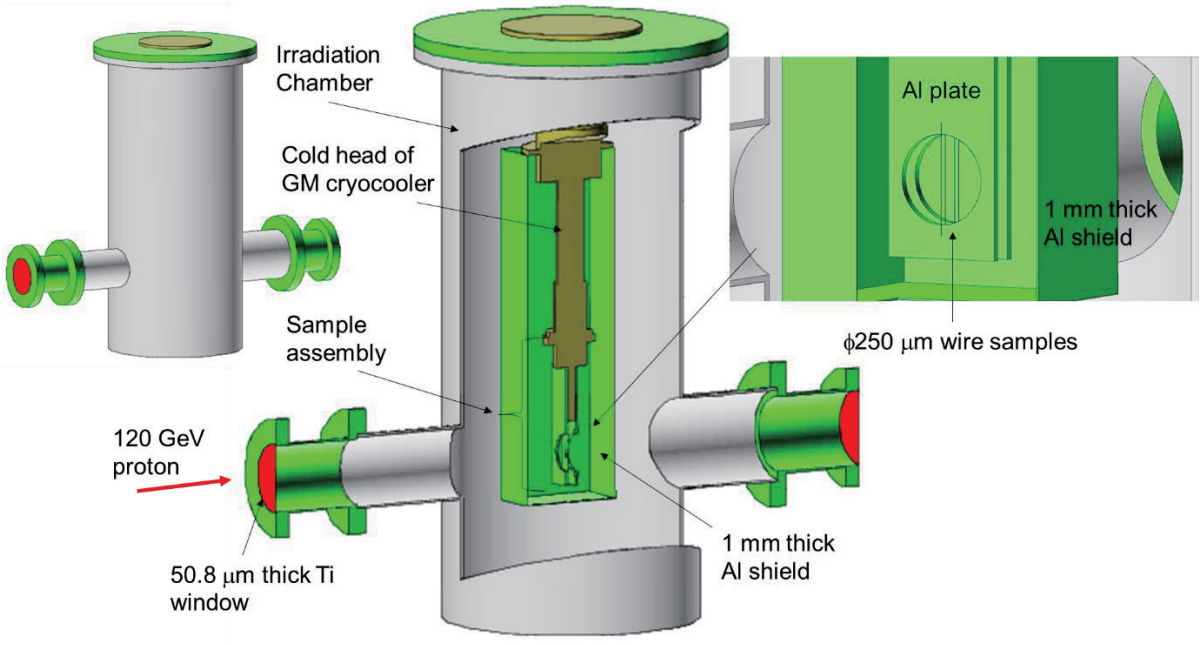

Figure 2: Layout of the irradiation chamber with the cold head of the GM cryocooler drawn by PHITS.

The sample assembly is connected with the cold head of the GM cryocooler and 1-mm-thick aluminum shields cover the entire sample assembly to intercept any thermal radiation from the irradiation chamber. Two 50.8 μm thick titanium windows will be connected with the irradiation chamber as a vacuum partition. Figure 3 shows the sample assembly connected with the cold head of the GM cryocooler in the irradiation chamber and the data taking system.

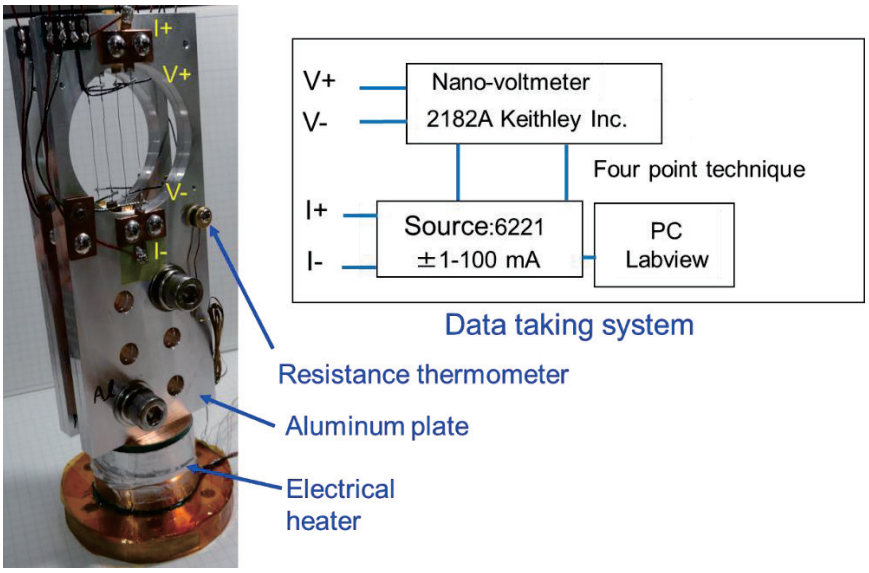

Figure 3: The sample assembly connected with the cold head of the GM cryocooler in the irradiation chamber (left) and the data taking system (right).

The aluminum plate is a support plate of a wire sample with a beam hole open to the beam. A root mean square (RMS) beam size can be 4 mm for protons. Since a 5-sigma of beam size or more is needed for the beam clearance in this experimental area at M03, the diameter of the beam hole was set to 48 mm (6-sigma). Since beam loss permits less than 3 % of the interaction length at M03, which is 12 mm for 120 GeV proton on aluminum, we cannot use aluminum nitride plates and the aluminum plates covering the sample wire in the beam line in the same way as our previous experiments at RCNP, Osaka university [9,10]. In the experiment at M03, four wire samples, aluminum, copper, niobium, and tungsten, with a 250-μm diameter were attached as shown in Figure 3 to minimize a beam loss. Before attaching an aluminum plate, wire samples were annealed with a vacuum electric furnace for aluminum and copper and an electron gun for niobium and tungsten. Table 1 lists the annealing temperature for these samples.

Table 1: Melting point, annealing temperature and annealing time for wire samples.

	Melting point (K)	**Annealing temperature (K)**	**Time (min.)**
Al	933.5	840	30
Cu	1358	1289	30
Nb	2750	1923	15
W	3695	2473	15

Annealing under vacuum conditions (~10^{-4} Pa) was performed by heating the samples to the temperatures shown in Table 1.

The electrical resistance of wire will be measured using an apparatus combining a current source (model 6221, Keithley Instruments Inc.) and a nano-voltmeter (model 2182A, Keithley Instrument Inc.). This apparatus is based on four-point technique with cancel effects of thermal electromotive force. The precision of the electrical resistance at 3 K was 0.001 μΩ. A CX1050-CU-HT Cernox resistance thermometer was attached in the aluminum plate near samples. A 48 Ω electrical heater was attached to the copper block for the study of the recovery of accumulated defects through isochronal annealing after the cryogenic beam irradiation. The measurement procedure of recovery of defect is as follows: the sample is warmed to the annealing temperature with a heater, and sample temperature holds with constant for about 10 minutes. After the sample is cooled to 4 K by the GM cryocooler, electrical resistivity of the sample is measured [8-11].

2.2. Estimation of required beam time and heat load

The required beam time for this experiment was estimated from arc-dpa displacement cross sections calculated by PHITS. The displacement cross section σ can be related to the resistivity increase and the beam fluence:

$$\sigma = \frac{1}{\rho_{FP}} \frac{\Delta\rho_{sample}}{\phi} \tag{1}$$

$$\Delta\rho_{sample} = \frac{A}{L} \Delta R_{sample} \tag{2}$$

where ρ_{FP} is the Frenkel pair resistivity of sample, ϕ is the beam fluence, $\Delta\rho_{sample}$ is the electrical resistivity change of sample and ΔR_{sample} is the electrical resistance change under the beam irradiation. Table 2 lists the estimation of the required beam fluence for samples.

Table 2: Estimation of required beam fluence.

	Al	Cu	Nb	W
Calculated arc-dpa displacement cross section σ (m^2)	2.36×10^{-26}	9.44×10^{-26}	1.66×10^{-25}	2.9×10^{-25}
Frenkel pair resistivity ρ_{FP} (μΩm)	3.7	2.2	14	27
Length of two potential points (mm)	40	37.5	38.5	37.5
Geometry factor (A/L) (m)	4.91×10^{-6}	5.24×10^{-6}	5.10×10^{-6}	5.24×10^{-6}
Resistance increase ΔR_{sample} (μΩ)	0.4	1.0	10	35
Beam fluence ϕ ($1/m^2$)	2.25×10^{19}	2.52×10^{19}	2.19×10^{19}	2.34×10^{19}

In Table 2, the arc-dpa displacement cross section σ was calculated by PHITS, ρ_{FP} was obtained from Ref. [12], and the geometry factor was obtained by the ratio of the area (A) of the cross section of the wire to the length of two potential points (L) of the wire. ϕ was estimated with ΔR_{sample}, which is a measurable value. On the other hands, the proton beam intensity is around 5×10^{11} (protons/minute) and estimated beam area is about 5×10^{-5} (m^2) at M03. In this beam condition, the beam fluence on the wire sample is 1.2×10^{19} (protons/m^2) for 20 hours irradiation, 2.4×10^{19} (protons/m^2) for 40 hour irradiation, and 3.6×10^{19} (protons/m^2) for 60 hours irradiation, respectively. To obtain the resistance increase listed in Table 2, approximately 40 hour irradiation is needed.

Since the cold head of the GM cooler has 1.0 W cooling capacity at 4.2 K, we estimated the heat load of beam in the cold head and sample wires using PHITS. The heat load in the cold head was regarded as a sum of the energy deposition in the cold head, the sample assembly including wire samples and the 1 mm thick aluminum shields as shown in Figure 2. Table 3 lists the heat loads in the wire samples and the cold head calculated by PHITS.

Table 3: Heat load in wire samples and cold head calculated by PHITS.

	Heat load	
	J/proton	J/shot
Wire samples	4.81×10^{-14}	2.41×10^{-2}
Cold head	5.68×10^{-13}	2.84×10^{-1}

The beam intensity was estimated to be 5×10^{11} (protons/shot). Since the results are lower than 1 W, the cooling power of the cold head is enough to cool samples during the beam irradiation.

3. Summary

The paper describes the plan to measure displacement cross sections of aluminum, copper, niobium and tungsten with 120-GeV protons at FTBF in FNAL. Experiments will be performed at the M03 beam line

high-rate tracking area. For preparation of experiments, we developed the sample assembly with four wire sample with 250-μm diameter. The sample assembly will be maintained at around 4 K by using the GM cryocooler in a vacuum chamber. Then, changes in the electrical resistivity of samples will be obtained under 120-GeV proton irradiation. To obtain the sufficient resistance increase under the beam irradiation, approximately 40 hours is needed for all samples. The cooling power of the cold head is enough to cool samples during the beam irradiation. Recovery of the accumulated defects through isochronal annealing will also be measured after cryogenic irradiation.

References

[1] Sato, T. et al., Features of Particle and Heavy Ion Transport code System (PHITS) version 3.02, J. Nucl. Sci. Technol., vol.55, 2018, pp.684-690.

[2] Iwamoto, Y. et al., Calculation of displacement cross-sections for structural materials in accelerators using PHITS event generator and its applications to radiation damage, J. Nucl. Sci. Technol., vol.51, 2013, pp.98-107.

[3] Iwamoto, Y. et al., Estimation of reliable displacements-per-atom based on athermal-recombination-corrected model in radiation environments at nuclear fission, fusion, and accelerator facilities, J. Nucl. Mater., vol.538, 2020, 152261.

[4] Mokhov, N.V. and James, C.C., The MARS code system user's guide, version 15 (2016), Fermilab-FN-1058-APC, 2017; https://mars.fnal.gov (accessed:2021-11-17).

[5] Böhlen. T.T. et al., The FLUKA code: developments and challenges for high energy and medical applications, Nucl. Data Sheets, vol.120, 2014, pp.211-214.

[6] Norgett, M.J. et al., A proposed method of calculating displacement dose rates, Nucl. Eng. Des., vol.33, 1975, pp. 50-54.

[7] Nordlund, K. et al., Primary radiation damage: a review of current understanding and models, J. Nucl. Mater., vol.512, 2018, pp. 450-479.

[8] Iwamoto, Y. et al., Measurement of the displacement cross-section of copper irradiated with 125 MeV protons at 12 K, J. Nucl. Mater., vol.458, 2015, pp. 369-375.

[9] Iwamoto, Y. et al., Measurement of displacement cross sections of aluminum and copper at 5 K by using 200 MeV protons, J. Nucl. Mater., vol.508, 2018, pp. 195-202.

[10] Iwamoto, Y. et al., Measurements of displacement cross section of tungsten under 389-MeV proton irradiation and thermal damage recovery, Materials Science Forum, vol.1024, 2021, pp. 95-101.

[11] Matsuda, H. et al., Measurement of displacement cross-sections of copper and iron for proton with kinetic energies in the range 0.4 – 3 GeV, J. Nucl. Sci. Technol., vol.57, 2020, pp.1141-1151.

[12] Broeders, C.H.M, and Konobeyev, A.Yu., Defect production efficiency in metals under neutron irradiation, J. Nucl. Mater., vol.328, 2004, pp. 197-214.

Acknowledgements

The authors wish to express their gratitude to Dr. Adam C. Watts and the staff at FNAL for their generous support. This work is supported by JSPS KAKENHI Grant Number JP19H02652 and performed under the Radiation Damage In Accelerator Target Environments (RaDIATE) international collaboration.

26. Comparison of photon spectra emitted from fuel debris using different decay data libraries

Taichi MATSUMURA*, Keisuke OKUMURA, and Manabu FUJITA
Collaborative Laboratories for Advanced Decommissioning Science (CLADS), Japan Atomic Energy Agency (JAEA),
790-1 Ootsuka, Motooka, Tomioka-machi, Futaba-gun, Fukushima, 979-1151, Japan

We compared the photon spectra calculated for the fuel debris using three recent decay data libraries: JENDL/DDF-2015, the decay sub-libraries of ENDF/B-VIII.0 and JEFF-3.3. We found that X-ray data for ^{137m}Ba, γ-ray data for ^{241}Am at 60 keV, and γ-ray data for ^{106}Rh in the energy region 3.0–3.4 MeV are missing in JENDL/DDF-2015. In addition, we found that the 33 radioactive daughter nuclides are not defined in the decay chains in JENDL/DDF-2015.

1. Introduction

Evaluated nuclear data has been used for the development of new sensors, non-destructive assay technologies, and the optimization of radiation shielding in connection with the decommissioning of the Fukushima Daiichi Nuclear Power Station (1F). We need reliably evaluated nuclear data in order to determine the radiation characteristics of the fuel debris. However, different collections of evaluated nuclear data give different results, and it has been difficult to clarify the causes of the differences. This is because different decay calculation codes deal with so many different nuclides and their decay data in different numerical solutions and different conditions. To overcome this problem, we have developed a reliable new code for calculating the radiation decay and radioactive-source spectra, and it can accurately treat large amounts of nuclides and all the decay modes in the decay data library.

In this study, we focused on the photon spectrum of the fuel debris, and we investigated the causes of the differences in the photon spectra calculated by our new code using three evaluated decay data libraries: JENDL/DDF-2015 [1], the decay sub-libraries of ENDF/B-VIII.0 [2] and JEFF-3.3 [3]. We expect the results to be reflected in the next JENDL release (e.g., JENDL-5) and to be utilized as reliable nuclear data for Fukushima 1F R&D.

2. Method

In this study, we calculated the X-rays and γ-rays emitted from the Fukushima fuel debris using JENDL/DDF-2015, ENDF/B-VIII.0, and JEFF-3.3 as follows. As shown in Fig.1, in the first step, we performed a three-dimensional fuel-inventory calculation, taking into account the burnup and void distributions in the core of unit-2. We also performed an activation calculation for the structural materials in the core. Then we mixed all the nuclides so-obtained together to imitate the fuel debris. In the second step, we calculated the amounts of all the nuclides remaining after the 10 years that have passed since the 1F

accident. We used the Chebyshev rational-approximation method (CRAM), in which the complete nuclear-transmutation matrix from each decay library can be considered. Finally, we evaluated the photon spectrum using the photon-emission data from each decay data library. Since the photon spectrum of the fuel debris consists of many line spectra with different energies, for easy comparison we converted the photon spectrum into the 18-energy-group structure (Table 1) used in the ORIGEN-S code [4].

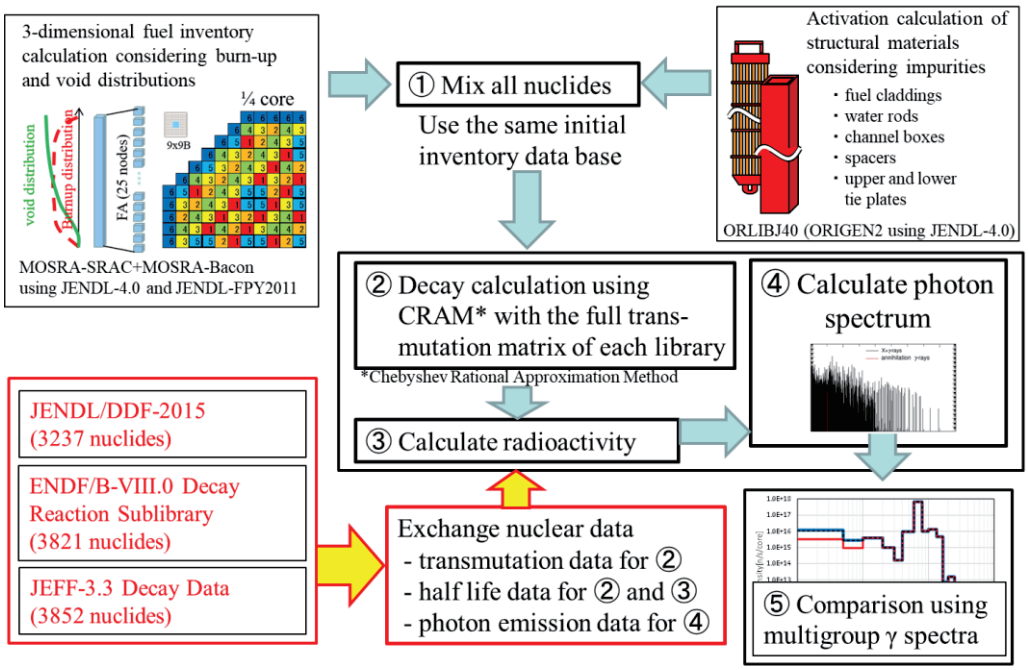

Figure 1 Method used to calculate the photon spectrum.

Table 1 18-energy-group structure.

	Group Energy (MeV)		
Group	Lower boundary	Upper boundary	Average
1	8.00E+00	1.00E+01	9.00E+00
2	6.50E+00	8.00E+00	7.25E+00
3	5.00E+00	6.50E+00	5.75E+00
4	4.00E+00	5.00E+00	4.50E+00
5	3.00E+00	4.00E+00	3.50E+00
6	2.50E+00	3.00E+00	2.75E+00
7	2.00E+00	2.50E+00	2.25E+00
8	1.66E+00	2.00E+00	1.83E+00
9	1.33E+00	1.66E+00	1.50E+00
10	1.00E+00	1.33E+00	1.17E+00
11	8.00E-01	1.00E+00	9.00E-01
12	6.00E-01	8.00E-01	7.00E-01
13	4.00E-01	6.00E-01	5.00E-01
14	3.00E-01	4.00E-01	3.50E-01
15	2.00E-01	3.00E-01	2.50E-01
16	1.00E-01	2.00E-01	1.50E-01
17	5.00E-02	1.00E-01	7.50E-02
18	1.00E-02	5.00E-02	3.00E-02

3. Results

We compared the 18-energy-group photon spectra obtained by using decay data from JENDL/DDF-2015, ENDF/B-VIII.0, and JEFF-3.3. The results are compared in Fig. 2. The ratio of JENDL/DDF-2015 to ENDF/B-VIII.0 is 93% over the total energy range, and the actual shape of the energy spectrum is important for purposes like the development of detectors or radiation shielding. In the energy regions where there are differences, we confirmed the differences in the photon intensities of the decay data library by each nuclide. We extracted nuclides that do not emit X-rays or γ-rays or those for which the intensity is smaller compared with other libraries, especially those that have a strong influence on photon intensities in the 18-energy-group structure.

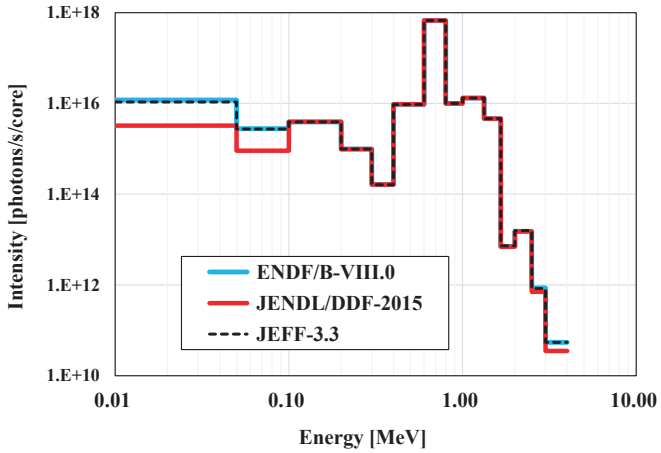

Figure 2 The different photon spectra obtained using recent decay data libraries for the Fukushima fuel debris 10 years after the 1F accident (using core-averaged values for unit-2 in 2021, for which there was no volatile fission-product release).

In the energy region from 10–50 keV, X-rays from ^{137m}Ba are not defined in JENDL/DDF-2015 and are therefore underestimated. Figure 3 shows the photon intensities of the ^{137m}Ba line spectra evaluated from JENDL/DDF-2015 and ENDF/B-VIII.0. In JENDL/DDF-2015, the X-ray intensities are defined for most of nuclides, but not for ^{137m}Ba. Although the half-life of ^{137m}Ba is short (about 2.6 min.), the X-rays from ^{137m}Ba are not negligible because this (nuclear) state is produced by the β^- decay of a large amount of ^{137}Cs, which has a half-life of about 30 years.

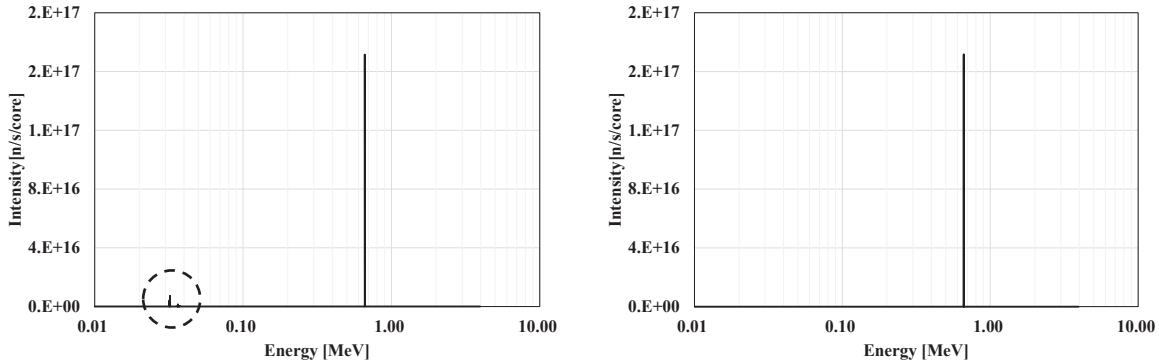

Figure 3 Photon spectra of ^{137m}Ba using ENDF/B-VIII.0 (left) and JENDL/DDF-2015 (right)

In the energy region from 50–100 keV, JENDL/DDF-2015 underestimates the γ-rays from ^{241}Am because they are not defined in this library. Figure 4 shows the ^{241}Am line spectra from JENDL/DDF-2015 and ENDF/B-VIII.0. The famous γ-ray line at 59.5 keV is defined in ENDF/B-VIII.0, but not in JENDL/DDF-2015. In addition, photons with strong intensities are observed at lower energies only in ENDF/B-VIII.0.

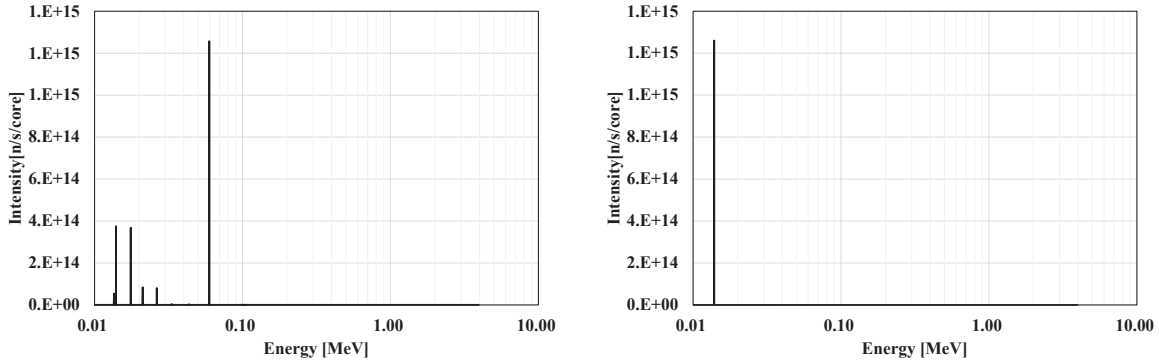

Figure 4 Photon spectra of ^{241}Am using ENDF/B-VIII.0 (left) and JENDL/DDF-2015 (right).

In the energy region from 3–3.4 MeV, JENDL/DDF-2015 underestimates the γ-rays from ^{106}Rh, because the γ-ray production is smaller in this energy region than is that obtained from ENDF/B-VIII.0. Figure 5 shows the line spectra of photons above 1 MeV for ^{106}Rh from JENDL/DDF-2015 and from ENDF/B-VIII.0. While ENDF/B-VIII.0 defines multiple photon intensities above 3 MeV, JENDL/DDF-2015 defines only one photon intensity above 3 MeV. Although the photons from ^{106}Rh may be negligible in the fuel debris considered in this study, it is usually important as a photon source from the β^- decay of ^{106}Ru, which has a half-life of 1.0 y, and the ^{106}Rh is in radiation equilibrium.

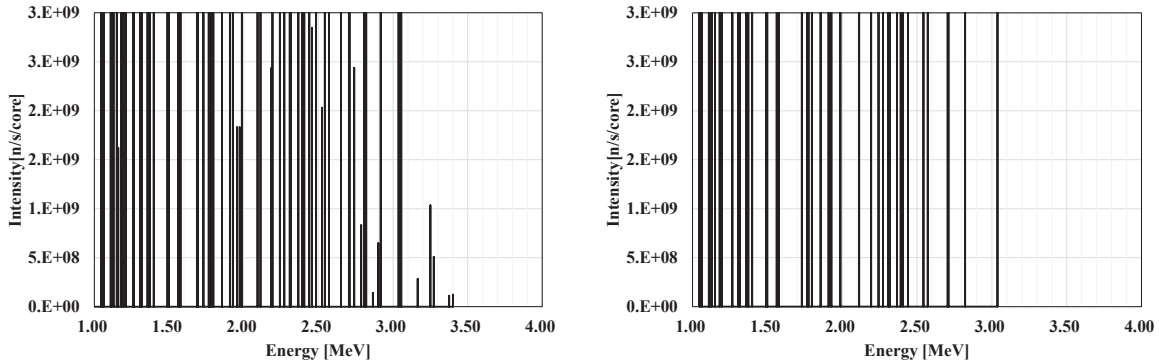

Figure 5 Photon spectra of ^{106}Rh using ENDF/B-VIII.0 (left) and JENDL/DDF-2015 (right).

By comparing the 10-year-elapsed photon spectra obtained using JENDL/DDF-2015, ENDF/B-VIII.0, and JEFF-3.3, we conclude that ^{137m}Ba, ^{241}Am, and ^{106}Rh are the main causes of the differences in the overall photon spectrum from JENDL/DDF-2015. To confirm this, we replaced the decay data for these three nuclides in JENDL/DDF-2015 with those from ENDF/B-VIII.0. The 18-energy-group spectrum obtained with the modified JENDL/DDF-2015 then agreed with those obtained using ENDF/B-VIII and JEFF-3.3, as shown in Fig. 6. The differences in the energy-integrated photon intensities became smaller, and the ratio of the modified JENDL/DDF-2015 to ENDF/B-VIII.0 improved to 99%.

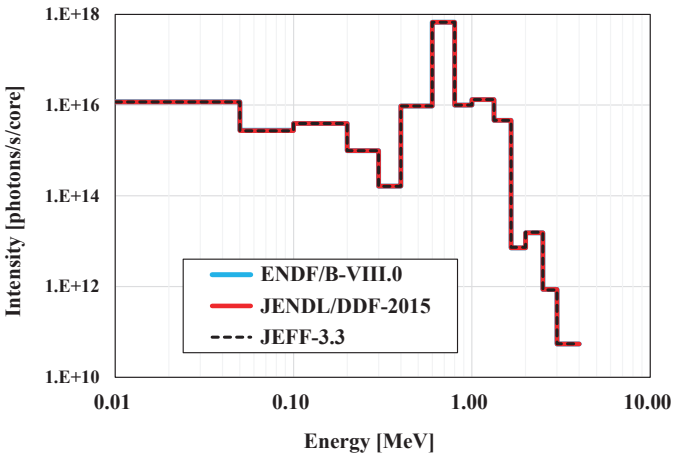

Figure 6 Modified photon spectrum.

Unlisted daughter nuclides also exist in JENDL/DDF-2015. Table 2 shows the nuclides for which the parent nuclide is defined in JENDL/DDF-2015 but the daughter nuclide is not defined, together with their main production paths. Therefore, the decay chain breaks off. For example, the α-decay of ^{239}Pu ($T_{1/2}$ = 2.4×10^4 y) is expressed as ^{239}Pu → ^{235m}U + α, but ^{235m}U does not exist in this library. As a result, the amount of ^{235}U and its daughter nuclides will be underestimated by about 20% after a long decay time such as 1000 years, because the immediate decays from ^{235m}U to ^{235}U are not counted. We found 33 nuclides for which the daughter nuclides are not defined.

Table 2 The unlisted daughter nuclides.

1	$^{9}_{3}\mathrm{Li}$ $^{9}_{5}\mathrm{B}$ $^{9}_{6}\mathrm{C}$	$^{9}_{3}\mathrm{Li} \rightarrow {}^{8}_{4}\mathrm{Be} + \beta^{-} + n$ $^{9}_{5}\mathrm{B} \rightarrow {}^{8}_{4}\mathrm{Be} + p$ $^{9}_{6}\mathrm{C} \rightarrow {}^{8}_{4}\mathrm{Be} + \beta^{+} + p$	$^{8}_{4}\mathrm{Be}$
2	$^{9}_{6}\mathrm{C}$	$^{9}_{6}\mathrm{C} \rightarrow {}^{5}_{3}\mathrm{Li} + \beta^{+} + \alpha$	$^{5}_{3}\mathrm{Li}$
3	$^{22}_{6}\mathrm{C}$	$^{22}_{6}\mathrm{C} \rightarrow {}^{20}_{7}\mathrm{N} + \beta^{-} + n + n$	$^{20}_{7}\mathrm{N}$
4	$^{110}_{53}\mathrm{I}$	$^{110}_{53}\mathrm{I} \rightarrow {}^{110}_{52}\mathrm{Te} + \beta^{+}$	$^{110}_{52}\mathrm{Te}$
5	$^{116}_{55}\mathrm{Cs}$	$^{116}_{55}\mathrm{Cs} \rightarrow {}^{115}_{53}\mathrm{I} + \beta^{+} + p$	$^{115}_{53}\mathrm{I}$
6	$^{154}_{72}\mathrm{Hf}$ $^{158}_{73}\mathrm{Ta}$	$^{154}_{72}\mathrm{Hf} \rightarrow {}^{154}_{71}\mathrm{Lu} + \beta^{+}$ $^{158}_{73}\mathrm{Ta} \rightarrow {}^{154}_{71}\mathrm{Lu} + \alpha$	$^{154}_{71}\mathrm{Lu}$
7	$^{169m}_{77}\mathrm{Ir}$	$^{169m}_{77}\mathrm{Ir} \rightarrow {}^{165m}_{75}\mathrm{Re} + \alpha$	$^{165m}_{75}\mathrm{Re}$
8	$^{171m}_{77}\mathrm{Ir}$	$^{171m}_{77}\mathrm{Ir} \rightarrow {}^{167m}_{75}\mathrm{Re} + \alpha$	$^{167m}_{75}\mathrm{Re}$
9	$^{173m}_{77}\mathrm{Ir}$	$^{173m}_{77}\mathrm{Ir} \rightarrow {}^{169m}_{75}\mathrm{Re} + \alpha$	$^{169m}_{75}\mathrm{Re}$
10	$^{170}_{76}\mathrm{Os}$	$^{170}_{76}\mathrm{Os} \rightarrow {}^{170m}_{75}\mathrm{Re} + \beta^{+}$	$^{170m}_{75}\mathrm{Re}$
11	$^{172m}_{79}\mathrm{Au}$	$^{172m}_{79}\mathrm{Au} \rightarrow {}^{168m}_{77}\mathrm{Ir} + \alpha$	$^{168m}_{77}\mathrm{Ir}$
12	$^{175m}_{79}\mathrm{Au}$	$^{175m}_{79}\mathrm{Au} \rightarrow {}^{171m}_{77}\mathrm{Ir} + \alpha$	$^{171m}_{77}\mathrm{Ir}$
13	$^{180}_{79}\mathrm{Au}$	$^{180}_{79}\mathrm{Au} \rightarrow {}^{176m}_{77}\mathrm{Ir} + \alpha$	$^{176m}_{77}\mathrm{Ir}$
14	$^{187}_{80}\mathrm{Hg}$	$^{187}_{80}\mathrm{Hg} \rightarrow {}^{183m}_{78}\mathrm{Pt} + \alpha$	$^{183m}_{78}\mathrm{Pt}$
15	$^{181}_{81}\mathrm{Tl}$	$^{181}_{81}\mathrm{Tl} \rightarrow {}^{177m}_{79}\mathrm{Au} + \alpha$	$^{177m}_{79}\mathrm{Au}$
16	$^{185m}_{81}\mathrm{Tl}$	$^{185m}_{81}\mathrm{Tl} \rightarrow {}^{181m}_{79}\mathrm{Au} + \alpha$	$^{181m}_{79}\mathrm{Au}$
17	$^{185m}_{82}\mathrm{Pb}$	$^{185m}_{82}\mathrm{Pb} \rightarrow {}^{181m}_{80}\mathrm{Hg} + \alpha$	$^{181m}_{80}\mathrm{Hg}$
18	$^{186m}_{83}\mathrm{Bi}$	$^{186m}_{83}\mathrm{Bi} \rightarrow {}^{182m}_{81}\mathrm{Tl} + \alpha$	$^{182m}_{81}\mathrm{Tl}$
19	$^{188m}_{83}\mathrm{Bi}$	$^{188m}_{83}\mathrm{Bi} \rightarrow {}^{184m}_{81}\mathrm{Tl} + \alpha$	$^{184m}_{81}\mathrm{Tl}$
20	$^{192}_{83}\mathrm{Bi}$	$^{192}_{83}\mathrm{Bi} \rightarrow {}^{188m}_{81}\mathrm{Tl} + \alpha$	$^{188m}_{81}\mathrm{Tl}$
21	$^{193}_{83}\mathrm{Bi}$	$^{193}_{83}\mathrm{Bi} \rightarrow {}^{189m}_{81}\mathrm{Tl} + \alpha$	$^{189m}_{81}\mathrm{Tl}$
22	$^{193m}_{84}\mathrm{Po}$	$^{193m}_{84}\mathrm{Po} \rightarrow {}^{189m}_{82}\mathrm{Pb} + \alpha$	$^{189m}_{82}\mathrm{Pb}$
23	$^{193m}_{83}\mathrm{Bi}$ $^{197}_{84}\mathrm{Po}$	$^{193m}_{83}\mathrm{Bi} \rightarrow {}^{193}_{82}\mathrm{Pb} + \beta^{+}$ $^{197}_{84}\mathrm{Po} \rightarrow {}^{193}_{82}\mathrm{Pb} + \alpha$	$^{193}_{82}\mathrm{Pb}$
24	$^{217}_{84}\mathrm{Po}$	$^{217}_{84}\mathrm{Po} \rightarrow {}^{213}_{82}\mathrm{Pb} + \alpha$	$^{213}_{82}\mathrm{Pb}$
25	$^{226}_{93}\mathrm{Np}$	$^{226}_{93}\mathrm{Np} \rightarrow {}^{222m}_{91}\mathrm{Pa} + \alpha$	$^{222m}_{91}\mathrm{Pa}$
26	$^{230}_{93}\mathrm{Np}$	$^{230}_{93}\mathrm{Np} \rightarrow {}^{226m}_{91}\mathrm{Pa} + \alpha$	$^{226m}_{91}\mathrm{Pa}$
27	$^{239}_{94}\mathrm{Pu}$	$^{239}_{94}\mathrm{Pu} \rightarrow {}^{235m}_{92}\mathrm{U} + \alpha$	$^{235m}_{92}\mathrm{U}$
28	$^{238}_{95}\mathrm{Am}$	$^{238}_{95}\mathrm{Am} \rightarrow {}^{234m}_{93}\mathrm{Np} + \alpha$	$^{234m}_{93}\mathrm{Np}$
29	$^{240}_{98}\mathrm{Cf}$	$^{240}_{98}\mathrm{Cf} \rightarrow {}^{236}_{96}\mathrm{Cm} + \alpha$	$^{236}_{96}\mathrm{Cm}$
30	$^{254}_{98}\mathrm{Cf}$	$^{254}_{98}\mathrm{Cf} \rightarrow {}^{250}_{96}\mathrm{Cm} + \alpha$	$^{250}_{96}\mathrm{Cm}$
31	$^{243}_{99}\mathrm{Es}$	$^{243}_{99}\mathrm{Es} \rightarrow {}^{239}_{97}\mathrm{Bk} + \alpha$	$^{239}_{97}\mathrm{Bk}$
32	$^{245}_{100}\mathrm{Fm}$	$^{245}_{100}\mathrm{Fm} \rightarrow {}^{241}_{98}\mathrm{Cf} + \alpha$	$^{241}_{98}\mathrm{Cf}$
33	$^{249}_{101}\mathrm{Md}$ $^{253}_{102}\mathrm{No}$	$^{249}_{101}\mathrm{Md} \rightarrow {}^{249}_{100}\mathrm{Fm} + \beta^{+}$ $^{253}_{102}\mathrm{No} \rightarrow {}^{249}_{100}\mathrm{Fm} + \alpha$	$^{249}_{100}\mathrm{Fm}$

4. Conclusion

We need reliable nuclear data to evaluate the radiation characteristics of fuel debris appropriately for the purpose of developing new sensors and non-destructive assay technologies and for optimizing radiation shielding for use in decommissioning. This research revealed the following main points. We found that X-ray data for ^{137m}Ba, γ-ray data for ^{241}Am at 60 keV, and γ-ray data for ^{106}Rh in the range 3.0–3.4 MeV are missing from JENDL/DDF-2015. In addition, in JENDL/DDF-2015 we found that the 33 daughter nuclides are not defined. We anticipate that these problems will be corrected in the next JENDL release.

5. References

[1] J. Katakura and F. Minato “JENDL Decay Data File 2015, JAEA-Data/Code 2015-030 (2016).

[2] D.A. Brown, et al., ENDF/B-VIII.0: the 8th major release of the nuclear reaction data library with CIELO-project cross sections, new standards and thermal scattering data. Nucl. Data Sheets, 148. 1-42 (2018).

[3] OECD/NEA Data Bank, JEFF-3.3, https://www.oecd-nea.org/dbdata/jeff/jeff33/index.html (2017).

[4] I. C. Gauld, O. W. Hermann, R. M. Westfall, Origen-S: Scale system module to calculate fuel depletion, Actinide transmutation, fission product buildup and decay, and associated radiation source terms, Vol. II (2009).

27. Experimental program of nuclear data for accelerator-driven nuclear transmutation system using FFAG accelerator –First subprogram: spallation neutron measurement

Keita NAKANO[†1], Hiroki IWAMOTO[1,2], Shin-ichiro MEIGO[1], Katsuhisa NISHIO[3], Yoshihiro ISHI[4], Kentaro HIROSE[3], Yosuke IWAMOTO[2], Yasutoshi KURIYAMA[4], Fujio MAEKAWA[1], Hiroyuki MAKII[3], Kota OKABE[1], Riccardo ORLANDI[3], Akito OIZUMI[2], Daiki SATOH[2], Fumi SUZAKI[3], Kazuaki TSUKADA[3], Tomonori UESUGI[4], Hiroshi YASHIMA[4], and Yoshiharu MORI[4]

[1]J-PARC Center, Japan Atomic Energy Agency, Tokai-mura, Ibaraki 319-1195, Japan
[2]Nuclear Science and Engineering Center, Japan Atomic Energy Agency, Tokai-mura,Ibaraki 319-1195, Japan
[3]Advanced Science Research Center, Japan Atomic Energy Agency, Tokai-mura, Ibaraki 319-1195, Japan
[4]Institute for Integrated Radiation and Nuclear Science, Kyoto University, Kumatori-cho, Osaka 590-0494, Japan,
[†]Email: nakano.keita@jaea.go.jp

Abstract

For accurate prediction of neutronic characteristics for accelerator-driven nuclear transmutation system (ADS) and a source term of spallation neutrons for reactor physics experiments for the ADS at Kyoto University Critical Assembly (KUCA), we have launched an experimental program to measure nuclear data on ADS using the Fixed Field Alternating Gradient (FFAG) accelerator at Kyoto University (Period: October 2019 – March 2023). This program consists of two subprograms, focusing on two nuclear reaction mechanisms, (1) spallation reactions and (2) high-energy fission, for incident proton energies from several tens of MeV to 100 MeV. In the first subprogram, we will measure double-differential cross-sections (DDXs) and thick-target neutron-yields (TTNYs) for several targets (*i.e.*, Pb, Bi, and Fe); in the second subprogram, mass distribution of fission product and neutron multiplicity in high energy fission of Pb and Bi will be measured. In this paper, the present status of the first subprogram is described.

1 Introduction

Accelerator-driven nuclear transmutation systems (ADSs) have attracted attention as one of the promising options to solve the nuclear issue of high-level radioactive waste management [1]. In terms of the neutronic design of the ADS, precise experimental nuclear data and reliable theoretical nuclear models are required. So far, much effort has been devoted to measure nuclear data at incident proton energies from several hundred MeV to GeV range, and these experimental nuclear data play a significant role in the improvement of the nuclear models. However, it has been pointed out that lack of nuclear data in the energy range from several tens of MeV to

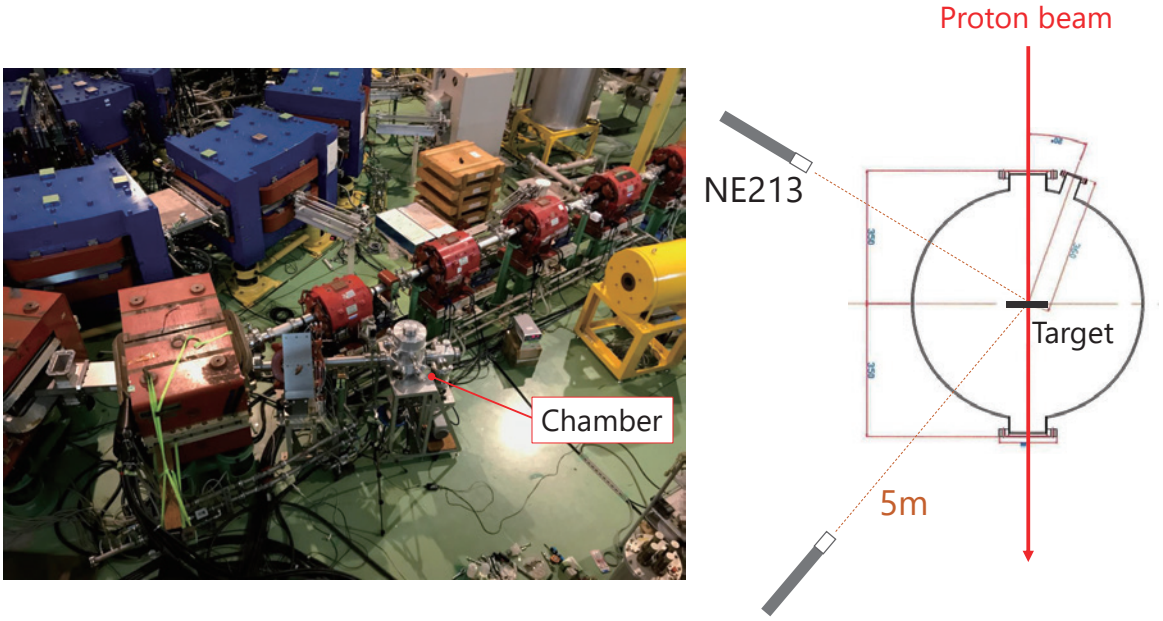

Figure 1: Schematic drawing of a vacuum chamber and neutron detectors.

100 MeV makes it difficult to improve the nuclear models, which results in large uncertainty in the neutronic characteristics of the ADS. Satoh *et al*. demonstrated that recent nuclear models such as the Liège Intranuclear Cascade model [2] failed to predict the measured spectra of emitted neutrons in the most-forward direction at the incident proton energy below 78 MeV [3]. Therefore, accumulation of experimental data on important nuclides in ADS such as neutron production cross sections in proton-induced reactions at incident energies from several tens of MeV to 100 MeV and mass distribution of fission product and neutron multiplicity from high energy fission are strongly desired.

In this circumstance, a new experimental campaign has been launched to measure nuclear data related to ADS. The campaign consists of two subprograms: measurement of neutron energy spectra from spallation reactions of Fe, Pb, and Bi by protons from several tens of MeV to 100 MeV and that of mass distribution of fission product and fission multiplicity in high energy fission of Pb and Bi. For the first subprogram, the Double-Differential neutron production cross sections (DDXs) and Thick-Target Neutron Yields (TTNYs) for such materials will be measured using a proton beam accelerated by Fixed Field Alternating Gradient (FFAG) accelerator at Kyoto University. In this paper, the experimental plan of the first subprogram and a detector test performed for the experiment are described.

2 Plan of Experiment at FFAG Facility

The experiment of the first subprogram will be conducted at FFAG Facility, Kyoto University. In this experiment, proton-induced DDXs and TTNYs for Fe, Pb, and Bi targets will be measured using the time-of-flight method. Also, sensitivity check of a ^{237}Np fission chamber under the spallation neutron field will be investigated. Figure 1 shows a photo of the FFAG facility and a schematic drawing of a vacuum chamber and neutron detectors. One of the targets is placed at the center of the chamber. Target thicknesses for the DDX experiment are 2 mm for all targets to achieve enough statistics, and those for the TTNY experiment are 30 mm for the Fe

Figure 2: Configuration of the measurement geometry at FRS.

and Pb targets and 35 mm for the Bi target, which are designed so that 150-MeV protons stop in the targets. The range of incident protons was calculated by SRIM code [4]. Diameters of the targets for both the DDX and TTNY experiments are 48 mm which is larger than beam size of 40 mm calculated by beam optics. An NE213 liquid organic scintillator (size: 20 mm in length and 8 mm in diameter) coupled with a photomultiplier tube (H3164, Hamamatsu Photonics) will be placed 5 m far from the target to detect neutrons. Signals from the detector will be fed to a digitizer (SIS3316). Current of the proton beam is planed to be 0.1 nA for the TTNY measurement and 1 nA for the DDX measurement. To eliminate contribution of room-back neutrons to the DDX and TTNY experiments, room-back neutron measurements will also be conducted with a shadow bar made of stainless steel (size: 1 m in length and 50 mm in diameter), whose length is designed to reduce the neutrons produced from the targets to several percent. Measurements at several emission angles will be conducted by changing the position of the detector. The ^{237}Np fission chamber (size: 25.4 mm in length and 6 mm in diameter) will be used to check the reaction rate under the spallation neutron field around the target vacuum chamber. The activity of coated ^{237}Np is 31.3 kBq on June 30, 1982.

3 Detector test at Facility of Radiation Standard

In advance of the experiment at the FFAG facility, measurement of neutron detection efficiency for the neutron detector (NE213 + H3164) and response of the ^{237}Np fission chamber were conducted at Facility of Radiation Standard (FRS) [5], Japan Atomic Energy Agency (JAEA). In this experiment, 14.8 MeV monoenergetic neutrons generated by T(d, n) reaction was used. The RF repetition frequency was 4 MHz. Figure 2 shows a photo of the measurement geometry. Neutrons generated at a production target directly irradiated to the neutron detectors such as the NE213 and the ^{237}Np fission chamber placed at approximately 1 m downstream to the beam port at 60 degree from the most-forward direction. The measurement with a shadow bar was also performed in the NE213 measurement to estimate background neutrons. Scintillation photons produced in the NE213 were converted to electric pulses by the photomultiplier tube and fed to the digitizer after passing through a 40 meter-long low-attenuation cable. To determine the time-of-flight, RF signals of the accelerator were used as start timing and the signals from NE213 as stop timing. The ^{237}Np fission chamber was connected to a preamplifier and a

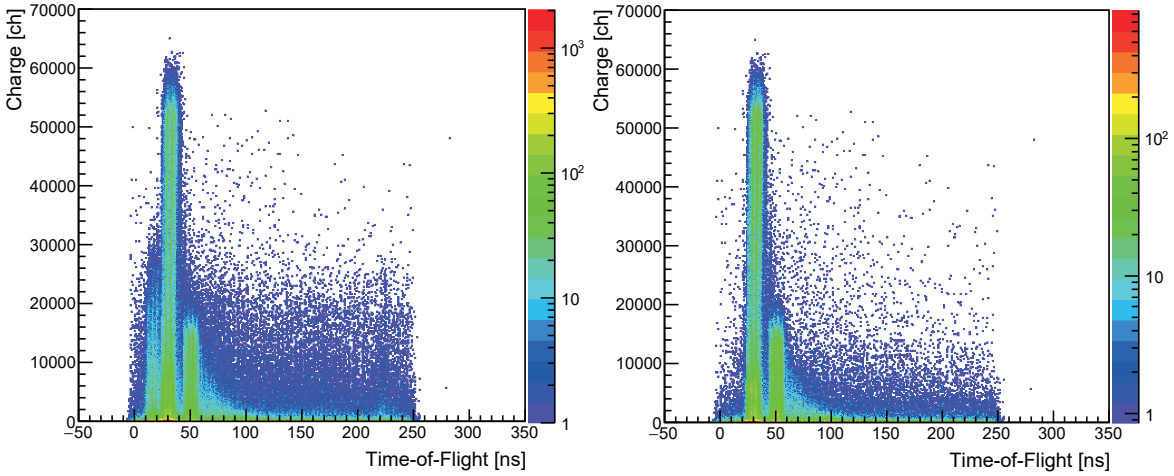

Figure 3: Two-dimensional plot of the obtained signal by the time-of-flight and the charge spectrum for the NE213 before (Left) and after (Right) the gamma-ray elimination.

spectroscopy amplifier. Then signals from the spectroscopy amplifier were fed to the digitizer and a multichannel analyzer.

4 Results and Discussion

4.1 Result for NE213 Detector

Figure 3 shows two-dimensional plot by the time-of-flight and the charge spectrum for the NE213 neutron detector. Three peaks at approximately 15, 30, and 50 ns can be seen, which correspond to prompt gamma-rays, 14.8-MeV neutrons, and 3.0-MeV parasitic neutrons, respectively. The parasitic neutrons were produced by the D(d, n) reactions between incident deuteron beam and deuterium accumulated in the tritium target. The neutron energies were estimated from the flight length and the difference of time-of-flight between the prompt gamma-rays and the neutrons. The gamma-ray events were rejected by the two-gate method of the pulse shape analysis. After eliminating the gamma-ray events, the number of detected 14.8-MeV neutrons is estimated with paying attention to the parasitic neutrons. The detection efficiency of the NE213 neutron detector was calculated from the neutron fluence measured by a reference long counter consists of a thermal neutron detector and a polyethylene moderator and the obtained counts by the NE213 neutron detector. The uncertainty of the neutron fluence measured by the long counter was 6%. Figure 4 shows the detection efficiency of the NE213 neutron detector as a function of the neutron energy. The black circles correspond to the ^{241}Am-quarter and ^{137}Cs-double biased efficiencies measured in the present experiment. Here the ^{241}Am-quarter biased efficiency means to neutron detection efficiency with larger light output than quarter of 59-keV electron equivalent (keVee) which corresponds to a photo peak of 59-keV γ-ray from ^{241}Am. Also the ^{137}Cs-double biased efficiency corresponds to that with larger output than 986 keVee [6]. The black square is the ^{241}Am-quarter biased efficiency measured in the previous experiment at lower neutron energy [7]. The solid and dashed lines are calculated efficiencies by SCINFUL-R [8, 9] code in each bias. The calculations almost reproduce the obtained data. However, small difference can be seen in the ^{241}Am-quarter biased efficiency. It is considered that the parasitic neutrons is not completely removed in the time-of-flight spectrum. Time

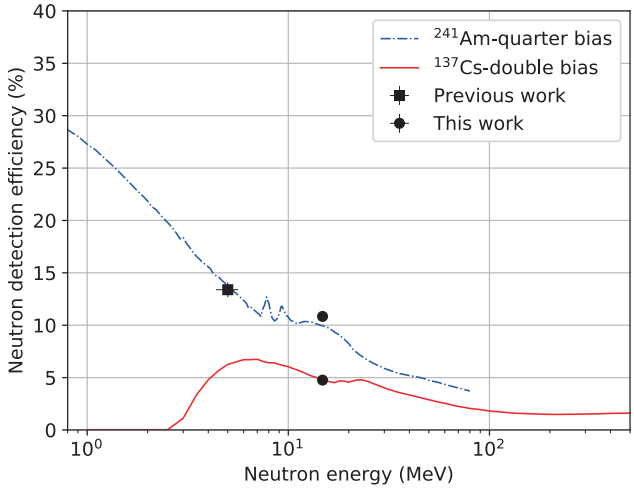

Figure 4: Detection efficiency of NE213 as a function of neutron energy [7].

resolution of the time-of-flight is approximately 4 ns which is originated from the inner clock of the digitizer, the pulse width of incident deuteron beam, and the flight path length.

4.2 Result for ^{237}Np fission chamber

Figure 5 shows charge distribution from the ^{237}Np fission chamber. The large number of low charge events and several high charge events are seen. The former is signals induced by α-decay of ^{237}Np nuclei and the latter are fission events of them. The fission events are clearly separated from the α-decay component by their much larger deposit energy. We assume that the events with charge larger than 4.5×10^4 channel are fission events. The counts per fluence is estimated to be 9.0±2.5 counts/(n/cm^2). We also derive the calculated one from fission cross section of ^{237}Np at 14.8-MeV neutron and the number of ^{237}Np nuclei calculated by the activity of deposited ^{237}Np. The calculated one is 6.8 counts/(n/cm^2), which agrees with the measured one within 1σ of the statistical error. However, the statistics is little bit poor to check the consistency between the measured count rate and the calculated one. Also, the contribution of the parasitic neutron as seen in the time-of-flight spectrum measured by the NE213 should be considered carefully because ^{237}Np has a comparable fission cross section at 3-MeV neutron energy to 14.8-MeV neutron.

5 Summary

For the development and design of ADS, more nuclear data measurements are desired especially the proton incident energy ranging from several tens of MeV to 100 MeV. In this situation, new experimental campaign has been launched to measure the TTNYs and the DDXs at FFAG facility, Kyoto University, and mass distribution of fission product and neutron multiplicity in high energy fission. At present, design of the measurement and detector tests are in progress. In advance of the experiment at FFAG, the detectors planned to be used in FFAG facility were tested with 14.8-MeV monoenergetic neutron at FRS, JAEA. The detection efficiency of NE213 liquid organic scintillator shows good agreement with calculation by SCINFUL-R. Also, count rate of ^{237}Np fission chamber under the 14.8-MeV neutron field was consistent with the calculated value from the activity of deposited ^{237}Np. From these measurements, the detector

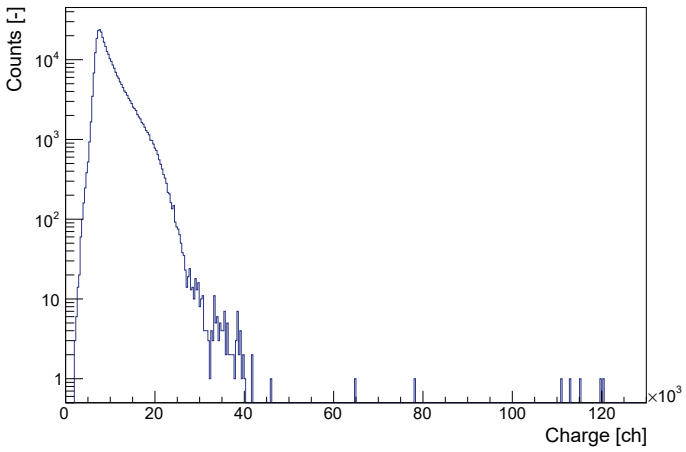

Figure 5: The measured charge distribution from ^{237}Np fission chamber.

test and response check have been done and tuning towards the FFAG experiment will be conducted.

References

[1] Tsujimoto K, Oigawa H, Ouchi N, et al. Research and Development Program on Accelerator Driven Subcritical System in JAEA. J Nucl Sci Technol. 2007;44(3):483-490.

[2] Boudard A, Cugnon J, David JC, et al. New potentialities of the Liège intranuclear cascade model for reactions induced by nucleons and light charged particles. Phys Rev C. 2013;87:014606.

[3] Satoh D, Iwamoto Y, Ogawa T. Measurement of neutron-production double-differential cross sections of ^{nat}C, ^{27}Al, ^{nat}Fe, and ^{nat}Pb by 20, 34, 48, 63, and 78 MeV protons in the most-forward direction. Nucl Instrum Meth A. 2019;920:22-36.

[4] Ziegler JF, Ziegler MD, Biersack JP. SRIM - The stopping and range of ions in matter (2010). Nucl Instrum Meth B. 2010;268(11):1818-1823.

[5] Tanimura Y, Fujii K, Tsutsumi M, et al. Neutron fluence monitoring system in monoenergetic neutron fields at FRS/JAEA. Prog Nucl Sci Technol. 2014;4:388-391.

[6] Dietze G and Klein H. Gamma-calibration of NE 213 scintillation counters. Nucl Instrum Meth. 1982;193(3):549-556.

[7] Matsuda H, Iwamoto H, Meigo S, et al. Measurement of thick target neutron yield at 180° for a mercury target induced by 3-GeV protons. Nucl Instrum Meth B. 2020;483:33-40.

[8] Dickens JK. SCINFUL: A Monte Carlo Based Computer Program to Determine a Scintillator Full Energy Response to Neutron Detection for E_n Between 0.1 and 80 MeV: User's manual and FORTRAN program listing. Oak Ridge National Lab TN (USA); 1988.

[9] Meigo S. Measurements of the response function and the detection efficiency of an NE213 scintillator for neutrons between 20 and 65 MeV. Nucl Instrum Meth A. 1997;401:365–378.

Acknowledgments

This work was supported by MEXT Innovative Nuclear Research and Development Program Grant Number JPMXD0219214562.

28. Neutron Filtering System for Fast Neutron Cross-section Measurement at ANNRI

Gerard ROVIRA[†1], Osamu IWAMOTO[1], Atsushi KIMURA[1], Shoji NAKAMURA[1], Nobuyuki IWAMOTO[1], Shunsuke ENDO[1], Tatsuya KATABUCHI[2], Kazushi TERADA[*2], Yu KODAMA[2], Hideto NAKANO[2], Jun-ichi HORI[3], and Yuji SHIBAHARA[3]

[1]Nuclear Data Center, Japan Atomic Energy Agency
[2]Laboratory for Advanced Nuclear Energy, Tokyo Institute of Technology
[3]Institute for Integrated Radiation and Nuclear Science, Kyoto University
[†]Email: gerard.rovira@jaea.go.jp

Abstract

The double-bunch pattern of the J-PARC facility introduces serious ambiguities in the neutron-induced cross-section measurement for fast neutrons. The neutron filtering technique is implemented in the ANNRI beamline in order to produce quasi-monoenergetic neutron peaks. Different filter configurations with Fe and Si were tested by means of capture and transmission experiments and with Monte-Carlo simulations using the PHITS code. In this work, the characteristics of the neutron filtering system using Fe and Si are presented together with a preliminary cross-section results for the ^{197}Au neutron capture cross-section.

1 Introduction

The double-bunch mode is employed in the Japanese Proton Accelerator Research Complex (J-PARC) in which two 0.1 μs-wide proton bunches are shot into a spallation target with a time difference of 0.6 μs at a repetition rate of 25Hz. This mode is intended to increase the thermal neutron beam intensity as, for that energy, the doublet structure of the neutron beam is negligible due to Doppler broadening and moderation time. Nonetheless, for fast neutrons experiments in the Accurate Neutron-Nucleus Reaction Measurement Instrument (ANNRI) beamline, this time difference is no longer trivial. Fast neutrons reach the target position within 10 μs and the 0.6 μs time difference becomes a significant source of ambiguities in the cross-section measurements. Neutrons detected with a certain time-of-flight (TOF) can have two different energies as it is impossible to ascertain the originating proton bunch. For example, for the case of 100 keV neutrons, the expected TOF for the NaI(Tl) spectrometer target position is about 6.4 μs. However, at 6.4 μs, neutrons with an energy of 120 keV coming from the delayed proton shot can also be detected. In this work, we propose a solution to bypass the double bunch structure of ANNRI using a neutron filtering system. The characteristics and performance of the neutron filtering system implemented at ANNRI are presented in this paper. The filtering system was analyzed using both experimental analysis and Monte-Carlo simulations.

[*]Present address: Institute for Integrated Radiation and Nuclear Science, Kyoto University

2 Neutron Filtering System

A neutron filtering system has been designed at the ANNRI beamline in order to circumvent the double-timed structure of the neutron beam within the "Study on accuracy improvement of fast-neutron capture reaction data of long-lived MAs for development of nuclear transmutation systems" project [1]. Using the neutron filtering tecnique, the incident white neutron flux can be tailored into quasi-monoenergetic peaks using materials that present a sharp minimum in the neutron total cross-section [2]. Several cylinders of ^{nat}Fe and ^{nat}Si were used in different configurations and expected to create quasi-monoenergetic filtered neutron peaks with energies of 24 keV (Fe) and 54 and 144 keV (Si).

3 Experimental Analysis

3.1 Neutron Filtering Setup

The neutron total cross-section for ^{nat}Fe and ^{nat}Si can be seen in figure 1(a). Neutron filtered peaks are expected with energies of 24, 54 and 144 keV. Three different filter assemblies consisting of 20 cm of Fe and 20 and 30 cm of Si were implemented in the rotary collimator of the ANNRI beamline (see Fig. 1(b)).

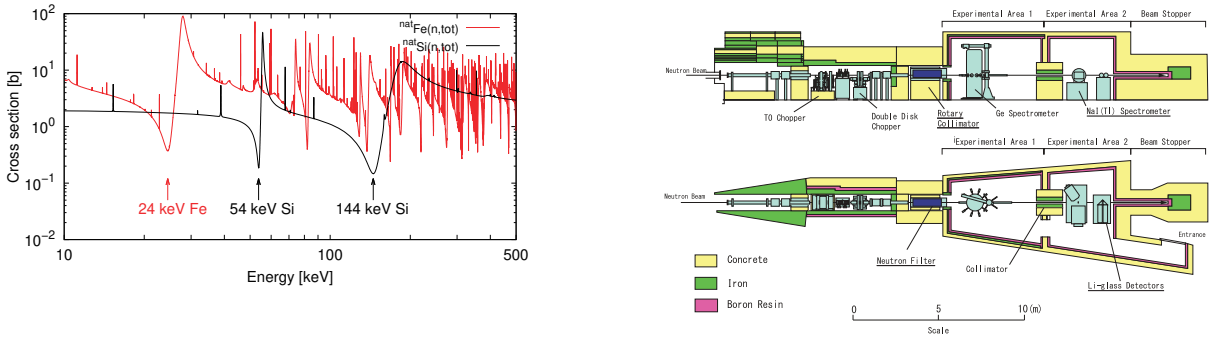

(a) (b)

Figure 1: (a)Neutron total cross-section of ^{nat}Fe and ^{nat}Si. (b) Schematic view of the ANNRI beamline. The neutron filter material was introduced in the rotary collimator.

3.2 Neutron Capture Experiments

The NaI(Tl) spectrometer of the ANNRI beamline was employed to determine the filtered incident neutron flux [3]. The samples were situated at a neutron flight path of 27.9 m. A boron sample with a 10 mm diameter and thickess of 0.5 mm and a Au sample with a 10 mm diameter and 1 mm thickness were used in the experiments. The incident neutron flux was determined by measuring the 478 kev γ-rays from the ^{10}B(n,$\alpha\gamma$)^{7}Li reaction. The Au sample measurement was used to normalize the incident neutron flux derived from the boron sample measurement at the energy point of the first resonance (4.9 eV) since it was completely saturated. More information about the experimental analysis can be found here [4].

3.3 Transmission Experiments

The incident neutron flux was also measured in transmission experiment using two types of Li-glass detectors. A Li-glass detectors enriched with ^{6}Li (GS20) and a Li-glass detector enriched with ^{7}Li (GS30) were simultaniously employed in the experiments. The detectors were situated at a flight-path of 28.6 m having the ^{7}Li enriched detector in the upstream position. The GS20 detector is used to detect the incident neutrons via the ^{6}Li(n,α)^{4}He reaction whereas GS30 detector is employed to estimate the background due to γ-rays. Further details on the transmission analysis are provided there [5].

3.4 Experimental Results

The results obtained from both experimental techniques provide very good agreement and are able to show the filtering performance of the neutron filtering system. The results for the Fe filter array of 20 cm is provided is Fig. 2.

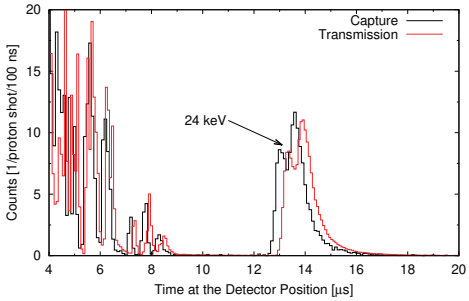

Figure 2: Filtered neutron flux by 20 cm of Fe obtained from capture (black) and transmission (red) experiments.

The filtered neutron peak of 24 keV is clearly isolated for both capture and transmission experiments in one double-humped peak that includes overlapped neutrons from both proton bunches. Other filtered peaks can also be seen between 7 and 9 μs but the counting rate seems to be too small to be used in experiments. The results for the two different Si filter assemblies can be seen in Fig. 3(a) for 20 cm of Si and in Fig. 3(b) for 30 cm of Si. As is the case for the Fe array, both capture and transmission experiments present high agreement for both filtered peaks of 144 and 54 keV. Here the contributions from each proton bunch are clearer as these peaks occur at a higher energy. The difference in time between the results from both detectors is due to the fact that that the detectors are installed at different positions with respect to the incident neutron beam (see Fig. 1(b)). The NaI(Tl) spectrometer is situated at a distace of 27.9 m from the moderator surface whereas the Li-glass detectors are situated at a slightly longer distance of 28.6 m.

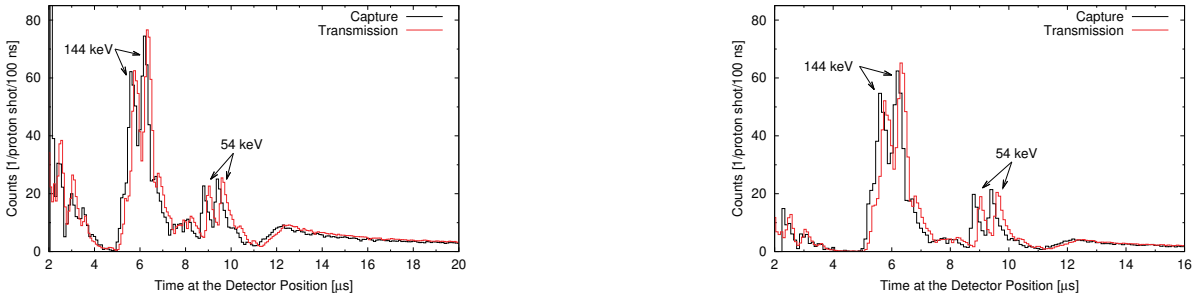

(a) (b)

Figure 3: Filtered neutron flux by 20 cm of Si (a) and 30 cm of Si (b) determined from capture (black) and transmission (red) experiments

4 PHITS Simulations

Monte-Carlo simulations with the code PHITS [6] were employed as benchmark for the filtering system performance analysis. Since the straight relationship between time and energy for the detected neutrons is no longer applicable for fast neutrons due to the double-bunch structure, simulations with PHITS are used the neutron transmition ratio through all the materials, including not only the filter materials but also structural materials, in the ANNRI beamline. The neutron transmitted ratios were then unfolded taking into account the time structure of the ANNRI beamline as was described by Kino *et al* [7] using the model function suggested by Ikeda and Carpenter [8].

The derived time distribution results from the PHITS simulations can be seen in Fig. 4(a) and 4(b) for the 20 cm Fe and 20 cm Si filter arrays, respectively, compared with the results with no filter present. The PHITS results are also compared with the experimental results obtained from the capture experiments. The Monte-Carlo simulations are able to accurately reproduce the experimental results with both filter assemblies and when no filter material is used. Hence, the energy distribution obtained from the PHITS simulations is deemed reliable.

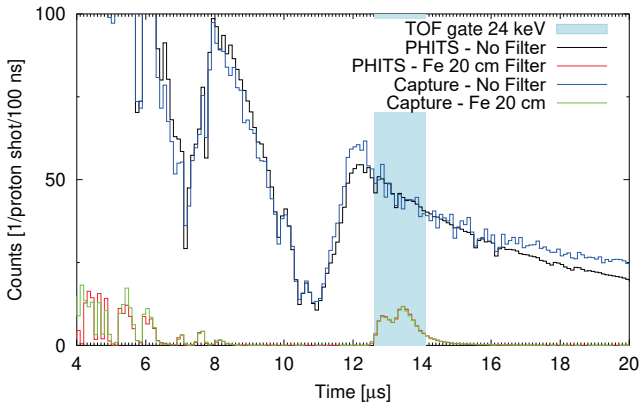

(a)

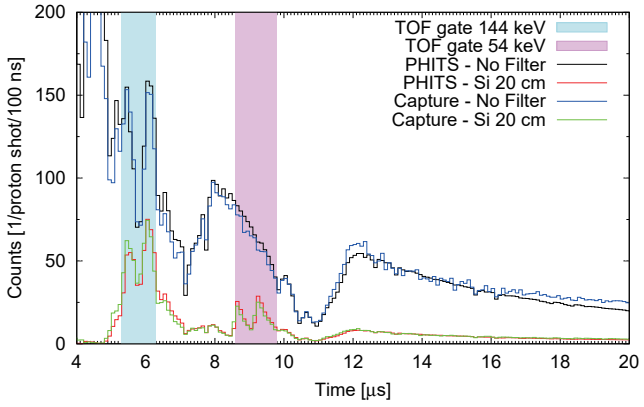

(b)

Figure 4: Time distribution of the PHITS results and capture experiments using a 20 cm Fe filter (a) and a 20 cm Si filter (b) compared with the results when no filter is present.

In order to analyze the neutron energy distribution derived with PHITS at the filtered peaks, TOF gated were created enclosing the three filtered neutron peaks. For the Fe filter array, a TOF gate was created from 12.6 to 14.6 μs to wrap the 24 keV filtered neutron beam. This gate is shown in Fig. 4(a). From the gated TOF data, a centroid energy of 23.6 keV was determined for the Fe 24 keV window. On the other hand, the neutron energy distributuon of the filered peaks of 144 keV and 54 keV were derived using TOF gates from 5.4 to 6.4 μs and from 8.6 to 9.8 μs, respectively. For the Si array, centroid peaks of 127.7 and 51.5 keV were derived from the PHITS results. The result of 127.7 keV is much lower than the expected value of about 144 keV. The reason for this is that

the peak is shifted to a lower energy due to the presence of ^{27}Al in the beamline which has a resonance peak at the energy around 150 keV in the neutron total cross-section. Neutrons with energies from 135 to 160 keV are scattered by the several layers of ^{27}Al present at ANNRI used to compartimentalize the beamline and cannot reach the experimental areas.

5 Cross-section results

Preliminary results of the ^{197}Au neutron capture cross-section were derived as the final step to evaluate the perfomance of the neutron filter and their viability for neutron-induced reaction measurement. The Au cross-section was derived from the obtained Au capture yield using the Pulse-Height Weighting Technique (PHWT) [9] at each TOF gate (G_i) using the following:

$$\sigma_{Au}(G_i) = \frac{Y_{Au}(G_i)C(G_i)}{\phi_n(G_i)} \frac{1}{n_{Au}} \tag{1}$$

being $\sigma_{Au}(G_i)$ the absolute cross-section for each of the three TOF gates (G_i); $Y_{Au}(G_i)$ and $C(G_i)$ are the Au neutron capture yield and the coeficient to correct for the self-shielding and multiple-scattering effects for each TOF gate (G_i), respectively. $\phi_n(G_i)$ means the normalized incident neutron flux at the TOF gate (G_i) and n_{Au} stands for the sample area density in at/barn.

The preliminary results for the ^{197}Au neutron capture cross-section are shown in Fig. 5. The results are compared with the JENDL-4.0 evaluated data [10] and the IAEA standard library[11]. The x-axis bar are the mininum and maximun neutron energy determined at each TOF gate by PHITS.

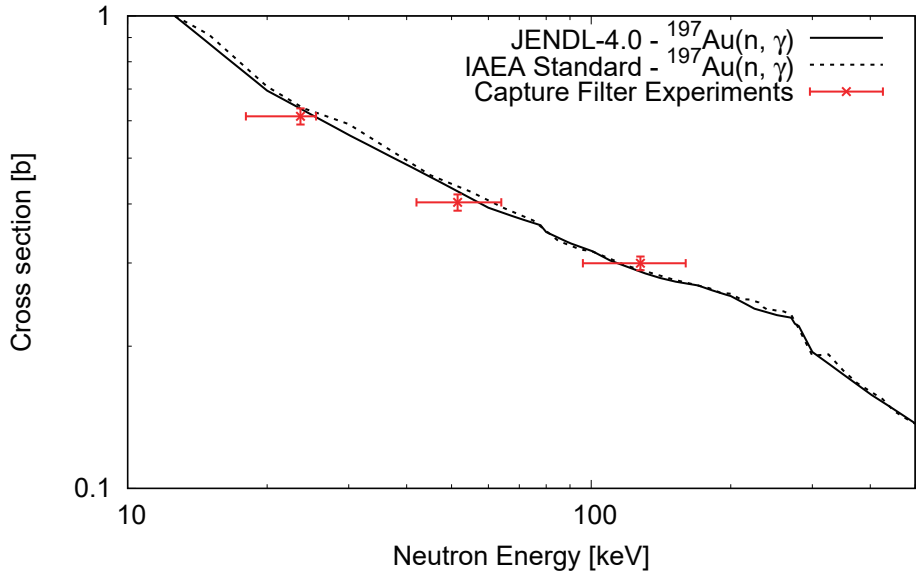

Figure 5: Preliminary results for the ^{197}Au neutron capture cross section using the ANNRI filtering system

The present preliminary results agree within uncertainties with the evaluated data from JENDL-4.0 and present slightly lower values than those included in the IAEA standard library.

6 Conclusions

The neutron filtering system applied in the ANNRI beamline is able to tailor the incident neutron flux into quasi-monoenergetic neutron peaks. The filter configurations of 20 cm of Fe and 20 cm of Si have proven to be a feasible solution in order to circumvent the double-bunch structure for fast neutron cross-section measurements. Using experiments and simulations with PHITS, the characteristics of the three peaks molded by the Fe and Si assemblies were determined with centroid energies of 23.6 keV (Fe) and 51.5 and 127.7 keV (Si). Furthermore, a preliminary cross-section measurement of the ^{197}Au neutron capture cross-section using the neutron filtering system was performed. The present results agree within uncertainties with the evaluated data from JENDL-4.0.

References

[1] Katabuchi T, Iwamoto O, Hori J, Kimura A, et al. Fast neutron capture reaction data measurement of minor actinides for development of nuclear transmutation systems. EPJ Web of Conferences, 2020;239.

[2] Greenwood RC, Chrien RE. Filtered reactor beams for fast neutron capture γ-ray experiments. Nucl. Inst. and Meth., 1976;138:125-143.

[3] Katabuchi T, Igashira M, Matsuhasi M, Mizumoto M, et al. Nuclear data measurement using the accurate neutron-nucleus reaction measurement instrument (ANNRI) in the Japan Proton Accelerator Research Complex (J-PARC), IAEA-TECDOC, 2014.

[4] Rovira G, Katabuchi T, Tosaka K, Matsuura S, et al. Neutron capture cross-section and resolved resonance analysis of ^{237}Np. J. Nucl. Sci. Technol. 2020;57:24-39.

[5] Terada K, Kimura A, Nakao T, Nakamura S, et al. Measurements of neutron total and capture cross section of ^{241}Am with ANNRI at J-PARC. J. Nucl. Sci. Technol. 2018;55:1198-1211.

[6] Sato T, Iwamoto Y, Hashimoto S, Ogawa T, et al. Features of particle and heavy ion transport code system (PHITS) version 3.02. J. Nucl. Sci. Technol. 2018;55:684-690.

[7] Kino K, Furusaka M, Hiraga F, Kamiyama T, et al. Measurement of energy spectra and spatial distribution of neutron beams provided by the ANNRI beamline for capture cross-section measurements at the J-PARC/MLF. Nucl. Inst. and Meth. A, 2011;626-627:58-66.

[8] Ikeda S, Carpenter JM. Wide-energy-range, high-resolution measurements of neutron pulse shapes of polyethylene moderators. Nucl. Inst. and Meth. A, 1985;239-3:536-544.

[9] Macklin R, Gibbons J., Capture cross-section studies for 30-220 keV neutrons using a new technique. Phys. Rev., 1967;159:1007.

[10] Shibata K, Iwamoto O, Nakagawa T, Iwamoto N, et al. JENDL-4.0: A new library for nuclear science and engineering. J. Nucl. Sci. Technol. 2011;48:1-30.

[11] Carlson A, Pronyaev V, Capote R, Hale G, et al. Evaluation of the neutron data standards. Nucl. Data Sheets, 2018;148:143-188.

29. A New Method to Reduce Systematic Uncertainties of Capture Cross Section Measurement Using a Sample Rotation System

Y. Kodama[1*], T. Katabuchi[1], G Rovira[2], H. Nakano[1], K. Terada[3]
A. Kimura[2], S. Nakamura[2], S. Endo[2]

1) Tokyo Institute of Technology
2) Japan Atomic Energy Agency
3) Kyoto University
author: kodama.y.ae@m.titech.ac.jp

A new method to reduce systematic uncertainties of capture cross section measurement using a sample rotation system has been developed. Theoretical and experimental tests on the method have been conducted. Calculations using Monte Carlo simulation code were performed. Experiments using a sample rotation system at the Accurate Neutron Nucleus Reaction Measurement Instrument in Materials and Life Science Facility of the Japan Proton Accelerator Research Complex were also conducted.

I. Introduction

Accurate nuclear data for neutron-induced reactions are necessary for the design of nuclear transmutation systems to reduce minor actinides (MA) and long lived fission products (LLFP) contained in nuclear waste. However, current uncertainties of nuclear data for MA and LLFP do not fulfill the requirements for the design of transmutation facilities. Measurements of the neutron capture cross section are ongoing at the Accurate Neutron Nucleus Reaction Measurement Instrument (ANNRI) in the Materials and Life Science Facility (MLF) of the Japan Proton Accelerator Research Complex (J-PARC).

The neutron capture cross section σ [cm^2] is determined in the experiments based on the following equation:

$$\sigma = \frac{1}{nt}\frac{Y(E_n)}{\phi(E_n)}, \tag{1}$$

where n [atoms/cm^3] is density of sample, t [cm] is thickness of sample, Y is neutron capture reaction yield and ϕ is neutron energy specrum.$Y(E_n)$ is derived using pulse-height weighting techniue [1]. $\phi(E_n)$ is measured using a neutron flux monitor. The neutron capture cross section can be determined by measuring $Y(N_n)$ and $\phi(E_n)$. In the determination of capture cross section, the systematic uncertainty of final cross section is governed by the incident neutron energy spectrum.

In ANNRI experiments, the neutron energy spectrum can be determined by measuring 478 keV γ-rays from the ^{10}B(n,$\alpha\gamma$)^{7}Li reaction. Detected γ-ray counts are converted to the numbers of neutrons using the reaction rate of the ^{10}B(N,$\alpha\gamma$)^{7}Li reaction. The energy dependence of the reaction rate depends on the atomic area density of ^{10}B in the boron sample because the neutron self-shielding factor increase with the ^{10}B area density and also changes with the neutron energy. Thus, ^{10}B atomic area dinsity is very important to determine the incident neutron energy spectrum.

In the present work, we suggest a new method to reduce systematic uncertainties related to the incident neutron using a sample rotation system. Theoretical and experimental studies were also performed.

II. Methodology

1. Principle

The new method employs the change of the self-shielding effect with the sample rotation angle. When a sample is tilted with respect to the beam axis, the effective thickness of the sample becomes larger than the actual thickness. The reaction yield at the tilted angle θ in consideration of the self-shielding effect can be expressed as follows:

$$Y_\theta = c \cdot \frac{\sigma_{cap}}{\sigma_{tot}} \cdot \phi \cdot \left(1 - e^{Nt\sigma_{tot}\frac{1}{cos\theta}}\right) \tag{2}$$

where c is the correction factor for the multiple-scattering effect, and σ_{cap} and σ_{tot} are the capture and total cross sections, respectively. The new method suggested below is based on the yield change with sample rotation.

2. Sample Area Density Determination

The new method is for atomic area density determination of ^{10}B sample which is used for measurement of the incident neutron spectrum in ANNRI experiments. The ratio of the reaction yield at a rotation angle of 0Âž, Y_{0° to the yield at θ, Y_{θ° is written as:

$$R = \frac{Y_{\theta^\circ}}{Y_{0^\circ}} = \frac{1 - e^{Nt\sigma_{tot}\frac{1}{cos\theta}}}{1 - e^{Nt\sigma_{tot}}}. \tag{3}$$

The energy dependence of the yield is measured by the neutron time-of-flight (TOF) method. Thus, the yield ratio $R(t)$ is explicitly written as a function of TOF t.

The reaciton yields of ^{10}B(n,$\alpha\gamma$)^{7}Li for different area density were calculated using a Monte Carlo simulation code. A typical calculated results of the yield ratio $R(t)$ is of 0Âž to 60Âž is shown in Fig. 1. The yield ration $R(t)$ is equal to unity at low energies (slow TOF) and increases up to $1/\cos\theta$ that is 2.0 for 60Âž at high energy area. The transient TOF region between the two constant values 1.0 and 2.0 changes with the sample atomic area density. We define T_{half} as the TOF value where $R(t)$ becomes the half of the maximum. T_{half} changes with the sample atomic area density. In other words, the sample area density can be determined from T_{half}. Figure 2 shows a plot of T_{half} vs the sample atomic area density.

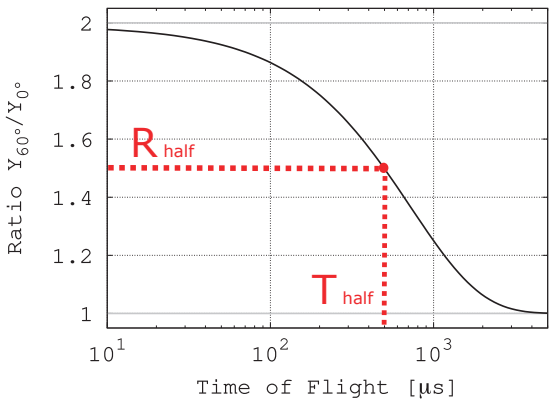

Figure 1: *Reaction ratio TOF spectrum*

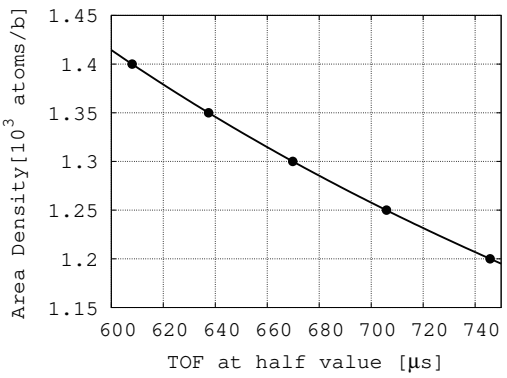

Figure 2: *Sample atomic area density calibration curve*

III. Analysis

1. Simulation

We performed simulations of the sample rotation measurement by using the Monte Carlo simulation code PHITS [3]. A ^{10}B 90% enriched B_4C sample calculated $^{10}B(n,\alpha)Li^7$ reaction counts. The ratio at each a tilted angle and at each thickness was derived from the calculated reaction counts. The calibration curve was obtained at a tilted angle of 45Âž.

2. Experiment

The sample rotation measurement was performed at ANNRI beam line in MLF of J-PARC. The sample rotation system installed at the beam line was used to rotate samples. A ^{10}B 90% enriched B^4C sample with an area density of 1.259×10^{-3}atoms/b, a diameter of 10 mm and a thickness of 0.5 mm was used for the test of the rotation system. A ^{nat}C sample with a diameter of 10 mm and a thickness of 0.5 mm was used to derive the background events due to scattered neutrons. Neutrons were produced from the spallation reactions coused by a 3-GeV proton beam shot to a mercury target of the MLF [4]. The neutron beam was collimated to a diameter of 13 mm at the sample position. A TOF method was employed in this experiment with a neutron flight path of 27.9 m from the spallation source to the sample position. γ-rays emitted from the sample were detected by a NaI(Tl) detector.

IV. Results and Discussion

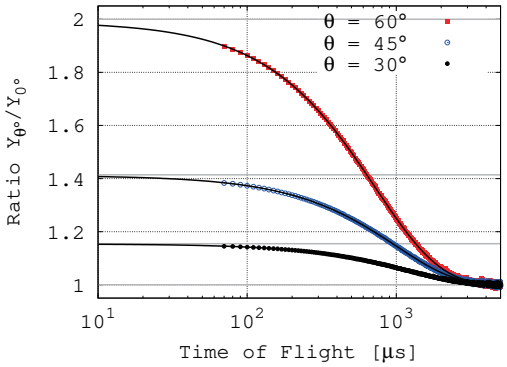

Figure 3: *Reaction ratio at each a tilted angle*

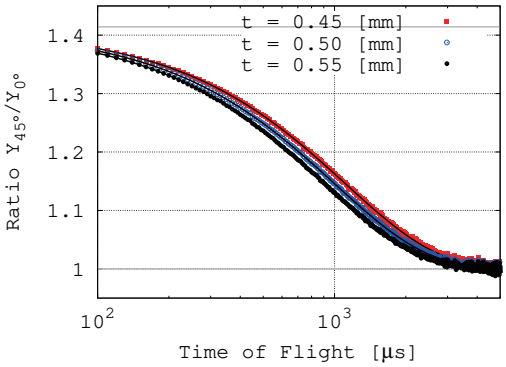

Figure 4: *Reaction ratio at each a thickness*

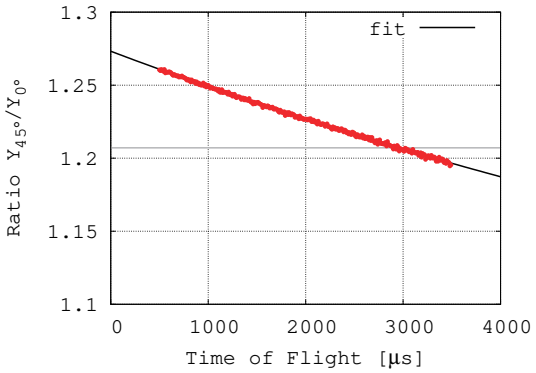

Figure 5: *Reaction ratio TOF spectrum*

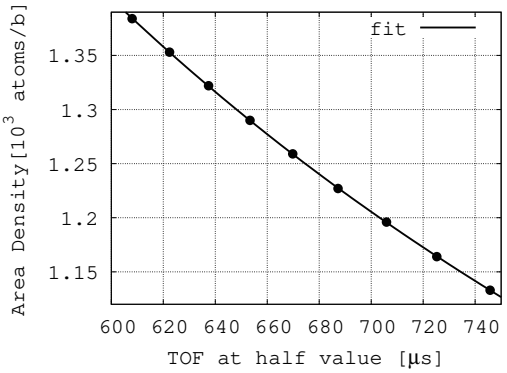

Figure 6: *Sample atomic area density calibration curve*

1. Simulation of Boron Sample Rotation

The ratio at each a tilted angle with different thicknesses were plotted in Fig. 3 and Fig. 4 respectively. These results were fitted to the following equation.

$$R(t) = \frac{1 - e^{(c_1 + c_2 t)/cos\theta}}{1 - e^{(r_2 + c\ t)}} \tag{4}$$

The energy dependence of the ratio changes with thickness and the tilted angle. The ratio at a thickness of 0.45 and a tilted angle of 45 degree was shown in Fig. 5. The boron calibration curve to determine the boron sample thickness (Fig. 6) was derived from the result calculated at each thickness. In the analysis, the area density value of the boron sample of 1.259 $\pm$ 0.025 [10^{-3}atoms / b] was obtained. The calculation results of the first method to determine the boron sample area density is reasonable agreement.

2. Rotation experiment of a boron sample

The TOF spectrum of ^{10}B(n,$\alpha\gamma$)^{7}Li reaction shown in Fig. 7 was obtained by using a sample rotation system. In this analysis, blank background, the background events induced due to scattered neutrons at the sample were subtracted. Correction for smaller sample size than the neutron beam was employed. The ratio Y_{45°/Y_{0° was obtained as shown in Fig. 8. The experimental results differ from the calculated one. The applied correction seems insufficient. T his d isagreement i s p ossibly c aused b y system asymmetry or system axis misalignment. A larger boron sample than the neutron beam is necessary in the future work.

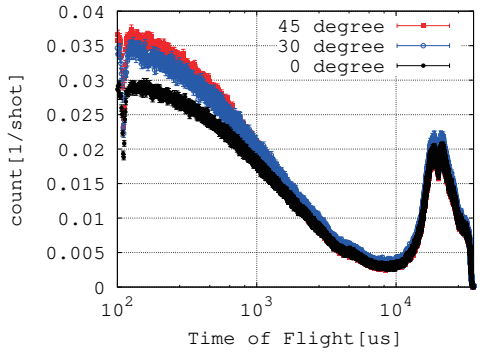

Figure 7: *TOF spectrum of the $^{10}B(n,\alpha\gamma)^{7}Li$ reaction*

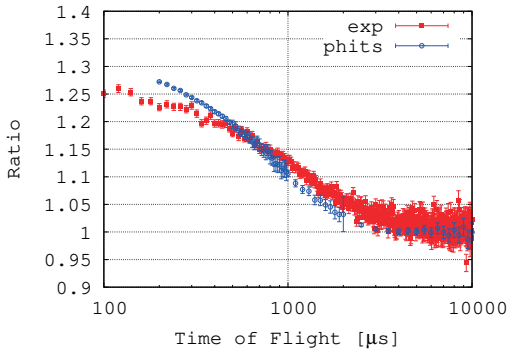

Figure 8: *Reaction yield ratio*

V. Summary

In order to reduce systematic uncertainties of neutron capture cross section measurement, a new method using a sample rotation system were proposed to determine a sample atomic area density for a neutron energy spectrum. The calibration curve for the area density of the boron sample can be obtained by using Monte Carlo calculation code. A test measurement to determine the boron area density were conducted. The experimental result were different from the calculated result. We plan to use a larger boron sample than the neutron beam to test the sample rotation system in the future.

References

[1] R. L. Maklin et al. Phys Rev. 159, 1007-1015(1967)
[2] R. L. Macklin et al. ,Nuc. Ins. and Meth vol.164, 1, 213-214(1979)
[3] T. Sato et al. ,J. Nucl. Sci. Technol. 55, 684-690(2018)
[4] F. Maekawa et al., Nuc. Ins. and Meth vol.620, Issues 2-3, 11-21(2010)

30. Development of a neutron beam monitor for nuclear data measurement using spallation neutron source

Hideto Nakano[1*], T. Katabuchi[1], G. Rovira[1], Y. Kodama[1], K. Terada[1],
A. Kimura[2], S. Nakamura[2] and S. Endo[2]

1) Laboratory for Advanced Nuclear Energy, Tokyo Institute of Technology
2) Japan Atomic Energy Agency
e-mail: nakano.h.ag@m.titech.ac.jp

Neutron beam intensity for nuclear data measurement is increasing. The qualities of cross section measurement of radioactive nuclides were significantly improved. In neutron capture cross section measurement, the number of the incident neutrons is necessary to derive the neutron capture cross section. However, conventional neutron detectors do not have fast response to adapt high counting rate measurement with spallation neutron sources. To avoid possible failure of a proton pulse counting method and make measurement with ANNRI more robust, an additional neutron beam monitor is under development. A plastic scintillator with a thin ^{6}Li layer is adopted for a detector. A test detector system was built to study the feasibility of the present method. Test experiments demonstrated that the new detection system was able to detect neutrons from the spallation neutron source.

I. Introduction

The qualities of cross section measurements of radioactive nuclide were significantly improved with high intensity neutron beams. It has been difficult to measure neutron-induced reaction cross sections of radioactive nuclides due to large background of the decay gamma-rays from radioactive samples. In recent years, with the advent of spallation neutron sources, the qualities of cross section measurement were significantly improved. The Japan Proton Accelerator Research Complex (J-PARC) was started in operation in 2008 and its beam power has been increased year by year [**1**]. To measure neutron-induced nuclear data using the high intensity neutron beam from the J-PARC spallation neutron source, the Accurate Neutron Nucleus Reaction Measurement Instrument (ANNRI) was built in the Materials and Life Science Experimental Facility (MLF) of J-PARC.

In neutron capture cross section measurement, the number of the incident neutrons is important physical quantity. To normalize the detected gamma-ray yield to the number of the incident neutrons, the neutron count is usually monitored by with a neutron detector. However, in measurement with ANNRI, the number of proton beam pulses injected into the spallation target has been used instead of direct neutron monitoring. This method is based on the assumption that the number of proton beam pulses is proportional to the number of incident neutrons. This assumption is mostly plausible but could fail when the conditions of the proton accelerator or the neutron source change. To avoid possible failure of the proton pulse counting method and make measurement with ANNRI more robust, an additional neutron beam monitor is under development.

II. Detector Design

To develop a neutron beam monitor for ANNRI, there are two requirements. Fast time response adapts very high intensity neutron beam and low gamma-ray sensitively reduces background. In order

to fulfill the requirements, a thin sheet-type plastic scintillator combined with a thin ^{6}Li layer on an aluminum film is adopted for the present neutron monitor. The incident neutrons react with ^{6}Li and the ^{6}Li(n,t)^{4}He reaction occurs. The emitted particles, tritons and alphas, are detected with the plastic scintillator. The short ranges of tritons and alphas allow for using a thin plastic scintillator film, and the thin detector leads to low gamma-ray sensibility. Another requirement for fast detection is achieved by the fast response property of plastic scintillator with 3.7 ns decay time. Simulation studies using Monte Carlo simulation code PHITS [2] were performed to optimize the detector design, especially thickness of the ^{6}LiF layer. In Fig. 1, the concept of the detector system is shown schematically.

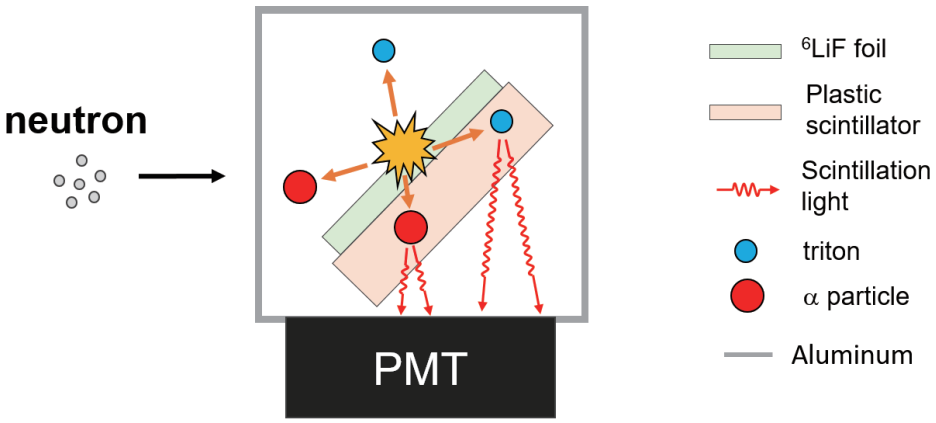

Figure 1: *Detector geometric design.*

III. Experiments

A test detector system was built to study the feasibility. LiF was deposited on an aluminum film by a vacuum deposition method. The LiF layer was thin enough for tritons and alpha particles to penetrate and reach the plastic scintillator. ^{6}Li was isotopically enriched 95%. The photomultiplier tube was HAMAMATSU R1306-22ASSY. Test experiments were carried out at ANNRI. The detector was placed at a flight length of 29.62 m from the spallation neutron source. The beam power was about 500 kW. The pulse height (PH) and the time-of-flight (TOF) were acquired. TOF measurement was started by a signal from the J-PARC accelerator and stopped by PMT signal. In addition to measurement with the LiF foil, measurement without the LiF foil was conducted for background evaluation. Measurement time with ^{6}Li was about 11 min.

As shown in Fig. 2, pulse-height (PH) spectra are shown. The spectra were normalized with the number of proton pulses. In Fig. 2, the ^{6}Li(n,t)^{4}He reaction was successfully observed as a strong peak in the region from 22 ch to 36 ch. In Fig. 3, time-of-flight spectra are shown. Difference between the spectra with and without LiF is observed in the TOF region from 400 to 35000 μs that corresponds to the thermal neutron region. The peak of the resonance of ^{6}Li(n,t)^{4}He at 250 keV was also observed in the TOF region from 7 to 9 μs. The neutron energy spectrum was derived from TOF spectrum by dividing the detected neutron counts by the reaction rate calculated from the ^{6}Li(n,t)^{4}He cross section.

To evaluate the system performance, the present results were compared with neutron spectra measured with different methods in previous experiments [3]. In Fig. 4, the neutron spectrum (red) measured in this work was compared with a neutron spectrum (black) at 27.9 m obtained detecting 478 keV gamma-rays from the ^{10}B(n,α)^{7}Li reaction placing a ^{10}B sample [3]. The neutron spectra agree well in the thermal neutron region but the present neutron spectrum is slightly higher than the previous measurement in the higher energy region, and deviates from 10 eV. The difference comes from insufficient subtraction of background that is mainly gamma-ray from the neutron source. The background subtraction must be improved in the future development. Statistical error was 0.68 % at 6 meV. Figure 5 shows another comparison of the present results (red) with a TOF spectrum (black) measured with

a Li glass detector in a previous experiment [**4**]. The beam power of the previous experiment was 200 kW. A Pb filter with a thickness of 5 cm was inserted upstream to reduce the gamma flash from the neutron source while no Pb filter was used in the present experiment. Detector paralysis caused by the gamma-flash occurred in the previous experiment. Detector paralysis leads to count loss observed in the TOF region from 3 to 20 μs in the previous experiment. On the other hand, detector paralysis did not occur and significant count loss did not appear in the present system, despite no use of the Pb filter. This experiment was successfully measured without detector paralysis at fast TOF region.

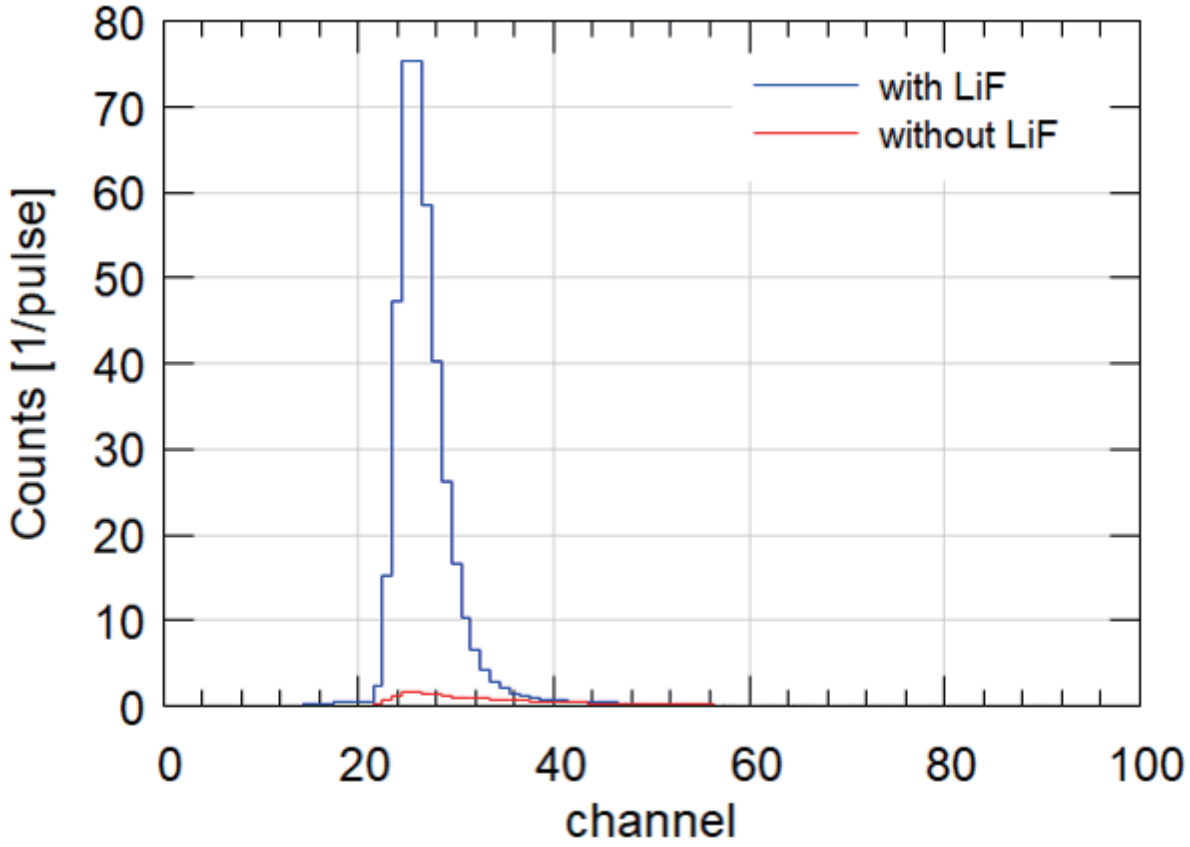

Figure 2: *Pulse height spectra with and without LiF.*

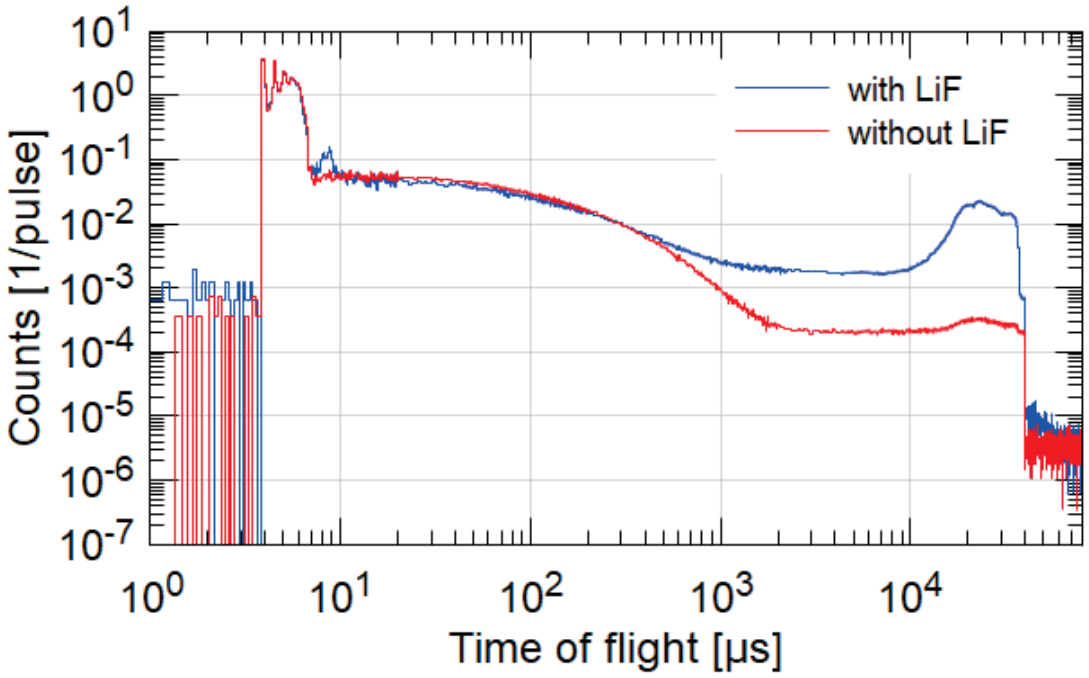

Figure 3: *TOF spectra with and without LiF.*

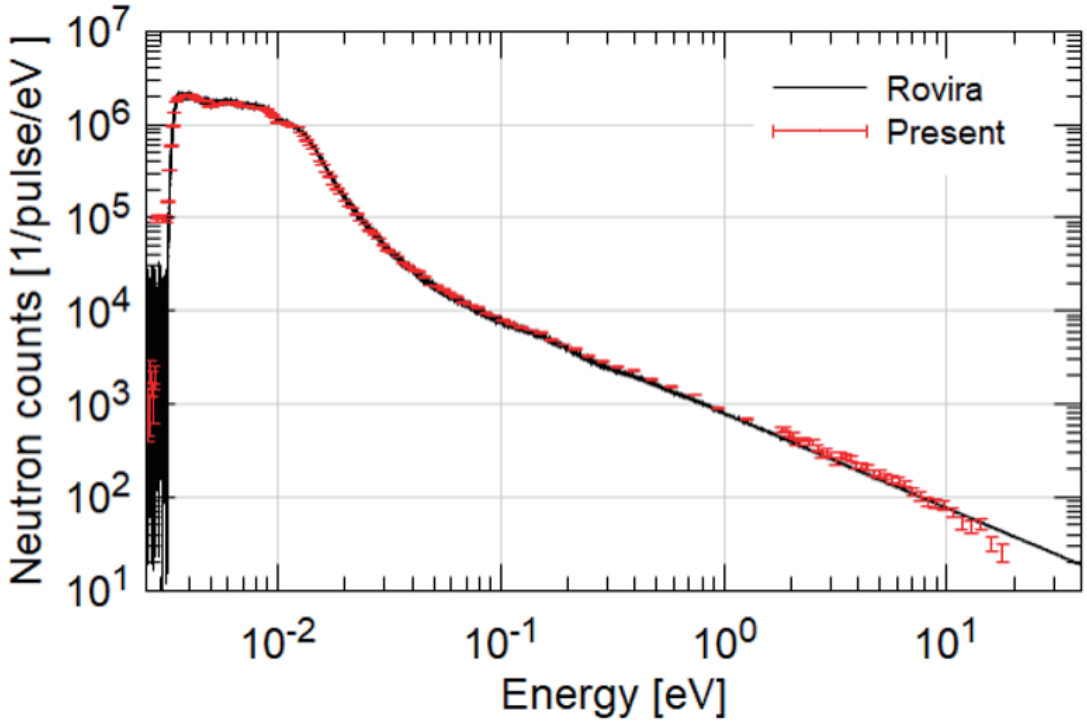

Figure 4: *Comparison of neutron spectra of the present work with the previous measurement by Rovira et al [**3**].*

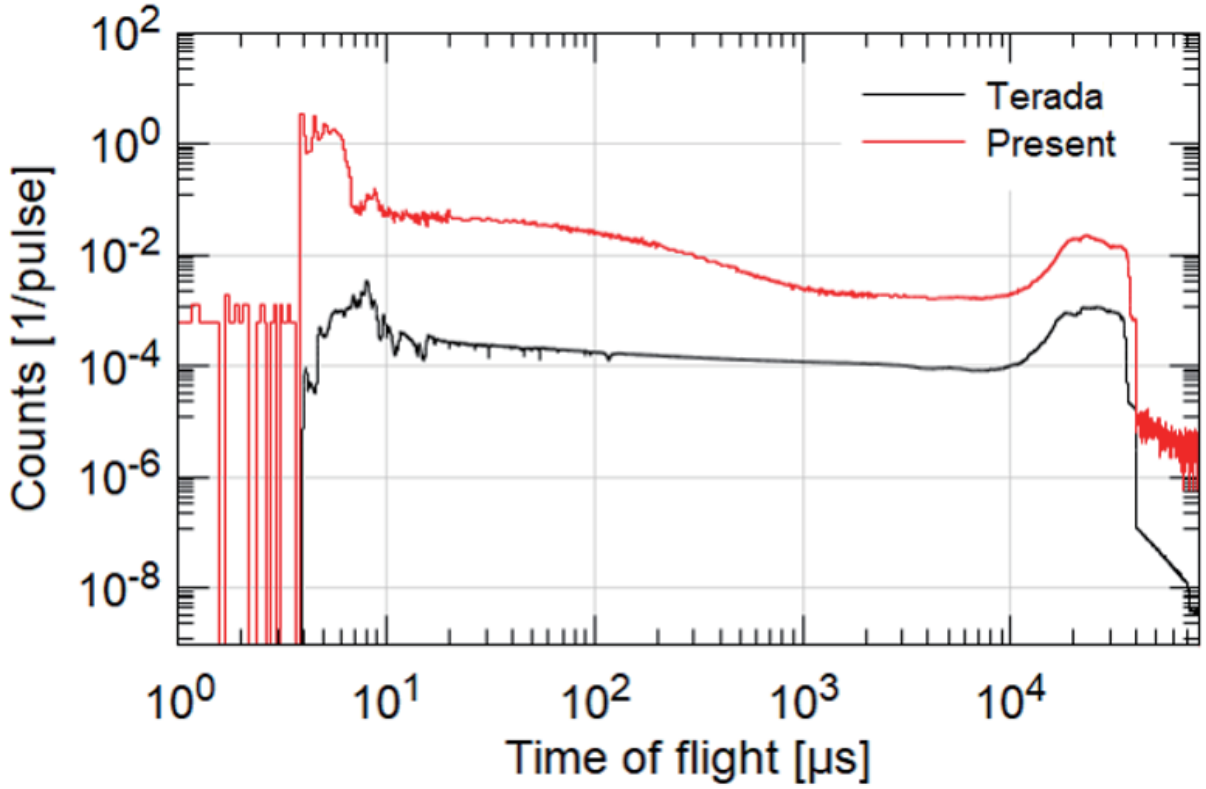

Figure 5: *Comparison of TOF spectra of the present work with the previous measurement by Terada [**4**].*

IV. Summary

A new neutron monitor system was designed and built. Signal from the ^{6}Li(n, t)^{4}He reaction was clearly observed. Neutron spectrum was derived from TOF spectrum in data analysis. Statistical error was 0.68 % at 6 meV. In the future plan, this system will be used as an incident neutron monitor in nuclear data measurement. Moreover, application to other nuclear cross section measurement is planned.

References

[1] Kino K, Furusaka M, Hiraga F, et al. Measurement of energy spectra and spatial distributions of neutron beams provided by the ANNRI beamline for capture cross-section measurements at the J-PARC/MLF. Nucl Instruments Methods Phys Res Section A. 2011;626-627:58-66.
[2] Sato T, Iwamoto Y, Hashimoto S, et al. Features of particle and heavy ion transport code system (PHITS) version 3.02. J Nucl Sci Technol. 2018;55:684-690.
[3] Rovira G, Katabuchi T, Tosaka K, et al. Neutron capture cross-section measurement and resolved resonance analysis of 237Np. J Nucl Sci Technol. 2020;57:24-39.
[4] Terada K. private communications.

31. Development of Absolute Epi-thermal and Fast Neutron Flux Intensity Detectors for BNCT

Kazushi Aoki[†1], Shingo Tamaki[1], Sachie Kusaka[1], Fuminobu Sato[1], Isao Murata[1]

1 Graduate School of Engineering, Osaka University, 2-1 Yamada-oka, Suita-shi, Osaka-fu 565-0871, Japan

† aoki@qr.see.eng.osaka-u.ac.jp

Abstract

An absolute epi-thermal neutron (0.5 eV ~ 10 keV) flux intensity detector and a fast neutron (10 keV~1 MeV) flux intensity detector were designed and developed for Boron Neutron Capture Therapy (BNCT). After fabricating the detectors, in order to test the performance of the epi-thermal and fast neutron detectors, verification experiments were conducted at KUR [1], Kyoto University and FNL facility [2], Tohoku University, respectively. As the result, the epi-thermal neutron flux intensity could be measured with an error of 3.9 % after theoretically correcting the high energy neutron contribution. The fast neutron flux intensity could also be measured accurately, that is, the experimental and calculated values agreed well within the statistical uncertainty.

1. Introduction

BNCT is a promising cancer therapy which kills tumor cells while suppressing exposure dose to normal tissues. Normally, the neutron field of BNCT, which is produced by a nuclear reactor or an accelerator, has an energy distribution spreading within thermal, epi-thermal and fast neutron regions. Because epi-thermal neutrons are generally used for BNCT, we must measure the epi-thermal neutron flux intensity to evaluate the therapeutic effect and patient's exposure dose. In addition, we also have to evaluate the exposure dose of the fast neutrons that may be harmful to the human body. However, it is quite difficult to know such intensities directly and accurately, because there is no suitable neutron spectrometer and no activation material covering epi-thermal or fast neutrons separately. The objective of this work is hence to develop new detectors to precisely measure the absolute integral flux intensities of epi-thermal (0.5 eV ~ 10 keV) and fast neutrons (10 keV ~ 1 MeV).

2. Design

2.1 Design of epi-thermal neutron detector

The followings are design requirements for the epi-thermal neutron detector. (1) It should have flat sensitivity for epi-thermal neutrons and no sensitivity for thermal neutrons and fast neutrons. (2) It should be as small as possible not to distort the neutron field. (3) It should be available in a strong neutron field. Therefore, we decided to employ the foil activation method. In previous

research [3, 4], it was considered to adopt a spherical shape as the detector, but to make the sensitivity flat in epi-thermal energy region, we adopted a rectangular shape detector shown in Fig. 1 [5]. The epi-thermal neutron detector controls its sensitivity by using Cd thermal neutron absorber and polyethylene neutron moderator (P.E.). An activation foil is positioned in the center and the foil is covered with P.E. moderator surrounded with a Cd sheet to cut thermal neutrons. As for the calculation method, we used MCNP5 as neutron transport calculation tool and JENDL-4.0 as evaluated nuclear data library [6]. The design procedure consists of two processes. One is to fix the activation foil and P.E. moderator thickness to make the sensitivity flat to epi-thermal neutrons. The other is to design the Cd thickness to cut over 70 % of the sensitivity for 0.1 eV neutrons. The design goal is that fluctuation in the sensitivity to epi-thermal neutrons is to be within 10 %.

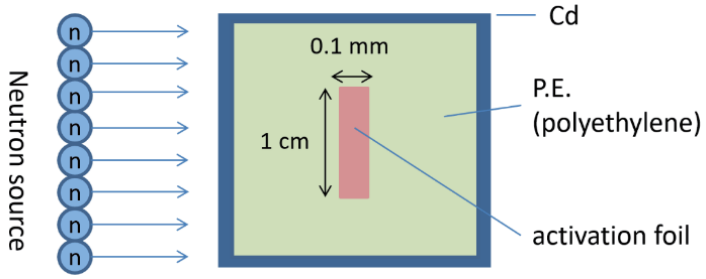

Fig. 1 Design calculation model.

As the design result, ^{71}Ga (n, γ) ^{72}Ga reaction was selected as the activation reaction and the shape of the detector was fixed to be a rectangular polyethylene (5.52 cm^3) covered with a cadmium sheet of 0.0025 cm in thickness. Fig. 2 shows the finally designed detector's sensitivity. The blue line shows the sensitivity of this detector. The green region is the epi-thermal neutron region, and the red line is the average sensitivity in that region. The fluctuation of the production yield of ^{72}Ga for epi-thermal neutron is 8.4 % and the shielding rate of 0.1 eV neutron is 74.6 %. However, this detector is a little sensitive to fast neutrons.

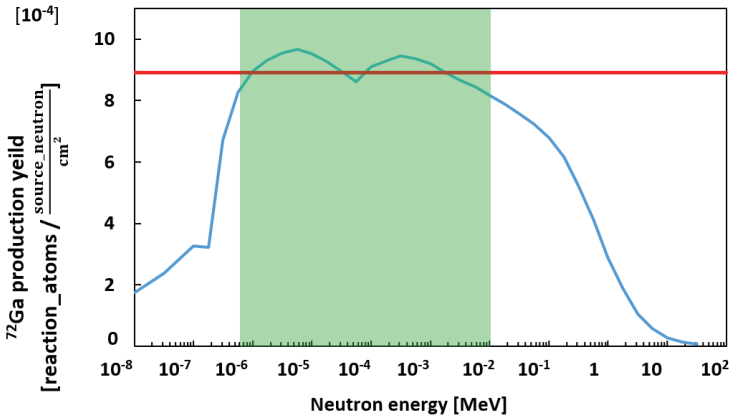

Fig. 2 Sensitivity of epi-thermal neutron detector.

2.2 Design of fast neutron detector

To clarify the fast neutron contribution, we develop the fast neutron detector. To extract only fast neutrons, the fast neutron detector consists of two sub-detectors, and the fast neutron flux is estimated from the difference in sensitivity between the two sub-detectors. A fast neutron detector controls the sensitivity by using cadmium, B_4C and polyethylene. The shape of one of the two is a cube covered with polyethylene with a side of 4.4 cm (P.E. type) and the other is a cube covered with B_4C with a side of 4.6 cm (B_4C type) as shown in Fig. 3. For both, GaN foils are covered with Cd sheets to eliminate thermal component.

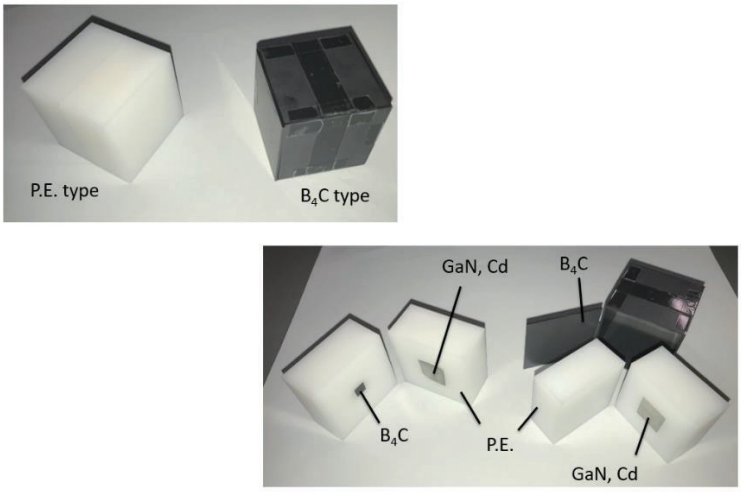

Fig. 3 Prototype fast neutron detectors.

However, in order to reduce the sensitivity to thermal and epi-thermal neutrons, the sensitivity of B_4C type was subtracted from that of P.E. type multiplied by a factor of A = 1.3. Here, the multiplication factor A was calculated so as to make the following equation to have the minimum value. Also, Fig. 4 shows the sensitivity of the fast neutron detector. The blue line shows the sensitivity of this detector. The green region is the fast neutron (10 keV~1 MeV) region, and the red line is the average sensitivity in that region.

$$\sum_{\mathrm{E}=0.01\mathrm{eV}}^{10\mathrm{keV}} \left(A \times Y_{\mathrm{P.E.}}(\mathrm{E}) - Y_{\mathrm{B4C}}(\mathrm{E})\right)^2 \quad (1)$$

where $Y_{\mathrm{P.E.}}(\mathrm{E})$ and $Y_{\mathrm{B4C}}(\mathrm{E})$ are the calculated ^{72}Ga production yields for P.E. type and B_4C type, respectively.

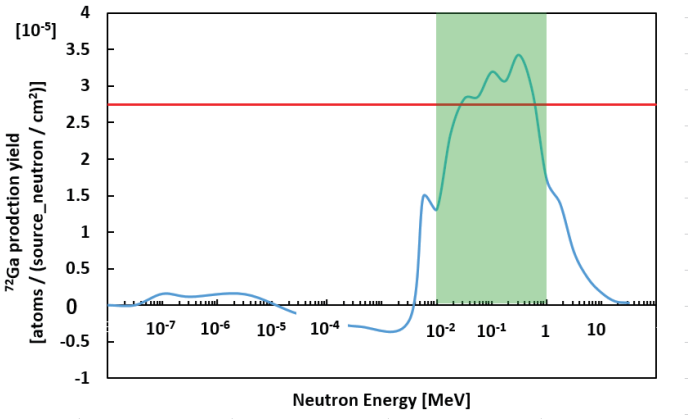

Fig. 4 Sensitivity of fast neutron detector.

3. Experiments

3.1 Validation experiment of epi-thermal neutron detector

In order to test the performance of the epi-thermal neutron detector, a verification experiment was conducted at KUR, Kyoto University. After the experiment, we can deduce the epi-thermal neutron flux intensity Φ_{epi} [n/cm²/sec] by following equation:

$$\Phi_{\mathrm{epi}} = \frac{Q}{\mathrm{Y} \times (1 - \mathrm{e}^{-\lambda t_{\mathrm{i}}})} \tag{2}$$

where Q [Bq] is radioactivity of ^{72}Ga, Y [$\frac{\text{reaction_atoms}}{\text{source_neutron/cm}^2}$] is ^{72}Ga production sensitivity, λ [1/sec] is decay constant of ^{72}Ga and t_{i} [sec] is irradiation time.

In the test, sufficient activity of ^{72}Ga can be induced only a short period irradiation.

Measurement conditions are shown in Table. 1. There are ^{69}Ga and ^{71}Ga in natural Ga. Since this detector uses ^{71}Ga (n, γ) ^{72}Ga reaction, only the radioactivity of ^{72}Ga (834 keV) was measured with the HP-Ge detector. The radioactivity immediately after irradiation of ^{72}Ga was 1.31 kBq [7]. Therefore, the epi-thermal neutron flux intensity is estimated to be 1.75×10^8 [n/cm²/sec] by using Eq. (2). The nominal value of the epi-thermal neutron (0.5 eV<En<10 keV) flux intensity is given to be 1.52×10^8 [n/cm²/sec] by KUR. Because this detector is a little sensitive to fast neutrons, a small discrepancy is seen between the experimental value and the nominal value.

To investigate the contribution from fast neutrons, we carried out a correction calculation by MCNP5. As a result, the amount of activation by fast neutrons was estimated to be 50 Bq when simulating with the same system as the experiment. Removing the contribution from fast neutron, the radioactivity becomes 1.26 kBq. Then, the epi-thermal neutron flux intensity is finally estimated to be 1.69×10^8 [n/cm²/sec] by using Eq. (2). It shows an excellent agreement with the given value by ~10 %.

Table. 1 Measurement conditions

Measuring Equipment	HP-Ge detector
Photon Peak Detection Efficiency (834 keV)	0.00384
Irradiation Time	10 min
Cooling Time	26 min
Measurig Time	55 min

3.2 Validation experiment of fast neutron detector

In order to test the performance of the fast neutron detector, a verification experiment was conducted at the FNL facility, Tohoku University. Three types of experiments were performed by changing the applied voltage of proton and the beam current. After the experiment, we can deduce the fast neutron flux intensity Φ_{fast} [n/cm^2/sec] by following equation:

$$\Phi_{\mathrm{fast}} = \frac{A \times Q_{\mathrm{PE}} - Q_{\mathrm{B4C}}}{\mathrm{Y} \times (1 - \mathrm{e}^{-\lambda t_{\mathrm{i}}})} \tag{3}$$

where A [-] is multiplication factor, Q_{PE} [Bq] is ^{72}Ga radioactivity of P.E. type, Q_{B4C} [Bq] is ^{72}Ga radioactivity of B_4C type, Y [$\frac{\mathrm{reaction\_atoms}}{\mathrm{source\_neutron/cm^2}}$] is ^{72}Ga production sensitivity, λ [1/sec] is decay constant of ^{72}Ga and t_{i} [sec] is irradiation time.

Table. 2 shows the experimental fast neutron flux intensities obtained by using the prototype detector compared to the calculated values. From this table, the fast neutron flux intensity could be measured accurately.

Table. 2 Estimated fast neutron flux intensity.

	Measurement Conditions		Fast Neutron Flux		
	Proton Applied Voltage [MeV]	Beam Current [μA]	Experimental Value	Calculated Value	C / E
①	2.5	5	7.15×10^6	6.41×10^6	0.856
②	2.65	7.8	9.34×10^6	9.25×10^6	0.99
③	2.8	2.5	2.84×10^6	3.26×10^6	1.148

4. Conclusion

Neutron flux intensity detectors for epi-thermal and fast neutrons were developed and experimentally tested at KUR, Kyoto University and FNL facility, Tohoku University, respectively. As a result, the epi-thermal neutron flux intensity in the neutron field for BNCT in KUR could experimentally be estimated with a good accuracy of 10 % error. The fast neutron flux intensity could also experimentally be estimated accurately in FNL of Tohoku University.

In the future, we will conduct a verification experiment of fast detector at KUR. And thereafter we would like to conduct experiments in a real neutron field of Accelerator-Based Neutron Sources (ABNS) for BNCT.

Acknowledgments

The authors would like to express their sincere gratitude to Dr. Hiroki Tanaka and Dr. Yoshinori Sakurai of Institute for Integrated Radiation and Nuclear Science, Kyoto University, who let us use the BNCT irradiation facility at KUR as a cooperative research, and Dr. Shigeo Matsuyama of Fast Neutron Laboratory, Graduate School of Engineering, Tohoku University, who allowed us to carry out experiments at the FNL facility with his warm support and guidance.

References

[1] 京都大学複合原子力科学研究所, “京都大学研究用原子炉(KUR),” [オンライン]. Available: https://www.rri.kyoto-u.ac.jp/facilities/kur. [アクセス日: 6 1 2021].

[2] 東北大学　松山・菊池研究室, “高速中性子実験室 -Fast Neutron Laboratory, Tohoku Univ.-,” [オンライン]. Available: http://web.tohoku.ac.jp/fnl/. [アクセス日: 26 12 2020].

[3] G. Xingcai, “Design of an epi-thermal neutron flux intensity monitor with GaN wafer for boron,” J. Nucl. Sci. Technol., Vol. 52, No. 4, pp.503–508, 2015.

[4] G. Xingcai, “Design study of neutron flux intensity monitor between ten and several hundred keV for BNCT,” J. Nucl. Sci. Technol.,Vol. 53, No. 8, pp.1112–1119, 2016.

[5] Y. Kashiwagi, “Development of epi-thermal neutron beam intensity detector with 71Ga(n, γ)72Ga reaction for boron neutron capture therapy,” Appl. Radiat. Isot. Vol.151, pp.145-149, 2019.

[6] K. Shibata et. al., "JENDL-4.0: A New Library for Nuclear Science and Engineering," *J. Nucl. Technol,* vol. 48(1), pp. 1-30, 2011.

[7] Glenn F. Knoll, "Radiation Detection and Measurement -4th ed.," Wiley, 2010, pp. 767-769.

32. Optimization of Activation Detector for Benchmark Experiment of Large-angle Elastic Scattering Reaction Cross Section by 14MeV Neutrons

Ryohei TAKEHARA, Kazuki FUKUI, Sota ARAKI, Shingo TAMAKI, Sachie KUSAKA and Isao MURATA
Graduate school of Engineering, Osaka University, Yamada-oka 2-1, Suita, Osaka 565-0871, Japan
Email: takehara.ryohei@eb.see.eng.osaka-u.ac.jp

The neutron elastic scattering reaction cross section data commonly show smaller in backward angles compared to those of forward angles when the energy of incident neutron is high. However, in a high neutron flux field, such as fusion reactor, the back-scattering reaction cross section is known to become not negligible. Practically, until now, there were differences reported between experimental and calculated values of neutron benchmark experiments using a DT neutron source (deuterium-tritium), which focused on back-scattering phenomena like a gap streaming experiment to verify the prediction accuracy of neutron streaming passing through narrow gaps while scattering. For this problem, we developed a benchmark method for large-angle scattering cross sections and has carried out experiments to measure the large-angle elastic scattering cross section of iron for the last few years. The benchmark method was successfully established based on activation reaction of Nb having a large activation cross section at around 14 MeV. However, Nb foil takes a long time to obtain the enough number of counts due to the long half-life (10.2 day) and low detection efficiency of the decay gamma-ray. In this study, to find a more suitable activation foil, we examined possible nuclides having appropriately short half-lives, not so high gamma-ray energies because high detection efficiency is essential, large activation cross sections, and not too low threshold energies of nuclear reaction. The optimization was carried out by calculating and comparing the number of counts per reaction per nuclide for all nuclides listed in JENDL/AD-2017.As a result, we have found that $^{197}Au(n,2n)^{196}Au$ was the most suitable reaction giving us the largest number of counts in an acceptable short experimental time.

1. Introduction

As shown in Fig. 1, The neutron large-angels scattering reaction cross section data with high energy neutron. This difference is not negligible in neutronics designs of high neutron flux fields in such as fusion reactor. Therefore, it is necessary to measure back-scattering cross sections of Fe, Li, C, B etc. to be used in the fusion reactor design. For this problem we designed the experimental system to extract the contribution of large angle scattering reaction. [1] The benchmark method was successfully established based on the activation of Nb foil normally used to characterize DT neutron sources. [2] However, Nb foil takes a long time to obtain the enough number of counts due to the long half-life of about 10 days and the low detection efficiency of the decay gamma-ray (energy of the decay gamma-ray = 934 keV). In this study, to solve this problem, we examined possible activation nuclides having appropriately short half-lives, not so high decay gamma-ray energies because high detection efficiency is essential, large

cross sections. And not too low threshold energies are required for the accuracy of benchmark experiments.

2. Benchmark experiments

Basic structure of the experimental systems and neutron transport paths we consider in benchmark experiments are shown in Fig. 2. A shadow bar is installed to prevent neutrons from directly incident on activation foil, which detects neutrons, from a neutron source. Possible paths that a neutron can transport and contribute to the activation of the foil are numbered from 1 to 7. Path 1 is the neutron path via the shadow bar. Path2 is the neutron path via the shadow bar and the sample. Path 3 is the backscattered neutron from the sample, which is an object to be extracted. Path 4 is the neutron path via the wall and shadow bar. Path 5 is the neutron path via the wall and the sample. Path 6 is the neutron path via the wall. Path 7 is the neutron path via the shadow bar and the wall and the sample.

The benchmark experiments are conducted in four experimental systems for extracting the contribution of large angle scattering reaction. Figure 3 shows the four experimental systems, two of which are with a thin shadow bar with and without the target, i.e., s1tc and s1c, and the rest two of which are with a thick shadow bar with and without the target, i.e., s2tc and s2c. Figure 3 also shows relation of the neutron transport paths that contribute to activation of the foil in each of the four systems. The contributions of paths 1, 4, and 6 are the same for s1tc and s1c, and for s2tc and s2c, because they depend on the size of the shadow bars, but not depend on that of the sample. That of path 5 is the same for s2tc and s1tc, and for s1c and s2c, because it depends on the presence of the sample. Therefore, calculating s1tc-s2tc-(s1c-s2c), we can estimate the amount of activation by neutrons through paths 2, 3 and 7. Those of paths 2 and 7 does not cancel each other out. However, they are relatively a rare event, because the transporting neutron through the paths experiences a large number of scatterings. It means the contributions of paths 2 and 7 show less than path 3 largely. We thus regard the two contributions as the experimental error of the present benchmark method. By comparing the amount of activation obtained by the experiment with MCNP simulation (the Monte Carlo simulation) [3], the correctness of the backscattering cross section of the nuclear data can be verified. As an example, the result of a benchmark experiment with the iron sample is detailed in Ref. [2].

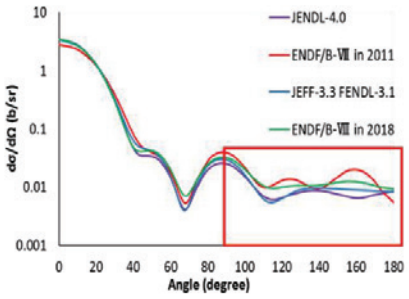

Figure 1 Angular distribution of neutron elastic scattering reaction cross section of ^{56}Fe at 14 MeV. [4-8]

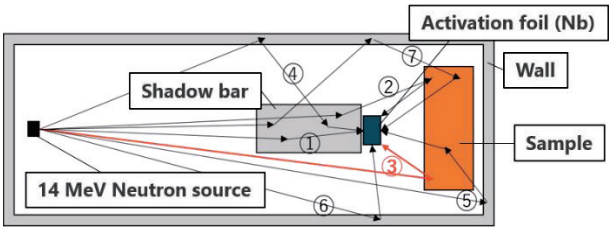

Figure 2 Basic structure of the experimental systems and neutron transport paths we consider in benchmark experiments. [1]

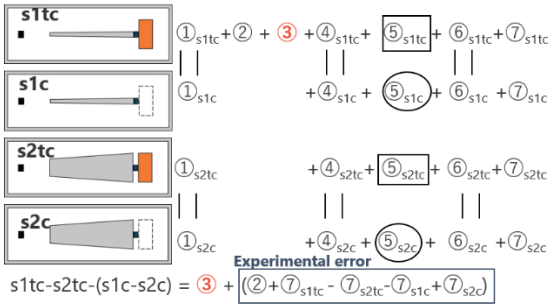

Figure 3 Four experimental systems and neutron transport paths that contribute to activation for each system. [1]

3. Method to optimize

At present, we need about one week to complete the benchmark experiments and another one week to finish measurement of the activation foils, in case of Nb foil is employed. To reduce the irradiation and measuring time, calculations of the number of counts for possible activation reactions were carried out for all nuclides stored in JENDL/AD-2017 using following equation:

$$\text{Count} = N \int_E \sigma f_n \varphi \, \mathrm{dE} \times \frac{1}{\lambda} \times f \times g \times I_r \times \varepsilon \times \left(1 - e^{-\lambda ti}\right) \times e^{-\lambda tc} \times \left(1 - e^{-\lambda tm}\right) \times DT \quad (1)$$

where N, σ, f_n, φ, λ, f, g, I_r, ε, ti, tc, tm DT represent the number of atoms, cross-section [cm^2] [9], factor of neutron self absorption [3], flux on foil calculated by MCNP with Fe sample [/cm^2/source neutron], decay constant [/s] [10], self shielding factor [11], isotopic ratio [12], gamma-ray emission ratio [10], gamma-ray detection efficiency, irradiation time [s], cooling time [s], measurement time [s] and neutron intensity [/s] ($=5 \times 10^9$), respectively. Consequently, candidate activation nuclides showing the highest accuracy (the largest number of counts) were found. To prevent the error of the count number from being dominant, we searched for an activation foil that can obtain 10,000 counts in the shortest time.

Since the present benchmark experiments are conducted in OKTAVIAN facility of Osaka University, Japan, there are constraints on the present calculation as follows. The maximum irradiation time per day is 8 hours, and in the case of consecutive day's experiment, the cooling time of 16 hours between irradiations is required. In addition, the maximum measurement time was set to 5 days. And gamma-ray detection efficiency used the value when the decay gamma-rays are measured at a distance of 3.1 cm from the detection window using germanium detector. The energy of backscattered neutrons by the sample is about 8-14 MeV depending on kind of the sample nuclides, because the incident neutron energy is 14 MeV. Even if the reaction threshold energy is below 8 MeV, the reaction cross section may still be low for the backscattered neutrons. Therefore, in this study, we do not take into account the threshold energy, i.e., the threshold energy condition is set to 0-14 MeV.

4. Result

The number of counts of the decay gamma-ray from Nb foil and the one that can realize the count number larger than 2,000 counts in the combination of irradiation and measurement are shown in Fig. 4.

This figure shows the increase in the number of counts measured for 1 to 5 days, when irradiation continues for 1 to 4 days. As can be seen from Fig. 4, it is found that the most efficient activation material to obtain 10,000 counts for the shortest irradiation and experimental period is gold using ^{197}Au(n,2n)^{196}Au reaction. Table 1 shows a comparison of the threshold energy, cross-sectional area, half-life, gamma ray energy and gamma ray emission ratio of ^{196}Au and ^{92m}Nb. However, since ^{196}Au has multiple excited state with a half-life of several minutes or more in Fig. 5 [13], it decays from two excited levels to the ground state over time. Then the number of counts of the decay gamma-ray from ground state is expected to be higher than estimation with Eq. (1).

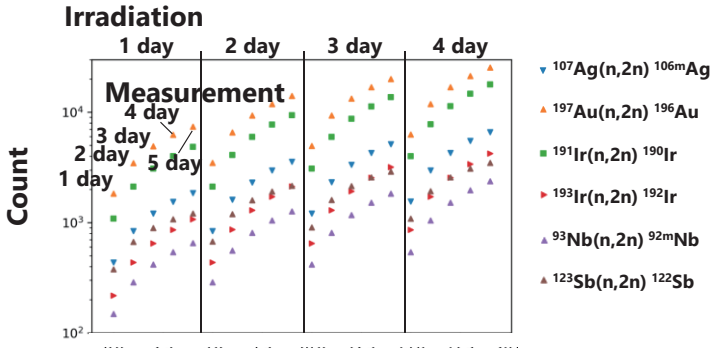

Figure 4 The number of counts of nuclides whose counts are larger than Nb foil.

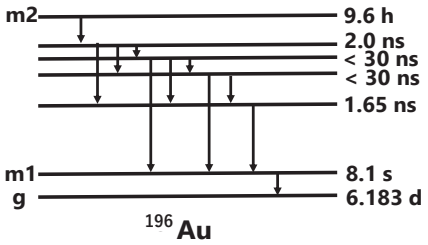

Figure 5 The multiple excited levels of ^{196}Au.

Table 1 Comparison of ^{92m}Nb and ^{196}Au.

	^{92m}Nb	^{196g}Au	^{196m1}Au	^{196m2}Au
Threshold energy [MeV]	9.1	8.1	8.2	8.7
Cross section at 14 MeV [barn] [8]	0.45	1.89	0.15	0.13
Half-life	10.1 d	6.1 d	8.1 s	9.6 h
Energy of emitted gamma ray [keV]	934	356	85	148
Emission ratio [%]	99	87	0.3	43

5. Formulation of foil activation method using gold foil

If the number of counts is represented by Eq. (1), reaction rate, $\int_E \sigma\varphi \, dE$, can be estimated from the number of counts of experiments. Then the correctness of the backscattering cross section of nuclear data can be verified by comparing the estimated reaction rate with the one calculated by the MCNP simulation. In the case of gold, the number of counts cannot be expressed simply by Eq. (1) with the fact described in Chap. 4. We thus need to formulate precisely to calculate the number of counts for gold in real applications. The number of counts in the case of two days of irradiation as shown in Fig. 6 is expressed by following equation:

$$\text{Count} = N_A \int_E \text{R}dE \times f \times g \times I_r \times \varepsilon, \tag{2}$$

where R is a term that includes cross section and decay constant, irradiation time, measurement time, and cooling time as shown in following equations. In these equations, σ_0, σ_1, σ_2, λ_0, λ_1, λ_2 represent cross sections of ground state, first excited state, second excited state, decay constant of ground state, first excited state, second excited state, respectively.

$$\text{R} = (\varphi_2 \text{A}_2 + \varphi_1 \text{B}_2)\left(1 - e^{-\lambda_0 t_m}\right) + (\varphi_2 \text{C}_2 + \varphi_1 \text{D}_2)\left(1 - \frac{\lambda_2}{(\lambda_2 - \lambda_0)} e^{-\lambda_0 t_m} - \frac{\lambda_0}{(\lambda_2 - \lambda_0)} e^{-\lambda_2 t_m}\right) \tag{3}$$

$$\sigma = \frac{\sigma_0 + \sigma_1 + \sigma_2}{\lambda_0} + \frac{\sigma_1 + \sigma_2}{\lambda_1} + \frac{\sigma_2}{\lambda_2 - \lambda_0} \tag{4}$$

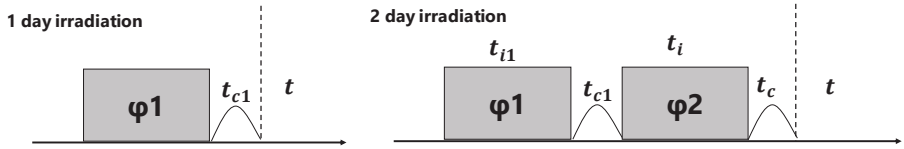

Fig. 6 Summary of the experiments.

For 1 day irradiation, irradiate with flux φ_1 for t_{i1}, cool for t_{c1} and then measure the decay gamma-ray for t_m. For 2 day irradiation, irradiate with flux φ_1 for t_{i1}, cool for t_{c1} and irradiate with flux φ_2 for t_{i2}, cool for t_{c2} and then measure the decay gamma-ray for t_m.

where A, B, C and D are given as below:

$$\mathrm{A} = \sigma\left(1 - e^{-\lambda_0 t_{i1}}\right) + \frac{\sigma_2}{\lambda_0 - \lambda_2}\left(1 - e^{-\lambda_2 t_{i2}}\right)e^{-\lambda_2 t_{c2}} + \frac{\sigma_2}{\lambda_1 - \lambda_2}\left(1 - e^{-\lambda_2 t_{i2}}\right)e^{-\lambda_2 t_{c2}}$$

$$\mathrm{B} = \frac{\sigma_2}{\lambda_2}\left(1 - e^{-\lambda_2 t_{i2}}\right)e^{-\lambda_2 t_{c1}} + \frac{\sigma_2}{\lambda_1 - \lambda_2}\left(1 - e^{-\lambda_2 t_{i1}}\right)e^{-\lambda_2 t_{c1} - \lambda_1 t_{i1}}$$
$$+\sigma\left(1 - e^{-\lambda_0 t_{i1}}\right)e^{-\lambda_0 t_{i2}} + \frac{\sigma_2}{\lambda_0 - \lambda_2}\left(1 - e^{-\lambda_2 t_{i1}}\right)e^{-\lambda_2 t_{c1} - \lambda_0 t_{i2}}$$
$$+\frac{\sigma_2}{\lambda_0 - \lambda_2}\left(1 - e^{-\lambda_2 t_{i1}}\right)e^{-\lambda_2 (t_{i2} - t_{c1} - t_{c2})} + \frac{\sigma_2}{\lambda_1 - \lambda_2}\left(1 - e^{-\lambda_2 t_{i1}}\right)e^{-\lambda_2 (t_{c1} - t_{i2} - t_{c2})}$$

$$C = \frac{\sigma_2}{\lambda_2}\left(1 - e^{-\lambda_2 t_{i2}}\right)e^{-\lambda_2 t_{c2}},\ D = \frac{\sigma_2}{\lambda_2}\left(1 - e^{-\lambda_2 t_{i1}}\right)e^{-\lambda_2 (t_{c1} - t_{i2} - t_{c2})}$$

Recalculating the number of counts of ^{197}Au(n,2n)^{196}Au using Eq. (2), considering increment due to decay of ^{196m1}Au and ^{196m2}Au, does not change significantly from Fig. 4 because σ_0 is one digit larger than σ_1 and σ_2.

It is generally known that the nuclear data of the activation cross sections may have errors. Since the errors of nuclear data of the activation cross sections (σ_0, σ_1, σ_2) cause the errors of R calculated from MCNP simulation, it would be better to normalize σ_0, σ_1, σ_2 with accurate re-measured values at 14 MeV experimentally. Since the number of counts of gamma rays emitted from ^{196m2}Au can simply be calculated by Eq. (1), σ_2 can be normalized accurately at 14 MeV. On the other hand, since the emission ratio of gamma rays emitted from ^{196m1}Au is small, the half-life is very short and the number of ^{196m1}Au changes largely depending on the decay of ^{196m2}Au, the number of counts of gamma rays emitted from ^{196m1}Au cannot be expressed by Eq. (1). As a result, σ_1 cannot be normalized easily. Similarly, the number of ^{196}Au changes irregularly due to existence of ^{196m1}Au and ^{196m2}Au, σ_0 cannot also be normalized easily. Therefore, we consider the following measuring procedure to utilize ^{197}Au(n,2n)^{196}Au in benchmark experiments.

First of all, paying attention to the fact that R can be represented by σ_2 and σ (including σ_0, σ_1, and σ_2) as shown in Eqs. (3) and (4), it can be seen that normalizing only σ_2 and σ can eliminate the error of activation cross section in R. For normalizing σ, cooling for 3 days after 1day irradiation. Then ^{196m2}Au and ^{196m1}Au almost decay and finally fall to the state of ^{196}Au. Therefore, ^{197}Au(n,2n)^{196}Au can be regarded as the virtual reaction in which ^{196}Au is just generated with the cross section σ, and the count number can be calculated by following equation:

$$\mathbf{Count} = N_A \int_E \varphi_1 \sigma dE \times \left(1 - e^{-\lambda_0 t_{i1}}\right)e^{-\lambda_0 t_{c1}} \times f \times g \times I_r \times \varepsilon \tag{5}$$

The virtual cross section value in Eq. (4), σ, can thus be normalized and to be used in real benchmark experiments in future.

The experiment to measure σ_2 and σ precisely in OKTAVIAN facility of Osaka University is currently underway.

6. Conclusion

It was found from the theoretical examination that gold was the best activation foil to replace Nb foil for the present benchmark experiment. In addition, the difficulty of using the reaction of ^{197}Au(n,2n) due to the multiple excited levels, ^{196m1}Au and ^{196m2}Au, in the activated gold foil is successfully overcome. After normalizing the cross section at 14 MeV at OKTAVIAN facility of Osaka University, the gold foil activation method would be utilized for our benchmark experiments in future.

References

1) N. Hayashi et al., “Optimization of Experimental System Design for Benchmarking of Large Angle Scattering Reaction Cross Section at 14 MeV Using Two Shadow Bars”, *Plasma and Fusion Research*, 2018; **13**: 2405002, 1-7.
2) A. Yamaguchi et al., “Benchmark experiment of large-angle scattering reaction cross section of iron at 14 MeV using two shadow bars – Comparison of experimental results with ENDF/B-VIII –”, *Journal of Nuclear Science and Technology*, 2021; **58** (1), 80-86.
3) Team, X-5 Monte Carlo, "MCNP –A General Monte Carlo N-Particle Transport Code, Version," Los Alamos National Laboratory, pp. LA-UR-03-1987, 2003.
4) K. Shibata et al., "JENDL-4.0: A New Library for Nuclear Science and Engineering," *J. Nucl. Sci. Technol*, 2011; **48** (1), 1-30.
5) M. B. Chadwick et al., “ENDF/B-VII.0: Next Generation Evaluated Nuclear Data for Nuclear Science and Technology”, *Nucl. Data Sheets*, 2006; **102**, 2931-3060.
6) JEFF-3.3 [Online]. France: The Nuclear Energy Agency; 2017 Nov. 20, Available from: https://www.oecd-nea.org/dbdata/jeff/jeff33/index.html [Accessed: Aug. 2, 2019].
7) FENDL-3.1 [Online]. Austria: International Atomic Energy Agency; 2016 July 1, Available from: https://www-nds.iaea.org/fendl/ [Accessed: Aug. 2, 2019].
8) D. A. Brown et al., "ENDF/B-VIII.0: The 8th Major Release of the Nuclear Reaction Data Library with CIELO-project Cross Sections, New Standards and Thermal Scattering Data", *Nuclear Data Sheets*, 2018; **148**, 1-142.
9) K. Shibata et al., “Activation Cross-section File for Decommissioning of LWRs”, *JAEA-Conf 2016-004*, 2016; 47-52.
10) S. Y. F. Chu, L.P.et al., WWW Table of Radioactive Isotopes [Online] 1999 Feb, Available from: http://nucleardata.nuclear.lu.se/toi/ [Accessed: November 17, 2021]
11) M. J. Berger at el., XCOM: Photon Cross Section Database (version 1.5) [Online]. USA: National Institute of Standards and Technology; 2010, Available from: http://physics.nist.gov/xcom [Accessed: Jul. 10, 2019].
12) J. S. Coursey et al., Atomic Weights and Isotopic Compositions (version 4.1). [Online]. USA: National Institute of Standards and Technology; 2015, Available from: http://physics.nist.gov/Comp [Accessed: May 30, 2020].
13) R. B. Firestone et al., “Table of Isotopes, 8th ed”. (Wiley, New York, 1999).

33. Nondestructive Determination of Water Content in Concrete Using Am-Be Neutron Source - Experimental Verification-

Yoshihiro Miyaji, Shingo Tamaki, Sachie Kusaka, Fuminobu Sato, Isao Murata,
Department of Sustainable Energy and Environmental Engineering, School of Engineering,
Osaka University, 2-1 Yamadaoka Suita, Osaka 565-0871, Japan
† Email: miyaji@qr.see.eng.osala-u.ac.jp

Abstract

New nondestructive measurement technique has been developed with an AmBe neutron source to evaluate the amount of water in concrete. A concrete wall is irradiated with fast neutrons to activate a gold foil set on the concrete. By evaluating in advance the relation of the gold activity and water content by calculations, we can determine the water content in the concrete, the water content of which is not known. In this study, to validate the present technique, experiments were performed with concrete samples having different water contents, which were made from only cement and water. It was confirmed from the experiments that water content could be estimated by the present nondestructive measurement technique for samples made of cement and water. Now we are examining the validity for concretes made of cement, water and sand.

1. Introduction

Concrete is often used in nuclear facilities for radiation shield. Shielding performance of neutrons depends mainly on water in concrete, because neutrons are mainly moderated by hydrogen atoms in water contained in concrete. However, concrete loses its contained water as time passes. It can affect the ability of radiation shield. We want to know water content in concrete for confirmation of the shielding performance of nuclear facilities and for high-precision neutronics experiments. However, destructive methods to measure water content in concrete are not suitable in nuclear facilities. So It is necessary to establish a new technique to nondestructively determine water content in concrete.

In the present study, a new nondestructive measurement technique is developed to evaluate the amount of water in concrete, and to validate the present technique experiments are performed with concrete samples having different water contents, which are made from only cement and water.

2. Nondestructive measurement technique

It is known from previous studies that when a concrete sample is irradiated with neutrons, the neutrons are moderated according to water content in the concrete. In other words, the number of fast neutrons moderated to thermal neutrons is determined mainly by the amount of water in the concrete. By combining the property explained above with the foil activation method, water content in concrete can be determined by the following

procedure developed in the previous study [1].

As in an experimental system shown in Fig. 2.1, a gold foil and Am-Be neutron source are placed on the concrete. The concrete is irradiated with fast neutrons by the Am-Be neutron source. Then, the neutrons are moderated mainly by hydrogens in the concrete, moderated neutrons are leaking from the concrete surface. The moderated neutrons enter the gold foil and activate it. Fast neutrons can be well moderated, if the amount of water increases. As a result, the gold foil can be well activated. It means that there should be a correlation between the water content in the concrete and the gold activity. In this study, to make the calibration curve of gold activity to water content, series simulation calculations were performed using MCNP5 [2], that is, gold activities are calculated for various concretes having various water contents. Other conditions are as follows: Irradiation time is one day. The source intensity of Am-Be is 2.4×10^{6} n/s. The composition of the concrete used by calculation is shown in Table 2.1. From the result, a calibration curve of the gold activity to the water content in the concrete was obtained.

Figure 2.2 shows the calibration curve obtained by the series simulations using MCNP5. Figure 2.3 shows an enlarged view of the calibration curve for the low water content region of 0 to 0.01 mol/cc. From Fig. 2.3, as an exception concrete containing carbon which is a light atom (ANSI) and extremely high density concrete (heavy concrete) deviate slightly from the trend of other concretes. However, for other concretes, regardless of the density and composition, it can be seen that the gold activity changes depending only on water content in the concrete. By using this calibration curve, it is possible to measure the water content in a concrete wall, the water content of which is not known, with a gold foil and AmBe neutron source. When the thickness of concrete is 40 cm or more, the activity of gold foil is constant regardless of the thickness of concrete, so Fig. 2.2 can be used. On the contrary, when the thickness of concrete is 40 cm or less, the activity of gold foil changes depending on the thickness of concrete. Therefore, for concrete with a thickness of 40 cm or less, it is necessary to create a calibration curve for each thickness.

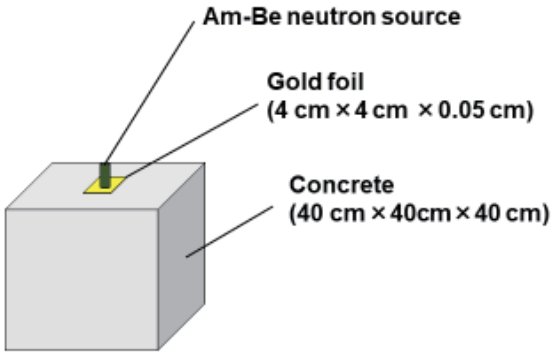

Fig 2.1 Simulation system.

Table 2.1 Composition of concretes. [3]

	Ordinary concrete			Serpentinite concrete (wt%)	Heavy concrete (wt%)
	JAERI (wt%)	**ANSI** (wt%)	**JRR-4** (wt%)		
H	0.416	0.208	0.894	1.916	0.45
C	0	5.582	0	0	0
O	50.74	49.339	50.534	50.415	31.392
Na	0	0	1.498	0.062	0
Mg	0.115	0.209	0.698	16.9	0.047
Al	0.446	0.511	5.501	1.28	0.199
Si	38.606	18.808	28.8	15.5	2.982
S	0.07	0.082	0.304	0.016	1.936
K	0	0	1.798	0.077	0
Ca	6.869	24.949	7.692	6.95	4.081
Ti	0	0	0	0.005	0
Mn	0	0	0	0.79	0
Fe	2.738	0	2.281	6.8	58.913
Ni	0	0.312	0	0	0
Total	100	100	100	100	100
density (g/cc)	2.05	2.33	2.24	2.275	3.35

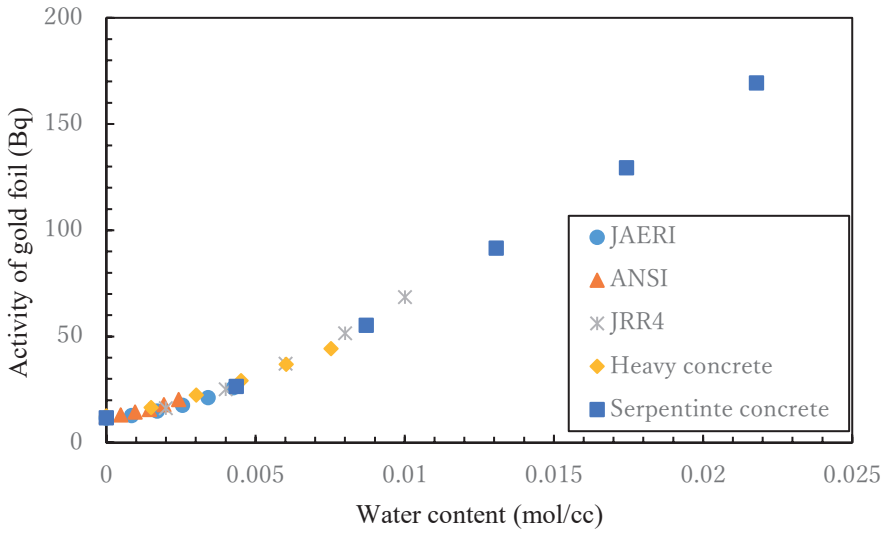

Fig 2.2 Calibration curves of gold activity to water content.

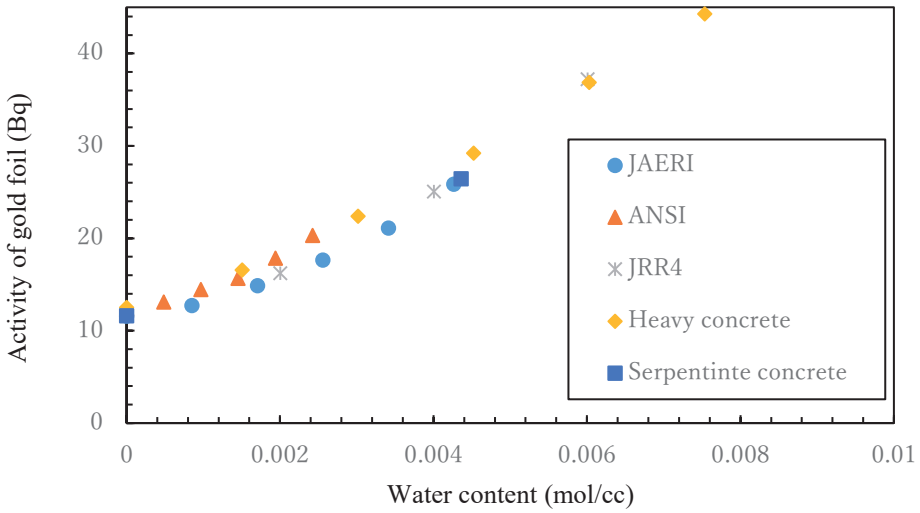

Fig 2.3 Calibration curves for low water content.

3. Experiment

In order to confirm the validity of the present technique, experiments were performed with four concrete samples having different water contents, which were made from only cement and water, meaning they have no aggregate. An example of the experimental system is shown in Fig. 3.1. Four concretes made very carefully by ourselves have water contents as 0.0209, 0.0241, 0.0267 and 0.0272 mol/cc. As a way to know the water content accurately, we measured the mass ratio of cement and water before mixing. Next, we mixed cement and water, and we measured the mass of the concrete before it hardens. After that, the water content in the concrete before solidification is measured by multiplying the mass and the mass ratio of water and water before mixing. Finally, the difference between the mass of the concrete after solidification and the mass

of the concrete before solidification is measured, and the difference is the amount of evaporation of water, and the water content in the concrete is obtained by subtracting that amount. The densities of the four concretes are 2.09, 2.05, 2.03, and 2.04 g/cc. The ratio of the amount of substance of four concretes is shown in Table 3.1, 3.2, 3.3 and 3.4. The size of concretes is 40 cm in length, 40 cm in width, and 40 cm in height. A gold foil and Am-Be neutron source were placed on the concrete as shown in Fig. 3.1, and a gold foil was activated on each concrete by neutron irradiation with the Am-Be neutron source for one day. The intensity of Am-Be source is 2.4×10^6 n/s. We measured the activation of each gold foil with a germanium semiconductor detector. The gold activities obtained by the experiments were compared with the predicted gold activities.

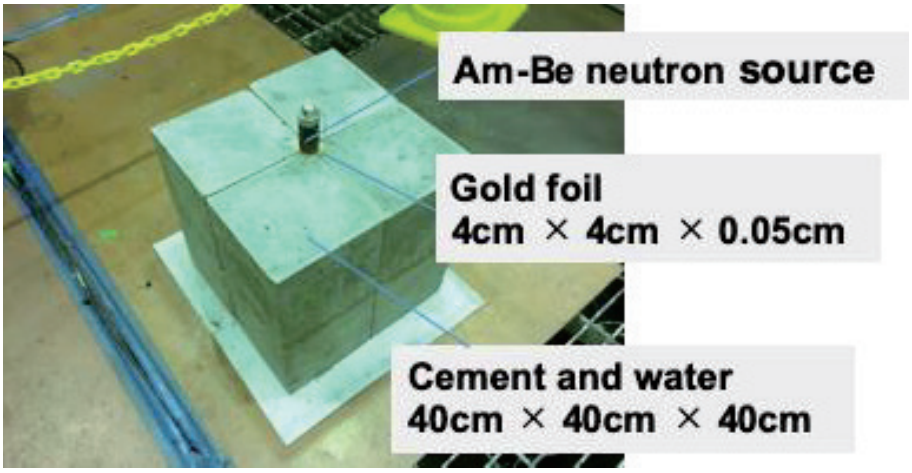

Fig 3.1 Experimental system.

Table 3.1 Ratio of the amount of substance in concrete 0.0209 (mol/cc)

element	H	O	Si	Al	Fe	Ca	Mg	S	Na	K
Amount of substance (%)	31.87	45.14	4.75	1.15	0.48	15.46	0.60	0.37	0.08	0.11

Table 3.2 Ratio of the amount of substance in concrete 0.0241 (mol/cc)

element	H	O	Si	Al	Fe	Ca	Mg	S	Na	K
Amount of substance (%)	35.20	44.01	4.30	1.04	0.43	13.98	0.54	0.33	0.08	0.10

Table 3.3 Ratio of the amount of substance in concrete 0.0267 (mol/cc)

element	H	O	Si	Al	Fe	Ca	Mg	S	Na	K
Amount of substance (%)	37.68	43.17	3.96	0.96	0.40	12.88	0.50	0.31	0.07	0.09

Table 3.4 Ratio of the amount of substance in concrete 0.0272 (mol/cc)

element	H	O	Si	Al	Fe	Ca	Mg	S	Na	K
Amount of substance (%)	37.90	43.11	3.93	0.95	0.39	12.76	0.49	0.31	0.07	0.09

4. Results

Figure 4.1 shows the result of comparing the experimental value of the gold activity with the calculated value. As a result, the calculated and experimental values agree well within the experimental errors. In the next step, we plan to carry out experiments with real concretes with aggregates, and thereafter measure a real concrete wall in our facility, OKTAVIAN. For that purpose, now we are examining how to fix the real number of hydrogens in concrete for validation of the presently proposed method.

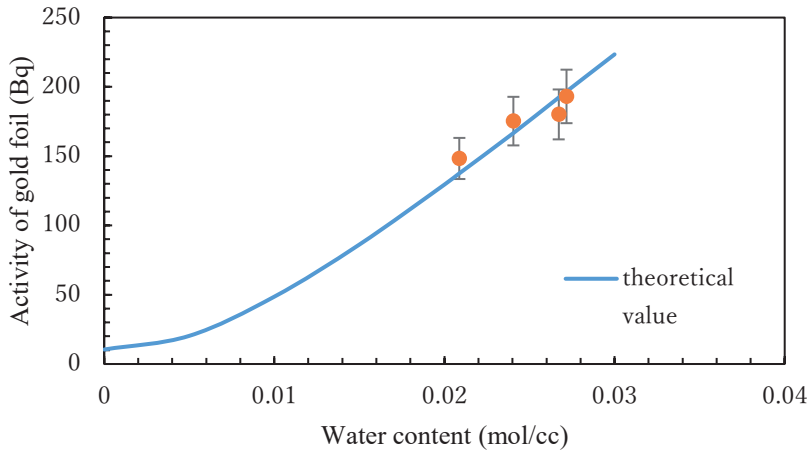

Fig 4.1 Experiment result.

5. Conclusion

It was confirmed from the experiments that water content could be estimated by the present nondestructive measurement technique for samples made of cement and water.

In the next step, we will confirm the validity for aggregate concretes, concretes containing carbon and heavy concretes. Finally, we will apply to a real concrete wall in an actual nuclear facility.

References

[1] Y. Nishiyama, et al., Nondestructive Determination of Water Content in Concrete by Foil Activation Method -Feasibility study by Numerical Simulation-, JAEA-Conf 2017-001, 2018, pp.211-217.

[2] Los Alamos National Laboratory, A General Monte Carlo N-Particle Transport Code ver.5, 2003.

[3] D. Ito, Monte Carlo Calculation Hand Book, AESJ, 2006, p.224.

34. Comparison of double-differential cross sections between JENDL/PD-2016.1 and experimental data for photo-neutron production of medium-heavy nuclei at 16.6 MeV

*T.K.Tuyet[1], Y.Sakaki[2], T.Sanami[1,2], H.Yamazaki[1,2], T.Itoga[3], A.Takeuchi[1], S.Miyamoto[4] and Y.Asano[2]
[1]SOKENDAI, Shonan Village, Hayama, Kanagawa 240-0193 Japan
[2]KEK, 1-1 Oho, Tsukuba-shi, Ibaraki-ken 305-0801 Japan
[3]JASRI, 1-1-2, Kouto, Kamigori-cho, Ako-gun, Hyogo 678-1205 Japan
[4]University of Hyogo, 1-1-2, Kouto, Kamigori-cho, Ako-gun, Hyogo 678-1205 Japan
Email: tuyet@post.kek.jp

Abstract: Understanding the photoneutrons' production from high-energy photons plays an important role in accelerators' shielding design. We measured the double differential cross sections (DDX) for the (γ,xn) with 16.6 MeV polarized photons on Pb, Au, Sn, Cu, Fe, and Ti targets and observed the low-energy and high-energy components on the neutron energy spectra. In this work, we present the first comparison between the DDXs from JENDL/PD-2016.1, used in Monte Carlo simulation tools to evaluate dose rate. There is a disagreement between the JENDL/PD-2016.1 and experimental data. The photoneutron's low energy component agrees with the JENDL/PD-2016.1, while the high-energy component does not.

1. Introduction

In an electron accelerator, high-energy photons can be produced as bremsstrahlung radiations. These photons can interact with surrounding accelerator components, and via the photonuclear reaction, and produce secondary particles including neutrons. The double differential cross-section (DDX) of the photoneutron is an essential quantity for radiation shielding and shielding calculation of the electron accelerator design.

Until now, there are researches about photo-neutrons production in photonuclear reaction [1-4]. In the previous study of our research group [1], photoneutrons' energy spectra produced by the reaction of 16.6 MeV polarized photons on the Pb, Au, Sn, Cu, Fe, and Ti targets were measured at various angles. The low-energy and high-energy components were identified in the energy spectra [1]. The angular distribution of the low-energy component showed isotropic, while the high-energy component showed a dependence on the interaction angle between photon polarization and neutron emission [1].

The evaluated nuclear data library is used in simulation tools (such as PHITS, which is mentioned in section 3) for shielding calculation and particle transportation. Comparison between the experimental data and the evaluated data on DDXs of medium to heavy targets provides new information on photo-neutron energy and angular distribution in addition to show contributions from evaporation and pre-equilibrium processes separately.

2. Experiment

The experiment was performed at NewSUBARU-BL01, Hyogo, Japan. The details of our experimental setup were mentioned in Ref. [1]. Figure 1 indicates a detector system and setup of photoneutron measurement.

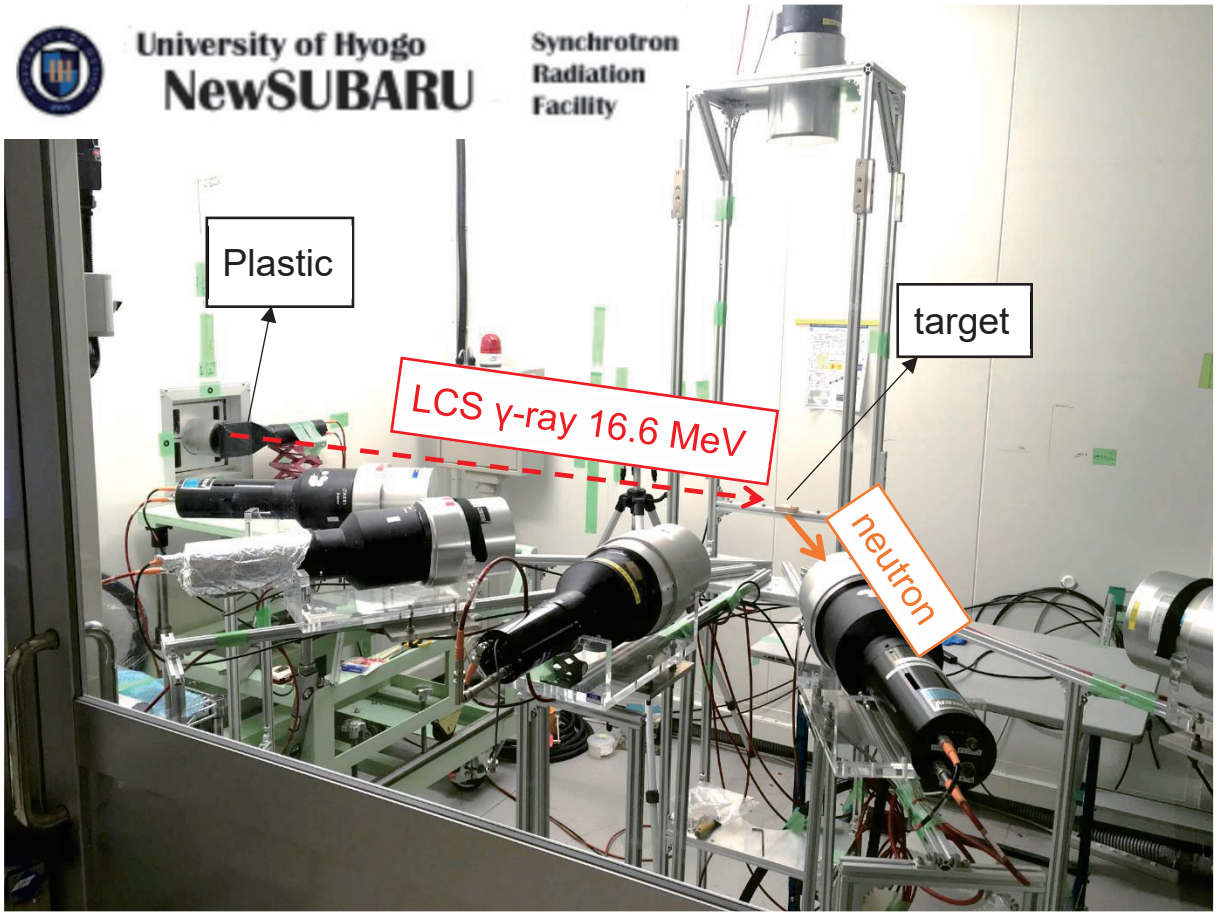

Figure 1. The experimental setup of the photo-neutron measurement

In this measurement, we determined the photoneutron production per incident LCS photon. We placed a plastic scintillator, with 0.5 cm thickness and 10 cm^2 surface area, at 179.7 cm upstream from the target to estimate the number of incidents LCS photons. The cylindrical-shaped targets of Pb, Au, Sn, Cu, Fe, and Ti, with 1 cm diameter and 1-4 cm thicknesses, were prepared in this experiment. The LCS photons interact with the prepared targets and generate neutrons. We placed six 12.7 cm×ϕ12.7 cm^L cylindrical detector filled with NE213 organic liquid scintillator at different angles 30°, 60°, 90°, 120°, 150° (horizontally), and 90° (vertically), with respect to the photon beam axis. The distances from the target center to the detectors ranged from 60 to 90 cm. As the neutron detector was sensitive to both photoneutrons and background gamma radiations, a pulse shape discrimination (PSD) method was employed. The time-of-flight (TOF) technique was employed to measure the neutron energy. A VME-based data acquisition (DAQ) system was set up to collect the tail and full charges of NE213's signals by using a QDC module and measure the time difference between the LCS photon and NE213 detector by using a TDC module. The energy deposited in the plastic scintillator was also measured by our DAQ.

The neutron was distinguished from gamma events by a two-dimensional plot of time-of-flight vs ratio of light outputs from slow and total gates (Slow/Total). Figure 2 displays neutron-gamma events separation. Figure 3 indicates neutron-gamma time-of-flight spectra after neutron-gamma events separation. An energy threshold of 0.25 MeVee employed in our data was determined by energy calibration using gamma radiations of ^{137}Cs, ^{22}Na, and ^{60}Co.

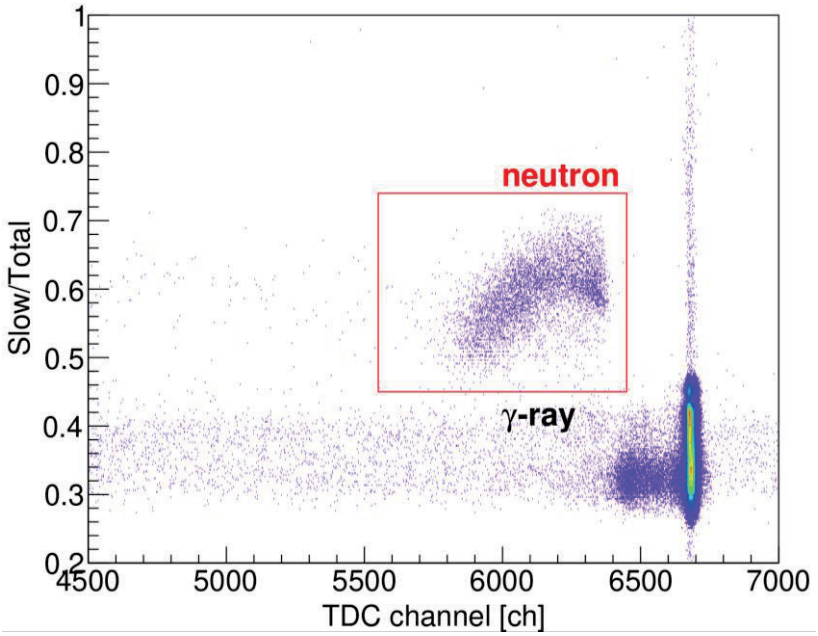

Figure 2. Separation of neutron and gamma events by using ratio of pulse heigh slow and total gates

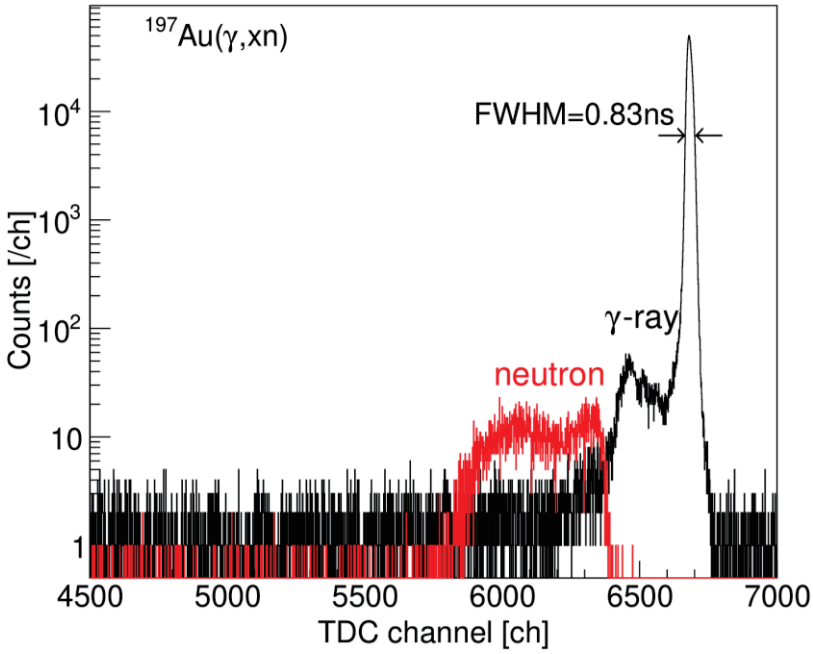

Figure 3. The neutron and gamma spectrum

We determined the efficiency of neutron detectors by measuring a ^{252}Cf source and the SCINFUL-QMD simulation [7] to evaluate the total number of neutrons emitted from the target. The photon self-

absorption factor inside the Au target was evaluated using the PHITS [8] simulation tool. With our setup, we obtained a time resolution of 0.83 ns at gamma peak and a neutron's energy resolution of less than 10%.

The experimental data was obtained by using the polarized photon. In this work, we presented the DDXs, which were obtained by detectors at vertical 90 degrees and horizontal 60 degrees (H60) to minimize the polarization effect of the photon.

3. Evaluated nuclear data library and PHITS calculation

In this work, the DDXs from the evaluated nuclear data library and PHITS calculation are compared with the experimental data. The DDXs were extracted from JENDL/PD-2004 and JENDL/PD-2016.1 library by our python-based software. The abundances of each target's isotopes were considered in calculating the DDXs from the JENDL/PD-2016.1 library. Because we experimented using the monoenergetic 16.6 MeV incident photons, the JENDL/PD-2016.1 DDXs of the incident photon's energy within 16 MeV – 17 MeV were taken average to yield the spectrum of the library that should be compared to the experimental data.

We used PHITS to calculate the DDX of photoneutron produced by the 16.95 MeV photons incident on the Au, Pb, Sn, Cu, Fe, and Ti, which were natural targets. This energy was equal to the maximum energy used in the experiment. The targets were cylindrical in this simulation with both diameter and thickness of 5 μm to remove the self-absorption effect due to the target's thickness. This self-absorption effect was considered in the experiment normalizing the DDX with the photon and neutron attenuation factors. The DDX was obtained on a detector cylinder, with both diameter and thickness of 12.7 cm, placed at 90 degrees and 60 cm away from the target.

4. Result and discussion

Figure 4 shows DDXs obtained from the experiment, the evaluated nuclear data libraries, the PHITS calculation for the Au target. The circles indicate the experimental data at horizontal 60^{o} (H60), and the squares are the data at vertical 90^{o} (V90). The experimental spectra indicate the low and high energy components.

The black and blue lines are PHITS results (version 3.16) and JENDL/PD-2004, respectively. The PHITS code has used the reaction cross-section from JENDL/PD-2004 and the Generalized Evaporation Model (GEM) to generate energy spectra. Different models predict the different DDXs, PHITS [9] has used the GEM, while JENDL/PD-2004 [10] has used exciton model-based code, CCONE, to produce the DDXs of photo-neutron. The both spectra are not consistent with the experimental spectra, the high-energy component was not reproduced by the PHITS and JENDL/PD-2004. In addition to this, the slope of the PHITS spectrum is lower than the experimental spectra.

The red line is the DDXs from JENDL/PD-2016.1. In this comparison, JENDL/PD-2016.1 produced the energy distribution in low energy, whereas this model cannot explain the high-energy component.

A maximum neutron energy was determined by subtracting Q_{value} of the (γ,xn) reaction from the photon energy. The maximum energy of results from the evaluated nuclear data and PHITS calculation are lower than the experimental data. The maximum energy in the JENDL and PHITS have been calculated using exactly the Q-value of the photonuclear reaction. In the photo-neutron measurement,

that was impacted by energy resolution of neutron and the incident photon. The comparison of other targets is similar to that of Au.

In this comparison, PHITS simulation does not produce the high-energy component, in spite of the good agreement in the low-energy region below 4 MeV. Besides, the evaluated nuclear data library could not reproduce the high-energy region.

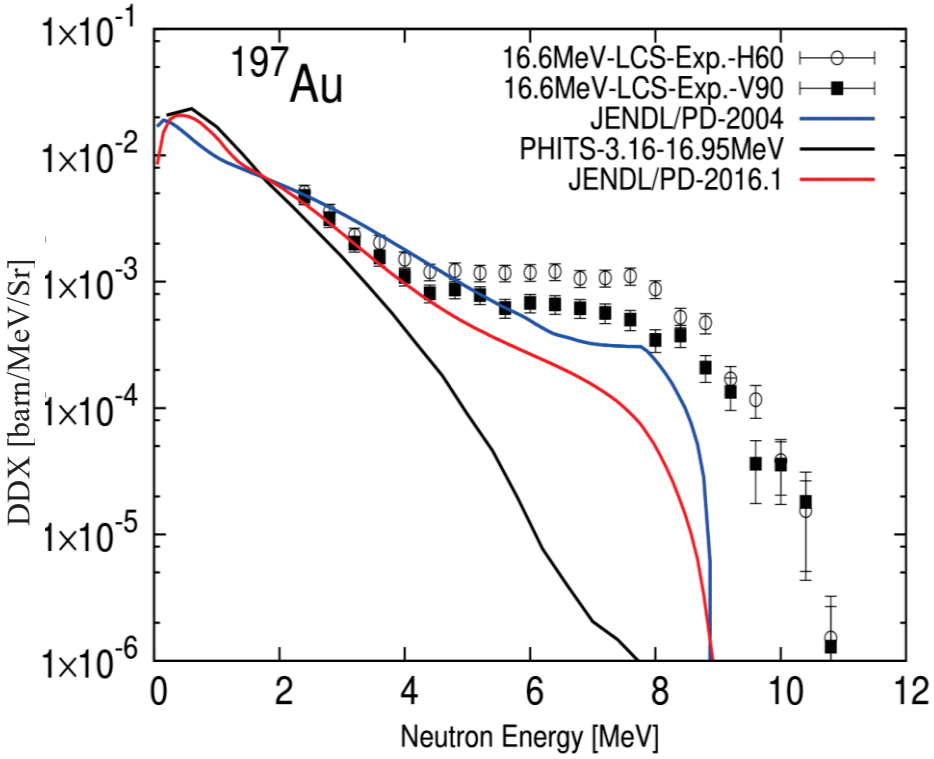

Figure 4. Results of PHITS, evaluated nuclear data libraries and experiment for the DDXs of ^{197}Au(γ,xn)

5. Conclusion

We compared the double differential cross-section from the evaluated nuclear data library (JENDL/PD-2016.1) and the experiment. The results show disagreement between JENDL/PD-2016.1 and the experiment in high energy region. Thus, a model to reproduce the high energy component should be included in the simulation. To develop a model of high prediction power, further measurement on DDX is strongly desired for various targets and energies.

References

[1] Tuyet T.K., Sanami T., Yamazaki H., et al., Energy and angular distribution of photo-neutrons for 16.6 MeV polarized photon on medium–heavy targets, Nucl. Instrum. Methods A, 989 (2021) 164965.

[2] Kirihara Y., Nakashima H., Sanami T., et al., Neutron emission spectrum from gold excited with 16.6 MeV linearly polarized monoenergetic photons, J. Nucl. Sci. Technol., 57 (2020) 444.

[3] Horikawa K., Miyamoto S., Mochizuki T., et al., Neutron angular distribution in (γ, n) reactions with linearly polarized γ -ray beam generated by laser Compton scattering, Phys. Lett., B 737 (2014) 109.
[4] Agodi A., Nuovo Cimento, 5, (1957) 21 (1).
[5] Asano Y., Miyamoto S., Shielding design of laser electron photon beamlines at SPring-8, Prog Nucl Sci Tech., (2014) 252.
[6] Miyamoto S., Asano Y., Amano S., et al., Laser Compton back-scattering gamma-ray beamline on NewSUBARU, Radiat Meas., 41 (2) (2007) S179.
[7] Satoh D., Kunieda S., Iwamoto Y., et al., Development of SCINFUL-QMD code to calculate the neutron detection efficiencies for liquid organic scintillator up to 3 GeV, J. of Nucl Sci Tech., 39 (2014) 657.
[8] Sato T., Iwamoto Y., Hashimoto S., et al., Features of Particle and Heavy Ion Transport code System, J. Nucl. Sci. Technol., 55 (2018) 684.
[9] Sato T., Niita K., Matsuda N., et al., Particle and Heavy Ion Transport Code System, PHITS, version 2.52, J. Nucl. Sci. Technol., 50 (2013) 913–923.
[10] Iwamoto N., Kosako K., Murata T., Photonuclear Data File, JAEA-Conf 2016-004 (2016) 53-58.

35. Development of Evaluation Method of Uncertainty of Radioactivity by Propagating Nuclear Data Covariance for Clearance Verification in Decommissioning of Nuclear Power Plants

Tatsuki AMITANI[1], Tsunenori INAKURA[1], Naoki YAMANO[1], Ken-ichi TANAKA[2], Chikako ISHIZUKA[1], Masato WATANABE[3], Ryoji MIZUNO[4], Satoshi CHIBA[1*]

[1] Tokyo Institute of Technology, 2-12-1 Ookayama, Meguro-ku, Tokyo, 152-8550, Japan

[2] The Institute of Applied Energy, 1-14-2 Nishi-shimbashi, Minato-ku, Tokyo, 105-0003, Japan

[3] Chubu Electric Power Co., Inc., 1 Higashi-shincho, Higashi-ku, Nagoya, Aichi, 461-8680, Japan

[4] Chuden CTI Co., Ltd., 1-3-10 Higashi-sakura, Higashi-ku, Nagoya, Aichi, 461-0005, Japan

[*]Email: chiba.satoshi@nr.titech.ac.jp

To optimize the disposal of low-level radioactive wastes originating from the decommissioning of nuclear facilities, required are 1) a reliable assessment of the radioactivity level by calculations and measurements and 2) a rational estimate of uncertainties of those results for the classification of the radioactive waste. We established a procedure to estimate uncertainties of a radioactivity concentration required in the clearance verification by evaluating and propagating covariance of nuclear data properly. For this aim, we estimated covariance of neutron cross sections of nuclides that account for over 90 % in the sum of D/C of concrete materials and carbon steels. Here, D stands for the radioactivity concentration, and C stands for the clearance level. The covariance of nuclear data was estimated by employing a propagation of uncertainties of nuclear model parameters in the resonance and smooth regions by a combination of nuclear model codes implemented in T6. Then, we developed a new method to calculate uncertainty of the radioactivity by "Total Monte Carlo" method by connecting randomly perturbed ENDF-6 format files generated by T6 to NJOY2016, and random 1-group activation cross sections were inserted to ORIGEN2 in ORLIBJ40. It was concluded that the uncertainty of the radioactivity due to that of nuclear data for nuclides which dominate the ΣD/C is of the order of 0.12 to 1.2%, which is sufficiently smaller than the uncertainty of the radioactivity originating from that of the neutron flux.

1. Background and Purpose

At present, more than 20 nuclear power plants are either in the process of decommission or planned to be decommissioned in near future in Japan. Therefore, decommissioning will become an important activity in nuclear industry, so the procedure must be standardized. Decommissioning of nuclear power plants produces huge amount of low-level radioactive waste. Radioactive wastes with extremely low radioactivity concentrations and therefore having negligible impact to general public are referred to as clearance wastes. They can be reused and disposed of in the same way as general industrial waste with the confirmation and permission of regulation authority. Promotion of clearance reduces the

environmental burdens and hence accomplishes streamlining and facilitating decommissioning in a proper way.

To be classified as clearance wastes, ΣD/C, sum of D/C by each specified nucleus, must be lower than 1. Here, D stands for radioactivity concentration, and C stands for clearance level. In near future, Nuclear Regulation Authority will stipulate that the uncertainty of radioactivity concentration must be considered as a part of clearance procedure [1]. Therefore, it is required to establish a method to evaluate the radioactivity concentration having rational uncertainty.

Uncertainty of radioactivity concentration depends on uncertainty of three factors, (1) nuclide composition of material, (2) neutron irradiation condition and (3) nuclear data. Uncertainty of nuclear data, namely, covariance data, was not considered in previous clearance studies. On the other hand, while nuclear data library JENDL-4.0 that is frequently used for radioactivation calculation in Japan has nuclear data for 406 nuclides, only 95 of them have covariance data. Evaluation of uncertainty of radioactivity cannot be performed correctly without covariance data. For example, it is known that simple square sum propagation of variance data gives underestimation of the uncertainty when the off-diagonal elements of the covariance matrix are positive, while it gives overestimation when the off-diagonal elements are negative. Accurate estimation of the uncertainty of the radioactivity is possible only when the full covariance matrix is taken into consideration. For this reason, considering covariance data in uncertainty evaluation is essentially important.

The purpose of this study is to establish a method to estimate the covariance data for nuclides without covariance data in JENDL-4.0, and also to construct a method to quantitatively evaluate the effect of uncertainty of nuclear data in the calculation of radioactivity by connecting to radioactivation calculation.

2. Developed evaluation method

As a method to quantitatively evaluate the influence of uncertainty in nuclear data, we developed an evaluation method using the TMC (Total Monte Carlo) method, which incorporates calculations by the nuclear data evaluation code group T6 [2]. Figure 1 shows our evaluation method.

T6 consists of 6 codes (TASMAN, TALYS, TARES, TEFAL, TANES, TAFIS) and produces nuclear data library. In this study, we used 4 codes in T6, TALYS, TARES, TASMAN and TEFAL (Table 1). T6 calculation generates perturbed cross sections in ENDF-6 format file. These files are denoted as random files. TMC calculation is the process of performing radioactivation calculation using ORLIBJ40 with these random files as input, and then statistically processing the result.

As preparation of T6 calculation, (1) reproduction of cross section in JENDL-4.0 and (2) adjustment of distributions of model parameters for random calculation are needed. For (1), resonance parameters in JENDL-4.0 were used to calculate cross sections in the resonance region with TARES and parameters including optical model parameters are adjusted manually to calculate cross sections in the continuous region with TALYS. For (2), uncertainties of resonance parameters evaluated by Mughabghab [3, 4] were employed in the resonance region. Uncertainties of negative resonances were adjusted to reproduce uncertainty of the thermal cross section. On the other hand, TALYS improves parameter distributions for each random calculation based on Bayesian Monte Carlo (BMC) method. The posterior distribution obtained by the BMC method starting from a uniform distribution given as the prior distribution was used as the parameter distribution in the main calculation. After configurating the above setting, 1,000 random files were produced by 1,000 random calculations as the main calculation.

In the TMC calculation, the random files were processed by NJOY2016 and then effective one-group

cross section was generated for each random file using neutron flux data. Then, it was incorporated into the one-group cross section library set ORLIBJ40, and ORIGEN2 was used to calculate the radioactivity. This procedure was repeated for the number of random files, and the results were statistically processed to obtain the mean value and standard deviation.

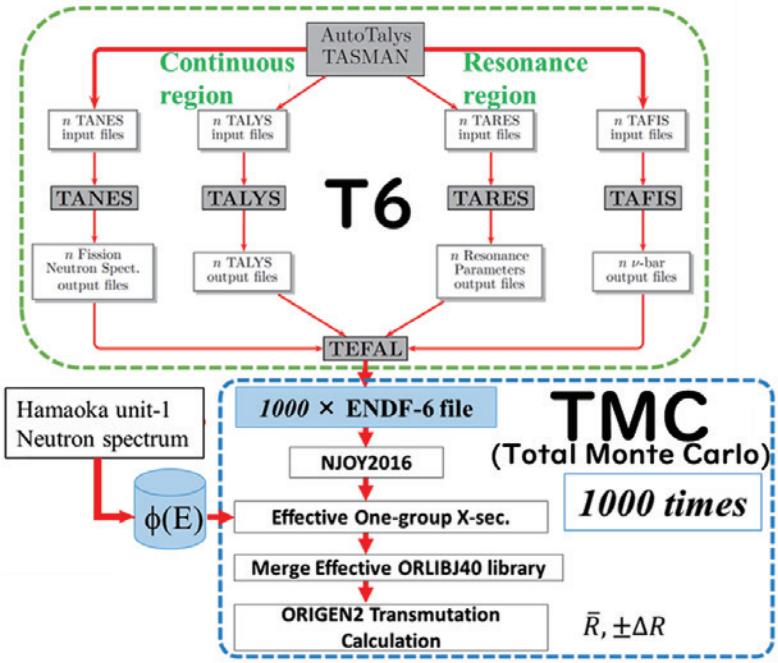

Figure 1 Overview of developed evaluation method

Table 1 Codes in T6 used in this study

TALYS	a nuclear reaction code to calculate cross sections in the continuous region.
TARES	a code to generate resonance cross sections.
TASMAN	a code for production of covariance data using result of TALYS and TARES.
TEFAL	a code for the translation of the nuclear reaction results from TALYS, TARES and TASMAN into ENDF-6 formatted nuclear data libraries.

3. Calculation Result of Covariance with T6

The nuclides to be evaluated were selected by performing calculation of radioactivity by ORLIBJ40. The assumed plant was Hamaoka unit-1. Evaluation position was located at 30 cm depth from the surface of the concrete of the RSW (Reactor Shielding Wall) at the center height of the reactor core. Materials were general concrete material (density = 2.3 g/cm^3) and carbon steel of primary containment vessel (PCV) (density = 7.86 g/cm^3). Material composition data and neutron flux data ware provided from Chubu Electric Power Co., Inc. Figure 2 shows neutron flux at the evaluation point. Effective full power year (EFPY) is 16.2 years. As a result of activation calculation, ^{60}Co and ^{152}Eu were found to be the dominant radionuclides. Therefore, their parent nuclides, ^{59}Co and ^{151}Eu, were selected as the nuclides to be evaluated.

Random calculations were carried out by reproducing the cross sections of JENDL-4.0 for the evaluated nuclides and adjusting the parameter distribution according to the procedure shown in Section

2. The top graph in figure 3 shows perturbed ^{151}Eu(n, γ)^{152}Eu cross sections generated T6. The bottom graph in Figure 3 shows the relative standard deviation when the generated cross sections were grouped by the VITAMIN-B6 structure and statistically processed.

Figure 4 shows correlation matrix of (n, γ) cross section of ^{151}Eu. In 1/*v* region, correlation is strongly positive since the energy-dependence of the cross section is fixed. On the other hand, correlation is weak and complex in resonance region. Correlation between continuous and resonance regions is zero because TALYS and TARES are independent calculations of each other. Similarly, we also calculated correlations between different reactions for calculations, including neutron transport calculation, other than this study.

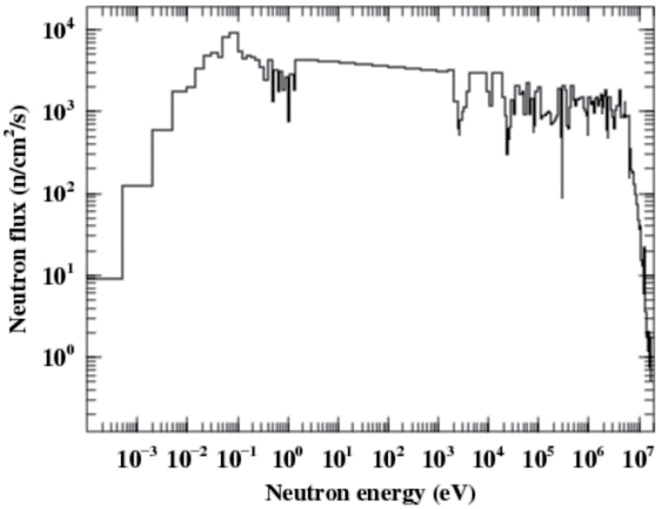

Figure 2 Neutron flux in the concrete 30 cm deep from the surface of the RSW at the center height of the reactor core (VITAMIN-B6 structure)

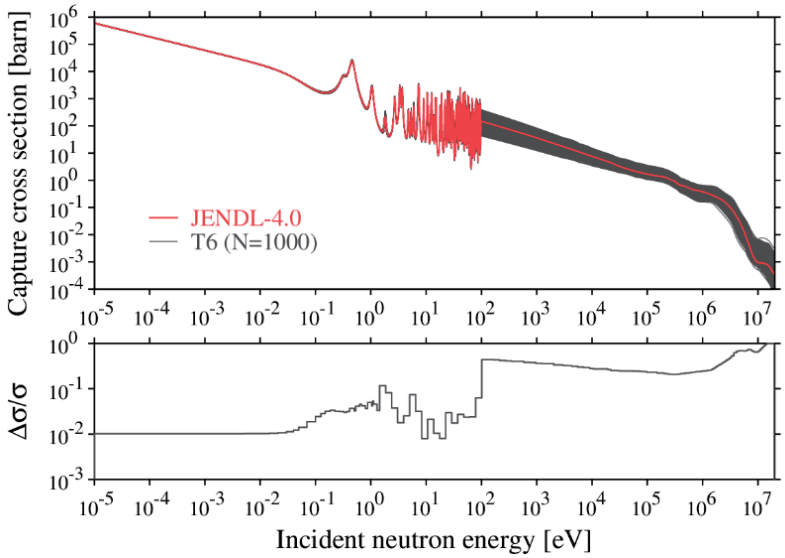

Figure 3 Perturbed ^{151}Eu(n, γ)^{152}Eu cross sections generated by 1000 times T6 calculation and relative standard deviation

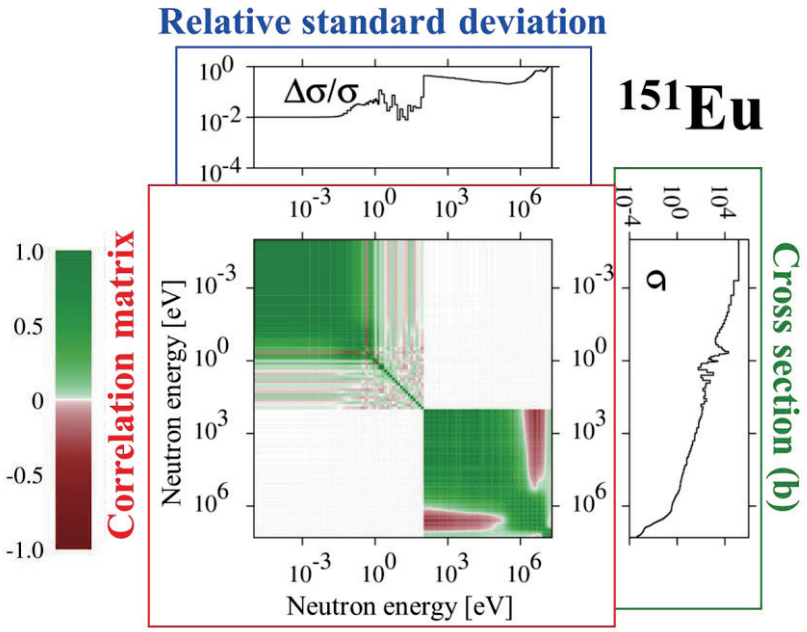

Figure 4 Correlation matrix of (n, γ) cross section of ^{151}Eu calculated with T6

4. Evaluation of Uncertainty of Radioactivity

We calculated D/C uncertainty due to nuclear data by TMC calculation. Figure 5 shows calculated D/C and relative standard deviation of that of dominant nuclides in concrete. From the result, Δ(D/C) of ^{60}Co is 0.12 % and that of ^{152}Eu is 1.2 %. Figure 6 shows similar calculation result in carbon steel (PCV). From the result, Δ(D/C) of ^{60}Co is 0.12 %. These results are smaller than uncertainty due to neutron flux data, which is dozens % [5]. Therefore, it can be concluded that the uncertainty due to nuclear data is not major factor in the uncertainty of the radioactivity.

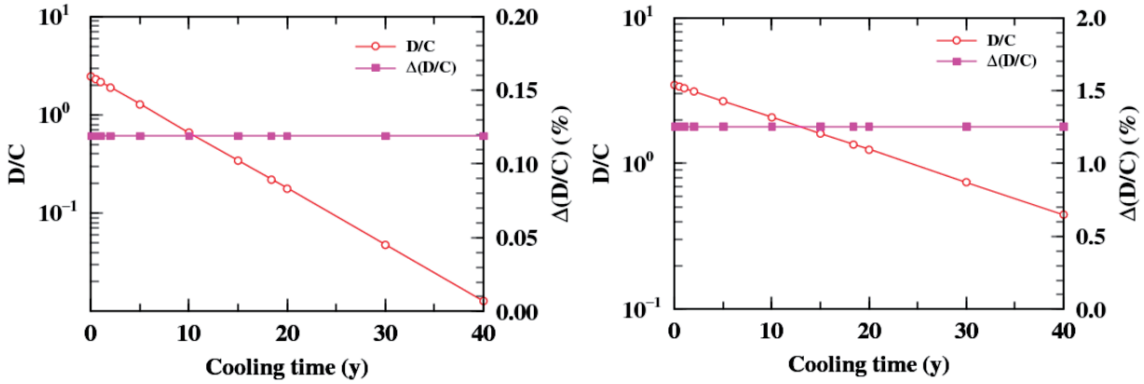

Figure 5 D/C and relative standard deviation of D/C (Δ(D/C)) of dominant nuclides in concrete (left: ^{60}Co, right: ^{152}Eu)

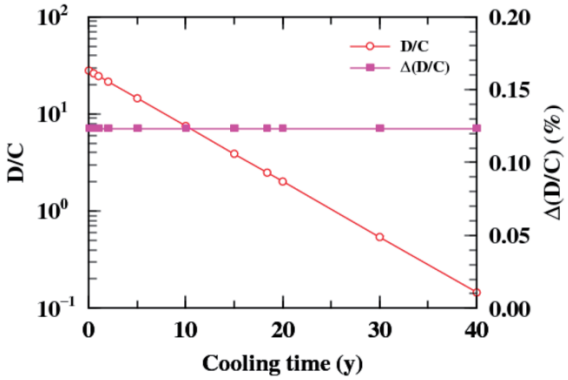

Figure 6 D/C and Δ(D/C) of dominant nuclide, ^{60}Co, in carbon steel

5. Conclusion

In order to contribute to the rationalization of the disposal of dismantled waste generated in the decommissioning of nuclear power plants, we developed quantitative evaluation method of the uncertainty in radioactivity due to uncertainty of nuclear data. Then, we applied our evaluation method to Hamaoka unit-1 and evaluated the uncertainty of D/C of important nuclides in clearance verification, ^{60}Co and ^{152}Eu.

Our evaluation method consists of T6 calculation and TMC calculation. T6 calculation generates perturbed cross sections in ENDF-6 format file for data that reproduces JENDL-4.0. TMC calculation is the process of performing activation calculation using ORLIBJ40 with generated cross sections as input, and then statistically processing the result.

We applied developed method to Hamaoka unit-1 and calculated uncertainty of D/C of dominant nuclides in concrete material and carbon steel. From the result, uncertainty of ^{60}Co due to nuclear data is 0.12 % and that of ^{152}Eu is 1.2 %. They are smaller than uncertainty due to neutron flux data, which is dozens %. Therefore, it can be concluded that the uncertainty due to nuclear data is not major factor in the uncertainty of the radioactivity.

References

1) Nuclear Regulation Authority, クリアランスの測定及び評価の方法の認可に係る内規の見直し方針について, (2019).
2) A.J. Koning and D. Rochman, Modern Nuclear Data Evaluation with the TALYS Code System, Nuclear Data Sheets **113**, 2841 (2012).
3) S.F. Mughabghab, Atlas of Neutron Resonances: Volume 1: Resonance Properties and Thermal Cross Sections Z=1-60, 6th ed., Elsevier, New York (2018).
4) S.F. Mughabghab, Atlas of Neutron Resonances: Volume 2: Resonance Properties and Thermal Cross Sections Z=61-102, 6th ed., Elsevier, New York (2018).
5) K. Yokoi, T. Endo, A. Yamamoto, R. Mizuno and Y. Kimura, Uncertainty Quantification of Activation Due to Cross Section Data in Neutron Shielding Calculation, Trans. Am. Nucl. Soc., **115**, pp.1085-1087 (2016).

Acknowledgements

This study includes results of collaborative study on “クリアランス検認で求められる放射能評価の不確かさの研究” between Tokyo Institute of Technology and Chubu Electric Power Co., Inc.

36. Study on characteristics of neutron and γ-ray fields at compact neutron source RANS-II facility by simulation by the PHITS code

Kenta SUGIHARA[†1,2], Yujiro IKEDA[3,4], Tomohiro KOBAYASHI[3], Kunihiro FUJITA[3], Nobuhiro SHIGYO[2], Kanenobu TANAKA[1], and Yoshie OTAKE[3]

[1]RIKEN Nishina Center, RIKEN, 2-1 Hirosawa, Wako, Saitama 351-0198, Japan
[2]Department of Applied Quantum Physics and Nuclear Engineering, Kyushu University, Motooka, Nishi-ku, Fukuoka 819-0395, Japan
[3]RIKEN Center for Advanced Photonics, RIKEN, 2-1 Hirosawa, Wako, Saitama 351-0198, Japan
[4]J-PARC Center, Japan Atomic Energy Agency, 2-4 Shirakata, Tokai-mura, Naka-gun, Ibaraki 319-1195, Japan
[†]Email: kenta.sugihara@riken.jp

Aiming at development of a compact neutron source for non-destructive inspection, RIKEN Accelerator-driven compact Neutron Source-II (RANS-II), based on the p-Li reaction with 2.49 MeV proton beam, has been under beam commissioning. As it is important to assess the validity of neutrons at the RANS-II facility, radiation fields in a rather narrow experimental room has been studied. The characteristics of neutron and γ-ray are calculated by simulation with Particle and Heavy Ion Transport code System (PHITS). As a result, except for a target station, neutrons and γ-rays distribute widely in the hall. The scattered radiation could be the major contributor to the background events in the future experiments. Thus, a collimator is designed to suppress the background radiation. In this article, we report the radiation fields in the RANS-II hall and the effectiveness of the collimator.

1 Introduction

RIKEN Accelerator-driven compact Neutron Source-II (RANS-II) has been under beam commissioning to demonstrate specific performance of the system[1]. At the RANS-II facility, neutrons are produced via ^{7}Li(p, n)^{7}Be reaction with 2.49 MeV proton beam. Through the studies of neutrons generated at RANS-II, RIKEN has a prospect of realizing novel non-destructive neutron inspection for infrastructures.

As prominent characteristics, RANS-II has the maximum neutron energy of 0.8 MeV, which is lower than that of 5 MeV at RANS based on the ^{9}Be(p, n)^{9}B reaction with 7 MeV proton injection[2]. Neutron at the RANS-II facility has extremely forward-favored angular distribution with respect to the proton beam direction. Also, it should be emphasized that the RANS-II system is installed in a relatively small space isolated by concrete shield with boron containment. Accordingly, there should be quite large differences in neutronic performances between RANS-II and RANS in terms of neutron spectrum and angular distributions. Prior to future experiments at RANS-II, the simulation of radiation fields for neutron and γ-ray in the RANS-II experimental hall plays a critical important role for designing experimental set-up in low background.

In this paper, we report characteristics of dose rate in the experimental hall. Major source of background and adequacy of shielding are discussed in viewing requirement from future experiment. Also we have preliminary designed collimators to provide neutron beam for the experiments. The effect of collimator is discussed from quality of neutron beam profile as well as reduction of radiation background in the hall.

2 Simulation

2.1 Cross section data and simulation code

We have performed simulations to characterize radiation fields of RANS-II with the use of Particle and Heavy Ion Transport code System (PHITS)[3]. To calculate neutron production via the ^{7}Li(p, n)^{7}Be reaction, Evaluated Nuclear Data File/B-VII.0 (ENDF/B-VII.0)[4] is employed. The cross section of ENDF/B-VII.0 is shown in Figure 1. Neutron energy spectra at six angles with respect to proton beam direction with ENDF/B-VII.0 is depicted in Figure 2. We use an angular width of $\pm 1.5^{\circ}$ in the figure. According to Figure 2, characteristics of the maximum energy and the angler distributions of forward-favored are visible. Japanese Evaluated Nuclear Data Library-4.0 (JENDL-4.0)[5] and Livermore Evaluated Photon Data Library '97 (EPDL97)[6] is applied to calculate interactions of neutrons and γ-ray, respectively.

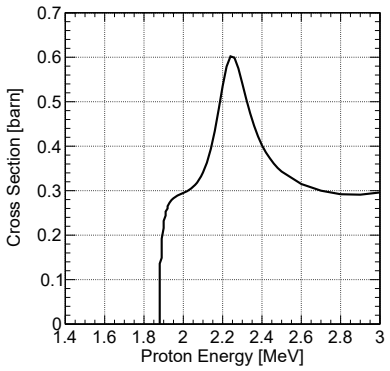

Figure 1: Cross section of ^{7}Li(p, n)^{7}Be reaction from ENDF/B-VII.0.

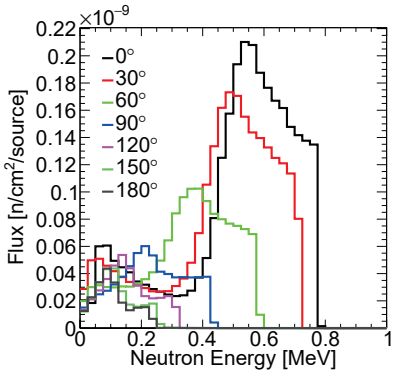

Figure 2: Neutron energy spectra from 0° to 180° at 30° intervals with respect to the proton beam direction.

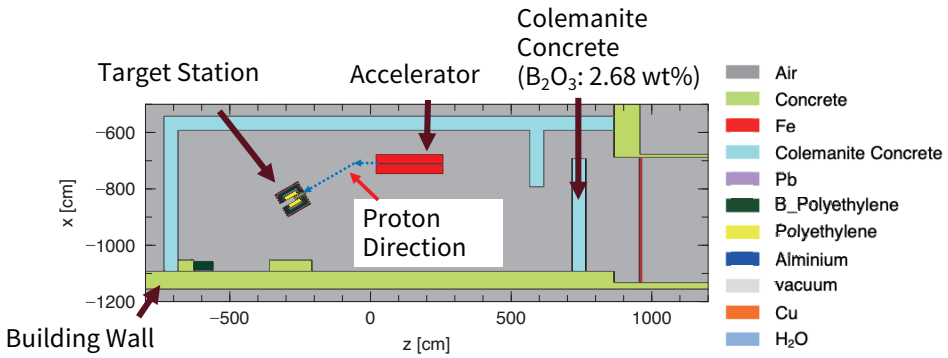

Figure 3: Plan view of the calculation model for the RANS-II experimental hall. Accelerator and target station of RANS-II are surrounded by concrete and partially colemanite concrete with boron.

2.2 Model for simulation

Simplified model of the RANS-II experimental hall, accelerator, target station in PHITS is illustrated in Figure 3. The size of the hall is about 14 × 5.5 × 3.0 m^3. An enlarged view of the target station is shown in Figure 4. The lithium(Li) target is made by depositing thin Li layer of about 100 μm on a 5 mm thick copper substrate cooled by water in the target station. The target station with all of the sides about 900 mm long has five layers, polyethylene(PE), lead(Pb), borated polyethylene with 10 % weight B_2O_3(BPE), lead and iron to reduce the radiation leakage. There is a hole with a 150 × 150 mm^2 cross section in the forward direction. Calculations introduced in the following chapters are performed with these systems.

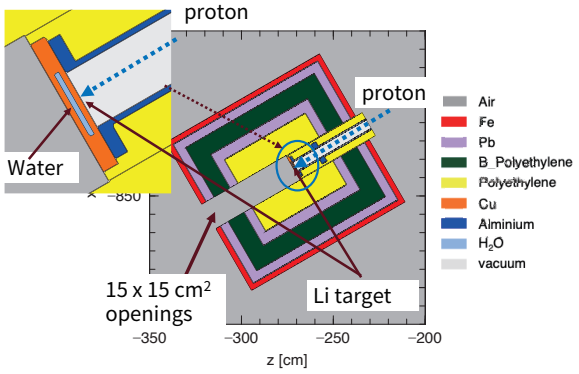

Figure 4: RANS-II target station.

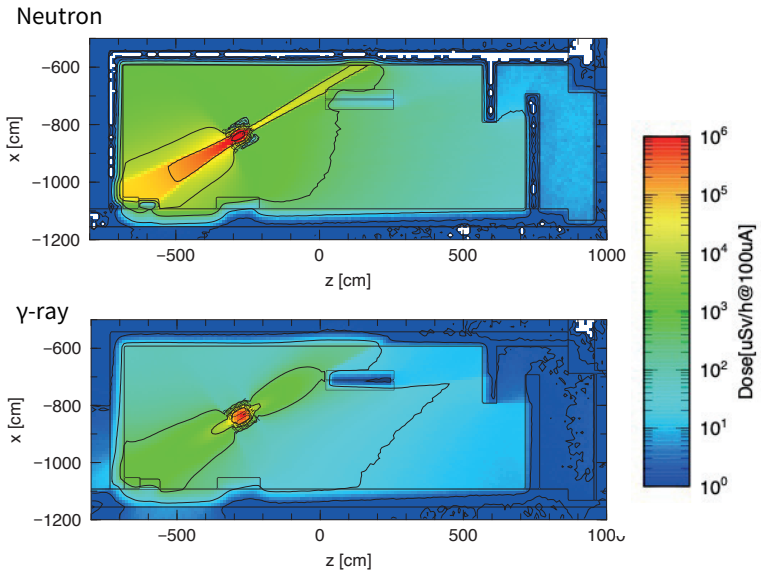

Figure 5: Dose rate distribution of neutrons and γ-rays at the RANS-II hall. The T-Track tally in PHITS is used. The mesh width for both x and z axis is 100 mm in the calculation.

3 Result and discussion

3.1 Dose rate distribution

We assume 100 μA for the proton beam current at the Li target. Dose rate distribution of neutrons and γ-rays at the RANS-II hall is depicted in Figure 5. The dose conversion coefficient[7] in PHITS is utilized in Figure 5. Along the downstream of the beam line, the highest dose rate of neutrons is shown. Except locations near the neutron production target and along the proton beam direction, dose rate distribute uniformly. Around the side of the target station, the dose rate is the order of 1.0 mSv/h and 0.1 mSv/h for neutron and γ-ray, respectively. For the neutrons, the dose rate is caused by the scattered neutrons with the down stream concrete

walls. Dose rate of γ-ray is mainly attributed to γ-ray from the reactions between neutrons and elements in the concrete. The ratio of the component scattered from the concrete walls is about 90% for both neutrons and γ-ray at the region. The scattered neutrons and γ-rays become background events in the future experiments. Suppression of the background radiation is important. Therefore, we have a plan to install a collimator in the target station to reduce the excessive spread of the neutron beam introduced in the following chapter.

3.2 Collimator

To suppress the spread of neutrons, it is intended to insert a collimator in the downstream openings at the target station as shown in Figure 6. There is a cylindrical cavity at the center of the collimator. The length of the collimator is 530 mm. It is necessary to examine the influence of the collimator's material and hole diameter for neutron suppression capacity. The material of the collimator is assumed to be PE or BPE. The hole diameter is 10, 30 and 50 mm. At the downstream of the target station, detectors in simulation are aligned along a surface perpendicular to proton beam direction. Sizes of the detectors are $10 \times 10 \times 10$ mm^3 and $100 \times 100 \times 100$ mm^3 at the central region and outside region, respectively. x' axis is defined as the axis along the detectors. The number of neutrons is obtained by the T-Cross tally implemented in PHITS. The energy range for fast and thermal neutrons is set from 10^{-2} to 10^{2} MeV and from 10^{-9} to 10^{-7} MeV, respectively.

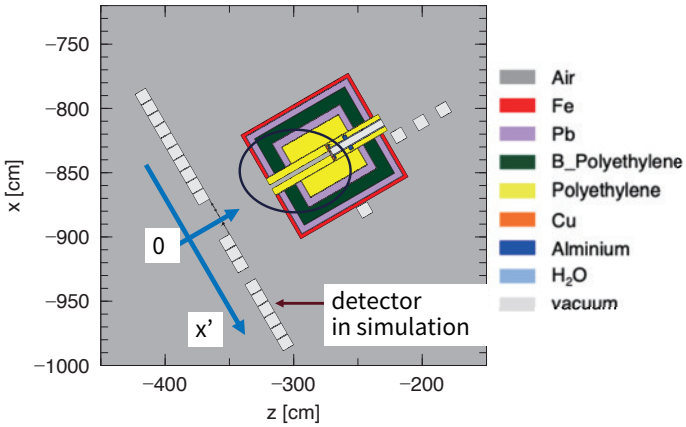

Figure 6: Target station with a PE collimator.

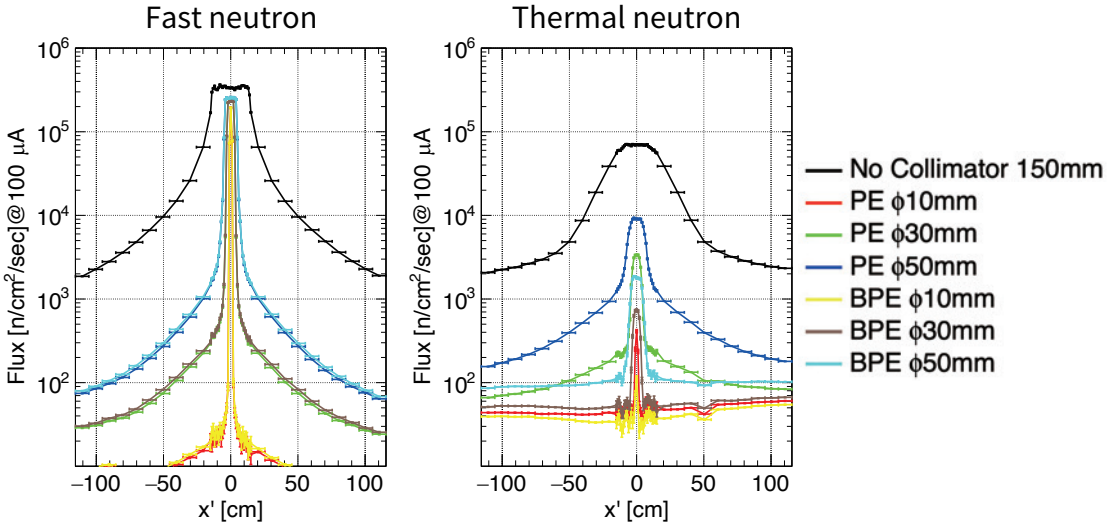

Figure 7: Fast and thermal neutron flux at the downstream. The horizontal axis means the value of x'. The vertical axis represents the flux of neutrons.

The results of neutron flux are shown in Figure 7. The black line stands for the result without the collimator. The red line means the outcome for the PE collimator with the 10 mm cylinder hole. The other colors' lines are similar to the red line. Because the PE or BPE collimator has elements with small mass number, it is effective for neutron suppression. According to the results of fast neutrons, the suppression ability for the PE collimator is a little greater than that for BPE collimator. This is attributed to the greater amount of hydrogen in the PE collimator than BPE one. For thermal neutrons, the BPE collimator has much stronger power than the PE collimator due to boron effect. The result suggests that the BPE collimator is appropriate to reduce the wide spreading of thermal neutrons. When the diameter of the collimator is 10 mm, the number of neutrons is too suppressed to utilize for future experiments. The collimator with 30 mm hole is enough to provide sharp neutron beam because the fast and thermal neutron flux are roughly to be less than 1/100 at the outer region from x' = 15 compared with the value at x' = 0. Accordingly, we conclude that BPE collimator with 30 mm hole is suitable for neutron suppression.

Because the γ-rays' attenuation in materials depends on the mass number, significant effect for γ-ray of the BPE collimator is not expected. To control γ-ray distribution, the material of the collimator is changed to BPE and Pb as shown in Figure 8. The length of the Pb collimator is 230 mm. The minimum and maximum energy in the tally is fixed to be from 10^{-9} to 10^{2} MeV for both neutrons and γ-rays. The other conditions for the calculation are the same as above calculation.

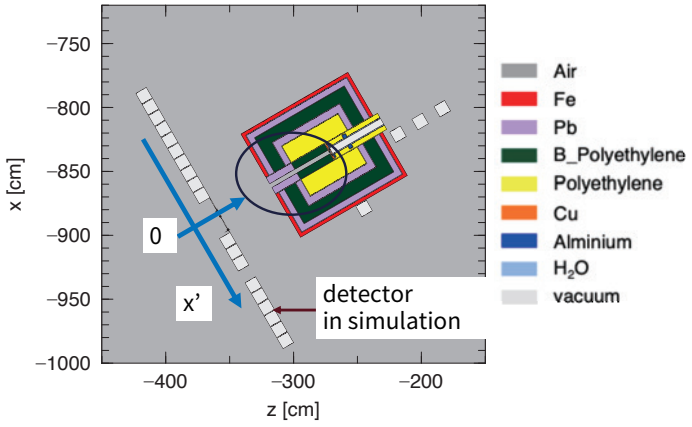

Figure 8: Target station with a BPE + Pb collimator.

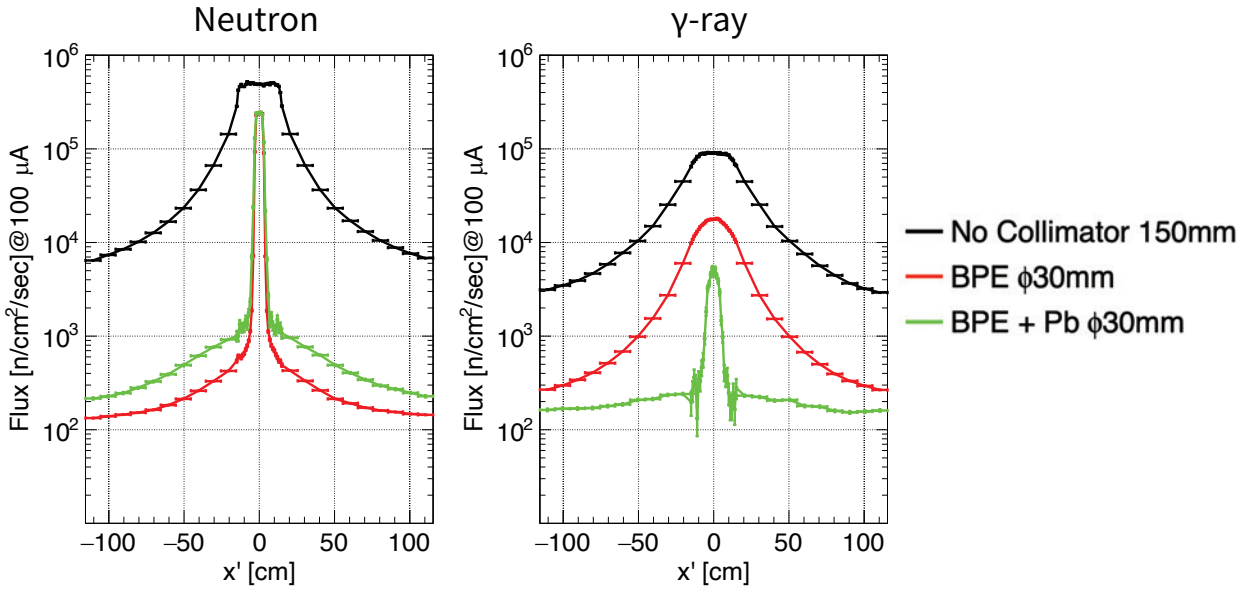

Figure 9: Neutron and γ-ray flux at the downstream.

The calculation results with BPE + Pb collimator are depicted in Figure 9. The black, red and green line stands for the result without the collimator, that with the BPE collimator and that with the BPE + Pb collimator, respectively. According to the neutron result, the neutron flux with the BPE and Pb collimator is a little greater than that of only BPE collimator due to the reduction of BPE area of the collimator. On the other hand, great contribution for γ-ray flux is observed. Compared with the value at the point of x' = 0, γ-ray flux drops by about 5% at the external area from x' = 15.

4 Conclusion

The distribution of neutrons and γ-rays in the RANS-II experimental hall are acquired with the use of PHITS. The interactions of neutrons and γ-rays are described by JENDL-4.0 and EPDL97, respectively. Due to the openings at the downstream of the target station and small experimental hall, neutrons and γ-rays spread widely in the hall. When the BPE and Pb collimator is installed in the openings of the target station, The RANS-II facility can supply sharp neutron beam with low background condition.

References

[1] Kobayashi T, et al., Completion of a new accelerator-driven compact neutron source prototype RANS-II for on-site use, Nucl. Instr. Methods, Phys. Res., Sect. A, vol. 994, 2021, pp. 1-6, 165091.

[2] Otake Y, RIKEN Compact Neutron Systems with Fast and Slow Neutrons, Plasma Fusion Res., vol. 13, 2018, 2401017.

[3] Sato T, et al., Features of Particle and Heavy Ion Transport code System (PHITS) version 3.02, J. Nucl. Sci. Technol., vol. 55, 2018, pp. 684-690.

[4] Chadwick, M.B., et al., ENDF/B-VII.0: Next Generation Evaluated Nuclear Data Library for Nuclear Science and Technology, Nucl. Data Sheets, vol. 107, 2006, pp. 2931-3060.

[5] Shibata K, et al., JENDL-4.0: A New Library for Nuclear Science and Engineering, J. Nucl. Sci. Technol., vol. 48, 2011, pp. 1-30.

[6] Cullen, D.E., et al., "EPDL97: the Evaluated Photon Data Library, '97 Version", UCRL-50400, Vol. 6, Rev. 5, Lawrence Livermore National Laboratory (1997).

[7] Sakamoto Y et al., Dose conversion coefficients for high-energy photons, electrons, neutrons and protons, JAERI-1345, 2003 [in Japanese].

Acknowledgement

The PHITS calculations were performed using the supercomputer system of RIKEN. This work was partially supported by Council for Science, Technology, and Innovation (CSTI), Cross-ministerial Strategic Innovation Promotion Program (SIP), "Infrastructure maintenance, renovation and management" (Funding agency: JST) and also partially supported by "Upgrading and sophistication of compact and high brightness neutron sysytem for high-degree application of industrial use" Photon and Quantum Basic Research Coordinated Development Program from the Ministry of Education, Culture, Sport, Science, and Technology, Japan.

37. Nuclide production cross section of ^{nat}Lu target irradiated with 0.4-, 1.3-, 2.2-, and 3.0-GeV protons

Hayato TAKESHITA[1,2], Shin-ichiro MEIGO[2], Hiroki MATSUDA[2], Hiroki IWAMOTO[2],
Keita NAKANO[2], Yukinobu WATANABE[1], Fujio MAEKAWA[2]
[1]Department of Advanced Energy Engineering Science, Kyushu University
[2]J-PARC Center, Japan Atomic Energy Agency
email: takeshita.hayato.890@s.kyushu-u.ac.jp

Proton-induced nuclide production cross sections of ^{nat}Lu target were measured at incident energies of 0.4, 1.3, 2.2, and 3.0 GeV by means of the conventional activation method. The targets were irradiated by the proton beam generated from the 3 GeV Rapid Cycling Synchrotron of Japan Proton Accelerator Research Complex. Gamma-rays emitted by the irradiated samples were detected by two high purity Ge detectors. The experimental data were compared with model predictions to benchmark reaction models used in the simulation of particle transport in matter, INCL4.6/GEM and INCL++/ABLA07.

1. Introduction

For the design of high-energy accelerator facilities such as accelerator-driven transmutation systems (ADSs) and spallation neutron sources, reliable assessment of radioactivity in target and structural materials requires sufficiently accurate estimation of the production yields of radioactive nuclides. Although a great deal of effort has been devoted to studying the spallation reactions from both the theoretical and experimental [1, 2] perspectives, the prediction powers of theoretical models are still insufficient. As for the experiments, relatively large uncertainties (~10%) in the experimental data make it difficult to improve the theoretical models. To obtain accurate experimental data required for improving the theoretical models, we have conducted a series of systematic measurements of nuclide production cross sections for various targets using the 3 GeV Rapid Cycling Synchrotron (RCS) accelerator at the Japan Proton Accelerator Research Complex (J-PARC). Our previous experiments for Al, Pb, and Bi targets [3,4] showed that a well-calibrated current transformer successfully reduced the uncertainty in the beam current, which finally achieved approximately 3.6% as the minimum total uncertainty.

To improve theoretical reaction models, further experimental data are required in the GeV range where the experimental data are insufficient. Recently, we have measured the nuclide production cross sections for Ho, Lu, and Re at 0.4, 1.3, 2.2, and 3.0 GeV to meet the requirement. In this paper, we show preliminary results of ^{nat}Lu. In addition, we compare the measured data with theoretical model calculations using INCL4.6/GEM [5, 6] and INCL++/ABLA07 [7, 8].

2. Experiment

The sample foils were assembled in four stacks as shown in Figure1. In each stack, Ho, Lu, and Re targets

were put in order of increasing atomic number. To prevent the products from escaping to the other target, Al foils were inserted between samples. All foils were 25 mm × 25 mm square and 0.1-mm thick. Four sets of stacks were enclosed in 0.1-mm-thick Al containers, and were fixed on movable stages in a vacuum chamber, which was installed in the beam dump line. Each stack was inserted to the irradiation position, and irradiated by proton beam with energies of 0.4, 1.3, 2.2, and 3.0 GeV. The beam profiles and currents were monitored by multi-wire profile monitors [9] installed in the beam transport line. Typical irradiation time was approximately 100 seconds.

After the irradiation, gamma-ray measurement was performed with two high-purity Ge detectors. Energy calibration and determination of detection efficiency of the detectors were performed with standard gamma-ray sources ^{137}Cs, ^{60}Co, ^{152}Eu, and ^{241}Am. The gamma-ray measurement was periodically performed with different intervals ranging from 0.5 hours to 7 days. During the measurement, an acrylic spacer was placed between the sample and the detector to keep the geometrical detection efficiency constant.

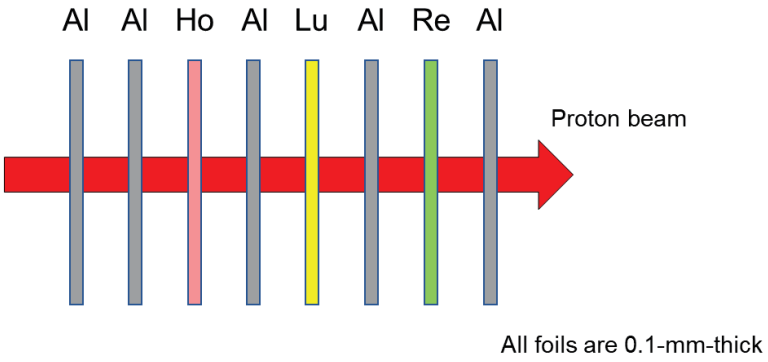

Figure 1. Schematic drawing of a sample stack.

3. Data Analysis

3.1 Determination of the number of protons

During the experiment, the total number of protons irradiated to the samples was monitored by the multi-wire profile monitors. However, a part of protons transits without bombarding the sample because of the spatial expanse of the proton beam. To determine accurately the number of protons that bombarded the sample foils, two-dimensional activation distributions of the foils were taken by the FUJIFILM BAS-SR2040 imaging plate. Here, we assumed that the activation distribution is identical to the proton-beam profile. Figure 2 shows an example of the activation distributions of Lu target irradiated by 3.0-GeV protons. The proton-beam profile is well approximated by the two-dimensional gaussian:

$$f(x,y) = \frac{N}{2\pi\sigma_x\sigma_y\sqrt{1-\rho^2}} \exp\left[-\frac{1}{2(1-\rho^2)}\left\{\frac{(x-\mu_x)^2}{\sigma_x^2} + \frac{(y-\mu_y)^2}{\sigma_y^2} - \frac{2\rho(x-\mu_x)(y-\mu_y)}{\sigma_x\sigma_y}\right\}\right], \quad (1)$$

where N, μ_x, μ_y, σ_x, σ_y, and ρ are the fitting parameters. By fitting the activation distribution, the number of protons that bombarded the sample, N_{proton}, were determined by

$$N_{proton} = N_{total\ proton} \times \frac{1}{N}\int_{foil} f(x,y)dxdy\,, \quad (2)$$

where $N_{total\ proton} = 2.30 \times 10^{14}$ was measured by the current transformer. For this correction, typical correction factor, $N_{proton}/N_{total\ proton}$ was approximately 0.97.

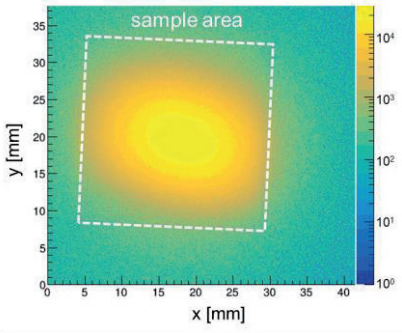

Figure 2. Example of activation distribution taken by an imaging plate

Table 1. Number of protons bombarding the sample

Proton energy [GeV]	N_{proton}
0.4	2.17×10^{14}
1.3	2.26×10^{14}
2.2	2.26×10^{14}
3.0	2.23×10^{14}

3.2 Cross section determination

Figure 3 shows an example of the gamma-ray spectrum for 3.0-GeV proton irradiation. The number of products at time t after proton irradiation was obtained by

$$N_{product}(t) = \frac{C(t, t_m)}{(1 - e^{-\lambda t_m}) I_\gamma \varepsilon_p}, \tag{3}$$

where $C(t, t_m)$ is the number of peak counts in a gamma line with the measurement time t_m, λ is the decay constant of the product nuclide, I_γ is the gamma intensity, and ε_p is the peak efficiency of the detector. Figure 4 shows some examples of decay curves obtained for ^{24}Na and ^{172}Lu. The fitting curve is expressed by

$$N_{product}(t) = N_{product}(t = 0) e^{-\lambda t}, \tag{4}$$

where the number of products at the end of proton irradiation, $N_{product}(t = 0)$, was determined as a fitting parameter. Finally, the production cross section σ was obtained by

$$\sigma = \frac{N_{product}(t = 0)}{n N_{proton}}, \tag{5}$$

where n is the areal number density of target nuclei in the sample foil.

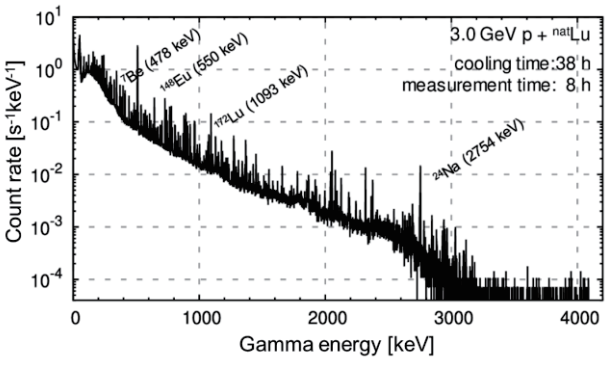

Figure 3. Example of gamma-ray spectrum

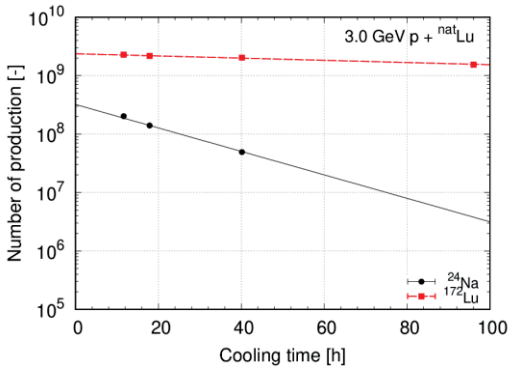

Figure 4. Example of decay curve fitting

3.3 Correction for incoming and escape of reaction products

In the sample stack, Al foils were inserted to prevent the reaction products in the sample foil from escaping to the other sample foils. However, light reaction products generated in the Al foil and other sample foils such as ^{7}Be, ^{22}Na, and ^{24}Na may escape to the neighboring foils. In this work, the contribution of product escape was corrected on the basis of the simulation by Particle and Heavy Ion Transport code System (PHITS) [10]. All input parameters were set to default values. For proton-induced reaction, the INCL4.6/GEM model was used. Particle transport of the reaction products including ^{7}Be, ^{22}Na, and ^{24}Na was simulated by using the same sample stack geometry as in the measurement. The simulation tallied the total number of the products of interest generated in the Lu foil (N_{pro}) and the number of reaction products which finally stopped in the Lu foil by ion transport among the reaction products generated in the Lu and neighboring Al foils (N_{stop}). The latter number N_{stop} corresponds to $N_{product}(t = 0)$ in Eq.(5). The correction factor for the Lu foil was defined as $N_{corr} = N_{pro}/N_{stop}$. In this work, the correction was applied only for the ^{7}Be production. It should be noted that the corrections for ^{22}Na and ^{24}Na heavier than ^{7}Be were negligibly small (less than 1%).

Table 2. Correction factors for ^{7}Be produced in the Lu target

Proton energy [GeV]	N_{corr}
0.4	0.52
1.3	0.80
2.2	0.97
3.0	0.99

4. Results and Discussion

4.1 Comparison with model predictions

Figure 5 shows the production cross sections of ^{7}Be, ^{24}Na, ^{148}Eu, and ^{172}Lu. In the figure, the previous data [11] are also plotted. The production cross sections of light nuclides, e.g. ^{7}Be and ^{24}Na, increase with increasing incident proton energy. This could be because the residual nuclei generated after INC process have higher excitation energy with increasing incident energy and are likely to emit nucleons and light ions including ^{7}Be in the subsequent evaporation processes. The INCL4.6/GEM calculation generally reproduced the energy dependence of the cross sections except for ^{24}Na. The INCL++/ABLA07 calculation showed good agreement with the experimental values for ^{24}Na, ^{148}Eu, and ^{172}Lu. Both the two model calculations underestimated the production cross section of ^{7}Be.

5. Summary and outlook

Nuclide production cross sections of ^{nat}Lu were measured by irradiation of 0.4, 1.3, 2.2, and 3.0-GeV protons at J-PARC. In the report, we showed preliminary results of production cross sections for ^{7}Be, ^{24}Na, ^{148}Eu, and ^{172}Lu. The present data is very useful for model improvement, because the cross section data of Lu target is very limited. To investigate the prediction power of the above-mentioned models for ^{7}Be production, ^{7}Be production

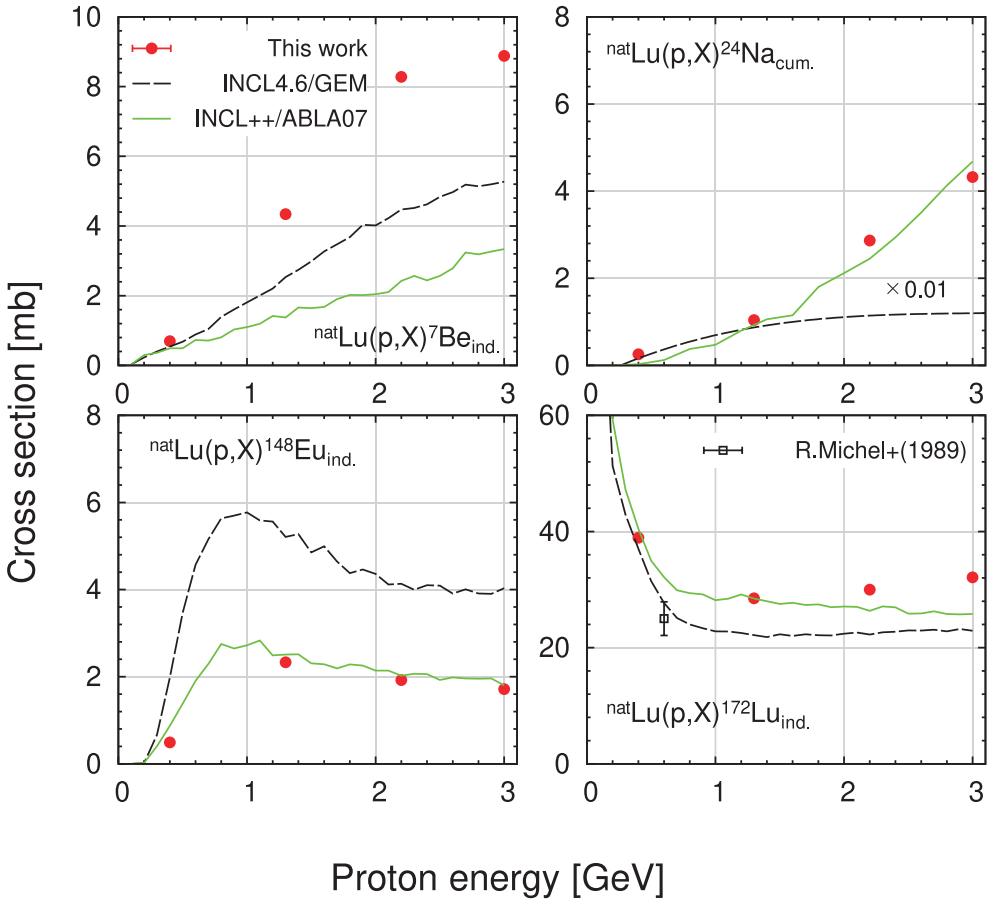

Figure 5. Experimental production cross sections for ^{7}Be, ^{24}Na, ^{148}Eu, ^{172}Lu produced by p + ^{nat}Lu reaction and model predictions by INCL4.6/GEM and INCL++/ABLA07. The subscripts ind. and cum. represent independent and cumulative cross sections. The experimental data were taken from [11]. The calculation results for ^{24}Na by the INCL4.6/GEM calculation was multiplied by 100. Our data shows statistical uncertainties, but included in the maker.

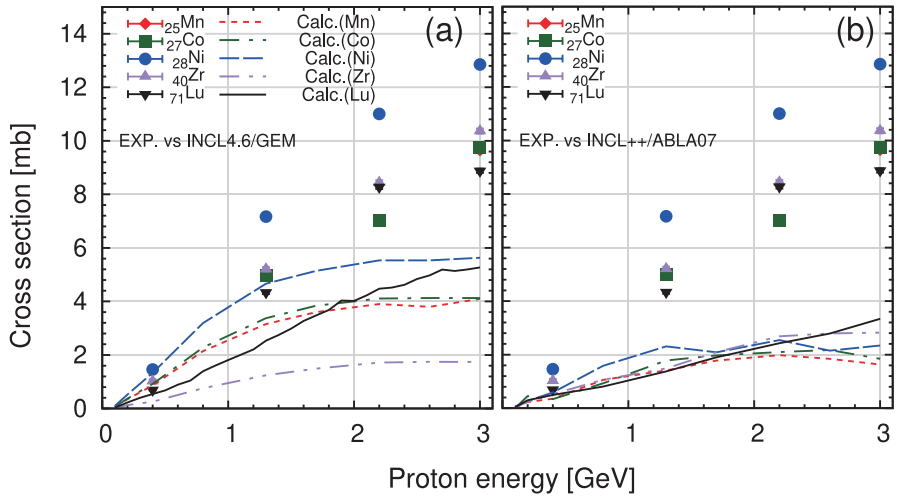

Figure 6. The ^{7}Be production cross sections for $_{25}$Mn, $_{27}$Co, $_{28}$Ni, $_{40}$Zr, and $_{71}$Lu measured at J-PARC and model predictions by INCL4.6/GEM (a) and INCL++/ABLA07 (b). The statistical uncertainties are included in the maker.

cross sections of Mn, Co, Ni, Zr, and Lu measured at J-PARC [12] were compared in Figure 6. It was found that the dependency of ^{7}Be production cross sections on the target nuclide is weak. The model calculations underestimate the experimental values as incident energy increases.

Model predictions with INCL4.6/GEM and INCL++/ABLA07 were compared with the measured data to validate their prediction powers. The INCL4.6/GEM generally reproduced the dependence of cross sections on incident proton energy, but the calculated cross sections do not necessarily agree with the experimental ones. The INCL++/ABLA07 model successfully reproduced the experimental data except for ^{7}Be production. The description of the two models should be improved to reproduce the ^{7}Be production in the future.

References

[1] Titarenko YE, Batyaev VF, Titarenko AY et al., Phys Atom. Nucl.2011;74(4):537 - 550.

[2] Michel R, Bodemann R, Busemann H et al., Nucl. Instrum. Meth. Phys. B 1997 Jan;129:153 - 193.

[3] Matsuda H, Meigo S, and Iwamoto H, J. Nucl. Sci. Technol. 2018 Apr;55(8):955 – 961.

[4] Matsuda H, Meigo S, and Iwamoto H, Maekawa F, EPJ Web Conf. 2020 239:06004.

[5] Boudard A, Cugnon J, David JC, et al. Phys Rev C. 2013 Jan;87:014606.

[6] Furihata S, Nucl. Instrum. Meth. B 2000;171:251 – 258.

[7] Mancusi D, Boudard A, Carbonell J et al., Phys. Rev. C 2015;91:034602.

[8] Kelic A, Ricciardi MV, and Schmidt KH, Proceedings of Joint ICTP-IAEA Advanced Workshop on Model Codes for Spallation Reactions, ICTP Trieste, Italy 2008;181.

[9] Meigo S, Ohi M, Kai T et al., Nucl. Instrum. Meth. Phys. B 2009:600(1):41 – 43.

[10] Sato T, Iwamoto Y, Hashimoto S et al, J. Nucl. Sci. Technol. 55(5-6), 684-690 (2018)

[11] Michel R, Dittrich B, Herpers U et al., J. Analyst 1989 Mar;114:287 – 293.

[12] Takeshita H, Meigo S, Matsuda H et al., Proceedings of J-PARC Symposium 2019 (to be published).

38. Estimation of Flux and Residual Radioactivity for the COMET Phase-I Experiment

Naoki TOKUNAGA[†1], Nobuhiro SHIGYO[1], Shunsuke MAKIMURA[2], Yoshinori FUKAO[2], Naoya KAMEI[2], and Makoto YOSHIDA[2]

[1]Department of Applied Quantum Physics and Nuclear Engineering, Kyushu University
[2]High Energy Accelerator Research Organization (KEK)
[†]Email: n.tokunaga@kune2a.nucl.kyushu-u.ac.jp

Abstract

COherent Muon to Electron Transition (COMET) is an experiment at J-PARC, which will search for coherent neutrino-less conversion of a muon to an electron in a muonic atom. The experiment will be carried out in two steps: Phase-I and Phase-II. In the Phase-I experiment, the 3.2-kW 8-GeV proton beam irradiates a 70-cm long graphite target to produce negative pions. The negative pions are captured in the magnetic field and delivered to pion-decay and muon-transport sections. The Phase-I experiment aims to detect the $\mu^- e$ conversion events and measure the beam-related background events for the Phase-II experiment. It has been planned that the maintenance by radiation workers would be conducted after the 150-day operation and the following 180-day cooling. It is necessary to evaluate the residual radiation dose for the safety of the workers during the maintenance. On this study, we calculated fluxes of neutron, photon, proton and other charged particles in the beam room during the beam operation and the residual activity after the cooling time by using the Monte Carlo simulation code PHITS version 3.22 and DCHAIN-PHITS version 3.21. The calculation results show that the design of components around the target and beam dump needs to be improved to reduce the radioactivities after the cooling time.

1 Introduction

Coherent muon to electron transition (COMET) experiment is planning to search for the lepton flavor violating process of $\mu^- N \rightarrow e^- N$ in the field of an aluminum nucleus [1]. The Phase-I experiment aims for the experimental sensitivity of 3.1×10^{-15}, which is a factor of 100 improvement from the current limit in SINDRUM-II [2] at PSI. Figure 1 shows the geometry of the beam room. In the Phase-I experiment, the 3.2-kW 8-GeV proton beam from the J-PARC main ring irradiates the 70-cm long pion production target made of graphite for 150 days. The energy loss of proton in the target is about 200 MeV. The components around the target are highly activated by the secondary particles. The magnetic field with the maximum magnitude 5 T is generated by the capture solenoid (CS). The produced pions are captured and transferred to the detection area by the magnetic field. The flange at the downstream of the beam has the obround shape beam hole with the 14.3-cm straight sides and the semicircles of 10.0-cm radius. Currently, it has been planned that the maintenance by radiation workers would be conducted after the 180-day cooling. It is, therefore, necessary to estimate the effective dose rate for the safety of the workers.

In this paper, we report the effective dose rate distribution calculated by the general purpose Monte Carlo radiation transport code PHITS [3] version 3.22 and the decay chain analysis code

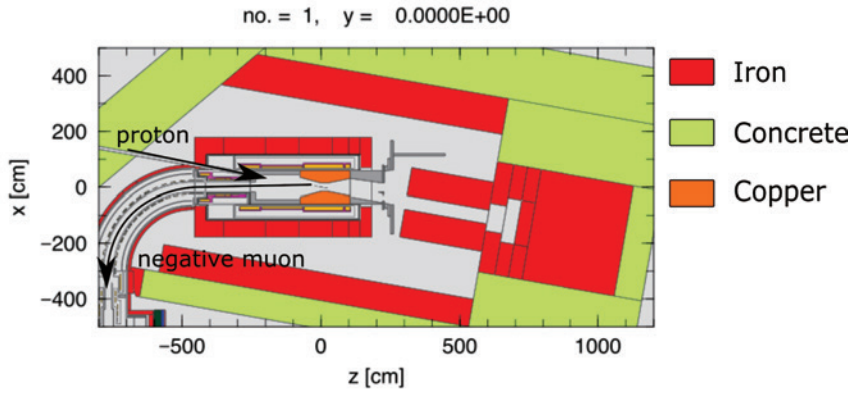

Figure 1: Plan view of the beam room.

DCHAIN-PHITS [4] version 3.21. Because the result shows that the effective dose rate is too high to work around the flange, we list the possible ways to reduce the radioactivity.

2 Simulation

First, neutron flux with kinetic energy of less than 20 MeV and production rates of radioactive nuclides are estimated by using PHITS when the 8.0-GeV proton beam irradiates a 70-cm long graphite target. The computational geometry and the magnetic field shown in Figures 2 and 3 are used. For the estimation of neutron production yields with kinetic energy of less than 20 MeV, JENDL-4.0 is used. For neutrons in the range of 20 MeV to 3 GeV and protons upto 3 GeV, INCL4.6 coupled with GEM is used. For neutrons and protons with kinetic energy of greater than 3 GeV, JAM coupled with GEM is used. For electrons and photons, EGS5 is used. We correct treatment of relativistic effect on transportation of charged particles in the magnetic field in PHITS version 3.21. The correction has been merged into PHITS version 3.22. With these data as input, DCHAIN-PHITS calculates radioactivity and gamma-ray spectrum at any given time. Again, photon flux is calculated by PHITS, and then it is converted to effective dose rate by using the conversion coefficient of AP irradiation based on ICRP103 as shown in Figure 4 [5].

3 Result

3.1 Particle fluxes during the beam operation

Figures 5, 6 and 7 show flux distributions of neutron, negative pion and negative muon during the beam operation, respectively. High neutron flux of $2.0 \times 10^{10}\,\mathrm{cm^{-2}s^{-1}}$ is estimated around the production target and the dump. Pions and muons are transported to the detection area by the magnetic field as expected. The maximum flux for the pion and the muon are $2 \times 10^{9}\,\mathrm{cm^{-2}s^{-1}}$ and $7 \times 10^{7}\,\mathrm{cm^{-2}s^{-1}}$, respectively.

3.2 Residual activities

Figure 8 shows how the residual activities change over time in four regions (production target, shield for CS, flange, and beam dump). The half lives of the nuclides shown in Figure 8 are listed in Table 1. In the graphite production target, more than 10^{8} Bq/cc of ^{11}C exists right

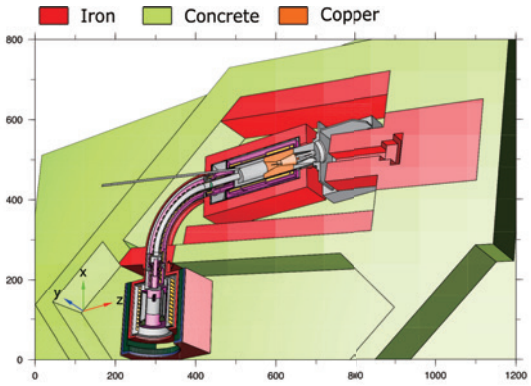

Figure 2: Geometry around the muon production target and the beam dump in the PHITS simulation.

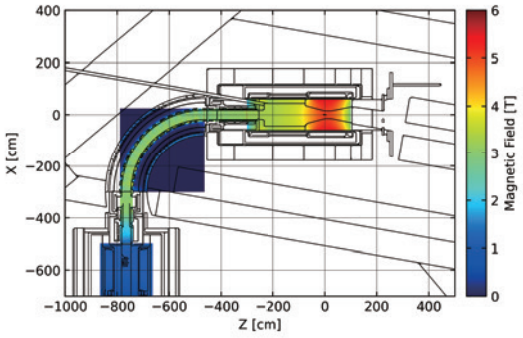

Figure 3: Magnetic field of the pion production target and the muon capture solenoid sections.

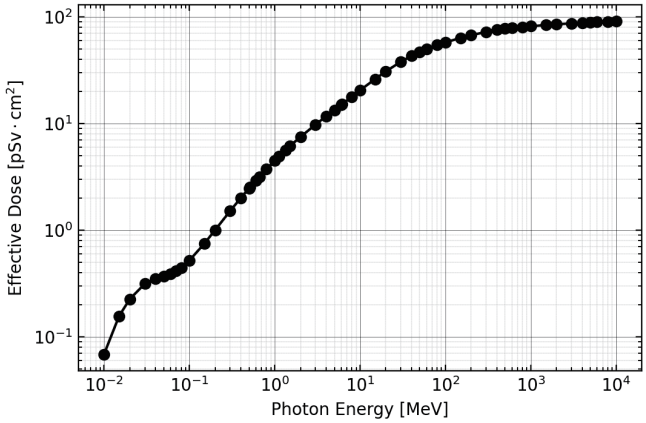

Figure 4: Conversion coefficient from the photon energy to the effective dose of AP irradiation based on ICRP103.

after the 150-day beam operation. It decays with half life of 20 minutes. Therefore after cooling time, ^{3}H and ^{7}Be are dominant. In the copper shield of CS, the radioactive isotopes of copper with short half life are dominant at first, and the radioactive isotopes of cobalts and ^{54}Mn are dominant after 180 days. In the flange and the dump, ^{54}Mn, ^{55}Fe and ^{49}V are the main radioactive nuclides.

3.3 Spatial distribution of dose rate

Figure 9 shows the effective dose rate distribution after the 150-day beam operation and the 180-day cooling time. The components along the proton beam line are strongly activated, and therefore high effective dose rates are estimated around them. Around area marked as star in the figure, where workers need to approach during the maintenance, the effective dose rate is 10 mSv/h. In front of the dump (marked as circle), the effective dose rate of 2.5 mSv/h is estimated.

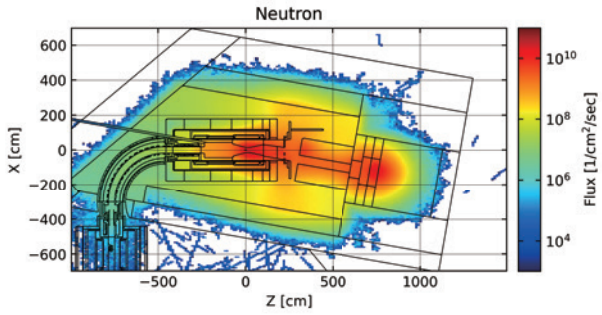

Figure 5: Neutron flux distribution of the beam room.

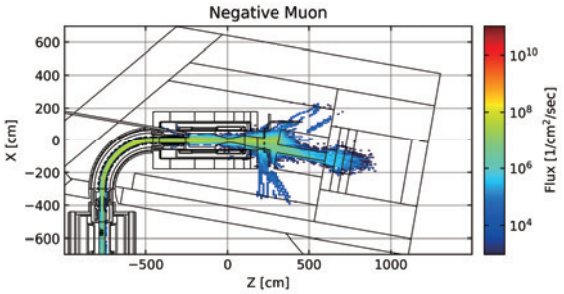

Figure 6: Negative pion flux distribution of the beam room.

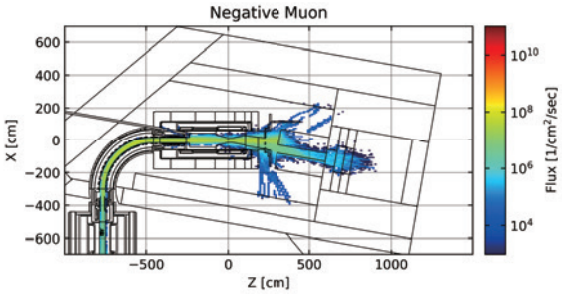

Figure 7: Negative muon flux distribution of the beam room.

4 Discussion

The calculated effective dose rate is much higher than 100 μSv/h as tentative target around area marked as star shown in Figure 9 in the beam room. The following options may reduce the residual radioactivity.

First thing is to have a longer cooling time. Figure 10 shows decrease of the effective dose rate in front of the flange over time. The main contributor to the effective dose rate from the flange is ^{54}Mn with half life of 312 days, the effective dose rate, therefore, only decreases by half in about a year.

Second thing is to make the beam window of the flange larger. As shown in Figure 11, high proton flux exists around the beam window. A larger beam window makes these protons go through without them interacting with the flange, which results in less activation. The size of the beam window, however, cannot be increased unlimitedly. The further calculation needs to be carried out in order to know the correlation the window size and the residual activity.

Third thing is to make the pion production target shorter. The amount of secondary particles produced in the target are proportional to the energy loss in the target. The energy loss of the primary beam is proportional to the length of the target. Therefore, a shorter production target suppresses the residual activity. However, a shorter production target also results in the undesired decrease in pion production.

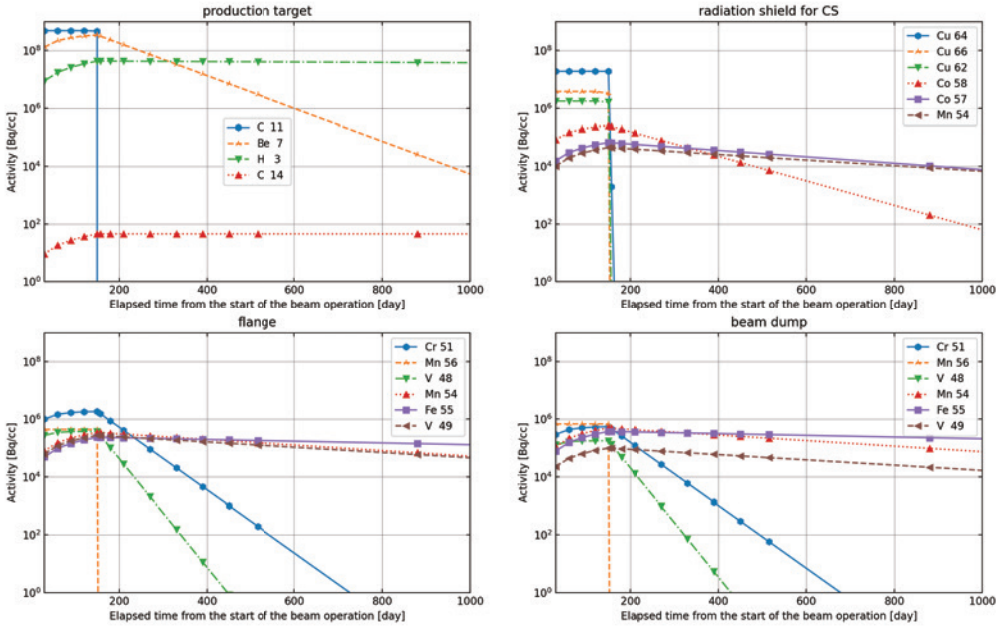

Figure 8: Residual activities of main isotopes from start of beam irradiation at (a) production target, (b) radiation shield for CS, (c) flange, and (d) beam dump.

Table 1: The half lives of the nuclides

nuclide	half life	nuclide	half life	nuclide	half life
^{51}Cr	27.7 days	^{56}Mn	2.5 hours	^{48}V	16.0 days
^{54}Mn	312 days	^{55}Fe	2.7 years	^{49}V	330 days
^{11}C	20 minutes	^{7}Be	53 days	^{3}H	12.3 years
^{14}C	5730 days	^{64}Cu	12 hours	^{66}Cu	5.1 minutes
^{62}Cu	9.7 minutes	^{58}Co	70 days	^{57}Co	271 days

With all available means, the design of the components needs to be optimized so as to suppress the effective dose rate as much as possible. If the effective dose rate cannot be lowered enough, a remote working is another possible option.

5 Summary

The effective dose rate distribution after 150-day beam irradiation by 3.2-kW 8-GeV proton beam and 180-day cooling for COMET Phase-I experiment is estimated by PHITS and DCHAIN-PHITS for the safety assessment. The results show that the residual radiation is too high for people to work in the beam room. Three possible ways are indicated to suppress the residual activity, but the further investigation is still necessary. Remote working might be another practical option.

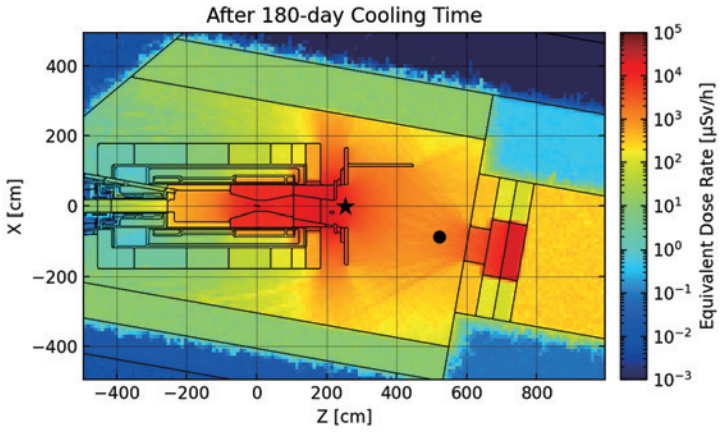

Figure 9: Spatial distribution of effective dose rate after 180-day cooling.

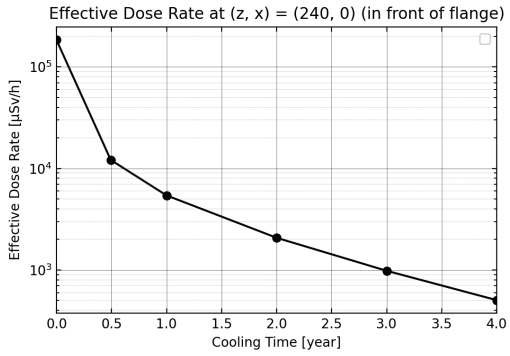

Figure 10: Decrease of effective dose rate in front of the flange.

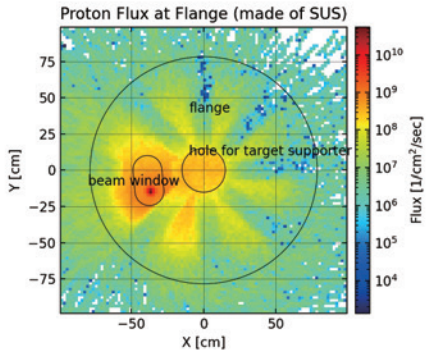

Figure 11: Proton flux at the flange in xy-plane. High flux of the beam is seen around (x, y) = (-40, -20). The black lines indicate the boundaries of the flange.

References

[1] Lee M.J., COMET Muon Conversion Experiment in J-PARC, Front. Phys. Vol. 6, 2018, 133.

[2] Bertl W. et al., A search for μ-e conversion in muonic gold, Eur. Phys. J. C, Vol. 47, no.2, 2006, pp.337-346.

[3] T. Sato, et al., Features of Particle and Heavy Ion Transport code System (PHITS) version 3.02, J. Nucl. Sci. Technol., Vol. 55, no.6, 2018, pp.684-690.

[4] Hunter N. Ratliff et al., Modernization of the DCHAIN-PHITS activation code with new features and updated data libraries, Nucl. Instrum. Meth. B, Vol. 484, 2020, pp.29-41.

[5] Petoussi-Henss N, Bolch WE, Eckerman KF, et al., Conversion coefficients for radiological protection quantities for external radiation exposures, Ann ICRP, Vol. 40, no. 2-5, 2010, pp.1-257.

39. Measurement of neutron total cross sections of Sn-Pb alloys in solid and liquid states

Takuya UEMURA[1], Jun-ichi HORI[2], Kazushi TERADA[2], Tadafumi SANO[3],
Jun NISHIYAMA[4], Rei KIMURA[5] and Ken NAKAJIMA[2]

[1] Departments of Nuclear Engineering, Kyoto University, Nishikyo-ku, Kyoto-shi, Kyoto, 615-8246, Japan

[2] Institute of Integrated Radiation and Nuclear Science, Kyoto University, Kumatori-cho, Sennan-gun, Osaka, 590-0494, Japan

[3] Kindai University Atomic Energy Research Institute, Higashiosaka-shi, Osaka, 577-8502, Japan

[4] Laboratory for Advanced Nuclear Energy, Tokyo Institute of Technology, Meguro-ku, Tokyo, 152-8550, Japan

[5] Toshiba Energy Systems & Solutions Corporation, Saiwai-ku, Kawasaki-shi, Kanagawa, 212-8585, Japan

Email : uemura.takuya.77n@st.kyoto-u.ac.jp

The use of a Sn-Pb alloy as an emergency in-core heat transport medium is being considered in the design of a small modular reactor proposed by Toshiba Energy Systems & Solutions Corporation. However, there exists no experimental data for the neutron cross sections of Sn-Pb alloy.

In the present study, the neutron total cross sections of Sn-Pb alloy were obtained from neutron transmission measurements by the time-of-flight (TOF) method using the Kyoto University Institute for Integrated Radiation and Nuclear Science – Linear Accelerator (KURNS-LINAC). The sample temperature was changed from room temperature (solid) up to 300 ℃ (liquid). The total cross sections of the solid and liquid states were compared with the evaluated data and the previous data of Pb and Sn.

Keywords: neutron total cross section, Sn-Pb alloy, time-of-flight, KURNS-LINAC, solid, liquid

1. Introduction

Recently, a small modular reactor (SMR), which has inherent and passive safety, has been receiving attention all over the world. In Japan, a very small modular reactor, namely, MoveluX^{TM} (Mobile-Very-Small reactor for Local Utility in X-mark) [1] is being developed by Toshiba Energy Systems & Solutions Corporation. MoveluX^{TM} is a thermal reactor that uses calcium hydride as a neutron moderator and its heat output is 10 MWth. As for the heat exhaust function in the core, some heat pipes are used, and heat can be transported by using temperature differences. On the other hand, when the heat exhaust function of the heat pipes is lost, an emergency in-core heat transport medium, instead, will carry the heat to the reactor wall by

natural convection, and the core wall will be cooled by ambient air circulation. The use of a Sn-Pb alloy as the emergency in-core heat transport medium is being considered.

Since the melting point of the Sn (60 wt%)-Pb (40 wt%) alloy is about 180 ℃, the alloy is solid state when the reactor is just started to work, and it becomes liquid state while the power increases, because the core temperature reaches 660 ℃ in full power operation. Change of the state of the alloy during operation will affect the core characteristics. In particular, the thermal neutron scattering cross section will change between the solid and liquid states, because solid metal has a crystal structure and it causes the coherent scattering effect, and when it melts the effect changes. Alloy also has a crystal structure and its orientation is different from that of single element metal. The wavelength of a thermal neutron is close to the lattice spacing of atoms in the crystal structure and the coherent scattering occurs. Therefore, the neutron cross section in the thermal neutron energy region also differs due to the influence of coherent scattering by the crystal structure and its orientation. However, there are no reports on experimental data for the neutron cross section of Sn-Pb alloy in both solid and liquid states. In the present work, the thermal neutron total cross sections of solid and liquid Sn-Pb alloy were measured and compared with the evaluated nuclear data of the free gas model in JENDL-4.0 [2].

2. Experiment

The neutron total cross section measurements of Sn-Pb alloy were carried out by using the TOF method at KURNS-LINAC. The experimental arrangement is shown in Figure 1. The KURNS-LINAC was operated with a pulse width of 1 μs, a repetition rate of 50 Hz, and an average current of 28.4 μA. The accelerated electrons were incident on a water-cooled Ta-target [3]. Then, fast neutron were produced by the photo nuclear reaction (γ , n). To obtain thermal neutrons, the Ta-target was set at the center of a water moderator tank (20 cm in diameter). The neutron flight tube was used in the direction of 135 degrees with respect to the LINAC beam line [4]. A ^{6}Li-galss scintillator detector, GS20, was used as a neutron detector. The flight length between the Ta-target and the ^{6}Li-glass detector was about 12.1 m.

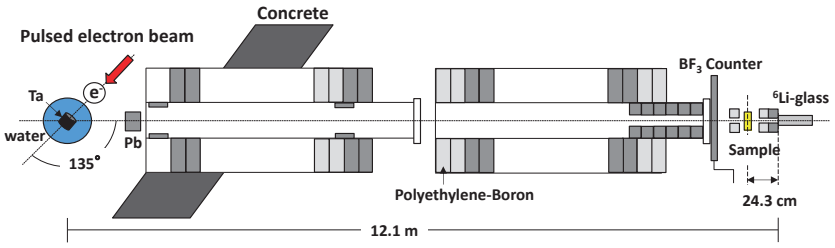

Figure 1: Experimental arrangement for neutron total cross measurement.

The specifications of the Sn-Pn alloy samples and the Al case are listed in Table 1. The Sn-Pb alloys containing 60 wt% natural tin and 40 wt% natural lead were used. We prepared two types of samples in the solid state, one is a re-solidified sample with 10 mm thickness contained in the Al case after melting, and the other is a commercially available rod with 6 mm thickness. To reduce the effects of neutron scattering from

the Al case, its thickness was reduced to 1 mm. The measurement times are listed in Table 2.

Table 1: Specifications of Sn-Pb alloys and Al case

	Sn-Pb alloy (Sn : 60 wt%, Pb : 40 wt%)			Al
Sample	liquid (in Al case)	solid (in Al case)	solid (rod sample)	Al case
Weight (g)	413.52	413.52	200.51	193.42
Size (mm^2)	2750	2625	3835	4200
Thickness (mm)	10	10	6	1 (beam line)

Table 2: List of measurement times

	Sample	Measurement time (h)
Sn-Pb alloy	liquid (300 ℃)	12.0
	liquid (250 ℃)	12.0
	liquid (210 ℃)	12.0
	solid (in Al case)	12.0
	solid (rod sample)	9.0
	Al case	12.0
	Blank	9.0
	Al case + res.filter	3.0

In the TOF method, the incident neutron energy was obtained by the following equation:

$$E = \left(\frac{72.3 \times L}{t}\right)^2 \quad (1)$$

where, E is the incident neutron energy, L is the neutron flight length and t is the TOF. The neutron total cross section $\sigma_{tot}(E)$ was obtained by the following equation:

$$\sigma_{tot}(E) = -\frac{1}{n}\ln\frac{(C_s(E) - C_{s,b}(E))/M_s}{(C_o(E) - C_{o,b}(E))/M_o} \quad (2)$$

where, $C_s(E)$ and $C_o(E)$ are the neutron count rates with the sample existed (hereafter, called as "sample-in") and not existed (hereafter, called as "sample-out") measured by the ^{6}Li-glass detector. $C_{s,b}(E)$ and $C_{o,b}(E)$ are the neutron background for the sample-in and sample-out. M_s and M_o are the neutron count rates by the BF_3 detector to monitor neutron intensity fluctuation between measurements. n is the atomic area density [atom/barn] of Sn-Pb alloy samples.

The γ-ray background level was estimated from the pulse height spectrum of each measurement. Figure 2 shows the pulse height spectrum of the ^{6}Li-glass detector. As shown in Figure 2, the counts for 320-420 ch. includes neutron and background γ-ray counts. On the other hand, the counts for 220-319 ch. is only background γ-ray one. Then, the γ-ray background level was evaluated from the TOF spectrum by interpolate the corresponding pulse height normalized by each event. Figure 3 shows the results of evaluated γ-ray background of the TOF spectrum, comparing with the one with resonance filters (Mn, Co, Ag, In and Cd). As shown in Figure 3, the evaluated γ-ray background shows good agreement with the dips of In (1.46 eV),

Ag (5.19 eV), Co (132 eV), and Mn (337 eV), which correspond to the large resonance peaks, respectively. Then, it was confirmed that the present background evaluation method is appropriate.

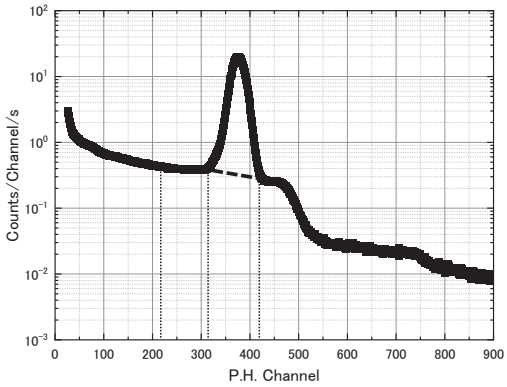

Figure 2: Pulse height spectrum of ^{6}Li-glass detector.

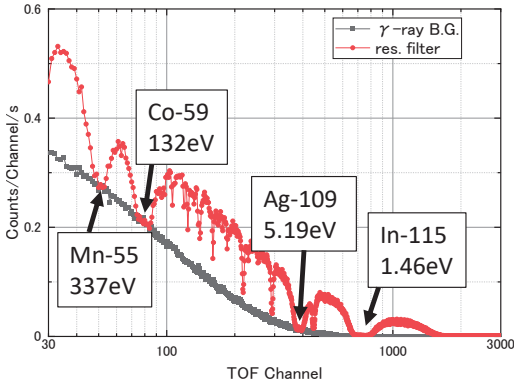

Figure 3: TOF spectra with resonance filters and evaluated γ-ray background.

3. Results and Discussion

We will discuss the results of the measurements from three perspectives. The first perspective is the effect of temperature of the liquid alloy. Figure 4 shows the neutron total cross sections of the liquid Sn-Pb alloys with different temperatures. There are some small differences in the total cross sections between 210 ℃ and other temperatures from 0.002 eV to 0.01 eV. This seems to be caused by the remaining crystal structure in liquid at 210 ℃, which is relatively low temperature. On the other hand, there is a little difference in the cross sections between 250 ℃ and 300 ℃. However, in the present study, it is difficult to say clearly that there is a difference due to sample temperature in the liquid state. Before the experiment, we had considered that the effect of the coherent scattering would disappear in the neutron cross section of the liquid state, and the cross section would be almost close to the one with the free gas model. However, the effect of coherent scattering still exists in the liquid state in the present study.

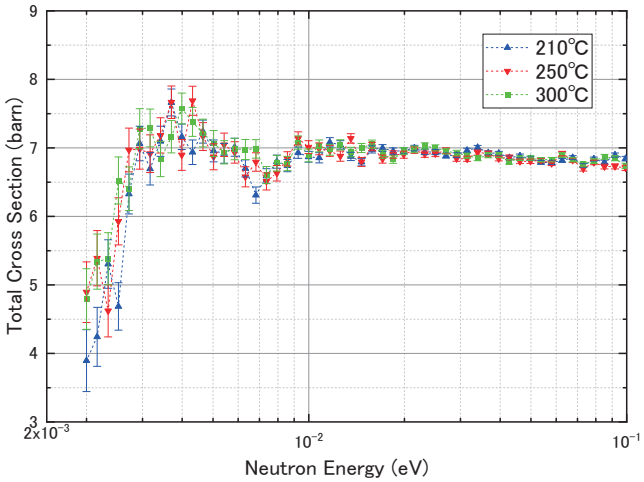

Figure 4: Comparison of neutron total cross sections of liquid Sn-Pb alloy between temperatures (210 ℃, 250 ℃ and 300 ℃).

The second perspective is the effect of the solid/liquid sates on the neutron total cross sections. The cross sections of the Sn-Pb alloy in the solid and liquid states, and the JENDL-4.0 data are compared in Figure 5. The JENDL-4.0 data shows the neutron total cross sections of the Sn-Pb alloy calculated using the Sb and Pb cross sections of the JENDL-4.0 with the weights of the atomic ratio of each composition. In the solid state, the Bragg edges due to the crystal structure are observed in the neutron energy below 0.05 eV. However, it turned out that the magnitude (or height) of Bragg edges in the liquid state decreased and widened in the energy region. This would be caused by change of the crystal structure of the solid due to melting. In comparison with the JENDL-4.0, although the measured data shows big difference in the low energy, they show good agreement above 0.05 eV. This is because the influence of coherent scattering due to the crystal structure is little above 0.05 eV.

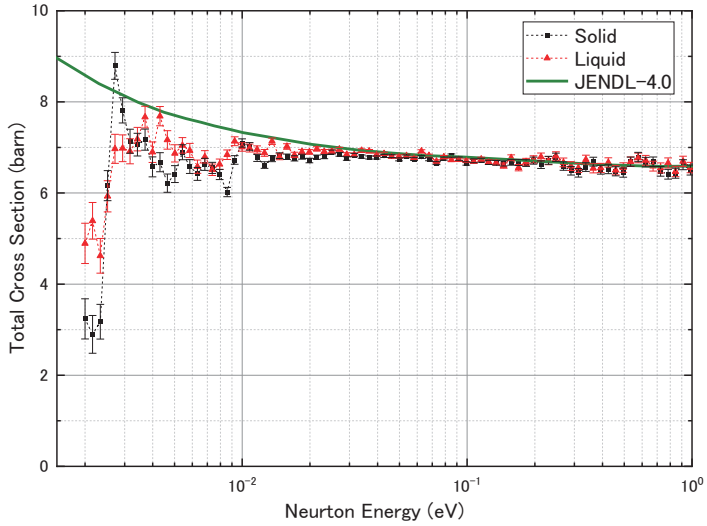

Figure 5: Comparisons between neutron total cross sections of Sn-Pb alloys in the solid, liquid states and JENDL-4.0.

The third perspective is the comparisons in the solid state measurements. In Figure 6, the neutron total cross sections of Sn, Pb measured in the past [5,6] and Sn-Pb alloys in the present measurement are shown. The present Sn-Pb alloy measurements are the results of the two solid samples, the re-solidified sample and the rod one (see Section 2, for detail). As seen in Figure 6, several Bragg edges are in good agreement between the re-solidified and rod samples, Sn, and Pb from 0.002 eV to 0.05 eV. However, there are differences in the Bragg edges between the re-solidified and rod samples. For the re-solidified sample, some Bragg edges of Pb tended to disappear at 3.42 meV, 6.82 meV, and 17.1 meV. The neutron cross section of the material with a crystal structure changes depending on its orientation. Therefore, this difference between the re-solidified and rod samples would be due to the change in crystal orientation caused by melting. However, there is still room for considering the reasons of the difference as further study.

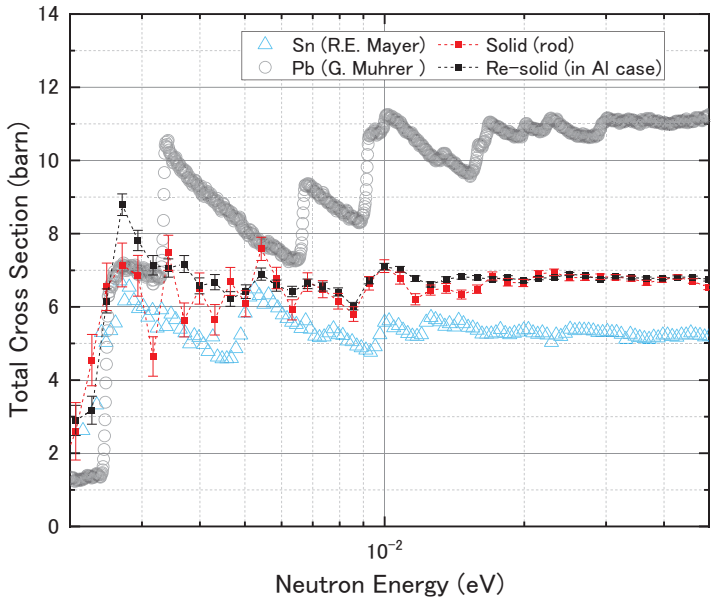

Figure 6: Comparison between the total cross sections of the rod sample (indicated as "solid (rod)"), the re-solidified sample after melting (indicated as "Re-solid (in Al case)") of Sn-Pb alloys and the previously measured data of Pb and Sn.

4. Conclusion

We have performed the neutron total cross section measurements of the Sn-Pb alloy in solid and liquid states using the TOF method at KURNS-LINAC. The measurement results were compared with the evaluated data in JENDL-4.0 and the previous experimental data of Sn and Pb. The total cross sections of the solid and liquid states were compared and changes in Bragg edges were observed in the energy range below 0.05 eV. Comparing the total cross sections of the rod and re-solidified samples, it was confirmed that Bragg edges, which is thought to be due to the crystal structure of Pb, was not observed in the re-solidified sample.

The present study shows important data for using the solid and liquid alloys as heat transport medium in the core of a thermal reactor.

References

[1] R. Kimura et al., Nucl. Sci. Eng., 2020; 194: 213-220.

[2] K. Shibata et al., J. Nucl. Sci. Technol., 2011; 48(1): 1-30.

[3] K. Kobayashi et al., Ann. Rep. Res. Reactor Inst. Kyoto Univ., 1989: 22; 142.

[4] Y. Takahashi et al., Phys. B: Condensed Matter, 2018; 551; 488-491.

[5] G. Muhrer et al., Nucl. Instrum. Methods Phys. Res. Sec. A, 2007; 572: 866-873.

[6] R. E. Mayer et al., Jour. Atomkernenergie, 1981: 39; 55.

40. Research for nuclear transmutation of high-radiotoxic nuclide ^{90}Sr via proton- and deuteron-induced reactions

Riku Matsumura[†1, 2], Hideaki Otsu[1], He Wang[1], Nobuyuki Chiga[1], Shoichiro Kawase[3], Keita Nakano[3], Hiroyoshi Sakurai[1, 4], Mizuki Shikata[5], Satoshi Takeuchi[5], Yasuhiro Togano[5], and for the ImPACT-RIBF collaboration

[1]RIKEN Nishina Center, Saitama 351-0198, Japan
[2]Department of Physics, Saitama University, Saitama 338-8570, Japan
[3]Department of Advanced Energy Engineering Science, Kyushu University, Fukuoka 816-8580, Japan
[4]Department of Physics, The University of Tokyo, Tokyo 113-0033, Japan
[5]Department of Physics, Tokyo Institute of Technology, Tokyo 152-8551, Japan
[†]Email: riku@ribf.riken.jp

The isotopic-production cross sections for high-radiotoxic nuclide ^{90}Sr on proton and deuteron at 104 MeV/nucleon were obtained in inverse kinematics at the RIKEN Radioactive Isotope Beam Factory. The experimental data were compared with those obtained from calculations using the Particle and Heavy Ion Transport code System. These were also compared with the existing data.

1 Introduction

The processing of spent fuels from nuclear power plants is a worldwide problem. The high-level radioactive wastes are the by-products of the reprocessing of spent fuels, which contain minor actinides and fission products. In this study, we focus on ^{90}Sr, which is the most radiotoxic nuclide in the fission products (see Figure 1 and Table 1).

Table 1: Nuclides contained in the high-level radioactive waste and its half-life, toxicity, and content.

Nuclide	Half-life [y]	Toxicity [μSv/kBq]	Content [kg/tHM]
^{79}Se	29.5 $\times 10^4$	2.9	0.006
^{90}Sr	28.8	28	0.6
^{93}Zr	15.3 $\times 10^5$	1.1	1
^{99}Tc	21.1 $\times 10^4$	0.64	1
^{107}Pd	65.0 $\times 10^5$	0.037	0.3
^{126}Sn	10.0 $\times 10^4$	4.7	0.03
^{129}I	15.7 $\times 10^6$	110	0.2
^{135}Cs	23.0 $\times 10^5$	2	0.5
^{137}Cs	30.1	13	1.5

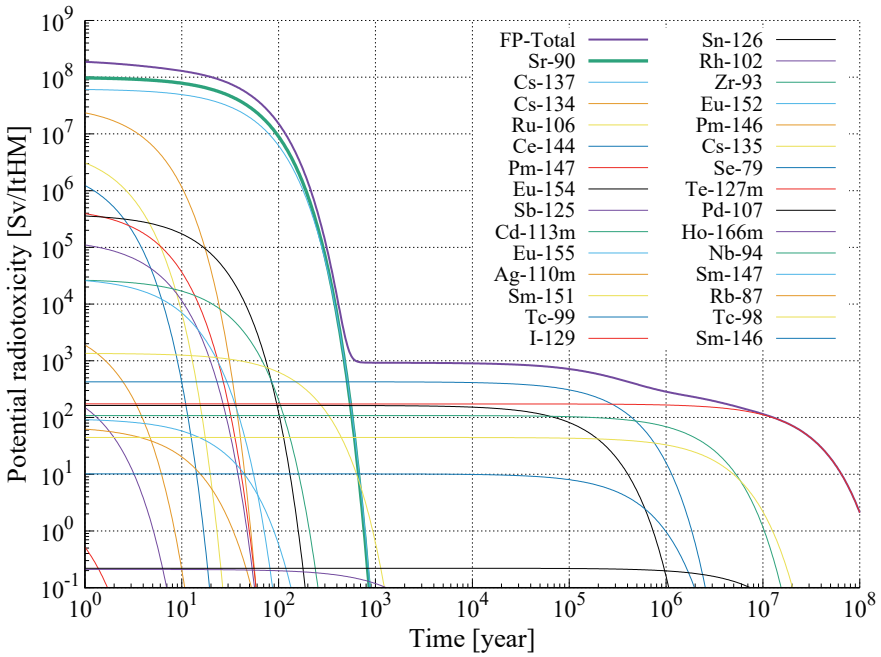

Figure 1: Potential radiotoxicity per one ton of spent fuels from a pressurized water reactor (nuclear fuel burnup: 45 GWd/tHM), after five years cooling, taken from Ref. [1].

There is a strong desire to develop nuclear transmutation technology using accelerator facilities to reduce these harmful nuclides. The simplest way can be irradiating a neutron beam on the radioactive waste. However, it is not well known how much and into which nuclide ^{90}Sr is transmuted in this reaction. Therefore, it is essential to study the reaction cross sections to each nuclide from ^{90}Sr in advance. From this point of view, the inverse kinematics, i.e., incident ^{90}Sr beam on light-particle targets, is an effective method for identifying reaction products in the forward direction.

2 Experiment

The experiment was performed at the RIKEN Radioactive Isotope Beam Factory (RIBF) by using the RIKEN Projectile-fragment Separator (BigRIPS) [2] and the ZeroDegree Spectrometer (ZDS) [2]. The setup is shown in Figure 2. The details of the experiment are given in Ref. [3]. The secondary beam, including ^{90}Sr, was produced by in-flight fission of ^{238}U at 345 MeV/nucleon on a 3-mm thick ^{9}Be production target at the BigRIPS first stage. In the following second stage, the beam particles were selected and identified event-by-event using the TOF-$B\rho$-ΔE method [4], as shown in Figure 3.

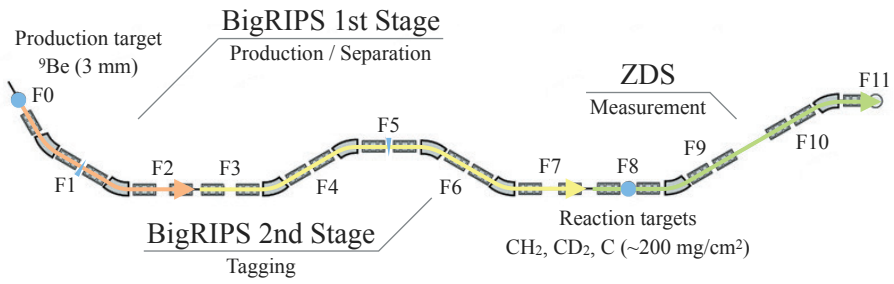

Figure 2: Schematic view of the RIKEN Projectile-fragment Separator (BigRIPS) and the ZeroDegree Spectrometer (ZDS).

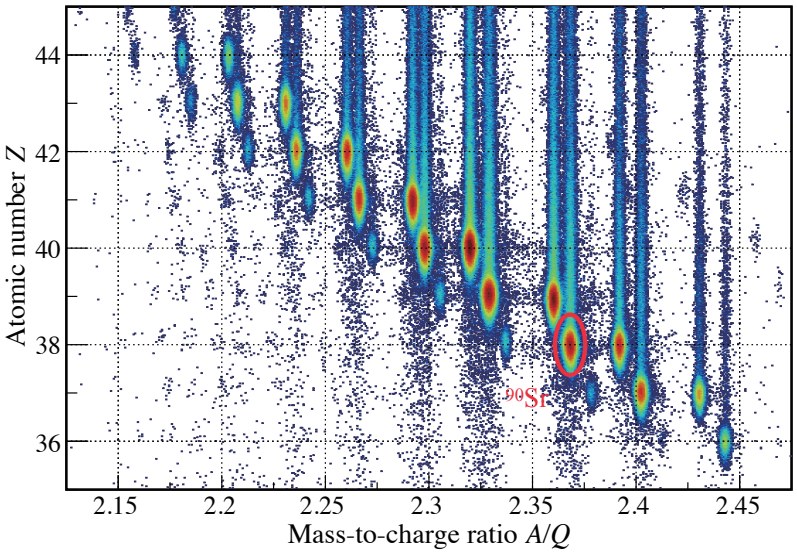

Figure 3: Secondary beam particle identifications at the BigRIPS.

The beam particles bombarded at 104 MeV/nucleon to CH_2 (179.2 mg/cm^2), CD_2 (218.2 mg/cm^2), and C (226.0 mg/cm^2) reaction targets, which placed at the entrance of the ZDS. The residual nuclei produced in reactions were identified in the ZDS with the same method as the BigRIPS. Because the momentum acceptance of the ZDS is limited to ±3 %, the experiment was carried out by using five different momentum settings ($\Delta(B\rho)/B\rho = -9$, -6, -3, 0, and $+3$ %) for each target to accept the wide range of mass-to-charge ratio A/Q. Figure 4 shows an example of particle identifications after selecting ^{90}Sr ($Z = 38$, $A/Q = 2.37$) for the projectile and the $\Delta(B\rho)/B\rho = -6$ % setting at the ZDS. The reaction cross sections were deduced from the number of incident ^{90}Sr, the number of each residual particle, and the thickness of the target. The backgrounds of carbon from CH_2 and CD_2 targets and beam-line materials were subtracted by using the empty and carbon target runs.

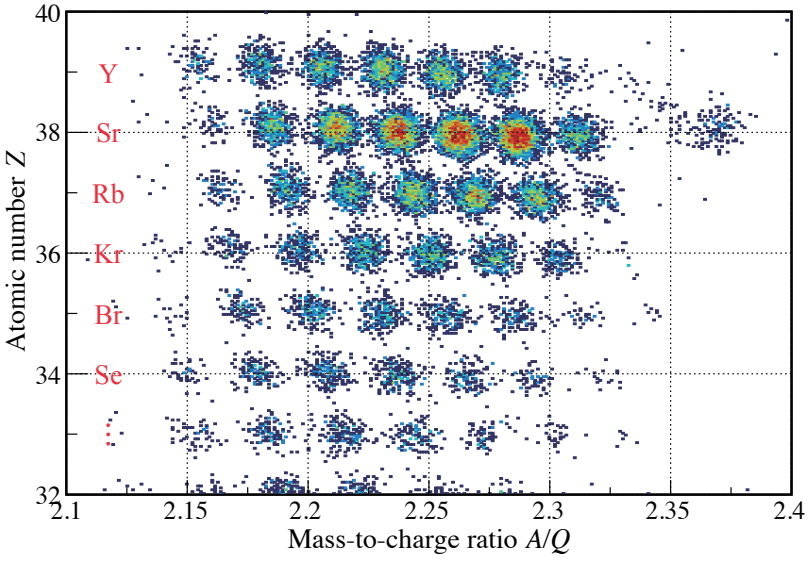

Figure 4: Residual particle identifications at the ZDS.

3 Results and Discussion

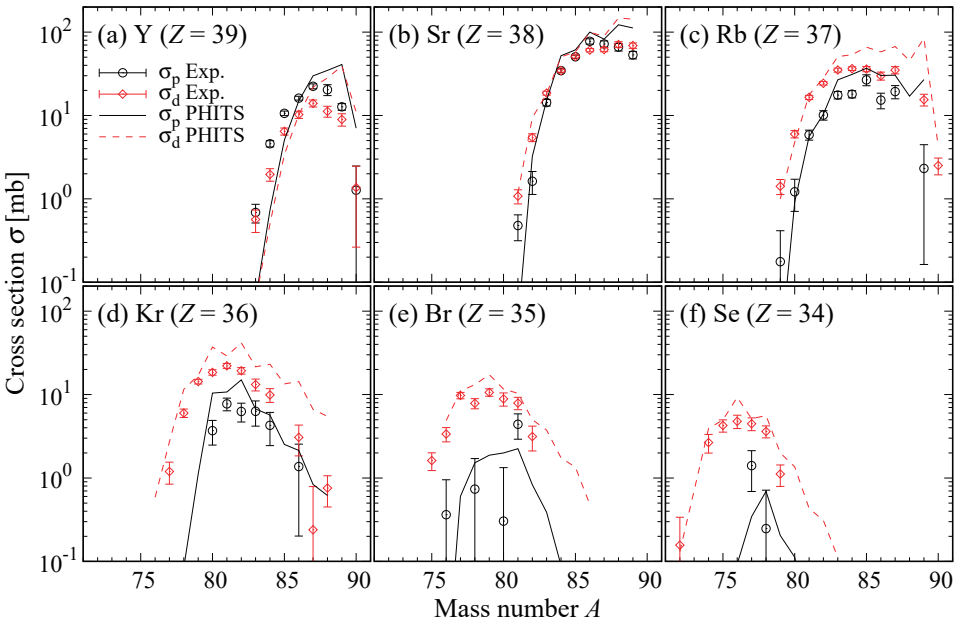

Figure 5: Isotopic-production cross sections of proton- (circles) and deuteron-induced (diamonds) reactions and those obtained from the PHITS calculations (proton for solid, deuteron for dotted).

The data points above 1 mb were obtained with good statistics. These were compared with the calculations using the Particle and Heavy Ion Transport code System (PHITS) [5] as shown in Figure 5. The Liége Intranuclear Cascade model (INCL4.6) [6] and the Generalized Evaporation Model (GEM) [7] were employed in the calculations. It is seen that the calculation results were overestimated around the mass number of the projectile. Few-nucleon removal reactions are not interpreted properly in the INCL because momentum distributions of the nuclear surface are treated in a semiclassical way [8]. In addition, even-odd staggering effects have appeared excessively for nuclides produced by emitting many nucleons. This may be controlled to some extent by considering the competition between particle and γ-ray emissions, and the discrete energy levels, in the GEM.

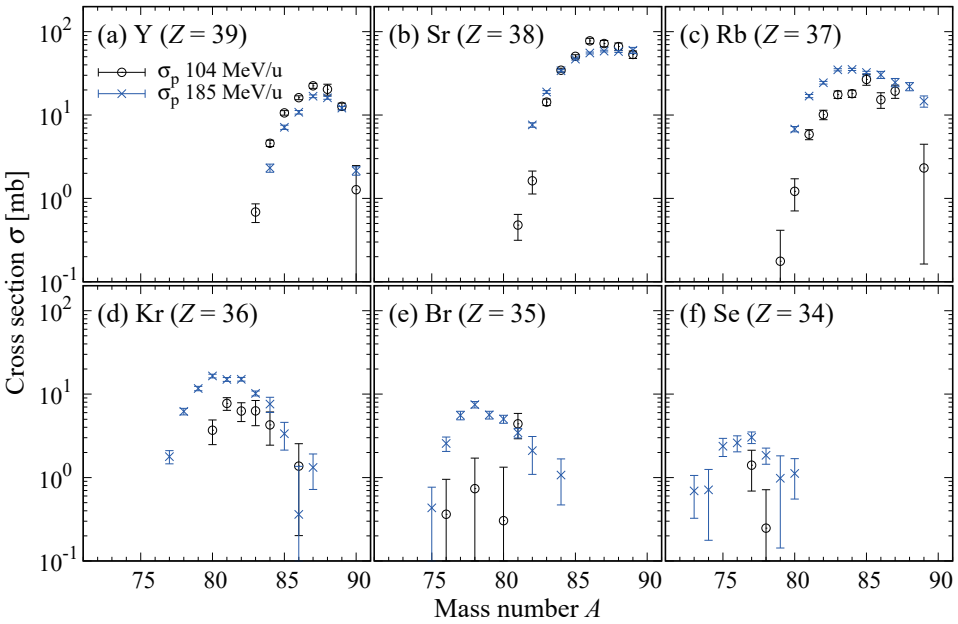

Figure 6: Results of proton-induced reaction cross sections at 104 MeV/nucleon (circles). For comparison, those at 185 MeV/nucleon (crosses) [9] are also shown.

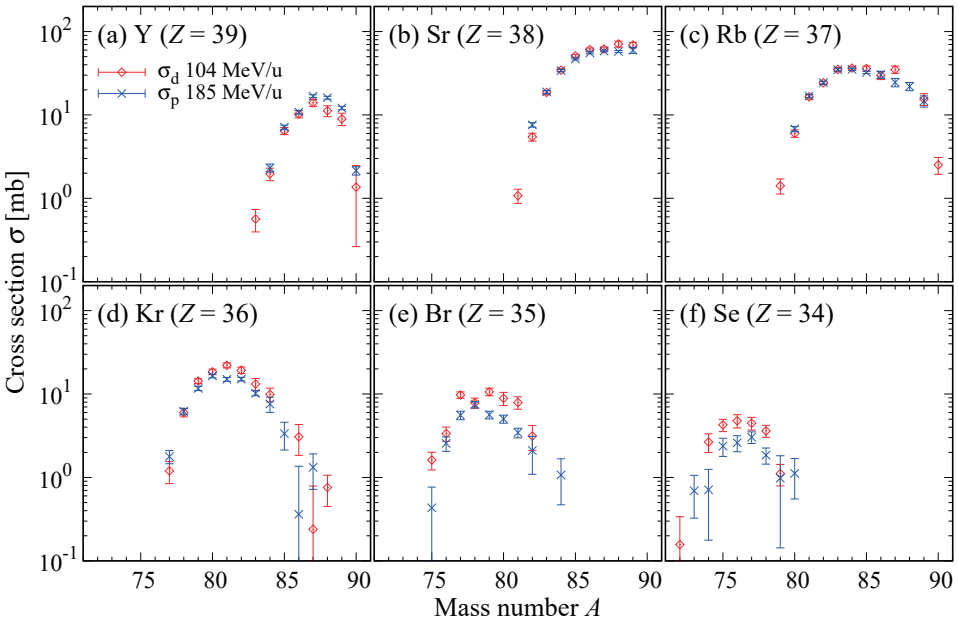

Figure 7: Same as Figure 6, but of deuteron-induced ones (diamonds).

Figure 6 shows the incident energy dependences of the cross sections with proton-induced reaction. In one-proton removal channel, which goes to ^{84,85,86,87}Rb at 104 MeV/nucleon, even-odd staggering effects were observed distinctly. This has not been reported in the previous ImPACT-related studies [3, 10].

Figure 7 shows the incident particle dependences of the cross sections with the total kinetic energies, 208 MeV for deuteron. The trends and orders of the cross section are in good agreement with 185 MeV for proton. However, the deuteron-induced reaction is expected the initial reaction mechanism to change drastically at lower energy [11], we would also like to obtain the reaction data for ^{90}Sr in the near future.

4 Conclusion

The isotopic-production cross sections for high-radiotoxic nuclide ^{90}Sr on proton and deuteron at 104 MeV/nucleon were obtained in inverse kinematics at the RIBF. The experimental data were compared with those obtained from the PHITS calculations. Some discrepancies to be improved still remain. In proton-induced reaction cross sections at 104 MeV/nucleon, one-proton removal channel which goes to ^{84,85,86,87}Rb observed even-odd staggering effects distinctly. More detailed analysis will be performed.

Acknowledgments

We are grateful to the accelerator staff of the RIKEN Nishina Center for providing a high-quality ^{238}U beam. This work was funded by the ImPACT Program of the Council for Science, Technology and Innovation (Cabinet Office, Government of Japan).

References

[1] K. Nishihara, "Data for Estimating Potential Radiotoxicity of Spent Nuclear Fuel", JAEA-Data/Code 2010-012 (2010).

[2] T. Kubo *et al.*,"BigRIPS separator and ZeroDegree spectrometer at RIKEN RI Beam Factory", Prog. Theor. Exp. Phys., 2012, 03C003 (2012).

[3] S. Kawase *et al.*, "Study of proton and deuteron induced spallation reactions on the long-lived fission product ^{93}Zr at 105 MeV/nucleon in inverse kinematics", Prog. Theor. Exp. Phys., 2017, 093D03 (2017).

[4] N. Fukuda *et al.*, "Identification and separation of radioactive isotope beams by the BigRIPS separator at the RIKEN RI Beam Factory", Nucl. Instrum. Meth. B 317, 323 (2013).

[5] T. Sato *et al.*, "Features of Particle and Heavy Ion Transport code System (PHITS) version 3.02", J. Nucl. Sci. Technol. 55, 684 (2018).

[6] A. Boudard *et al.*, "New potentialities of the Liége intranuclear cascade mode lfor reactions induced by nucleons and light charged particles", Phys. Rev. C 87, 014606 (2013).

[7] S. Furihata, "Statistial analysis of light fragment production from medium energy proton-induced reactions", Nucl. Instrum. Meth. B 171, 251 (2000).

[8] D. Mancusi *et al.*, "Improving the description of proton-induced one-nucleon removal in intranuclear-cascade models", Phys. Rev. C 91, 034602 (2015).

[9] H. Wang *et al.*, "Spallation reaction study for fission products in nuclear waste: Cross section measurements for ^{137}Cs and ^{90}Sr on proton and deuteron", Phys. Lett. B 754, 104 (2016).

[10] H. Wang *et al.*, "Spallation reaction study for the long-lived fission product ^{107}Pd", Prog. Theor. Exp. Phys. 2017, 021D01 (2017).

[11] H. Wang *et al.*, "Enhancement of element production by incomplete fusion reaction with weakly bound deuteron", Commun. Phys. 2, 78 (2019).

41. Detection of gamma ray from short-lived fission product at KUCA and KURNS-LINAC

Yasushi NAUCHI[1*], Jun-ichi HORI[2], Tadafumi SANO[3], Yoshiyuki TAKAHASHI[2], Koji KUSUMI[1] and Hironobu UNESAKI[2]

[1]Nuclear Technology Research Laboratory, Central Research Institute of Electric Power Industry
2-6-1 Nagasaka, Yokosuka-shi, Kanagawa 240-0196, Japan

[2]Institute for Integrated Radiation and Nuclear Science, Kyoto University
2, Asashiro-Nishi, Kumatori-cho, Sennan-gun, Osaka 590-0494, Japan

[3]Atomic Energy Research Institute, Kindai University
Kowakae, Higashi-Osaka, Osaka 577-8502, Japan

[*]Email: nauchi@criepi.denken.or.jp

Two kinds of γ ray spectrum measurement are performed. The one is for a critical core of enriched uranium (U) mocked up in Kyoto university critical assembly facility (KUCA). The other is for a U sample of natural enrichment to obtain microscopic nuclear data at an accelerator neutron source facility (KURNS-LINAC). In KUCA, discrete energy γ rays from 2.9 to 5 MeV are observed above prompt components. In KURNS-LINAC, also discrete energy γ rays of resemble spectrum are measured in a time-background region. By comparing the measured spectra to the numerical analyses of production and decay of isotopes originated in fission of ^{235}U, those discrete gamma rays are identified as those from decay of short -lived fission products.

1. Introduction

Fission products (FPs) play significant roles in power reactors. For example, the delayed neutron emissions from FPs mitigate power transient due to a reactivity insertion and the decay heat of FP may initiate a severe accident if it is not removed due to the station black out. In these regards, production and decay of FP must be predicted accurately. For those purposes, the data of the yield and the decay chains of FPs have been evaluated and compiled in libraries such as JENDL/FPY and FPD-2011 [1]. Those libraries have been developed based on γ ray spectra measured with scintillators and validated against measured decay heat [2,3]. However, they are seldom to be validated against isotopic data since γ ray data from short-lived FP are scarce.

Two kinds of experiments were conducted in the Kyoto university critical assembly facility (KUCA) and the LINAC neutron source facility of the institute of integrated radiation and nuclear science, Kyoto university (KURNS). In KUCA, γ ray spectrum was measured with a highly purified germanium (HP-Ge) detector for a critical core [4,5]. In KURNS-LINAC, U metal sample of the natural enrichment was irradiated by neutrons of white spectrum and the emitted γ rays from the sample were measured with the

same HP-Ge [6]. In the two experiments, resemble γ ray spectra were measured unexpectedly. In this work, the measurement and numerical analyses for the discrete γ rays are discussed to see whether the measured data are feasible for the validation of the yield and the decay chains of FPs.

2. Critical experiment

Details of the critical experiments and the identification of FPs had already been presented [4, 5], so only essential points are described. Schematic view of the set up is shown in Figure 1. The critical core was mocked up with fuel plates of uranium (U) - aluminum (Al) alloy, of which ^{235}U enrichment is 93 wt-%. The criticality is adjusted by the control rod position. 428 sheets of the plates were loaded into the C-core tank of KUCA. The effective core size was about 28 cm x 38 cm x 57 cm. The fuel plates were immersed in the light water. The core power was adjusted less than 4.6 mW. Outside the tank, a HP-Ge detector of the 35 % relative efficiency was put. Between the fuel plates and HP-Ge, there was light water layer of 60 cm thickness. By the arrangement, the neutron flux was well attenuated in the light water and the transmission γ rays were measured. γ ray count rate of was 13 kcps.

γ ray pulse height spectra of good resolution were obtained [4, 5]. In the spectra, 2.223 and 7.724 MeV γ rays from radiative capture of hydrogen (^{1}H) and ^{27}Al, respectively, are prominent. The spectrum in energy region from 2.9 to 3.9 MeV is magnified in Figure 2. The base continuum component of the spectrum is due to fission prompt γ rays.

Above the continuum spectrum, discrete energy γ rays are found. Distinct peaks are of the photo-electric, the single escape, and the double-escape components of γ rays from ^{27}Al(n,γ) reactions. However, peaks of fewer count rates are observed. By comparison of the small peaks to the calculation described in Section 4, the peaks are considered to be the components due to short lived FPs such as ^{87,88}Br, ^{89}Kr, ^{90,90m,91}Rb, ^{95,97,98}Y, ^{136}Te. Since 93 wt% -^{235}U metal fuel was used in the water, almost all the FP were originated in fission of ^{235}U. As for ^{90}Rb, the γ ray peak of 4136 keV is overwrapped ^{27}Al(n,γ) components. However, they were confirmed by the measurement posterior to the critical operation. Instead, γ rays of half-life shorter than 1 minutes could not be measured posterior to (from one to three minutes) that due to the statistical fluctuation. It is the advanced feature of the measurement under the critical condition to enable detections of γ rays from FPs of half-life shorter than 1 min ($^{97, 98}$Y, for example). Whereas, due to the prompt components, the peak to base ratio was small.

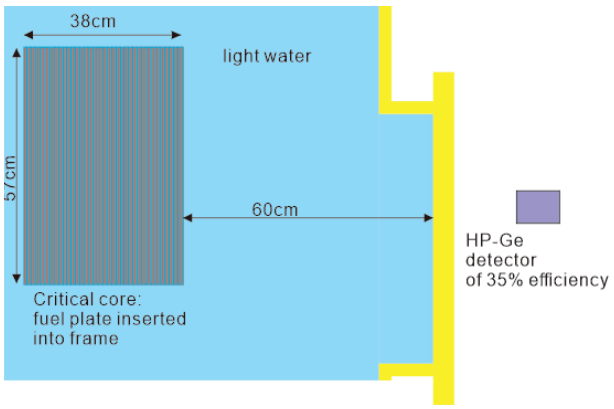

Figure 1. Side view of the critical core and HP-Ge detector. Yellow lines are of aluminum alloy.

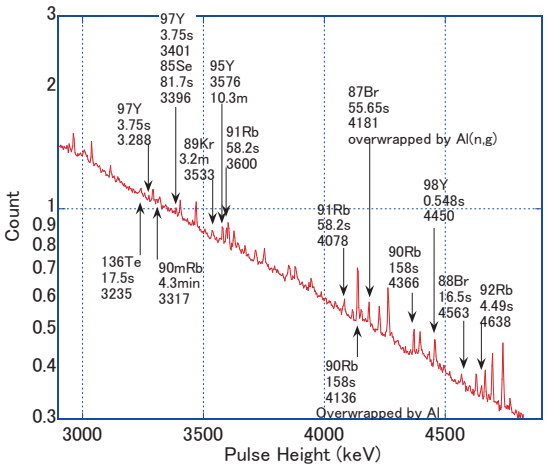

Figure 2. Measured γ ray spectrum for critical core.

3. Microscopic Nuclear Data Measurement

The original purpose of the microscopic nuclear data measurement was to obtain γ ray spectrum from reactions of ^{238}U induced by neutrons of thermal and resonance energies. The energy of the incident neutron is determined by the time of flight (TOF) of the neutron between the target and the sample.

At KURNS-LINAC facility, accelerated electrons were injected onto a tungsten (W) target and bremsstrahlung rays were radiated. Then photo-nuclear reactions were induced, and fast neutrons were emitted. The neutrons were moderated to the resonance and thermal energy regions in the light water surrounding the W target. U metal sample was set effectively 11.3 m from the W target. The size of the sample was 4 cm x 4cm and the thickness was 2.91 g/cm^2. For the TOF measurement, pulsed neutron source was used with frequency of 50 Hz. The same HP-Ge was set 5 cm from the sample. The detector was shadowed from the neutron and the γ ray flash from the W target with a collimator. The energy dependent γ ray detection efficiency was measured by detection of the γ ray spectrum from the radiative capture of ^{35}Cl.

The TOF spectrum was shown in Figure 3. Events of the earlier TOF is generally induced by the faster neutrons. The events induced by fast neutrons of energy greater than keV could not be measured since influence by the γ ray flash from the W target still remains in earlier TOF. The peak spectrum in Figure 3 corresponds to the radiative capture at the resonance neutron energy. In the lower energy, broad peak structure is found. It is called “thermal peak”. After the decay out of the thermal peak, flat component is found, which is treated as the time background components for the original purpose. In the present work, the γ ray pulse height spectrum in the time background region was focused on. Figure 4 shows the pulse height spectrum. Since the time region was after the thermal neutron decays out, prompt γ rays from radiative captures and the fissions do not exist. Accordingly, this component was considered due to decay of FP of half-life longer than 10 ms. By comparison of the peaks to the data in Figure 2, the same γ rays were measured although ^{92}Rb, ^{88}Br, and ^{136}Te are not observed. Generally, the counting statistics is poorer in this time-background condition. Instead, the better peak to base ratio was given thanks to the attenuation of the prompt γ rays from the radiative capture and the fission reactions.

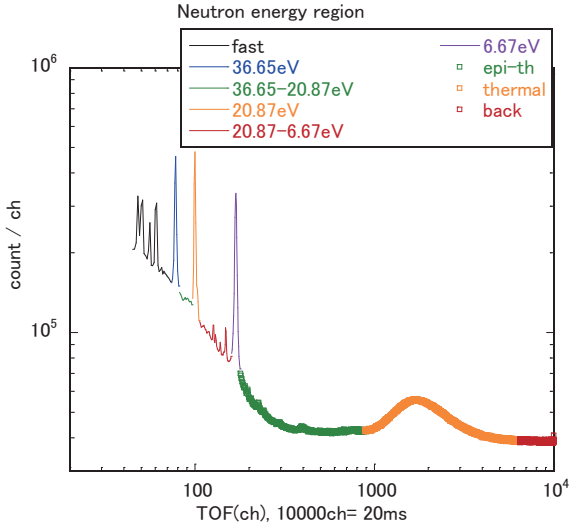

Figure 3. Time of flight spectrum for estimation of energy of incident neutron.

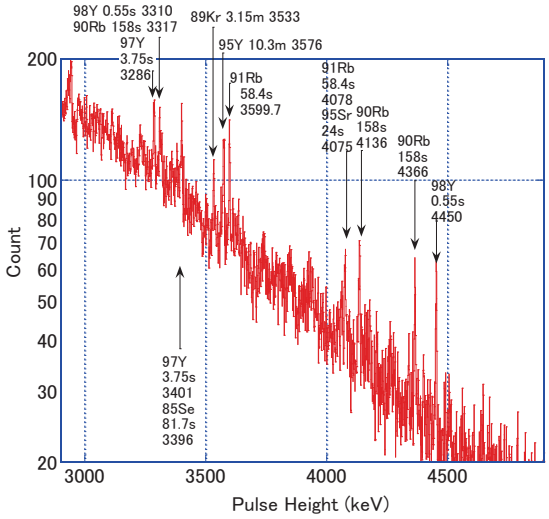

Figure 4. γ ray spectrum at time background. Nuclides in labels denote β-decay parents of delayed γ rays.

0.72% of the metal sample was ^{235}U and that was also irradiated by the thermal neutron. Accordingly, a part or almost all FPs might be generated by fission of ^{235}U. However, it should be also noted again that neutron flux in energy region higher than keV had never been characterized by the γ ray flash. Accordingly, there is a possibility that some FPs are generated by fission of ^{238}U induced by neutrons faster than the threshold energy (~MeV).

4. Comparison to Calculation

In the both measurements in KUCA and KURNS-LINAC, the neutron flux was low so that radiative captures of produced FPs can be neglected. In such cases, the activities of FPs are determined by the radioactive decay and the fission rate. In this work, it was assumed that all FPs were produced by fission of ^{235}U induced by the thermal neutrons. The depletion after the instant irradiation was calculated by Bateman's method [7] in an exact manner, based on the JENDL/FPY & FPD-2011 library. Then the activity was integrated for time lengths of the neutron irradiation and of the γ ray measurement. For the critical experiments, the flux variation with time was also considered. For the microscopic data measurement, fission rate was assumed as the continuous wave operation and the measurement time was also continuous, in spite that the fission occurred periodically induced by the pulsed neutron source and only γ ray spectrum during the time background region was measured. Then using the data in JENDL/FPD-2011, the number of emissions of the discrete γ rays were deduced. The measured γ rays were identified by comparison to the calculated γ rays of larger emission rates as shown in Figures 2 and 4.

Quantitative analyses were also performed. For the critical experiments, the γ ray pulse height spectrum was simulated with the MCNP-5 code [8] and the AcelibJ40 library [9] based on JENDL-4.0. At first, the fission reaction distribution in each fuel plate was estimated by a neutron transport calculation in the manner of the eigenvalue calculation. In the next step, the γ rays of each energy shown in Figure 5 were transported from the fuel. The spatial distribution of the γ ray emission is treated similar to that of calculated fission reaction rates. In the calculation, the threshold energy of the γ ray transport was set 1.6MeV outside the HP-Ge detector. Inside the detector, it was set down to 3 keV. For the tally, photon - electron coupled transport was done and the pulse height response was calculated. The calculated count rate for the pulse height was compared to the measured one in Figure 5.

For the microscopic data measurement, the experimental count rates were divided by the energy dependent efficiency measured using the $^{35}Cl(n, \gamma)$ reaction. The deduced ratio is considered proportional to the number of photon emission. Then, the calculated one was compared to the deuced one in Figure 6.

In the both figures, the absolute values of C/E do not make sense since the absolute efficiency was not known in the critical core and the continuous wave operation was assumed in the microscopic data measurements. C/E for each γ ray depends on FP and γ ray energy. However, variation of C/E with FP is resembled each other in the two measurements. That indicates significant part of the discrete energy γ rays were radiated from the same FP produced by the fission reactions of the same fissionable nuclide. Accordingly, the two kinds of experiment are considered worth to be investigated further to obtain the reference data for validating FP yield and decay data libraries.

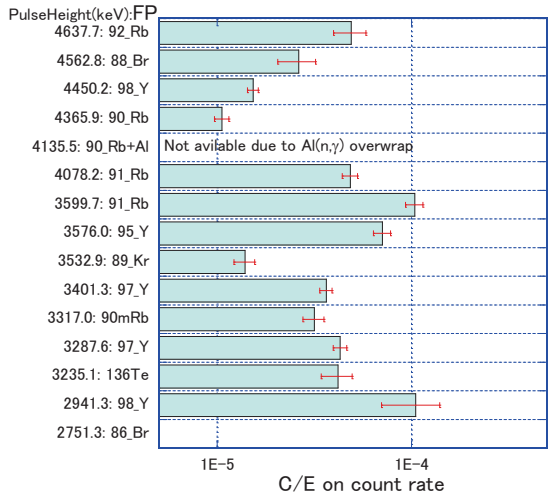

Figure 5. Comparison of calculated photo-electric peak counting to that by the measurement in KUCA.

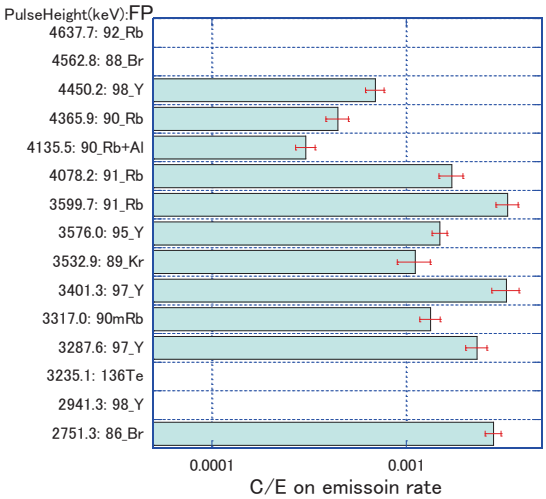

Figure 6. Comparison of calculated number of γ ray emission to that by measurement in KURNS-LINAC.

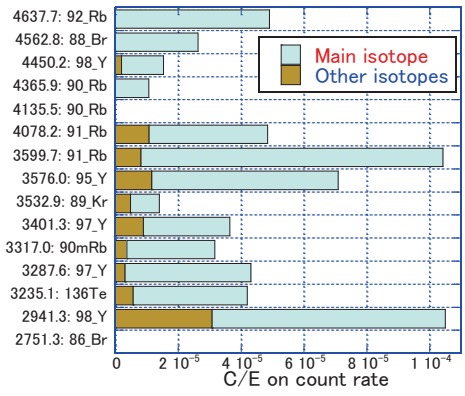

Figure 7 Contribution of other FPs to the count rate of target FP.

For the validation, additional measurements or improvements of the methods are required. For the critical core in KUCA-C, experimental methods to determine the energy dependent γ ray detection efficiency is desired. Besides, analyses of the prompt components by the radiative capture and the fission are mandatory. Whereas, for the microscopic data measurement in KURNS-LINAC, quantification of neutron flux in energy region higher than 500 keV was required to see whether fission reaction of ^{238}U was significant or not. Besides, the numerical analysis of the production of FP in the pulse mode operation and the decay of them in the time region posterior to decay out of the thermal neutrons must be achieved. Another issue is the resolution of the HP-Ge detector. Various energies of γ ray are radiated from FPs produced by the fission of ^{235}U. Consider a measurement of with a HP-Ge detector of a resolution of ± 5 keV. With the detector, γ rays of energies within the error of ±5 keV is measured in a peak spectrum. Based on the JENDL/FPY & DPF-2011, the contribution of the main isotope and the other isotopes are calculated. As shown in Figure 7, considerable fraction of counts of a peak are attributed to the other components. In that sense, validation of FP yield and decay data should not be focused only on a single γ ray but comprehensive set of evaluated FPs should be validated against the measured data.

5. Conclusion

At KUCA, γ rays radiated from short-lived FP were measured in a critical core under the intense background of prompt components of fission and radiative capture reactions. At KURNS-LINAC, they were also measured for metallic U sample irradiated by white neutron source in the time region where the thermal neutrons decayed out. The energy of the γ rays and corresponding FPs were identified by comparison of the measurement to the depletion calculations based on JENDL/FPY & FPD-2011 library. γ ray count rates and emission rates were numerically calculated and compared to the measured data of KUCA and KURNS-LINAC, respectively. The ratio of the calculation to the measurement varied with FPs. However, the trend of the ratio for the KUCA experiment is resemble to that for the KURNS-LINAC experiment. The results indicate that the FP γ rays produced by fission reaction of ^{235}U induced by thermal neutrons are the major components in the both measurements. The both measurement techniques are superior in detection of short-lived FPs compered to measurements posterior to neutron irradiation. Accordingly, the γ ray spectroscopy for the critical core and that for a uranium sample posterior to decay - out of the thermal neutrons are promising to give reference data to validate the FP yield and decay data. For that, necessary improvements of the methods shall be conducted.

References

1) Katakura, J., JENDL FP Decay Data File 2011 and Fission Yields Data File 2011, JAEA-Data/Code 2011-025, 2012.
2) Algora, A., et al., Reactor Decay Heat in ^{239}Pu: Solving the γ Discrepancy in the 4–3000-s Cooling Period, Phys. Rev. Lett., vol.105, 2010, p. 202501.
3) Dickens, J.K., et al., Fission Product Energy Release for Time following Thermal Neutron Fission of ^{239}Pu. Nucl. Sci. Eng., vol. 78, 1981, p.126.
4) Nauchi, Y., Sano, T., Unesaki, H., et al., Spectrum measurement of gamma ray from KUCA-C critical core, Proceedings of Fall meeting of Atomic Energy Society of Japan, On-Line, September, 2020.
5) Nauchi, Y., Sano, T., Takahashi, Y., et al., Gamma Ray Spectroscopy of Fission Product in Fuel Assembly, Proceedings of the 41th Annual Meeting of Institute of Nuclear Material Management, Japan Chapter, On-Line, October, 2020.
6) Nauchi, Y., Hori, J., and Sano, T., Quantification of Gamma Ray Emission from Capture Reaction of Uranium-238, KURNS Progress report 2019, 2020, CO2-2.
7) Bateman, H., The solution of a system of differential equations occurring in the theory of radioactive transformations. Proc. Cambridge Phil. Soc. 15, 1910, p.15.
8) X-5 Monte Carlo Team., MCNP^{TM} – A General Monte Carlo N-Particle Transport Code, Version 5, LA-UR-03-1987, Los Alamos National Laboratory (LANL) (2003).
9) Sato, T., Niita, K., Matsuda, N., et al., Particle and Heavy Ion Transport Code System PHITS, Version 2.52, J. Nucl. Sci. Technol., vol. 50, no.9, 2013, pp. 913-923.

Acknowledgements

The experiments at KUCA and KURNS-LINAC had been carried out in part under the visiting researcher's program of the Institute for Integrated Radiation and Nuclear Science, Kyoto University.